TENTH INTERNATIONAL SYMPOSIUM

on

UNMANNED UNTETHERED SUBMERSIBLE TECHNOLOGY

Proceedings of the Special Session on Bio-Engineering Research Related to Autonomous Underwater Vehicles

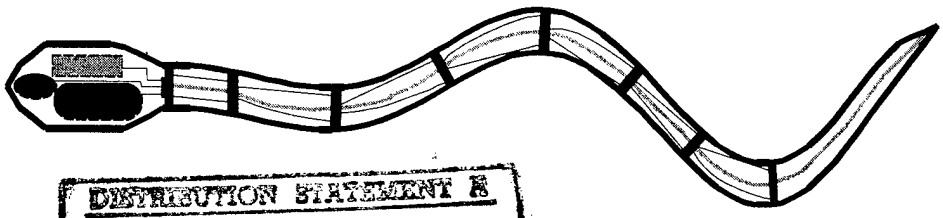

September 10 & 11, 1997

Organized by

Autonomous Undersea Systems Institute

Sponsored by

Office of Naval Research

REPORT DOCUMENTATION PAGE

Form Approved
OMB No. 0704-0188

1. AGENCY USE ONLY (Leave blank)	2. REPORT DATE	3. REPORT TYPE AND DATES COVERED
	10 October 97	Final Report

4. TITLE AND SUBTITLE

Special Session on Bio-Engineering Research Related to Autonomous Underwater Vehicles

5. FUNDING NUMBERS

G N00014-97-1-0971

6. AUTHOR(S)

James C. Jalbert, Compiler

7. PERFORMING ORGANIZATION NAME(S) AND ADDRESS(ES)

Autonomous Undersea Systems Institute
86 Old Concord Turnpike
Lee, NH 03824

8. PERFORMING ORGANIZATION REPORT NUMBER

ONR 0971

9. SPONSORING/MONITORING AGENCY NAME(S) AND ADDRESS(ES)

Office of Naval Research
800 N. Quincy Street
Arlington, VA 22217-5660

10. SPONSORING/MONITORING AGENCY REPORT NUMBER

11. SUPPLEMENTARY NOTES

12a. DISTRIBUTION/AVAILABILITY STATEMENT

12b. DISTRIBUTION CODE

13. ABSTRACT (Maximum 200 words)

A cross disciplinary session was organized by the Autonomous Undersea Systems Institute (AUSI) as part of the 10th International Symposium on Unmanned Untethered Submersible Technology. The Symposium was held at the New England Center at the University of New Hampshire during the period of September 8 - 11, 1997.

This special session was organized to promote cross disciplinary interchange of ideas, technology, and research advances between AUV investigators and Bio-engineering researchers. Fifteen papers were presented during this session and was attended by fifty people approximately equally divided between AUV investigators and Bio-engineering researchers.

This report is a compilation of the papers presented at the special session on Bio-Engineering. Feedback from attendees was very positive in terms of the two groups exchanging technology and ideas. A major suggestion from many attendees was to integrate the bio-engineering papers into the regular symposium, rather than have the session somewhat separate, to allow for more time to assimilate each others concepts and to provide more interpersonal discussion time.

14. SUBJECT TERMS

AUV, Bio-Engineering, Bio-locomotion, Artificial muscle actuators, biologically-based systems

15. NUMBER OF PAGES

165

16. PRICE CODE

17. SECURITY CLASSIFICATION OF REPORT	18. SECURITY CLASSIFICATION OF THIS PAGE	19. SECURITY CLASSIFICATION OF ABSTRACT	20. LIMITATION OF ABSTRACT
Unclassified	Unclassified	Uncassified	

TABLE OF CONTENTS

Title:

A Path to Highly Maneuverable Underwater Vehicles (HIMUVs): Simple Physical Modeling of Biolocomotion in Fluids

Authors:

Charles A. Pell (presenting),
Ian Keller, Brett Hobson,
Gordon Caudle, and Steve Wainwright

Bio-Design Studio,
at Duke University
and
Nekton Technologies, Inc.,
of Durham, NC.

Abstract:

Many UUV development teams seek to mimic the locomotor performance of aquatic organisms by using complex arrangements of rigid parts and complicated control schemes. Biologists point out that too little is known about the detailed function of the living structures to permit the true fidelity of such manmade designs. Accordingly, we model the exterior morphology and gross mechanical properties of living propulsive structures using one-piece flexible designs instead of articulated machinery. We have succeeded in reproducing biomimetic kinematics and maneuvering behaviors via single-channel oscillations of simple compliant bodies of appropriate shape and material properties. We have demonstrated that one channel of input is sufficient for the control of both thrust and the direction of thrust application. Compliance thus permits simplicity in the design of reliable, effective biomimetic propulsors, which we have named Nektors™. These propulsors form the foundation for our highly maneuverable underwater vehicle (HIMUV) prototype, the PilotFish™.

1. Goals

The goals of our group at the Bio-Design Studio in the Zoology Department at Duke are to study the functional morphology of aquatic animals in order to illuminate their mechanisms of propulsion, maneuvering, and control. The Bio-Design Studio's approach is 3-D modeling of the bodies and locomotor organs of aquatic animals in materials that are reasonable mimics of the tissues of which the structures are grown. Our mantra is "Simple Models."

Our current project at Nekton Technologies, Inc., is to design and build a HIMUV based on selected structural and functional features of highly maneuverable aquatic animals using the principles of modeling discovered at the Bio-Design Studio and in our zoological research. The goal of the commercial development is to use compliance to produce a simple, reliable and effective maneuvering propulsor for the UUV industry.

2. The challenge, and the approach

Animals are structurally complex, they can deform and propel themselves in diverse ways, and the degree of control they have over their motions is still being researched. No scientist has all of the data required to understand such systems completely. We have taken the approach to study the beast as it swims, take it apart to see how parts move and which can transmit force, and then to make simple, first approximation models.

The tricky part is to identify the few structural features in a complex animal that are essential for swimming. We do this by watching and filming swimming animals under controlled conditions and then by deciding which structural elements we see in dissections are critical to the observed motions (Westneat et al., 1993). When we think we know which features are important, we make a simple physical model embodying these and leave out 99% of the animal's complexity. We then actuate the model in the working fluid to see if it exhibits lifelike kinematics. If it doesn't, we go back and look again at the animal as scientists and repeat the design and test process.

By doing this first for parts of a fish, for example, such as the backbone or the swimming muscles and their force-transmitting collagenous septa and tendons, or the unpaired or paired fins, we can then assemble the parts into a whole fish model. Often during this

process, we discover short-cuts that show us even more of the fish that can be left out.

3. An early model

An early result of our work is the Twiddlefish™ (Figure 1). This is a 5" long rubber fish with a torsionally stiff cable extending up from the back of its head to a coaxial handle that can be rotated been your thumb and forefinger. If the fish is immersed in water and the handle oscillated in rotation about the axis of the cable, the head follows the cable input while the subsequent lateral motions of the body and tail exhibit a phase lag as momentum is transferred from the body to the fluid. The body thus exhibits a rearward traveling wave and thrust emerges via a reverse Von Karmon vortex street in the fluid, as happens when a live fish swims. This thrust is sufficient to allow it to get away from you if you don't hold the handle tightly. Twiddlefish™ is an educational toy that is for sale in science museums across the country. Devices much like it (the Nektor™ propulsor) form the basis of our development efforts, and are our entry into the world of AUVs.

We are developing Nektors™ as maneuvering thrusters much like the propulsive limbs of aquatic animals, from low aspect ratio forms (fishlike) to high-aspect ratio designs (winglike). These propulsors have proved capable of delivering the requisite forces for maneuvering small (1-2 meter) rigid-hulled AUVs. Aside from animals' producing these relatively large-magnitude, short duration forces, they can achieve maneuverability via body flexibility. Though NTI will eventually build flexible-hulled submersibles to take advantage of this fact, we believe that AUVs can achieve a large measure of biomimetic maneuverability right now through the use of Nektors™.

4. What we've learned: compliance permits simple design

The first thing we learned from our simple models are that only 3 features are required to swim: (1) an appropriate shape (streamlined, proper distribution of thickness, aspect ratios, etc.), (2) appropriate material properties (modulus, resilience, etc.) and (3) the application of an oscillating force along a single axis. This recipe works for fishlike bodies, wings, or any other biomimetic, oscillatory fluid propulsive structure.

In the case of our fish models, for example, this permits the construction of devices that produce thrust in water by propagating waves of bending backward along the body. The toy Twiddlefish™ swims in water, as opposed to air (low density) or Karo corn syrup (low Reynolds numbers). It swims best if the cable attaches to where in fish the swimming muscle becomes active just behind the head and the action is propagated backward along the body. We have made models that swim undulatory fashion in air, but their dimensions, actuation frequency, density and modulus differ from the rubber toy Twiddlefish™.

The next most important thing we have learned from these simple physical models is how important is the multi-axis motion of the head and body of a live fish. Fig. 2A shows a package of lines each of which represents the midline of a swimming fish model seen from above. Each line is labeled in sequence. If you look at a bend near the head of the model, you will see that it propagates backward in subsequent lines. Notice that all loci move sideways (heave), yaw (pitch), and fore and aft while the fish model is moving forward. This is no surprise: body segments, fins and wings of all swimming and flying animals that have been studied are known to sweep in such multi-axis paths, commonly figure-eight lissajous, due to the requisite phase lags.

Fig. 2B is a similar set of lines taken from a video of a swimming model cast of a bluegill that is driven from above by a rod that does not permit either the sideways or fore-and-aft motion of the forward swimming model. Note the node formed by the driveshaft's lack of compliance.

When we swam a model with such a restrictive driveshaft in a flow tank, we found the result typified by the graph in Fig. 3. Fig 3 is a schematic showing how fast a typical model swims as we increased the tailbeat frequency. The lower dashed curve shows the model driven by a rigid driveshaft. Swimming speed increased for a bit (the model exhibited a "normal" propagated wave) and then dropped to nearly zero (where the waveform of the body was a standing wave equal to the body length). By exchanging the rigid driveshaft for a compliant one that permits the multi-axis motion of the model, as in Fig. 2A, we learned that swimming speed can rise continuously: the models exhibited only propagated waves (Fig 3, upper curve).

Since we are developing a thrusting device to mount on AUV hulls, this tells us of an important design feature that our simple device must have if it is to work and to compete with propellers as thrusters for HIMUVs. It is worth noting that the off-axis motion of flapping wings, fins and tails is well documented in the literature for all swimming and flying animals. For AUVs using such biomimetic tuned compliant drives, the thruster stalks serve as low band pass filters allowing smooth thrust input for cruising.

We also learned that Nektors™ produce little radiated noise in the TRANSDEC acoustic pool. Their noise is nearly lost in the low frequency (<10 Hz) background noise of the quiet tank, suggesting stealthy operation at sea.

5. Our current project: the Pilotfish™

We have begun designing and building a HIMUV we call the Pilotfish™ (Fig.4). It has 4 Nektors™ mounted about the periphery a rigid spheroid hull platform 1 meter long. We measured the forces required to reorient such a hull in roll and in yaw (pitch), and we measured the drag acting on the same hull at 1 meter per second moving both axially and broadside. We also measured the thrust output of several small Nektor™ models, to compare with the forces mentioned above. We found that four 25 cm Nektors™ located about the hull periphery provide more than enough thrust to allow the PilotFish™ to equal or exceed the maneuvering performances (turning radius, turn rate, cruising speed, etc.) disclosed by the manufacturers of commercially available UUVs, several of which use more than PilotFish's™ four motors. In addition, it is likely that PilotFish's™ use of unsteady thrust production will allow maneuvers presently unobtainable by propeller-driven UUVs, as the non-lift-based hydromechanical mechanisms of force output (drag, dynamic stall, etc.) give multiples of the force output for lift-based foils of the same size moving at similar speeds, especially during accelerations from a standing start (Vogel, 1994).

We believe that simple, compliant propulsors offer effective means to achieve biomimetic maneuverability when combined with present UUV platforms and support systems.

Some advantages of a Nektor™ thruster, and the HIMUV:

- Single channel of input controls thrust and direction of thrust
- Uses just 4 thrusters to achieve full 6° of freedom
- Radical accelerations via unsteady thrust production
- Tuned compliance permits smooth hull motions when desired
- Permits bio-maneuverability using present UUV support systems
- Compliant thrusters flex & rebound on impact (also: diver safety)
- High work of fracture (toughness): resists abrasion and tearing
- Stealthy thrust production

Some challenges:

- Presently less appropriate for long-range cruising than high efficiency rotary propellers
- Control algorithms for UUV control yet to be refined

Next steps:

- Complete construction and testing of PIlotFish™ prototype
- Implement 6° of freedom control development program
- Hybrid design: combine HIMUV with long range

We are pleased to acknowledge the encouragement and financial support of ONR contracts N00014-96-0008 and N00014-96-0319, the expert guidance and straight talk of Dan Ladd at NRaD's Water Tunnel, Howard Lynch's help at the TRANSDEC acoustic facility, and the moral support and advice of our colleagues in the world of biology and biomechanics.

References:

Westneat, M.W., Hoese, W., Pell., C.A., and Wainwright, S.A.. *The Horizontal Septum: Mechanisms of Force Transfer in Locomotion of Scombrid Fishes (Scombridae, Perciformes)*. Journal of Morphology 217:183-204 (1993)

Vogel, S. Life in Moving Fluids. (1994) Princeton Press.

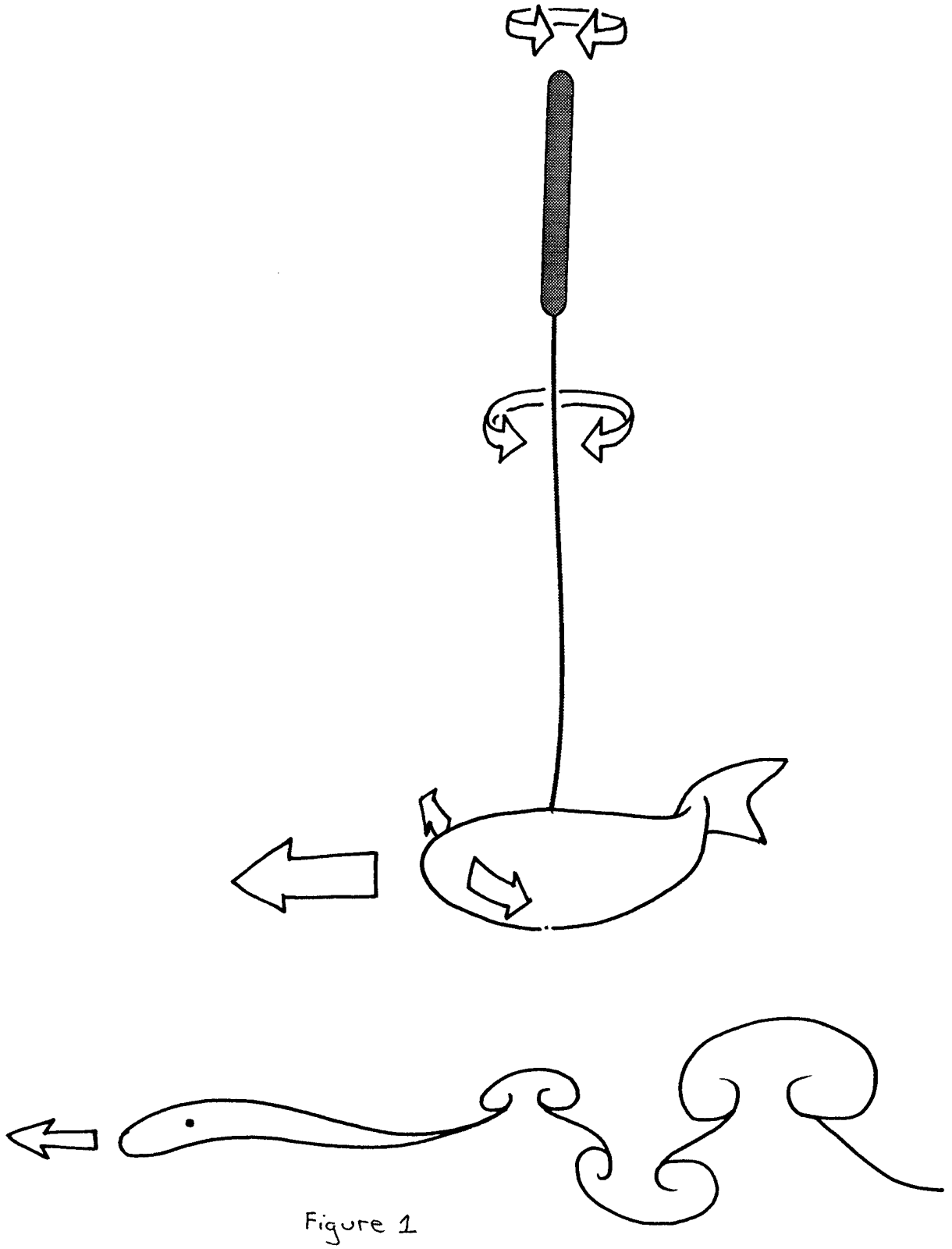

Figure 1

Waveform of Nektor with compliant driveshaft, 3 hz, 7 frames

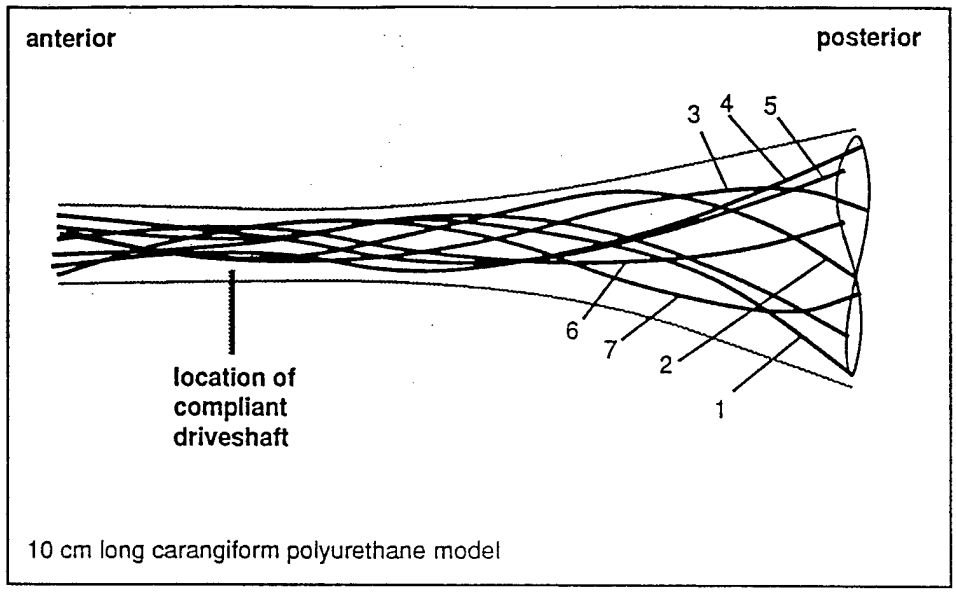

Figure 2A

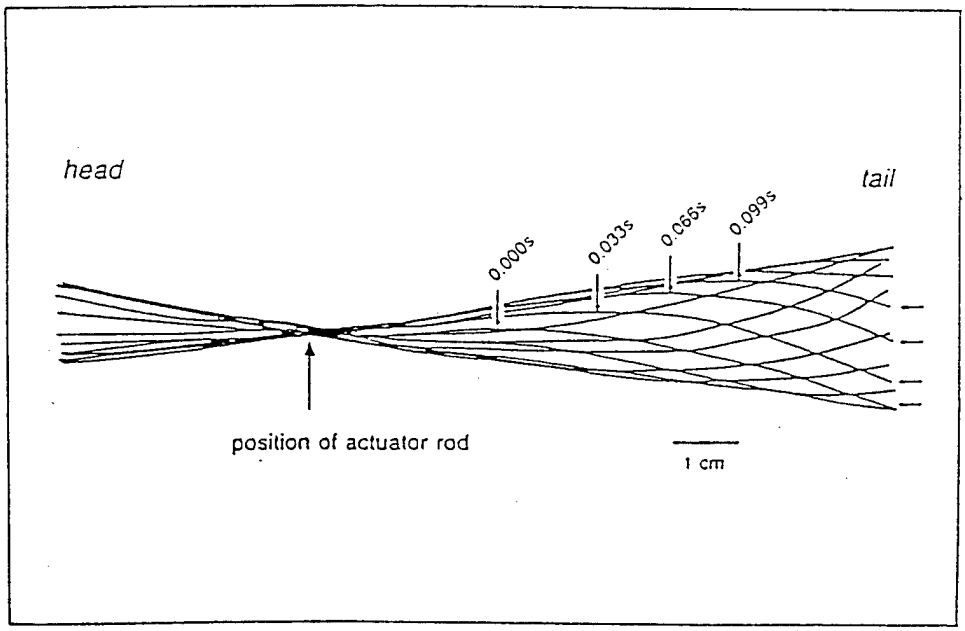

Figure 2B

Propulsor swimming speed as a function of driving frequency

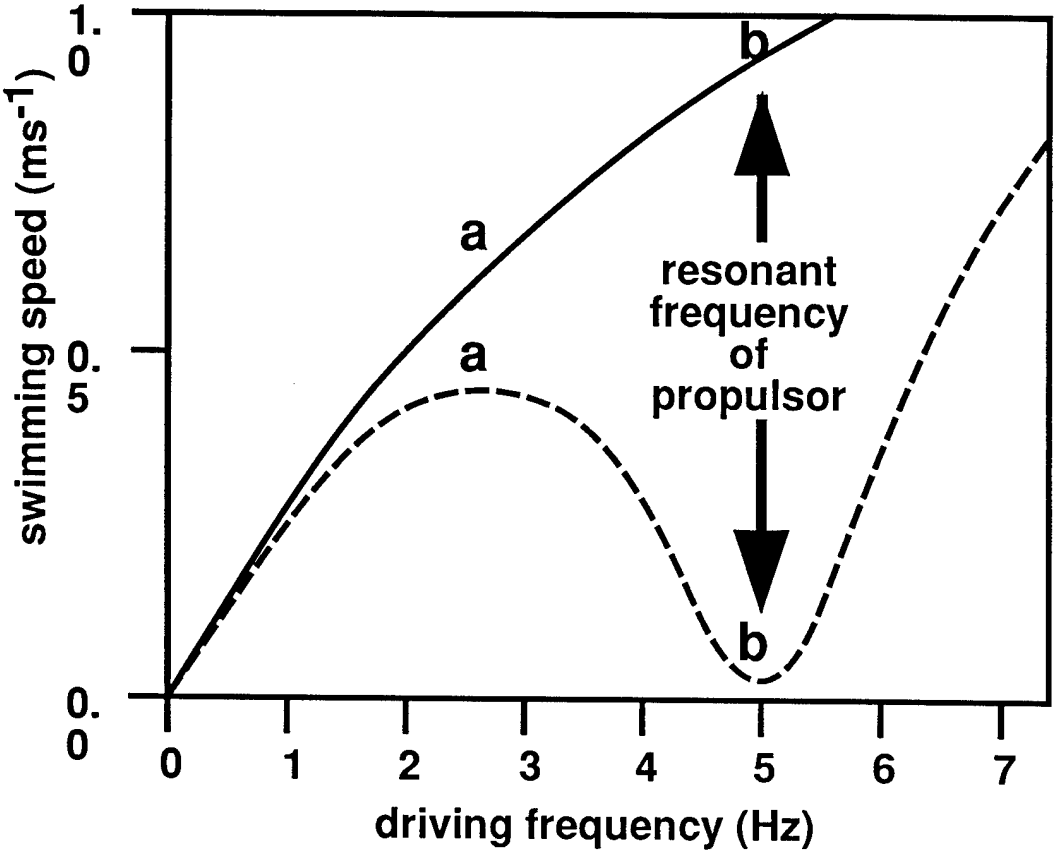

propulsor with compliant driveshaft
propulsor with rigidly mounted driveshaft

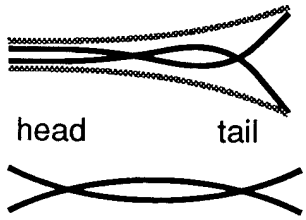

proper propagating waveform of a propulsor with our compliant driveshaft, at the resonant freq.

ineffective standing waveform of a propulsor with a rigidly mounted driveshaft, at the resonant freq.

Figure 3

PilotFish™

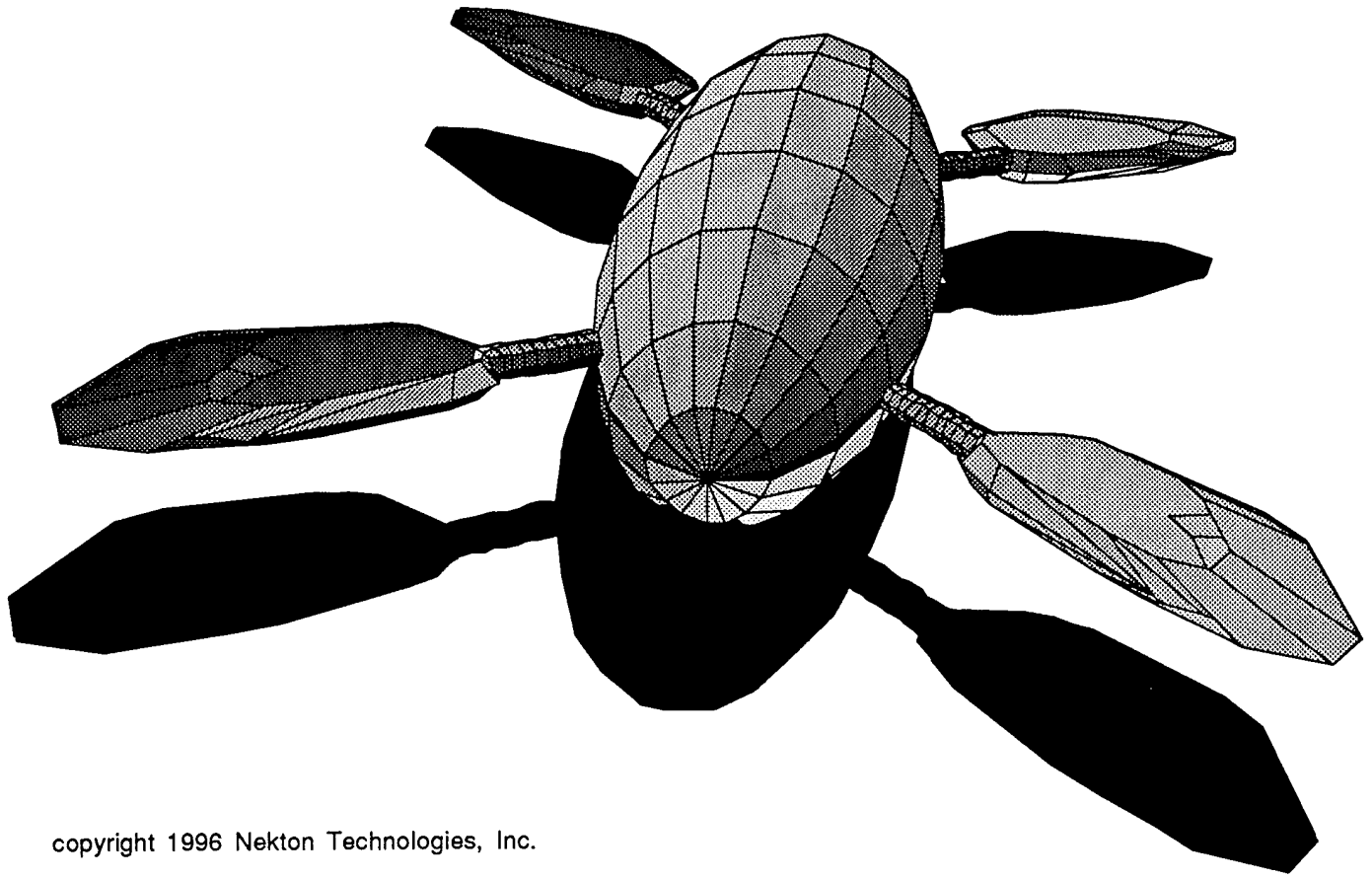

Figure 4

FLUID MECHANICS AND ROBOTICS OF FISH-LIKE LOCOMOTION

M. Triantafyllou, D.K.P. Yue
(617) 253-4335, mistetri@mit.edu; (617) 253-6823, yue@mit.edu
Massachusetts Institute of Technology, Cambridge, Massachusetts 02139

M. Grosenbaugh
(508) 457-2000, magross@loon.whoi.edu
Woods Hole Oceanographic Institution, Woods Hole, Massachusetts 02543

Vorticity control in fish–like locomotion has been shown to provide optimal propulsive efficiency and outstanding maneuvering characteristics. Novel flow visualisation methods allow detailed mapping of vortical patterns, which can be used for identifying the principal mechanisms at work, and for improving real–time vorticity control schemes. The robotics of flexible hull actuation have been succesfully developed and applied first in the RoboTuna *and then the* RoboPike, *but further progress is needed before we fully exploit the tremendous potential of fish–like locomotion.*

MASSACHUSETTS INSTITUTE OF TECHNOLOGY

September 1997

FISH GENERATE AND CONTROL LARGE EDDIES

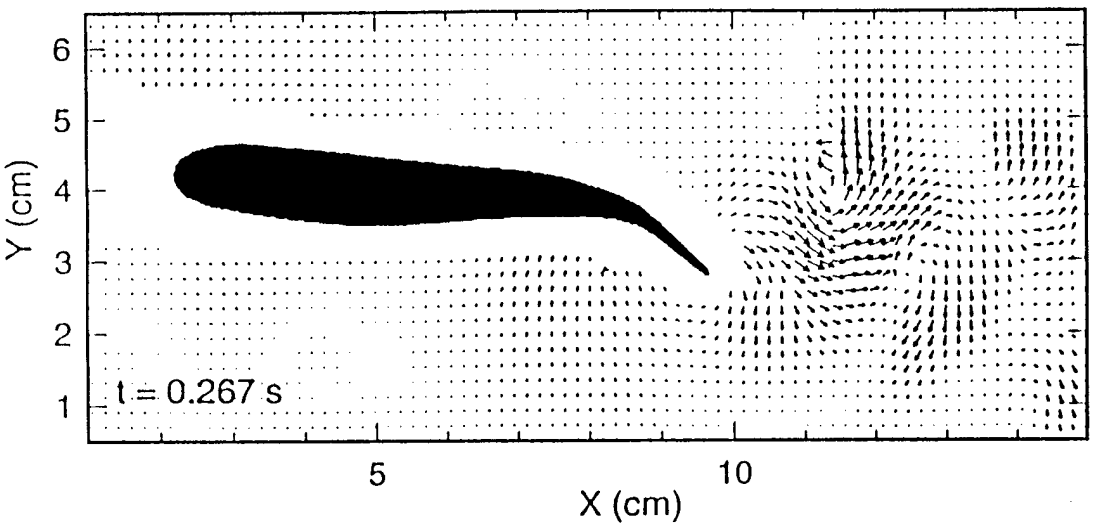

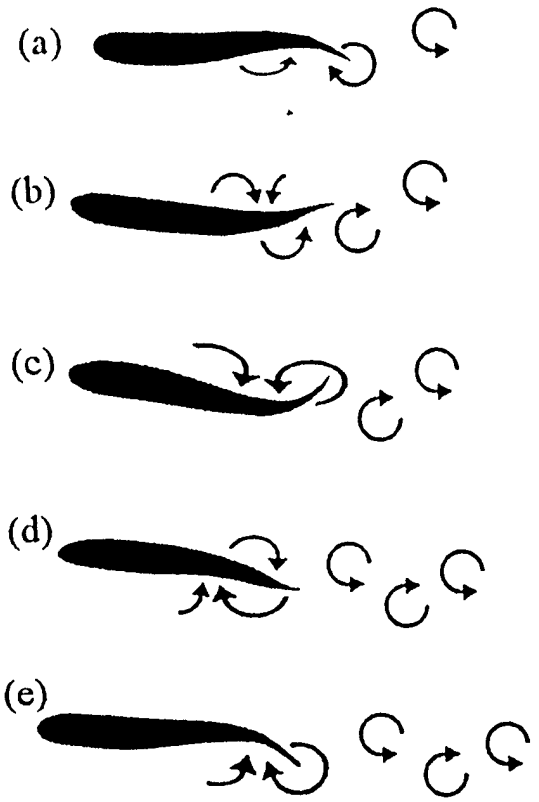

BASIC MECHANISM OF VORTICITY CONTROL

VORTICES DEVELOP
ALONG THE BODY
REDUCING DRAG

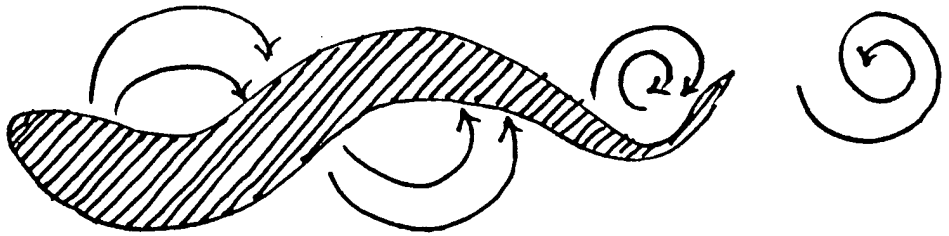

THE TAIL REPOSITIONS
THE VORTICES TO
CREATE PROPULSIVE JET

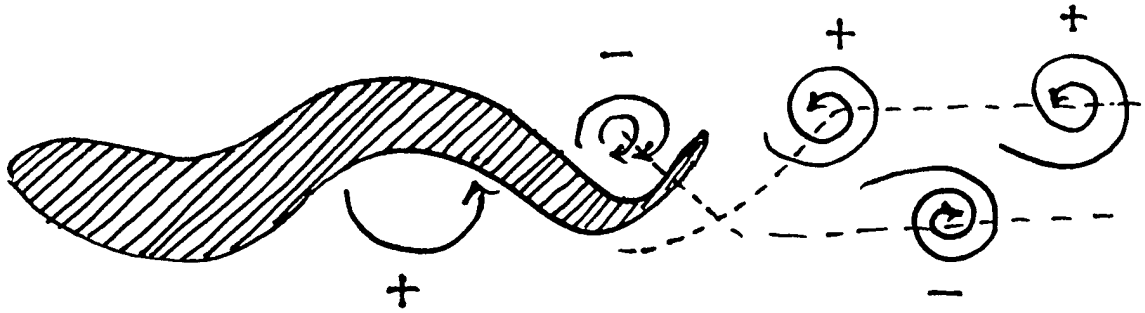

A TUNA OF ALUMINUM AND LYCRA

The body consists of aluminum links connected by hinges. Six motors, external to the robot, supply the power to mimic the undulatory swimming of a real tuna. Separate systems of pulleys and tendons transfer torque from each motor, while isolating the motion of the links. The robotic fish hangs from a carriage.

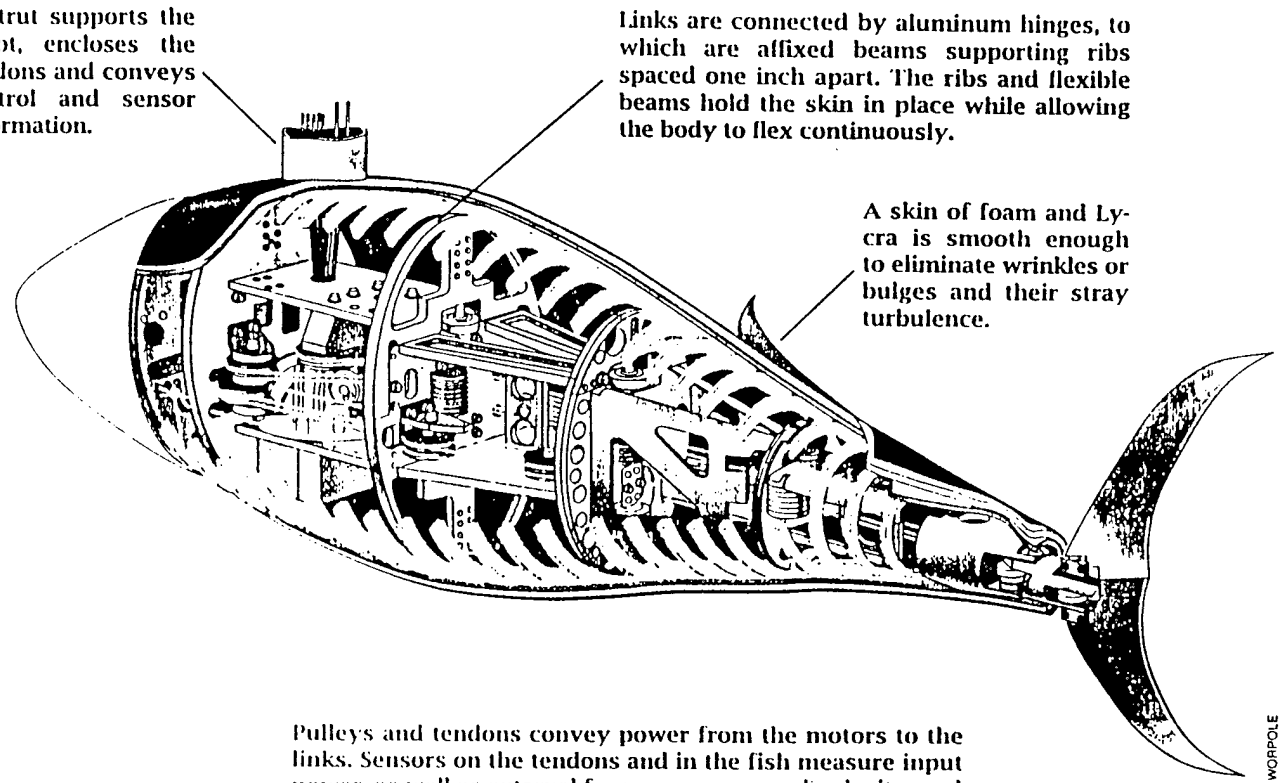

IDLERS DECOUPLE DEGREES OF FREEDOM FOR HIGH PRECISION MULTI-VARIABLE CONTROL

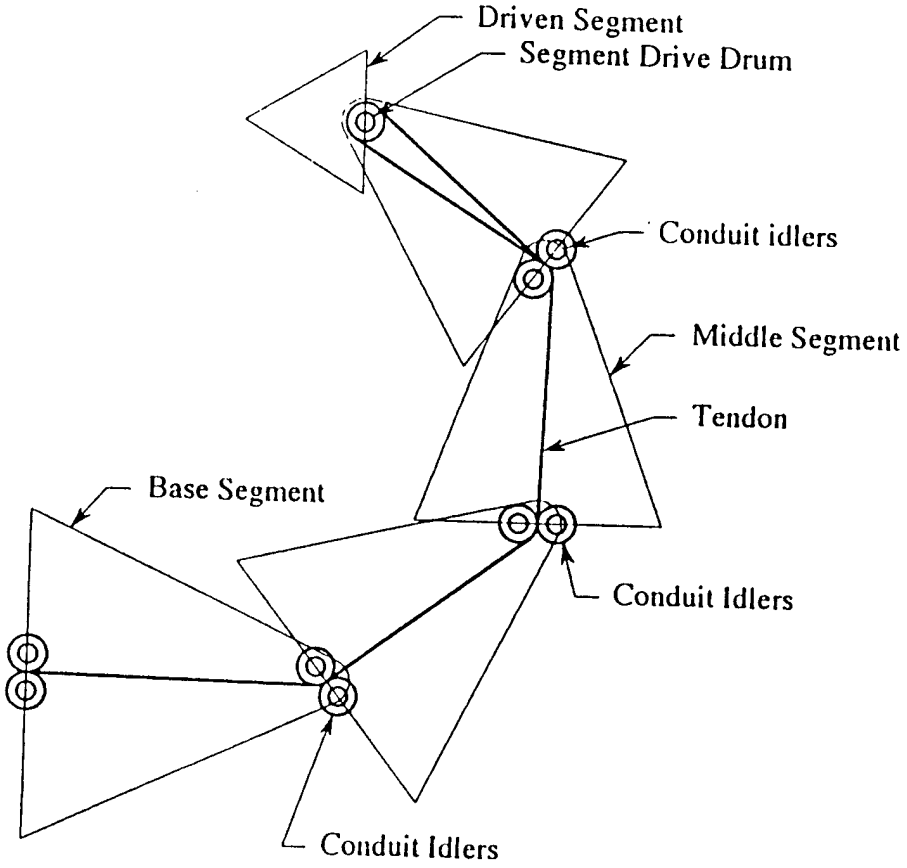

FORCE TRANSMISSION - 1

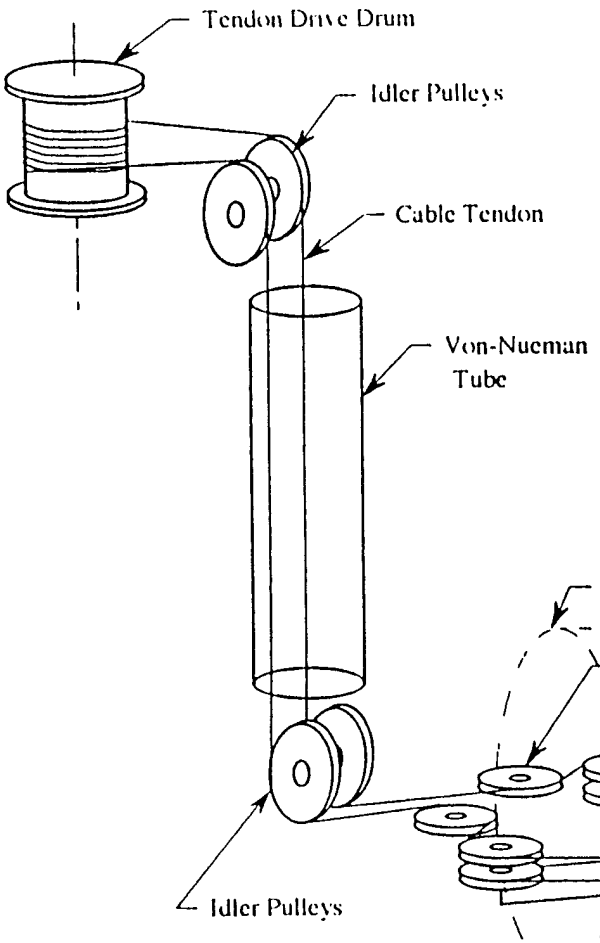

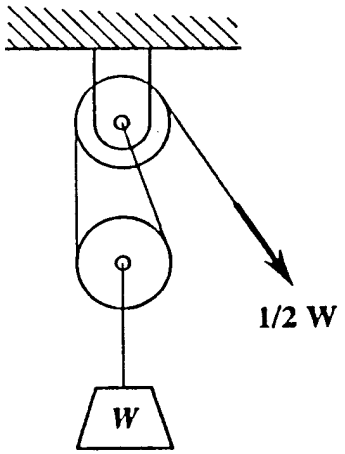

2:1 Block and Tackle Example

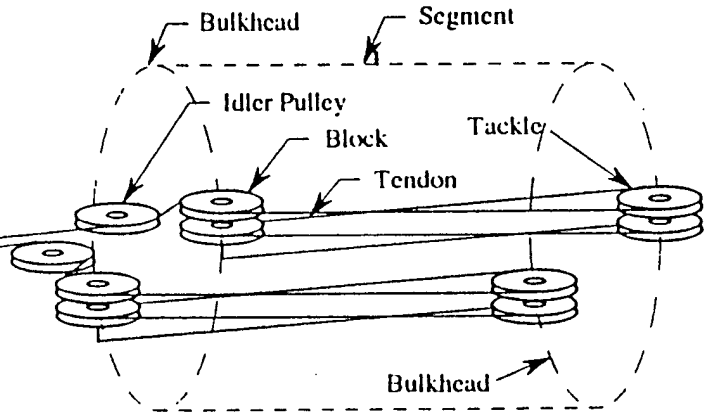

FORCE TRANSMISSION - 2

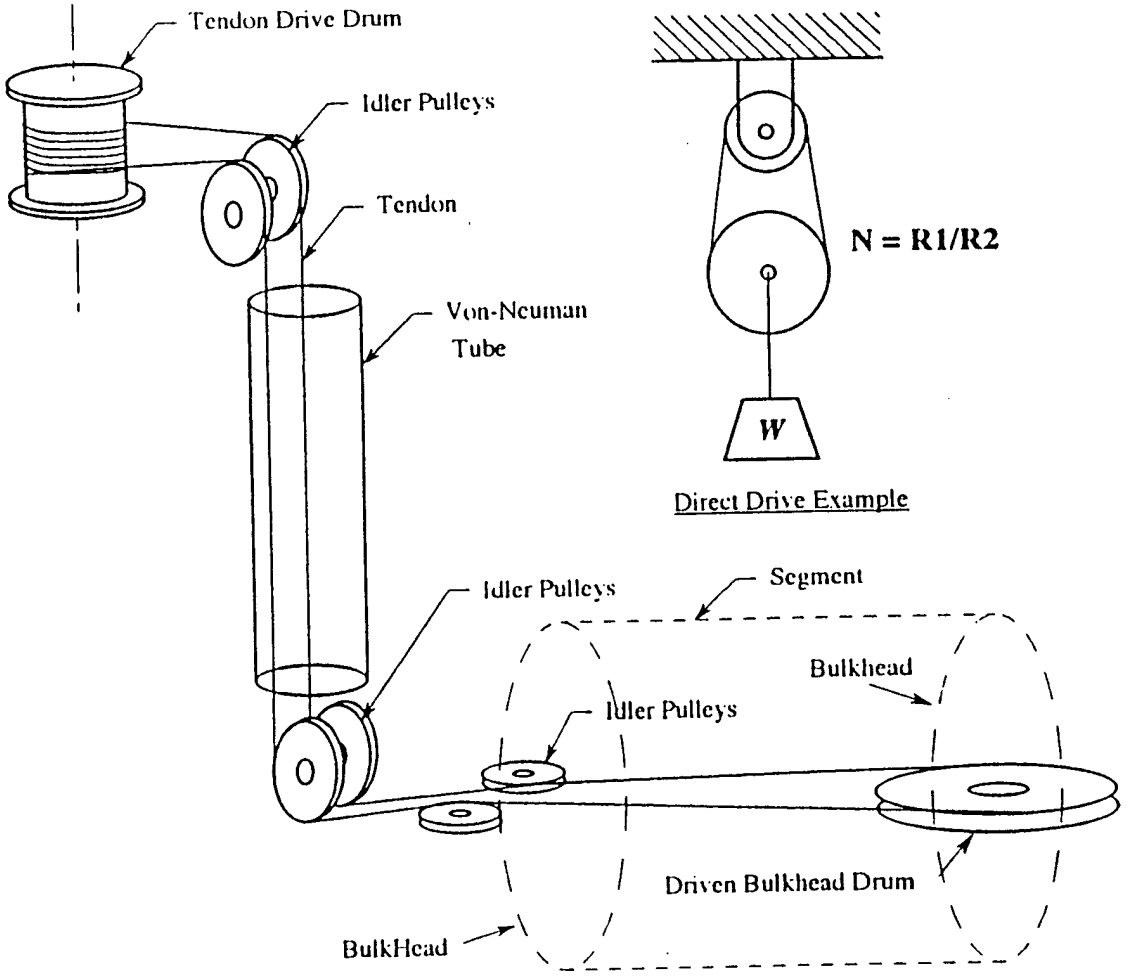

PRECISE FORCE MEASUREMENT IN THE LABORATORY

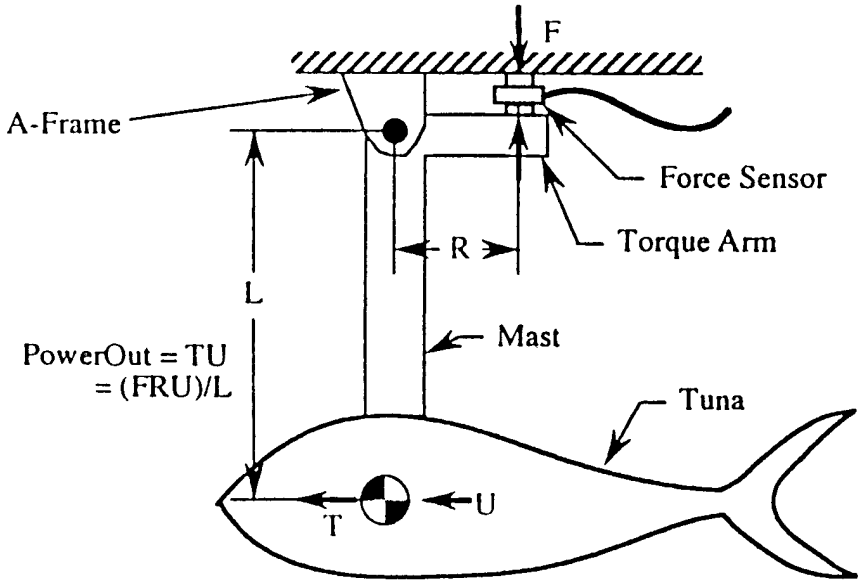

TL = FR

T = FR/L

Output Power Sensor

FORCE AND MOTION MEASUREMENTS IN SIX LINKS

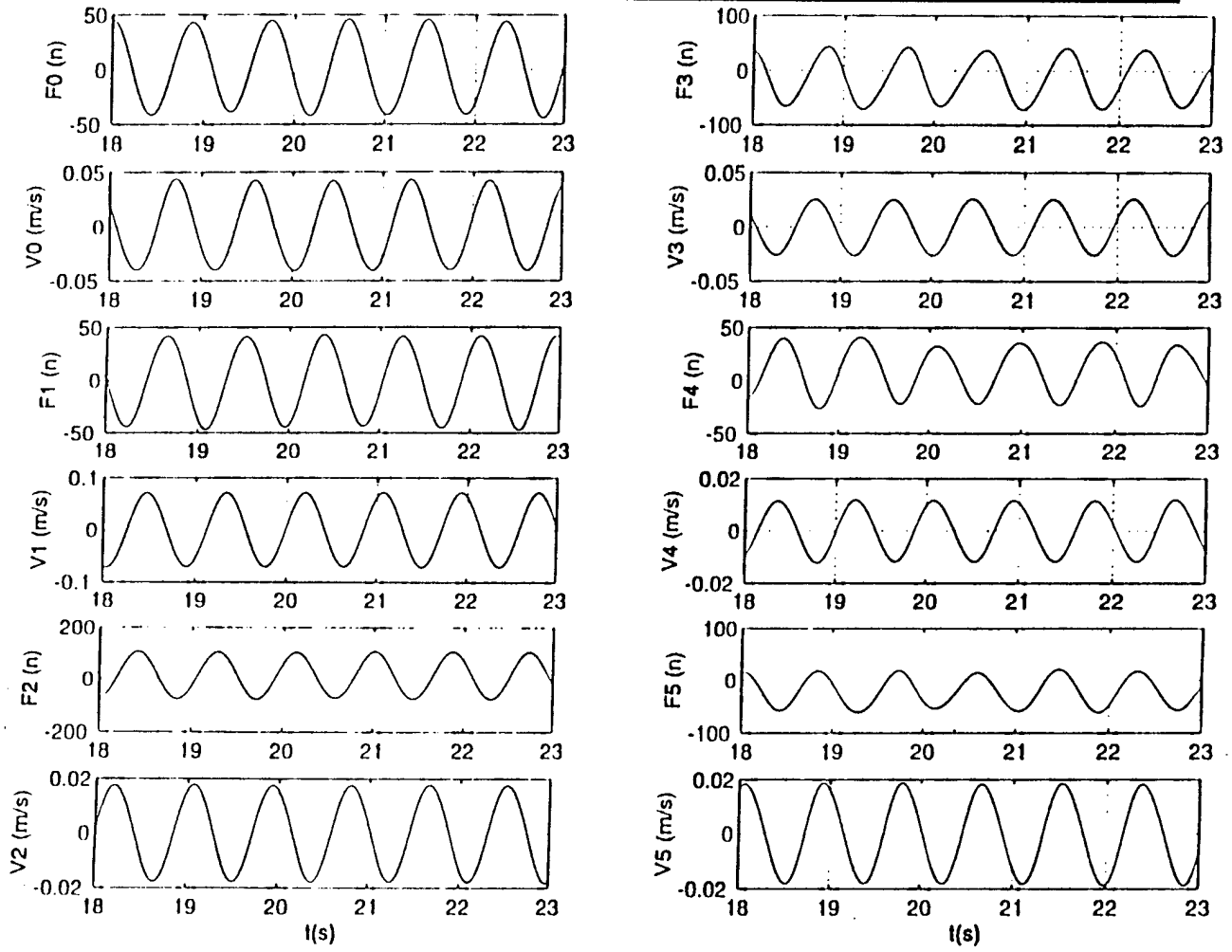

POWER RATIO VS. STROUHAL NUMBER

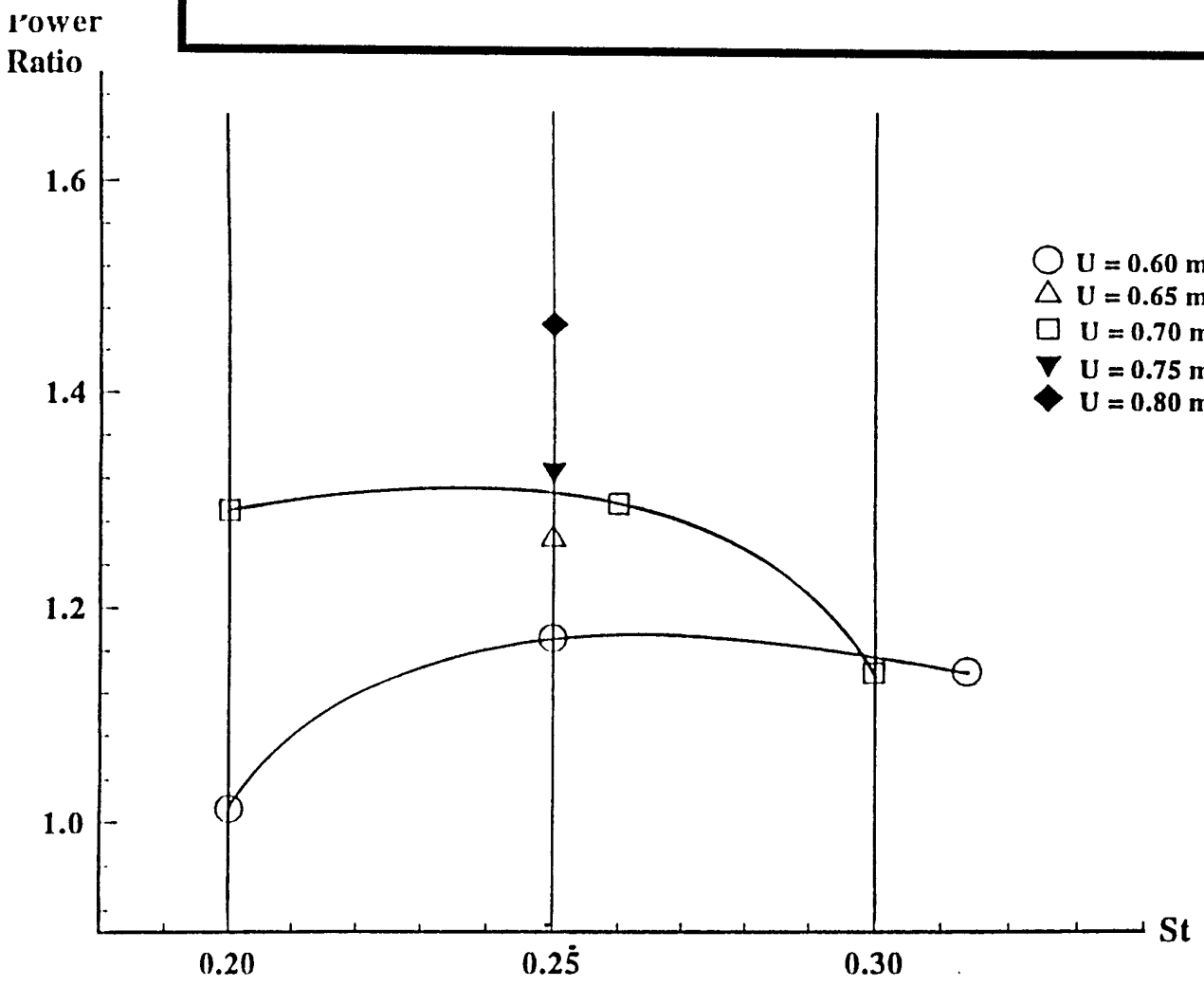

Drag Coefficient vs. Reynolds Number

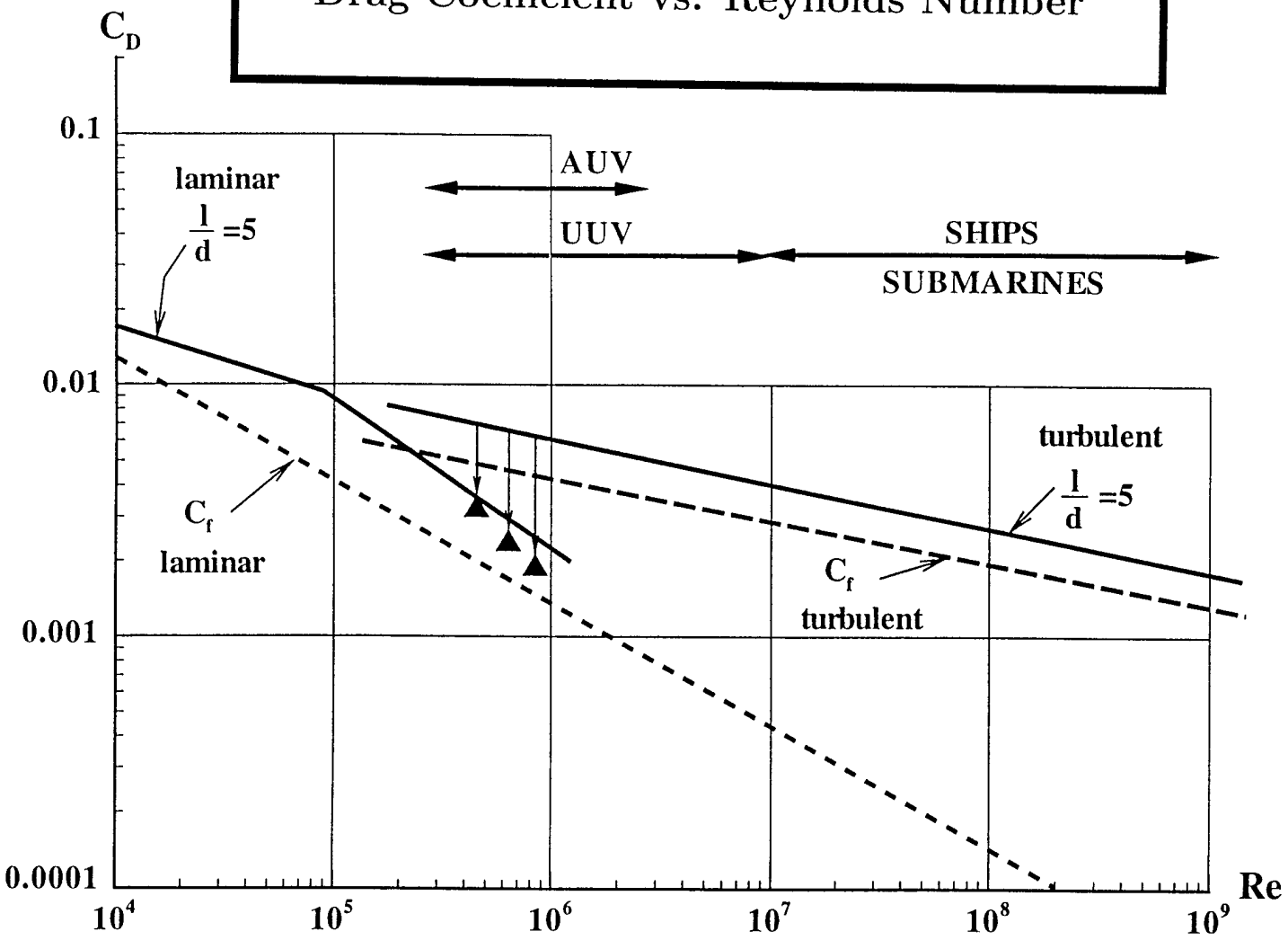

AUTONOMOUS BIOMIMETIC VEHICLE
THE ROBOPIKE

TESTED IN 1997 TO DEMONSTRATE:

FEASIBILITY OF RAPID MANEUVERING
THROUGH VORTICITY CONTROL

ACTUATION OF LARGE BODY FLEXING
REQUIRED FOR MANEUVERING

AUTONOMOUS BEHAVIOUR

MASSACHUSETTS INSTITUTE OF TECHNOLOGY

September 1997

BENEFITS ON SIGNATURE REDUCTION FROM BIOMIMETIC WORK

SIGNATURE REDUCTION BENEFITS:

DRAG REDUCTION IS DUE TO LAMINARIZATION OF BOUNDARY LAYER, HENCE BODY SIGNATURE IS REDUCED

VORTICITY CONTROL REDUCES SIGNATURE OF THE WAKE TRAILING BEHIND THE BODY

DISTURBANCE INDISTINGUISHABLE FROM NATURAL OCEAN NOISE

QUIET FLOW SIGNATURE AROUND AND IN THE WAKE OF THE BODY

BENEFITS ON MANEUVERING FROM BIOMIMETIC WORK

MANEUVERING AND FAST-STARTING BENEFITS:

FLEXIBLE HULL VEHICLES LEAVE NO DRAG WAKE WHEN MANEUVERING, HENCE SPEED REDUCTION IS SMALL

FLEXIBLE HULL VEHICLES CAN PRODUCE VERY LARGE, SHORT-DURATION FORCES, HENCE ACHIEVING RAPID MANEUVERING AND FAST STARTING

CAPABILITY TO OPERATE IN THE SURF ZONE AND IN HOSTILE ENVIRONMENTS

MASSACHUSETTS INSTITUTE OF TECHNOLOGY

September 1997

OPPORTUNITIES FOR ADVANCING MARINE TECHNOLOGY

A NEW GENERATION OF VEHICLES CAN BE DEVELOPED WITH RADICALLY IMPROVED PERFORMANCE, THROUGH VORTICITY CONTROL:

- CAPABLE OF VERY LONG RANGE
- CAPABLE OF MANEUVERING VERY FAST, HENCE OPERATING IN HOSTILE ENVIRONMENTS, PERFORMING COMPLEX TASKS AT HIGH SPEED
- CAPABLE OF VERY FAST STARTS, HENCE OPERATING NEAR THE SURF ZONE

FUTURE EFFORT IN FISH BIOMIMETICS

- BOUNDARY LAYER CONTROL
- REAL-TIME VORTICITY FEEDBACK CONTROL
- SERIES-ELASTIC ACTUATORS WITH NOVEL CONTROL SCHEMES
- MUSCLE-LIKE ACUATORS

THE SWIMMING HYDRODYNAMICS OF A PAIR OF FLAPPING FOILS ATTACHED TO A RIGID BODY

Promode R. Bandyopadhyay
Naval Undersea Warfare Center Division
Weapons Technology and Tactical Vehicle Systems Dept.
Newport, Rhode Island 02841 U.S.A.
and
Martin J. Donnelly
Virginia Polytechnic Institute and State University
Department of Engineering Mechanics
Blacksburg, Virginia 24061 U.S.A.

SUMMARY

Inspired by the natural action of flapping in aquatic locomotion, a dual flapping foil device was developed. The performance of the device in providing propulsive and maneuvering forces to small rigid axisymmetric bodies will be detailed. Two modes of flapping were investigated: waving and clapping. The clapping motion of wings is a common mechanism for the production of lift and thrust in the insect world, particularly in butterflies and moths. Waving is similar to the motion of the caudal fin of a fish. A model was built (1 m long, 7.6 cm diameter) with flapping foils at the end of the tail cone and various measurements were performed in a water tunnel. (In hindsight, the model can be described as a rigid-bodied mechanical seal because seals have remarkably similar dual flaps in their tails.) Time-dependent tests of thrust, drag, and yawing moment were conducted for several flapping frequencies commonly observed in relevant aquatic animals. Phase-matched laser Doppler anemometry measurements of the near wake were carried out and detailed vorticity-velocity vector maps of the vortex shedding process have been obtained for the axial and cross-stream planes. Dye visualization of wake was documented and a video recording was prepared of the entire dynamic process.

The ability of the dual flapping foil device to produce a net thrust and maneuvering cross-stream forces has been demonstrated, although the main body is rigid. Its wake, which is composed of jets, is extremely wide, nonrotating, and rapidly decaying. The thrust production greatly increases with Strouhal number. The results have been compared with two-dimensional inviscid flapping foil theories and measurements. The effect of the rigid cylinder on the flapping performance is extracted. The efficiency of thrust production generally increases in the waving mode which mimics the side-to-side head motion of a fish. Efficiency also tends to peak roughly in the Strouhal number range popular among fish. Axial thrust shows sensitivity to Strouhal number in the range popular among fish. However, existing non-linear inviscid theories do not capture this aspect and the strong viscous effects observed also need to be included.

1.0 INTRODUCTION

In nature, the inherent actions of swimming and flying have been perfected over millions of years. These actions have been the inspiration for many inventions in the fields of aero-dynamics and hydrodynamics. However, most studies have concentrated on mechanisms of thrust. The aspect of maneuverability has received scant attention. Aquatic locomotion generally deals with low absolute speeds. A more relevant speed parameter is body length traversed per second, which is frequently large. Thus, considering our current interest in shallow water and small vehicles, a natural place to look for new ideas for maneuvering and propulsion would be the hydrodynamics of aquatic locomotion. The transition from hydrodynamics in nature to engineering is not straightforward. Some recent developments are described in Bandyopadhyay et al. (ref. 1). This paper is a continuation of that effort.

Many varieties of fish use caudal fins for propulsion and pectoral fins for maneuvering. In this paper, we will consider the engineering reproduction of these control surfaces and use a pair of foils to simulate motions that are qualitatively similar. Propulsive and lifting forces produced by flapping foils were studied by Knoller and Betz from 1909-1912 (see ref. 2). From 1924-1936, Birnbaum, von Kármán, Burgers, and Garrick conducted theoretical studies that proved propulsive efficiency improved with slower flapping. Though there is no verification, it appears that German scientists tested a flapping foil device for torpedo propulsion during the early 1940s (see ref. 3). Gopalkrishnan et al. (ref. 4), Hall and Hall (ref. 5), and Jones et al. (ref. 2) have made recent progress. These works provide insight on the mechanism of propulsion and drag, and describe advanced diagnostics of the forces and turbulence in wake. Most importantly, the former authors (ref. 4) have indicated the existence of an optimum standard number for flapping, which squarely places the vortex shedding process at the center of the mechanisms for propulsion and maneuvering.

Several past studies of flapping foils dealt with flexible bodies and propulsion. However, we deal with the maneuvering of rigid bodies by means of flapping foils. A simplified momentum model of the dual flapping foil device (ref. 6) will first be described. Then, we will report the results of a detailed laboratory experimental investigation. An instrumented robust model (1 m long with a 7.6-cm diameter) was built with a pair of flapping foils installed at the end of the tail cone (Figs. 1 and 2). The flapping frequencies and flow speeds were varied. Phase-matched measurements of force and moments were carried out using a six-component dynamic drag balance.

Phase-matched measurements of the vortex shedding in the wake were also conducted using a laser Doppler anemometer. Data analysis included ensemble averaging of forces and moments and determination of net axial forces. The anemometry data were processed to produce phase-matched maps of vorticity-velocity vectors and circulation distributions. Vortex threading diagrams are constructed to gain insight into the mechanism for the production of maneuvering and propulsive forces.

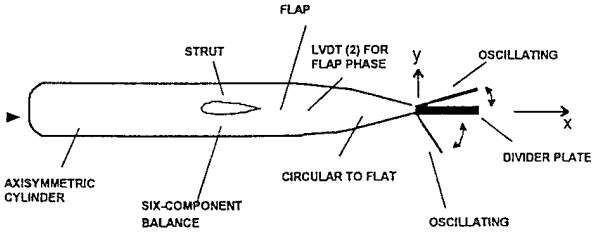

Fig. 1. Schematic diagram of the dual flapping foil device mounted at the end of the tail cone of a rigid cylinder. Axis z is along span of flap.

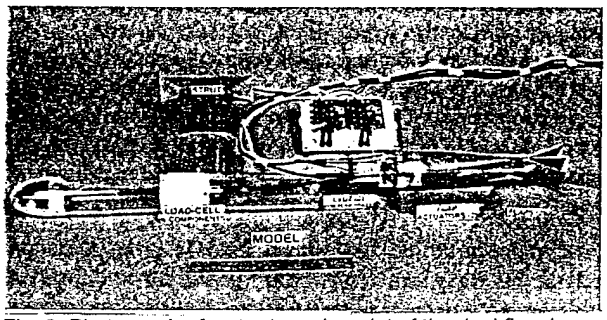

Fig. 2. Photograph of water tunnel model of the dual flapping foil device. Dual flapping foils and divider plate are shown on the right end; to the left of foils lie the actuators, two phase transducers, and actuator control circuits. The six-component load cell is located at the junction of the strut and cylinder.

The present work, while engineering in approach, needs to be placed in the perspective of hydrobionics. Unambiguous identification of the mechanism of maneuvering, thrust, and lift in swimming and flight in nature continues to be extremely difficult because of a lack of objective diagnostics and controlled experiments. The present experiment could help biology in this regard. Many quasi-steady aerodynamic explanations of biolocomotion have actually been an impediment to the uncovering of dynamic stall mechanisms for force enhancement believed to be widely practiced in nature (Ellington, 1995 ref. 7). Three-dimensional time-dependent accurate calculation methods need to be developed that can compute dynamic stall characteristics accurately. Measurements reported herein could help validate such methods.

What are the hydrodynamic differences between foils mounted on rigid and flexible bodies? According to Rayner (1995, ref 8), "For a swimming fish, drag is enhanced substantially because of body flapping (estimates range to up to five times the gliding drag; Webb, 1975, ref. 9). The fish must generate thrust to balance this enhanced flapping drag, but this force will not be reflected in the total momentum flow far from the fish if — as seems intuitively reasonable — much of the enhancement is due to induced drag. If the fish is well-streamlined, there may be only a weak thrust wake in steady swimming. Momentum representing the flapping-enhanced profile drag wake that will be transported in vortices generated close to the body; one explanation for the paradox is that these vortices approach and interact with the lifting vortices at the tail and annihilate one another before reaching the wake (Lighthill, ref 10)." The present experiment on the rigid body is unambiguous in the sense that the flap behavior and wake are not contaminated by any body flapping drag or associated vortices. Furthermore, because circulation is proportionate to the angular velocity of rotation, it is clearly ascribable to the flapping foils on a rigid body, but less so when the body is flexible.

The present work originated from a desire to apply the mechanisms of fish locomotion to rigid bodies and to focus on devices that would allow precision maneuvering. This led to a design of a tail on which two or three flapping foils are mounted on a ring and where they could be operated differentially. After the dual-flapping foil model was built (Figs. 1 and 2) and the measurements were completed, one of the authors (P. R. Bandyopadhyay) observed during a trip to the Mystic Marinelife Aquarium that seals and sea lions, which have a streamlined body and are known as wonderful swimmers, also have dual-flapping foils (Fig. 3). Figure 4 shows that the present experiment was carried out in the parameter range popular among fish.

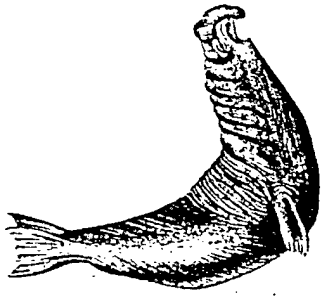

Fig. 3. The caudal fins of seals and sea lions are examples of dual-flapping foils which make them wonderful swimmers.

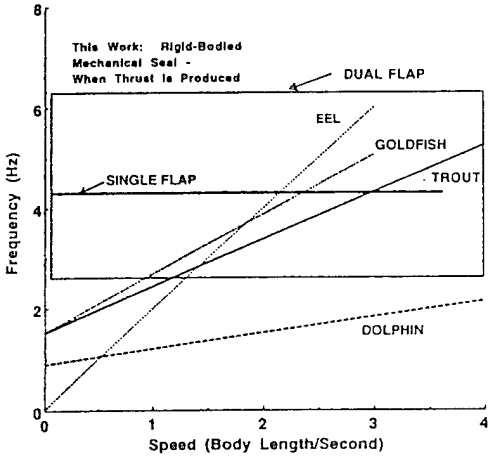

Fig. 4. Comparison of flapping frequencies of the rigid-bodied mechanical seal with those of aquatic animals (refs. 19, 20, 21, and 26). At a given speed, frequency range may be ±0.5 Hz.

2.0 SIMPLIFIED TWO-DIMENSIONAL MOMENTUM MODEL

A simplified two-dimensional momentum model of the maneuvering forces produced by the differential flapping device is developed here. This model assumes that the kinematics of the trailing edge of the flap holds the key to modeling the effects of the device. The basic importance of the trailing edge bears some similarity to the modeling of the propulsive forces produced by the caudal fins of fish (see refs. 10-13). In this simple model, induced drag and flap tip vortices are not considered.

2.1 Maneuvering and Axial Thrusts Generated

Consider the two-dimensional maneuvering device shown schematically in Fig. 5. Two flaps, numbered 1 and 2, are shown, although the basic approach is applicable if three flaps are mounted on a rotatable ring for finer control of maneuvering. Figure 5 pertains to thrust-producing maneuvering devices, rather than drag-producing maneuvering devices (Fig. 25 versus Fig. 26 — the two modes will be discussed later). In the thrust mode, two jets are assumed to be produced, each consisting of starting vortices as sketched. These jets are assumed to be similar to those observed behind a flexible tuna by Triantafyllou (see ref. 13).

As mentioned earlier, the differential flaps are both maneuvering as well as propulsive devices. The drag of the rigid body in Fig. 1 can be accounted for by proposing that the thrust-producing jets are produced after the drag is overcome. Consider flap #1.

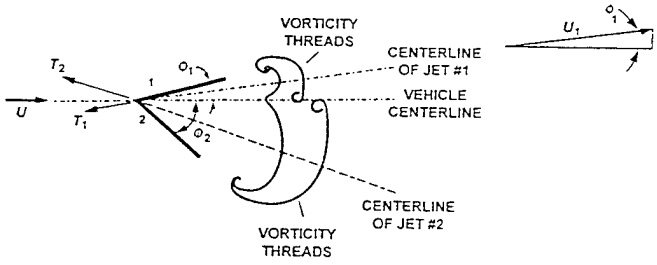

Fig. 5. Schematic of thrusts due to a pair of differentially operated oscillating flaps.

Propose that the thrust generated is proportional to the product of the mass of water affected and the increase in velocity given to that mass. The following definitions apply:

m_1, m_2 = Mass of water affected per unit span (normal to page in Fig. 5) by flaps 1 and 2, respectively,

T_1, T_2 = Thrusts due to flaps 1 and 2, respectively.

t_1, t_2 = Time periods of oscillation of flaps 1 and 2, respectively,

U = Forward speed of the vehicle generated by its propulsor,

U_1, U_2 = Velocities of water due to flapping acting at angles of $\phi_1/2$ and $\phi_2/2$, respectively, to the axial direction,

V_1, V_2 = Speeds imparted by flapping normal to the direction of vehicle motion,

x, y = Axial and normal directions, respectively, and

ϕ_1, ϕ_2 = Maximum flapping angles.

Therefore, thrust in the axial direction is

$$T_{1x} \propto m_1 \frac{U_1 \cos(\phi_1/2) - U}{t_1}, \qquad (1)$$

and

$$T_{2x} \propto m_2 \frac{U_2 \cos(\phi_2/2) - U}{t_2}. \qquad (2)$$

If $t_1 \neq t_2$ and if the phase is different when $t_1 = t_2$, a complex, perhaps even chaotic, pitching motion could result. Therefore, to simplify, assume that $\tau = t_1 = t_2$ and that both flaps oscillate at the same or opposite phase. Thrust vectors (Fig. 6) are then as follows:

Net Axial Thrust

$$T_a = T_0 + T_{1x} + T_{2x} \quad (\textit{in the x - direction}),$$
$$T_a = T_0 + \Delta T_x, \qquad (3)$$

where T_0 is vehicle axial thrust due to any additional independent means of propulsion, and ΔT_x is the contribution from the oscillating flaps.

Net Maneuvering Thrust

$$T_m = T_{2y} - T_{1y}. \qquad (4)$$

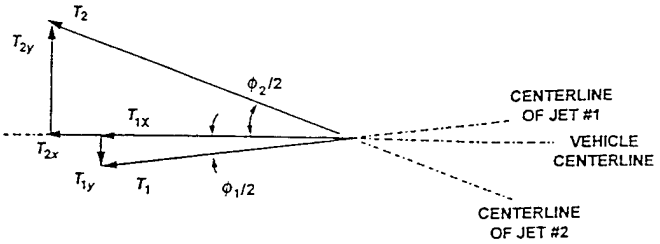

Fig. 6. Maneuvering and axial thrust vectors.

The vertical velocity vectors (in the y-direction) would be T_{1y} and T_{2y} (see Fig. 6).

Total axial thrust due to flapping is

$$\Delta T_x = m_1 \frac{U_1 \cos(\phi_1/2) - U}{\tau} + m_2 \frac{U_2 \cos(\phi_2/2) - U}{\tau}, \quad (5)$$

$$\Delta T_x = \frac{1}{\tau}[\{m_1 U_1 \cos(\phi_1/2) + m_2 U_2 \cos(\phi_2/2)\} - U\{m_1 + m_2\}].$$

(component determined by flaps alone) (component influenced by steady forward speed generated by main propulsor)

2.1.1 Axial thrust versus braking

Equation (5) shows that if $U_1, U_2 < U$, the flaps can be used as brakes. If both flaps are oscillated identically, then,

$$U_1 = U_2, \quad T_m = 0.$$

In this manner, the dual flaps can be used as brakes. If the vehicle is perfectly neutrally buoyant, and if the flaps are also slowed down in the manner of U, then the vehicle would come to a dead stop gradually.

However, if $U_1 \neq U_2 > U$, or $U_1 \neq U_2 < U$, then maneuvering thrusts will be produced.

In equation (5), if $U = 0$, $T_0 = 0$, then,

$$\Delta T_x = \frac{1}{\tau}[\{m_1 U_1 \cos(\phi_1/2) + m_2 U_2 \cos(\phi_2/2)\}].$$

If $(\phi_1, \phi_2)\uparrow, \Delta T_x \uparrow$. Note that $\phi_1, \phi_2 \neq 0$ when the flaps are operational.

2.1.2 Maneuvering thrust

From equation (4),

$$T_m = \frac{m_1 U_1 \sin(\phi_1/2)}{t_1} - \frac{m_2 U_2 \sin(\phi_2/2)}{t_2}.$$

If $t_1 = t_2 = \tau$,

$$T_m = \frac{1}{\tau}[m_1 U_1 \sin(\phi_1/2) - m_2 U_2 \sin(\phi_2/2)].$$

As $\phi_1 \uparrow$, or $\phi_2 \uparrow$, each part of T_m increases. The value of $|T_m|$ will be maximum if all flap variables are held the same when either flap is turned off.

It is implied that the rate of momentum shed by the flap trailing edge vortices is equal to the thrust produced. Therefore, the kinematics of the trailing edge gives the thrust and power generated. The key factors are the mass of water affected by flapping and movements of the trailing edge leading to acceleration of the water. These issues are considered next.

2.2 Mass of Water Affected

The mass of water affected by the flap's oscillation can be modeled in several ways. A simple body-geometry-based assumption would be that the diameter of the vortices produced is related to the distance of cross-stream travel of the oscillating flap. The following approach is based on the property of the vortices produced.

Consider the vortex doublet control volume shown in Fig. 7(a). These two contrarotating vortices are produced by one flap, say #1, in one time period of oscillation τ. The following assumptions are made:

1. The flaps are two-dimensional,

2. Both vortices are of the same strength ($|\Gamma|$) but of opposite signs,

3. There is no viscous dissipation, and

4. Vortex distance from flap center is c_1, i.e., the first vortex has not propagated downstream significantly more compared to c_1 during one cycle of flap oscillation.

Assume that the radial (r) distribution of azimuthal velocity v_θ within each shed vortex is as shown in Fig. 7(b). The distribution is linear in the core, followed by an exponentially dropping velocity (see ref. 14, fig. 5.5, p. 89):

$$v_\theta = k_1 r, \quad 0 \leq r \leq \ell, \quad (6)$$

$$v_\theta = k_2 \exp(-r^2), \quad r > \ell. \quad (7)$$

7(a)

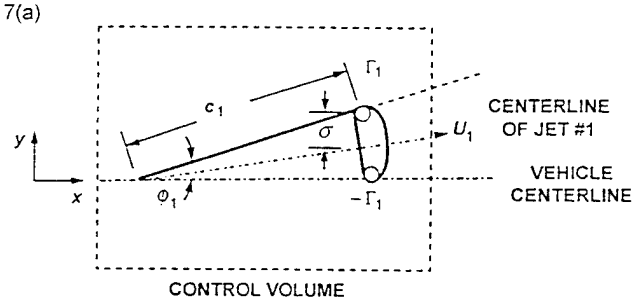

7(b)

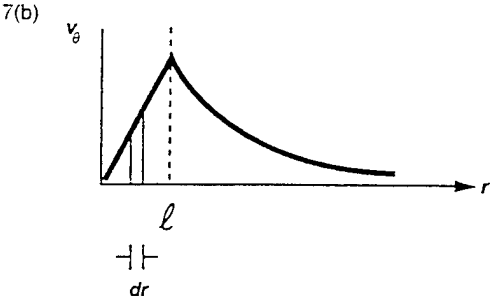

Fig. 7. Vortex doublet (a) and cross-sectional distribution of azimuthal velocity in the shed vortices (b).

Here, k_1 is a constant denoting the vortex property, viz., its vorticity (whose dimension is $1/T$), and k_2 is another constant that is largely dependent on vortex diffusion rate. Structural modeling of turbulent boundary layers (Bandyopadhyay and Balasubramanian, ref. 15) shows that, as a first approximation,

the distribution in equation (7) may be neglected, i.e., the decaying region due to viscous effects is ignored soon after the formation of the vortices. As proved successful in that model, it was also assumed that $\ell =$ the local mixing length ≈ 0.07 of the local width of the trailing jet.

Considering the two vortices in the control volume in Fig. 7(a), the mass of water affected by flap #1 per unit span is

$$m_1 = \rho k \pi \frac{(\ell_1)^2}{4}, \tag{8a}$$

where k is a constant dependent on the flap's sectional shape and is a property of the vortex, and ρ is the fluid density. Similarly,

$$m_2 = \rho k \pi \frac{(\ell_2)^2}{4}. \tag{8b}$$

Therefore, the maneuvering thrust is given by:

$$T_m = \frac{\rho k}{\tau} \frac{\pi}{4} \left[(\ell_1)^2 U_1 \sin(\phi_1/2) - (\ell_2)^2 U_2 \sin(\phi_2/2) \right], \tag{9}$$

where U_1 and U_2 may be obtained by Biot-Savart's law, if Γ is known from measurements. The vortices in Fig. 7(a) would move in a direction normal to the line joining them (see Batchelor, ref. 16, p. 441).

2.3 Velocity of Propagation of Shed Vortices

Let

c_1, c_2 = Chord lengths of flaps 1 and 2,

$\Gamma_1, -\Gamma_1$ = Strengths of vortices shown in Fig. 7(a), and

σ = Half-gap between the two vortex foci (Fig. 7(a)).

Referring to Batchelor (ref. 16, sec. 2.6.4) and Schlichting (ref. 14, p. 89) for a doublet,

$$U_1 = 2\frac{\Gamma_1}{2\pi\sigma} = 2\frac{\Gamma_1}{2\pi c_1 \sin(\phi_1/2)}. \tag{10}$$

2.4 Strength of Shed Vortices

Circulation from Joukowski's hypothesis is (see Batchelor, ref. 16, p. 441)

$$\Gamma_1 = A\sqrt{V_r^2}, \tag{11}$$

where A is a constant of proportionality that depends on the shape and orientation of the flap. For example, it will be different for a rigid or a flexible flap. (Note that a flexible flap would have a variable chord length.) The value of A would be different if trailing edge serrations are present. If a divider plate is present between the two flaps, it would alter the effective shape and orientation of the flap by introducing another length scale into the problem, whose effect would be to alter the value of the constant A. In equation (11), V_r is a representative speed of the flap.

2.5 Speed of Flap Oscillation

There are two forms of flapping speed, i.e., pendulum-like sinusoidal rotational speed and constant rotational, square wave speed. The sinusoidal pattern would be obtained if a pendulum-like variable torque is used to oscillate the flap. The square wave pattern would be generated by a drive that produces a constant rotational speed. In the model design, a pattern that is close to a square wave is expected. In this case, if W is the tip speed, c is flap's chord length, and Ω is the rotational speed (rad/s), then

$$W = c\Omega. \tag{12}$$

A flexible flap would have a variable chord length and the time signature of the tip speed would be distorted compared to those for rigid flaps.

In the present model design, a brushless magnet actuator, known commercially as Ultimags, was chosen to oscillate the flaps. The input current to the Ultimags was observed to follow a square wave pattern. This finding confirmed that, in the model, the flaps indeed operate at a constant rotational speed.

A relationship is required for the transfer of momentum between the solid and the liquid, i.e., between the rotational variables Ω and Γ. This relationship is modeled in section 4.3.2 where comparisons with measurements are presented.

2.6 Effects of Flap Travel, Body Thickness, Viscosity, and Virtual Mass

There may be a relationship, yet unknown, between maximum flap travel and body thickness (Fig. 1). Experiments are needed to determine if results become independent of body thickness when the maximum flap travel exceeds the body thickness (Webb, ref. 12, p. 208).

Virtual mass would be affected by viscosity via boundary layer displacement thickness δ^* on the flaps. An estimate suggests that virtual mass is reduced to

$$m - 2\rho\delta^* c, \tag{13}$$

where ρ is the density of water and c is the flap chord length. Equation (13) is analogous to that for a fish where virtual mass correction is of the order of only 1 percent. The viscosity correction to the mass of water affected can therefore be neglected.

The added mass effects due to the potential flow also need to be considered. The pressure drag, or the frontal area, is an indication of this effect. Therefore, it is expected that, as long as the flap travel is small or the flaps oscillate within the base of the tailcone, the added mass effect due to the potential flow would be low. However, if the flap tips protrude beyond the vehicle, the added mass effect would increase.

2.7 Power of Flap

Let

m_1 = Mass of water affected by flap #1 per unit span (in direction normal to page in Fig. 5),

U_1 = Velocity imparted to mass of water m_1 by flap #1, and

U = Vehicle speed.

Then, the momentum given to water by the flap = $m_1 U_1$, and the rate of momentum shedding into the wake (thrust) = $m_1 U_1 U$.

The flap is working against the fluid at the rate of tip speed W. Power is always positive—when accelerating and braking the vehicle. The flap power is, therefore,

$$P = m_1 U_1 U W. \tag{14}$$

(Units for equation (14) are: $(ML^3/LT^3) = ML^2/T^3$ = watts. In SI units: Power = watts = J/s) = (N/m)/s = (kgm/s^2) (m/s) = $kg(m^2/s^3) = M(L^2/T^3)$.)

However, all this power is not available for maneuvering and thrust. Some of it is used to overcome drag. The lost kinetic energy in the shed vortices is

$$P_k = 1/2 m_1 U_1^2 U. \tag{15}$$

Therefore, the available power for maneuvering and thrust is

$$P_m = P - P_k. \tag{16}$$

3.0 DESCRIPTION

3.1 The Dual-Flapping Foil Maneuvering Device

A schematic diagram of the water tunnel model is shown in Fig. 1. Figure 2 is a photograph of the partially assembled model. The cylinder diameter is 7.62 cm and the length is about 1 m. The two flaps are 7.62 cm x 7.62 cm in size. A fixed divider plate of the same size is located between the two flaps. The divider plate serves to reduce the rigid body drag and it also "trains" the vortex array allowing accurate phase-averaged wake vortex measurement. The flaps are activated by two magnetic actuators and phase is determined by two differential transducers that measure displacement. The actuators and phase sensors are housed internally. The entire model 'floats,' mounted on a six-component balance located under the strut. The strut is fixed and hangs from the tunnel's top wall. The vortices shed by the flapping foils are created by salient edge separation and, thus, their effects are independent of any boundary layer tripping. The data presented here are mostly for natural transition on the main cylinder because tripped cases show little effect. The two flaps can be operated in one of two modes, i.e., in a clapping or waving mode—so named because of the kind of animation they simulate (see Fig. 8). In the clapping mode, the two flaps approach or recede from each other simultaneously, while in the waving mode, the flaps always follow the direction of motion of each other. In other words, in clapping, the phase of the two flaps is opposite to each other, while phase is the same in the waving mode.

3.2 Experiment Details

All measurements were performed for both flapping modes, i.e., waving and clapping. The balance measurements were conducted with a single flap as well as the dual flap. The actions of the maneuvering device and the phase sensors in air and in a water tunnel were video taped (Bandyopadhyay et al., ref. 17). The robustness of the device was demonstrated by the fact that it worked in the water tunnel nonstop for about five days during which time the phase-matched turbulence measurements were carried out. These measurements were conducted in the water tunnel at Virginia Polytechnic Institute (Zeiger et al,. ref. 18). The cross-section of the test section is large for our purpose: 0.56 m wide and 0.61 m deep. The balance data were collected for flow speeds between 10 and 80 cm/s and flap frequencies of 2.65, 4.237, and 6.2 Hz. As shown in Fig. 4, these parameters are in the same range as those in several relevant aquatic animals. The flow visualization was carried out at 5 cm/s and the laser Doppler velocity data were collected at 20 cm/s with a flap frequency of 2.65 Hz. The flap tip travel was commonly 38 mm which made an angle of 30 degrees about the axis. Data acquisition was carried out in the following manner. First, the balance data were collected. One desk-top computer was used to operate the balance and another was used to read out, process, and store the data. Next, a two-component laser Doppler anemometer was used to make phase-matched turbulence measurements in the wake. The measurements were conducted first in three axial planes downstream of the flaps. Then they were conducted in three cross-stream planes. The data were processed to produce phase-averaged vorticity-velocity vector contours in the axial and cross-stream planes. Finally, distributions of circulation were calculated by two integral methods, i.e., velocity time integrals and vorticity areas. The efficiency measurements were carried out in the NUWC water tunnel which is 30 cm x 30 cm in cross-section.

4.0 RESULTS AND DISCUSSION

4.1 Flow Visualization

Dye flow visualization was carried out to examine the vortex shedding process at a flow speed of 5 cm/s. The vortex rollup at the flap tip is shown in Fig. 8 for the clapping and waving modes. The complete wake can be seen in the video (Bandyopadhyay et al., ref. 17). For a flap angle of 30°, the outer tip vortices were spread at an angle of 70° to the axis, the resulting wake spread angle being 140°. This is a very wide wake that produces thrust and maneuvering forces. As shown later, this wake dissipates very quickly.

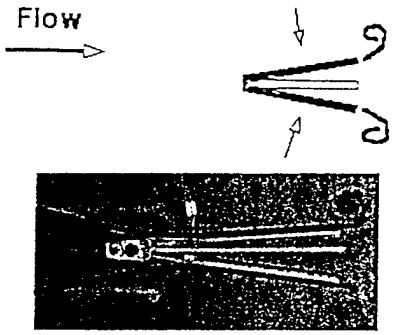

Fig. 8(a). Flow visualization tests of clapping mode: flaps closing (top, graphic depiction; bottom, photograph).

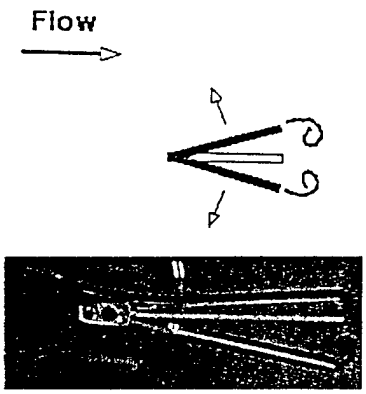

Fig. 8(b) Flow visualization tests of clapping mode: flaps opening (top, graphic depiction; bottom, photograph).

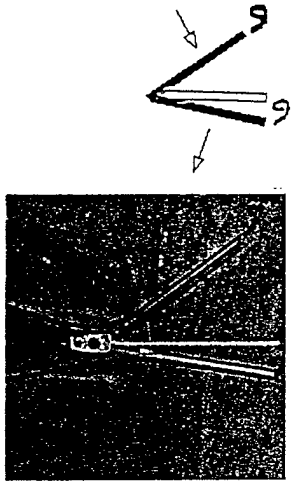

Fig. 8(c). Flow visualization tests of waving mode: Flaps toward port (top, graphic depiction; bottom, photograph).

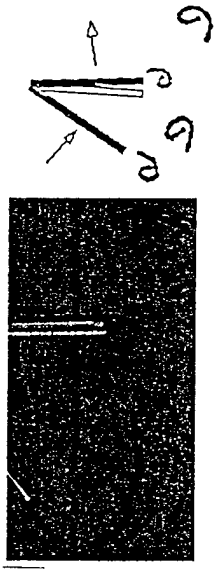

Fig. 8(d). Flow visualization tests of waving mode: Flaps toward starboard (top, graphic depiction; bottom, photograph).

4.2 Definition of Coefficients

The coefficient of axial force, c_a, is defined as

$$c_a = \frac{F}{\frac{1}{2}\rho U_\infty^2 D^2}, \tag{17}$$

where F is axial force, being positive for thrust, ρ is density of water and U_∞ is freestream velocity. When F is positive, $c_a = c_t$, the coefficient of thrust, and when F is negative, $c_a = c_d$, the coefficient of drag.

The coefficient of yawing moment is defined as

$$c_m = \frac{T}{\frac{1}{2}\rho U_\infty^2 D^3}, \tag{18}$$

where T is yawing moment, D is the length scale of the model and flaps. Time, t, is nondimensionalized as $t^* = tU_\infty/D$. The Reynolds number is defined as

$$\mathrm{Re} = \frac{U_\infty D}{\nu}, \tag{19}$$

where ν is kinematic viscosity of water. In calculating vorticity, velocity and circulation, nondimensionalization is performed using U_∞ for velocity scale, D for length scale, and D/U_∞ for time scale.

The Strouhal number, St, is defined as

$$St = \frac{fA}{U_\infty}, \tag{20}$$

where f is flapping frequency and A is maximum cross-stream travel of a flap tip.

Efficiency of the flapping foils was defined as

$$\eta = \frac{OutputPower}{InputPower} = \frac{T \cdot U_\infty}{\eta_a \int 2VIdt}, \tag{21}$$

where T is integrated thrust, η_a is actuator efficiency, V and I are actuator volts and currents, respectively. The factor 2 accounts for two actuators.

4.3 Forces and Moments

4.3.1 Time signatures

The ensemble-averaged coefficient of axial force (c_a) due to a single flapping foil is shown in Fig. 9(a-c). A net thrust is produced only at 4.24 Hz. For the dual-flapping foil case, the ensemble-averaged time histories of axial force and yawing moment are shown in Figs. 10 and 11, respectively. A thrust is produced at all three frequencies. In Fig. 10, positive values of force indicate thrust and negative values indicate drag. Clearly, the device has produced more thrust than drag. The net values of the moment can be made non-zero and acting toward port or starboard by operating the flaps differentially. The data in Fig. 11 can be used to design control laws for maneuvering. Observe the 90° phase difference between axial force and yawing movement.

9(a) 2.6 Hz

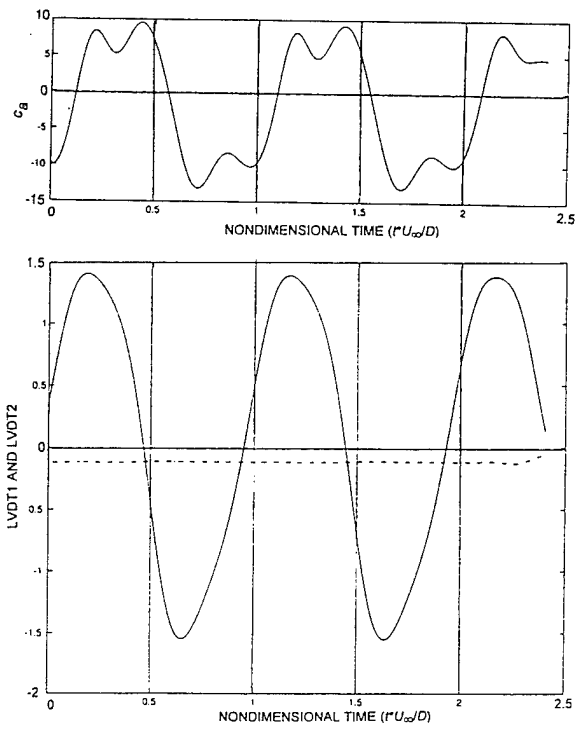

9(b) 4.24 Hz

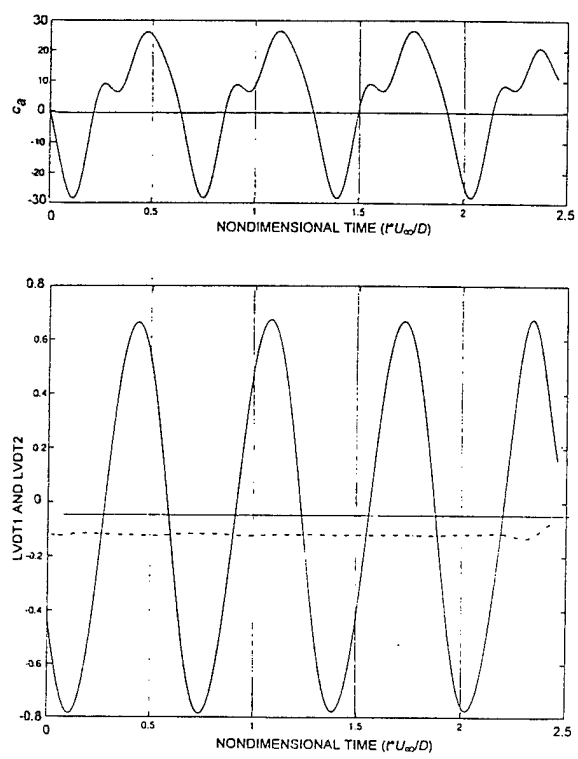

9(c) 6.2 Hz

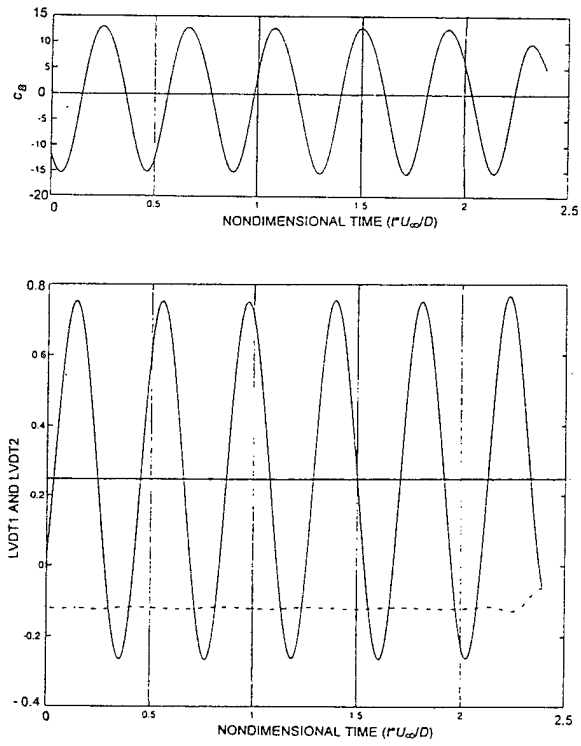

Fig. 9. Ensemble-averaged coefficient of axial force (c_a) due to a single flapping foil; positive values indicate thrust (c_t) and negative values indicate drag (c_d); U_∞ = 20 cm/s: (a) 2.6 Hz, (b) 4.24 Hz, and (c) 6.2 Hz. LVDT signature indicates flap phase ≡ highest values: flap fully open; lowest values, flap fully closed.

10(a) 2.6 Hz

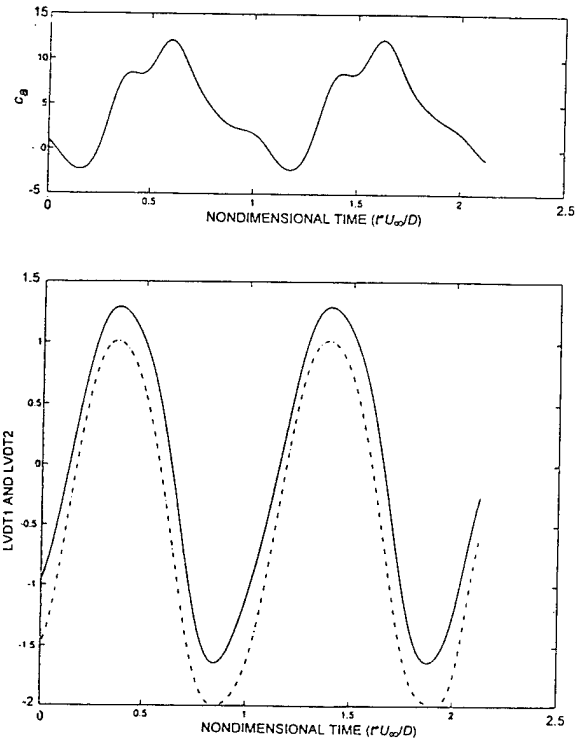

Fig. 10. Ensemble-averaged axial force and flap opening due to dual-flapping foils. High LVDT values ≡ flap fully open; low LVDT values ≡ flap fully closed. The flaps are actually in opposite phase.

10(b) 4.24 Hz

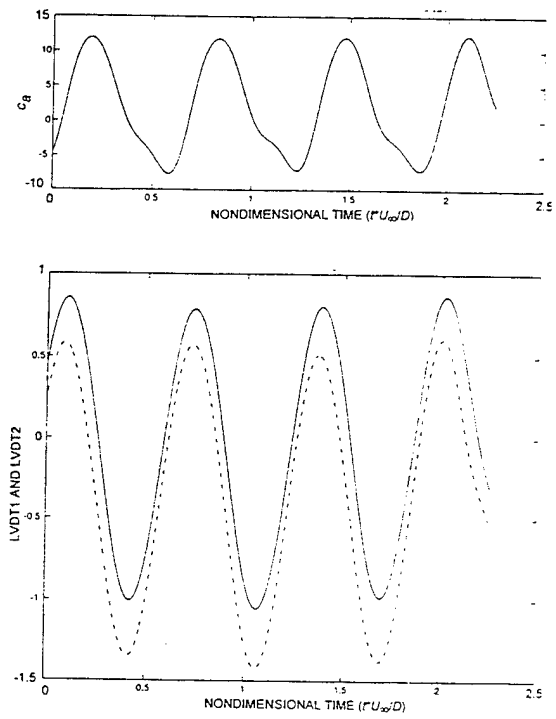

10(c) 6.2 Hz

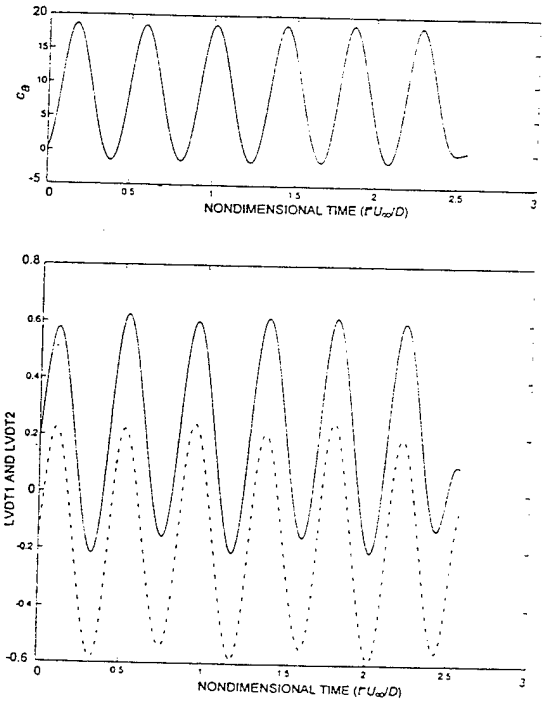

Fig. 10. (Cont'd) Ensemble-averaged axial force and flap opening due to dual-flapping foils. High LVDT values ≡ flap fully open; low LVDT values ≡ flap fully closed. The flaps are actually in opposite phase.

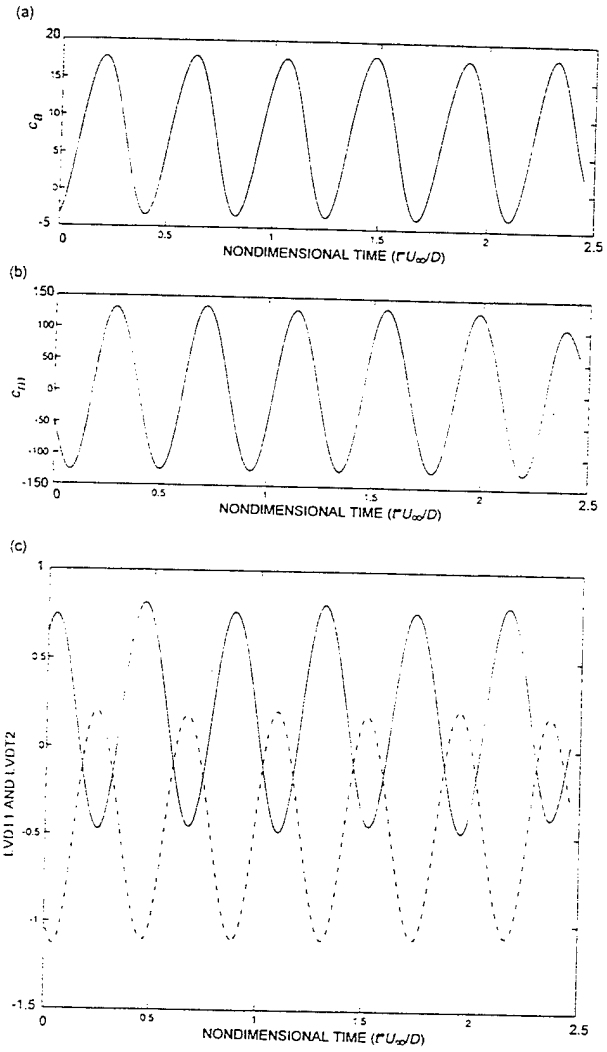

Fig. 11. Ensemble-averaged (a) axial force, (b) yawing moment, and (c) flap phase in waving mode; U_∞ = 20 cms/s; f = 6.2 Hz. The flaps are actually in phase.

4.3.2 Thrust coefficient

The distributions of coefficient of axial force with Strouhal number are shown in Fig. 12. The dual flapping foil data are compared with the two-dimensional theories of Lighthill (ref. 10) and Chopra (ref. 22) and the two-dimensional measurements of Triantafyllou et al. (refs. 23, 24) and Isshiki and Murakami (ref. 25). There is good agreement in the trend. Our measurements are also compared with the two-dimensional momentum model of Bandyopadhyay (ref. 6) described in section 2. In this model, the mass of water affected per unit span of flap was taken to be

$$2v_\theta \cdot R_v, \tag{22}$$

where $v_\theta = c \cdot \Omega$. Here v_θ is azimuthal speed of the flap time, R_v is vortex radius at the flap tip, c is flap chord = D; Ω is rotational speed of flap = $2\pi f$, and the factor 2 accounts for two vortices formed in each cycle of flapping.

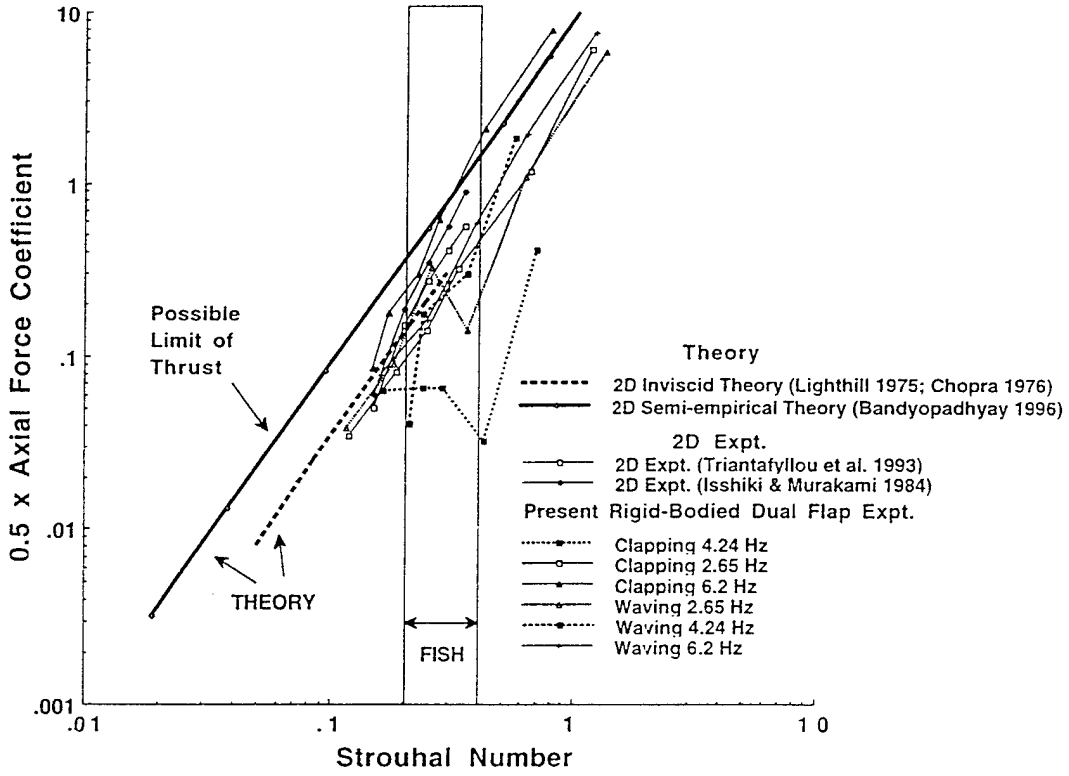

Fig. 12. Comparison of measurements of axial force (thrust) coefficient.

From flow visualization experiments, R_v was taken to be 0.173 cm at all values of U_∞ and f. From the phase-matched LDV measurements shown in Fig. 13, the axial jet speed relative to U_∞ was taken to be 60 cm/s at all values of U_∞ and f. Thrust coefficients calculated using these values of mass of water affected and jet speed are also shown in Fig. 12. The momentum model may be the asymptotic limit of thrust that can be produced by the flapping foil technique. In the St range common among fish (Triantafyllou, ref. 23), some of the dual flapping foil data exhibit sensitivity to St.

In the case of the rigid body, the shed vortices do not propagate tangential to the trailing edge when the flap is at the outer extremity. At 5-20 cm/s, while the flap trailing edge is at 30° to the axis, the outboard vortex moves away from the axis at 70°. There is also a rapid decay in the vortex circulation (discussed later, Figs. 23 and 24). Thus, the vortex self-induced dynamics is strong and the wake is affected by viscous non-linear mechanisms. Although, the two-dimensional non-linear theories generally agree with the mean data trend in Fig. 12, the detailed sensitivity in the range $0.2 < St < 0.4$ is not captured. We suggest that, in order to determine sensitivity to St and f, viscous non-linear stability dynamics need to be included in the theories.

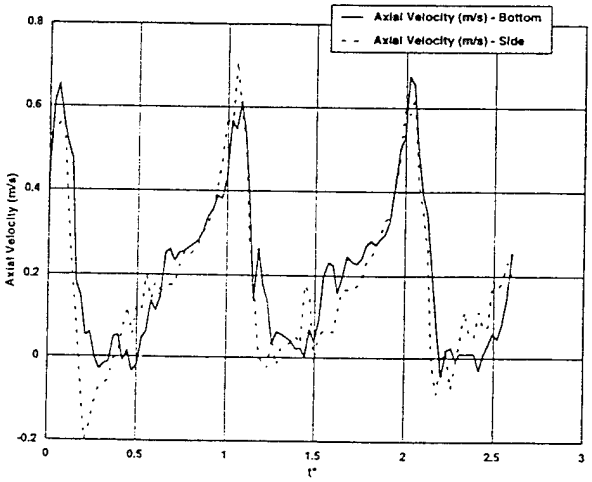

Fig. 13. Phased-average measurements of axial jet speed due to dual-flapping foil. Axial velocities shown are relative to U_∞ of 20 cm/s. Measurements in two different planes are compared.

The efficiency of the flapping foil (equation (21)) is shown in Fig. 14. The efficiency of the magnetic actuator, η_a , was assumed to be 18% as supplied by the manufacturer. The actual η_a is lower and, thus, the actual values of η of the dual flaps shown are higher. There is a general agreement with Triantafyllou's (ref. 23) experiment on a two-dimensional heaving and feathering foil. It is interesting to note that the dual flaps show a tendency to achieve a higher efficiency in the waving mode. This is intriguing. We propose that in the waving mode, the model nose yaws and sheds vortices. This either lowers the drag on the rigid body or it enhances the thrust (by augmenting jet speed) due to the vortices produced by flapping.

Because the efficiency plots shown in Fig. 14 include the cylinder drag, an attempt was made to estimate the efficiency of the flapping foils alone. The viscous and form (small) drag coefficient of the cylinder was estimated to be 0.145. When this is taken into account, the efficiency of the flapping foils alone are higher as shown in Fig. 15. At lower St, there is a tendency for the efficiency to depend on f. This has not yet been explained.

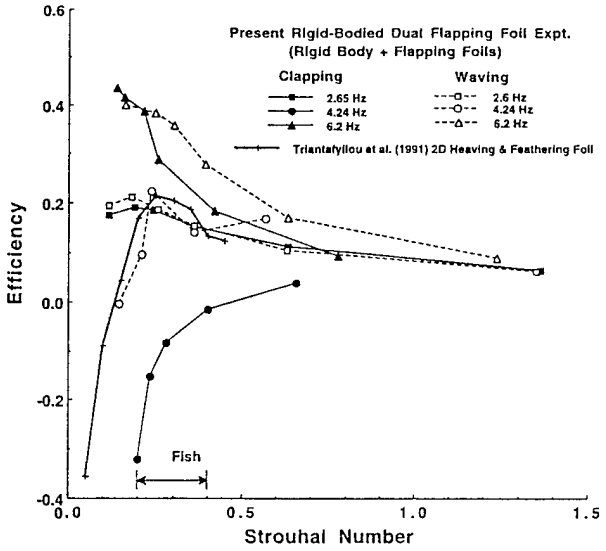

Fig. 14. Measurements of the axial force efficiency of the dual-flapping foils.

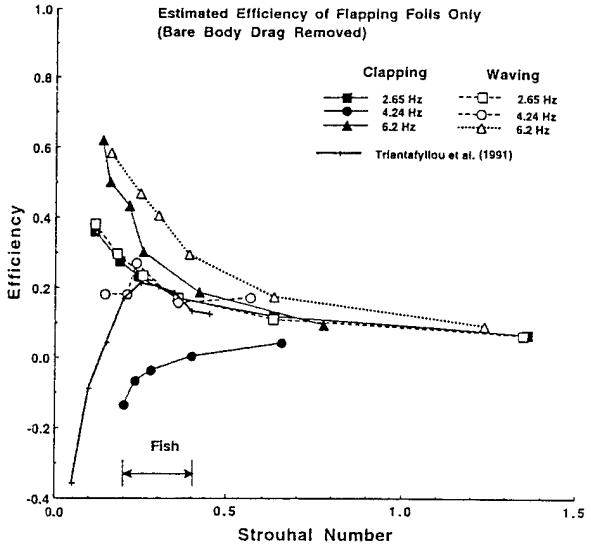

Fig. 15. Estimated efficiency of dual-flapping foils. Estimated values of bare body drag (viscous + form) removed from measurements of total efficiency (rigid body + flapping foils) shown in Fig. 14.

Measurements of all axial force coefficients due to single- and dual-flapping tails are shown in Fig. 16. Both thrust and drag production cases are included. Except at 4.25 Hz, one single foil is unable to produce thrust. This is due to the drag of the rigid cylinder. Tripping of the cylinder boundary layer has no effect on the thrust produced because that mechanism is inviscid — tripping only affects the drag of the rigid cylinder. The data indicate that the thrust produced is governed by *St*, drag of the rigid cylinder, and the total mass of water affected. The mass of the water affected is doubled when two flaps are used and the thrust produced overcomes the drag of the rigid cylinder. According to Triantafyllou (Pvt. Comm. 1997), the "robotuna" vortex cores make an angle of 10-15° to the forward direction. However, the wake angle is 140° in the present case. (The divider plate probably lowers the cylinder drag slightly.) This suggests that the drag of the flexible robotuna's main body could well be lower, but this remains a speculation. The two-dimensional flapping foil experiments do not have a main body and, thus, have the pure thrust produced. We believe that, in the future, by comparing our results with those of the robotuna of Triantafyllou, insight can be gained on the effect of a flexible body.

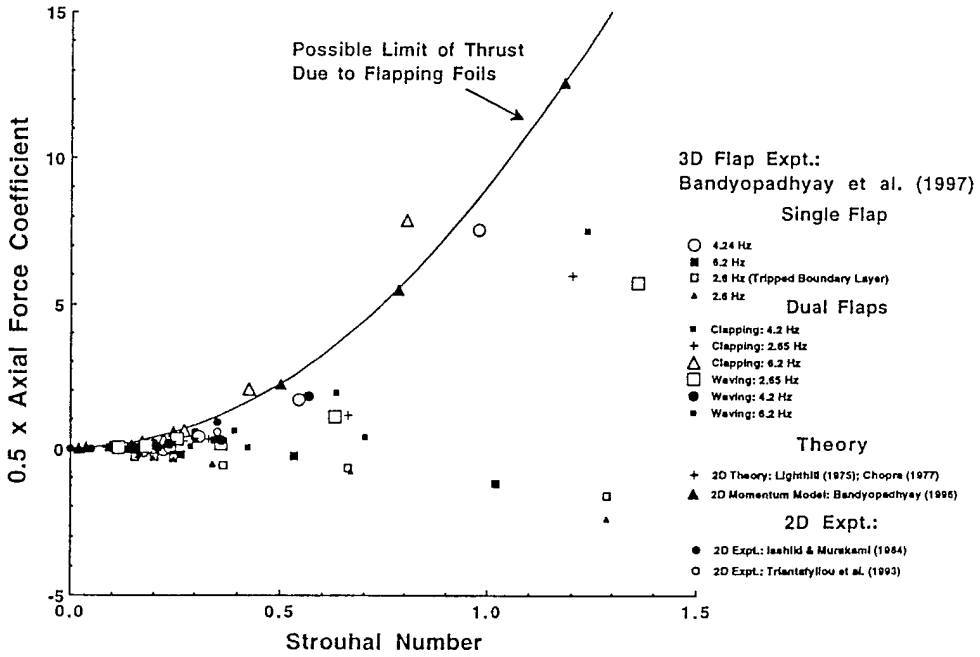

Fig. 16. Summary of all single- and dual-flap axial force coefficients. Both thrust- and drag-producing cases are shown. Note that body drag is included in axial force.

4.4 Vortex Shedding: Vorticity-Velocity Vector Maps

4.4.1 Vorticity-velocity vector maps

The phase-matched vorticity-velocity vector measurements were carried out at a flow speed of 20 cm/s. Their maps in the axial (diametral) midplane (z = 0) are shown in Figs. 17, 18 and 19 for waving and clapping modes (phase is given by $t^* = tU_\infty/D$). Similarly, the phase-matched vorticity-velocity vector maps in the cross-stream plane at the trailing edge of the flap ($x/D = 0.066$) are shown in Figs. 20 and 21 for the waving and clapping modes, respectively. Such maps were used to compute circulation values of the vortices by two methods: by calculating velocity line integrals and vorticity area integrals. The circulation distributions are shown in Figs. 22 and 23 for x/D = 0.0656 and 0.5577, respectively. The two methods of circulation calculation are in reasonable agreement. We note that within a short length after formation ($x/D \cong 0.5$), the minimum circulation has dropped by a factor of 3.

Measurement resolution is higher in Fig. 17. This figure captures the radially far-flung vortices. The maps in Figs. 17, 18, and 19 show the jets between vortex pairs which gives rise to thrust. The vortex arrays and the mechanism of thrust and yawing moment are depicted schematically in Figs. 27 and 28.

Figures 18 and 19 indicate that, in the clapping mode, the two flaps produce arrays of vortices that are mirror images. Thus, they would produce thrust but no maneuvering cross-stream forces (Fig. 27). On the other hand, in the waving mode, the two arrays of vortices from the two flaps are staggered in the streamwise direction. Due to this fact, the waving mode produces both axial and cross-stream forces (Fig. 28). The vortex shedding process is clarified in Figs. 25 - 28. Figure 25 shows a drag-producing wake behind a hydrofoil where the induced flow between a pair of shed vortices is pointed upstream. When the foil is oscillated, the wave train shown in Fig. 26 is produced when the induced velocity points in the downstream direction, which gives rise to thrust. The clapping mode produces the mirror-image vortex train shown in Fig. 27 and the waving mode produces the staggered vortex train shown in Fig. 28.

The cross-stream maps in Figs. 20 and 21 were examined to look for clues for higher efficiency in the waving mode. The wake is three-dimensional due to the finite nature of the flaps. The figures show that the shed axial vortex lying within the divider propagates inward towards the axis of the model while the outer shed axial vortex shows no such tendency. This is shown schematically in Fig. 24. After it is fully formed, the inner axial vortex is elliptic and takes an inclined position in the y-z plane. In the clapping mode, during the outward motion of the flaps, four axial vortices would tend to converge near the model axis increasing vortex-vortex and vortex-wall interactions. We suspect that induced drag will be affected more in the clapping mode than that in the waving mode.

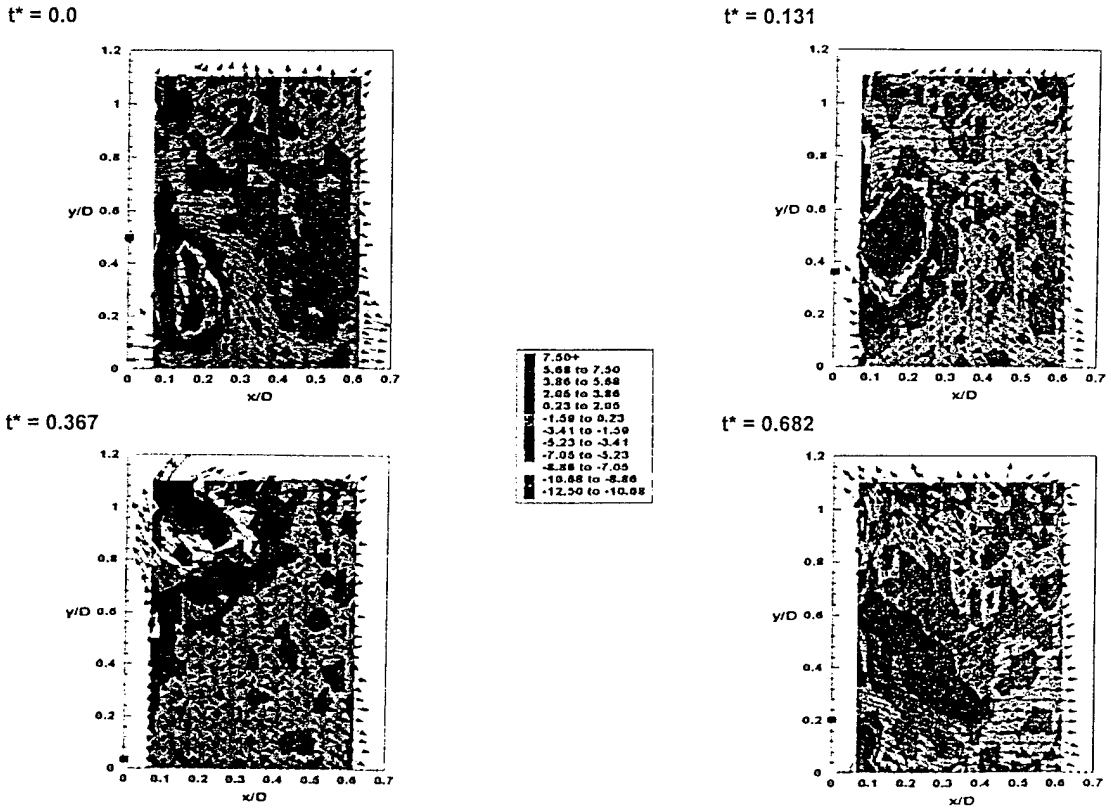

Fig. 17. Vorticity-velocity vector plots in the axial plane for clapping. The velocity perturbations are with respect to freestream velocity. Filled squares on the y-axis indicate the location of flap trailing edge in this and succeeding figures. Note that, when the flap is at outboard extremity, the outer-most vortex trajectory is at 70° to the x-axis which is much larger than the flap trailing edge angle of 30°.

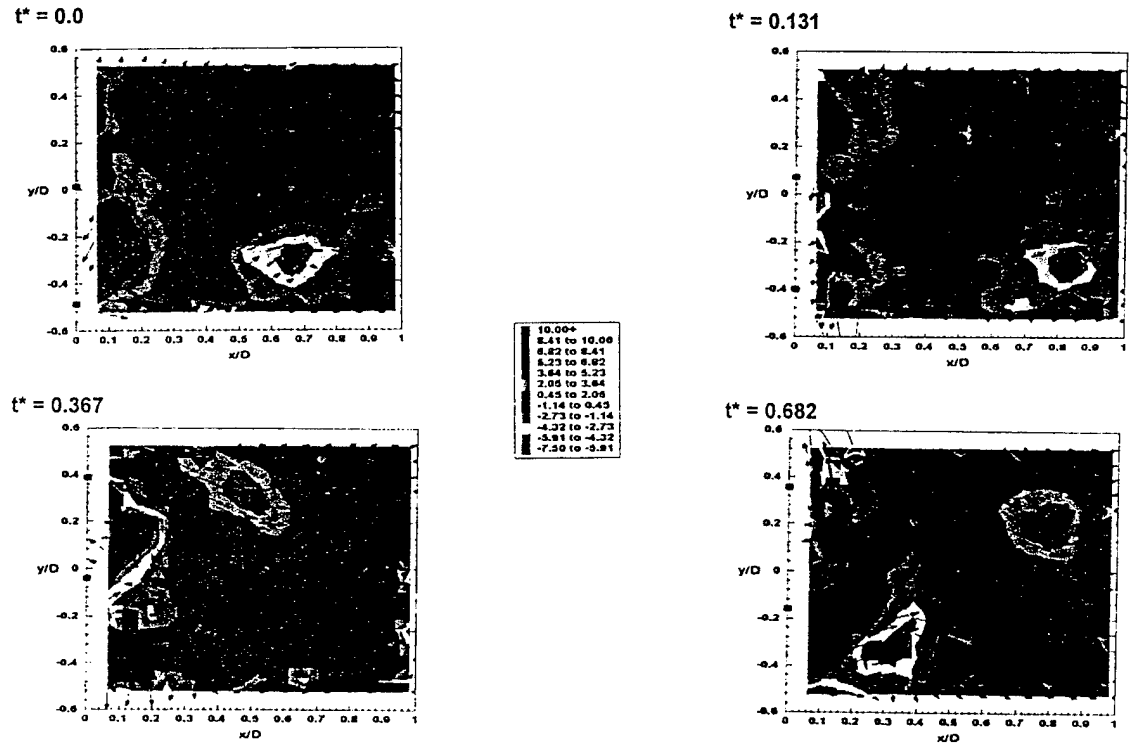

Fig. 18. Vorticity-velocity vector maps in the axial plane in the waving mode.

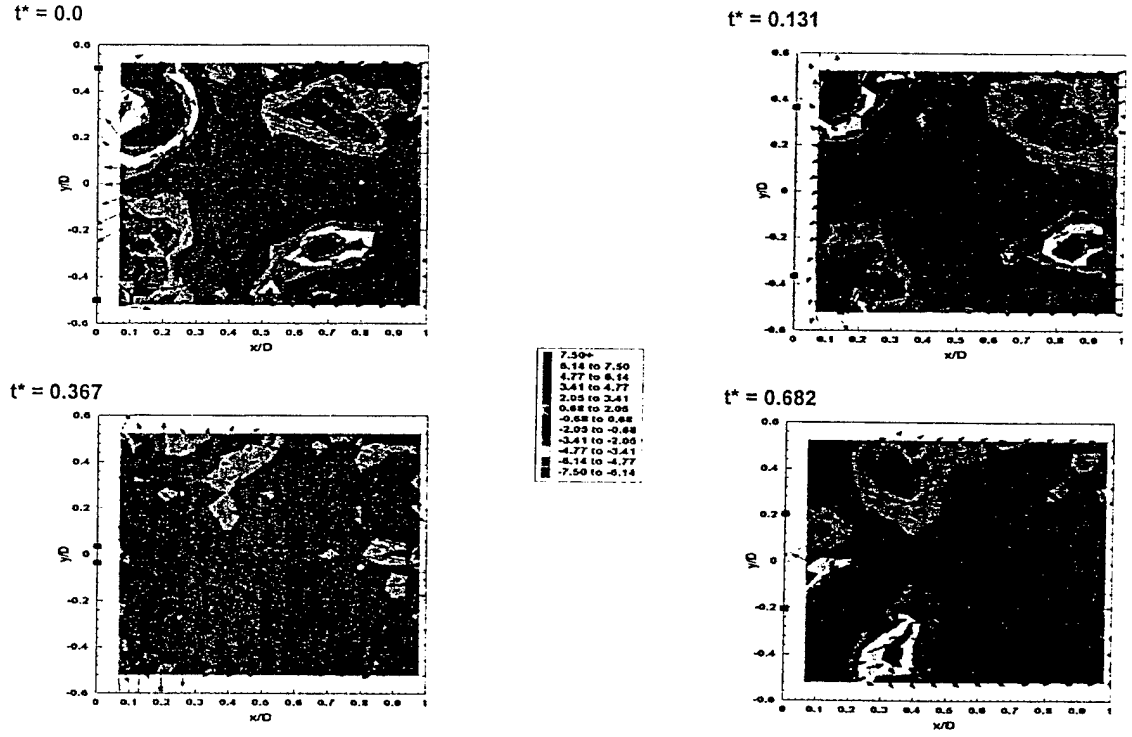

Fig. 19. Vorticity-velocity vector maps in the axial plane in the clapping mode.

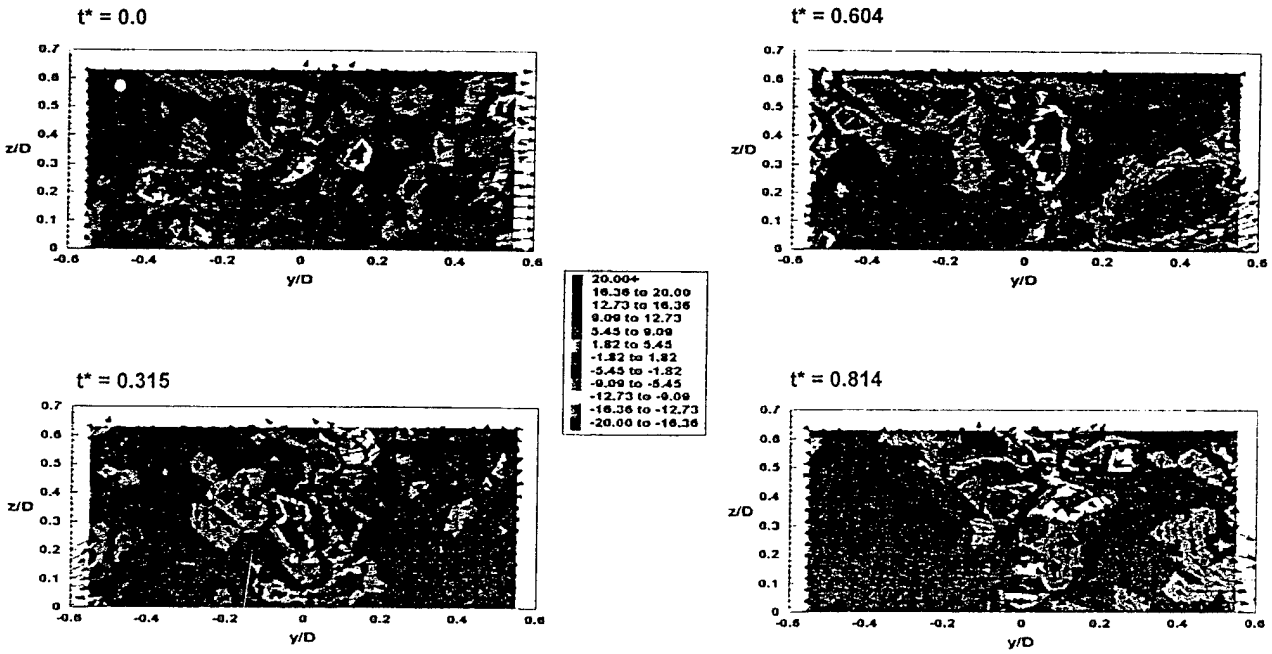

Fig. 20. Vorticity-velocity vector maps in the cross-stream plane in the waving mode; x/D = 0.066. Filled square markers at z/D = 0.5 within each frame indicates flap location.

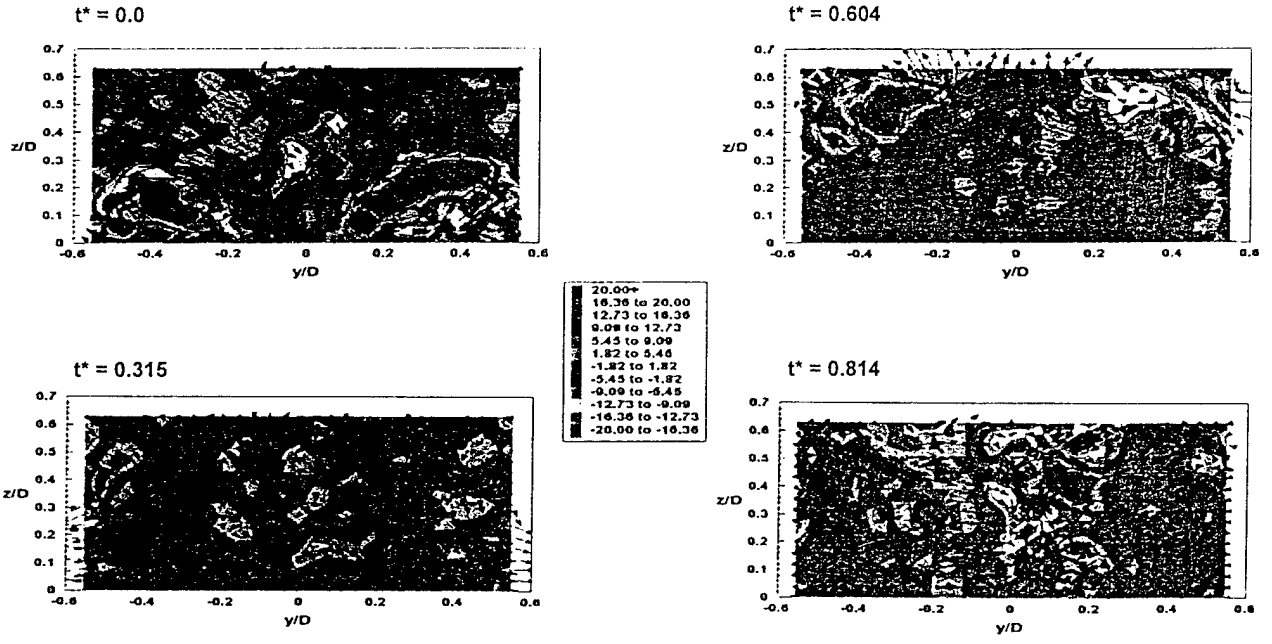

Fig. 21. Vorticity-velocity vector maps in the cross-stream plane in the clapping mode; x/D = 0.066. Filled square markers at z/D = 0.5 within each frame indicates flap location.

22(a)

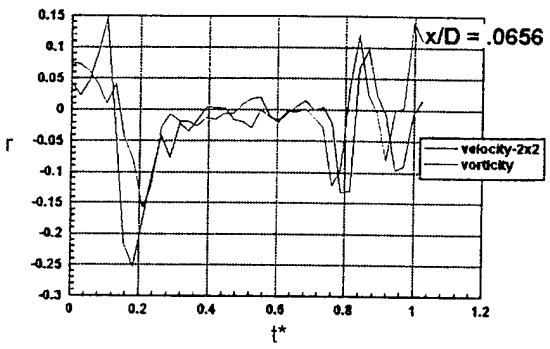

22(b)

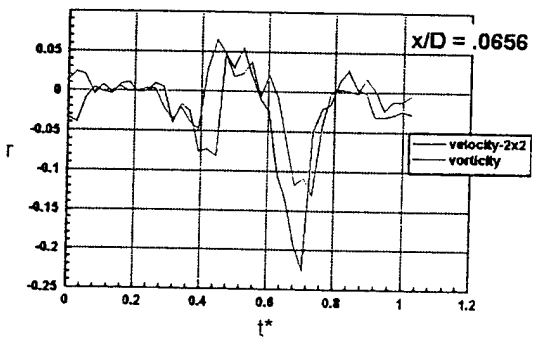

Fig. 22. Vortex circulation versus flap phase; starboard flap x/D = 0.0656, (a) waving and (b) clapping.

23(a)

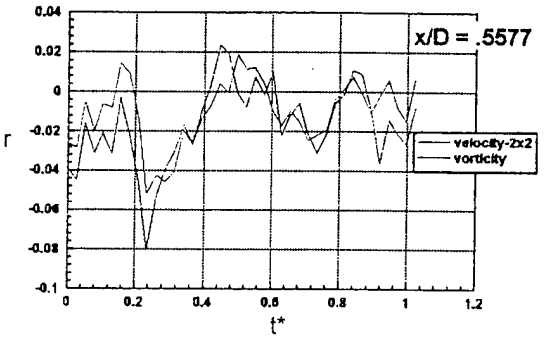

23(b)

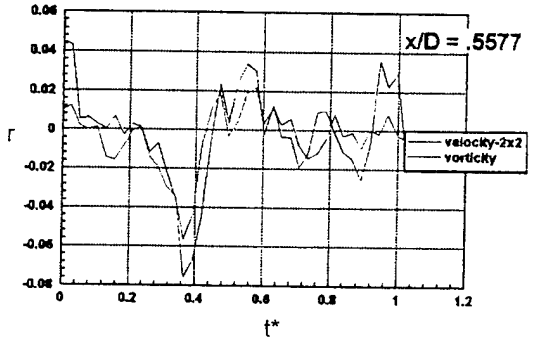

Fig. 23. Circulation distribution at a downstream station (x/D = 0.5577) compared to that in Fig. 22, (a) waving and (b) clapping

24(a)

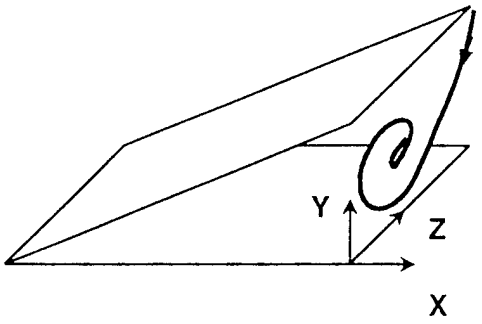

24(b)

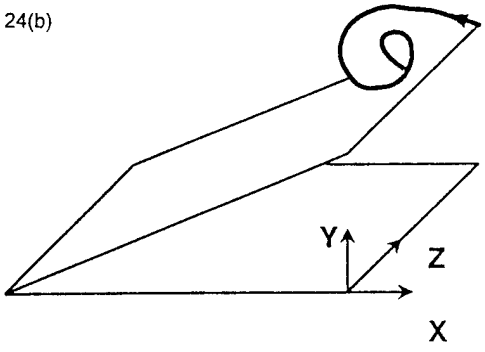

Fig. 24 Schematic diagram showing the inward trajectory of the inner shed axial vortex (a) as opposed to the outer shed axial vortex (b) in both modes of flap oscillation.

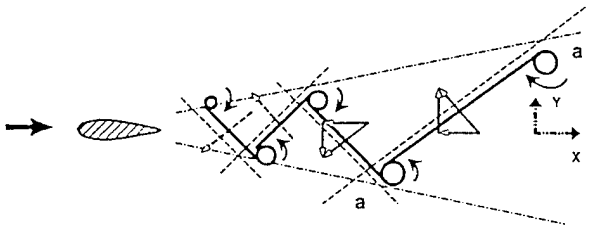

Fig. 25. Schematic of production of drag (momentum deficit) and yaw force due to a Kármán vortex train.

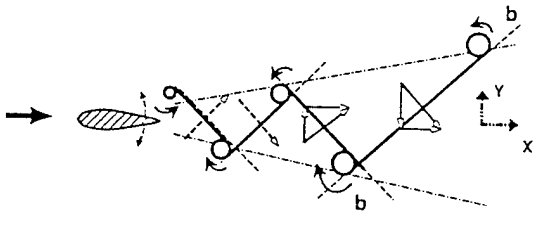

Fig. 26. Schematic of production of thrust (momentum excess) and yaw force due to a negative Kármán vortex train.

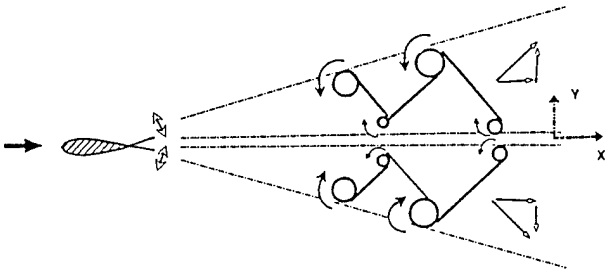

Fig. 27. Schematic of vortex train in clapping mode showing the origin of axial and cross-stream force vectors.

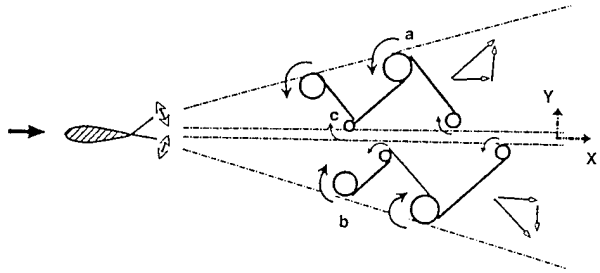

Fig. 28. Schematic of vortex train in waving mode showing the origin of axial and cross-stream force vectors.

5.0 CONCLUSIONS

A laboratory investigation has been conducted to examine the performance of a dual flapping foil device used as a maneuvering and propulsive tool for a rigid body. A model was built (1 m long, 7.6 cm diameter) with flapping foils at the end of the tail cone and various measurements were performed in a water tunnel. The flow speed range in water was between 5 and 80 cm/s and the flapping frequency varied from 2.6 to 6.2 Hz. These parameters, as well as the body length, are in the range popular among fish and seals. The flaps were operated in two modes: waving and clapping. These flaps mimic the motion of the caudal and pectoral fins of a fish. (This clapping motion is also found among insects.) It was demonstrated that, although attached to a rigid body, the device can produce a net thrust. By operating the flaps differentially, the device can also be used to produce a yawing moment for maneuvering purposes. The waving mode of the flaps is more efficient as a thruster compared to the clapping mode. This explains why a fish may use a caudal fin for propulsion and the pectoral fins for maneuvering. The waving mode involves a yawing motion of the nose. Thus, its higher propulsive efficiency suggests that the side-to-side motion of the head of a fish may have hydrodynamic benefits.

Comprehensive measurements of the vortex shedding process in the wake, matched to the phase of the flaps, have been carried out. These data can be useful to validate dynamic numerical simulation codes incorporating the effects of moving surfaces. Existing non-linear inviscid theories are inadequate to account for sensitivity to Strouhal number in the range $0.2 < St < 0.4$. Viscous stability effects also need to be included. In the dual-flapping foils attached to a rigid body, while the net drag is less than the net thrust, the wake is very wide compared to that for a fixed cylinder of same diameter and the wake decays rapidly. This is explained by clearly demonstrating that the wake of the device is predominantly composed of down-stream-pointing jets lying between pairs of shed vortices.

Past two-dimensional theoretical and experimental results in the low Strouhal number-axial force coefficient range, as well as the present work over a larger range, indicate that there is an universal asymptotic limit of thrust that can be produced by the flapping foil technique. However, the axial force produced may fall short when flapping foils are attached to rigid bodies. The interaction of the drag of the rigid body with the flapping foil flow is complicated. There is systematic variation in force generation with the mode of flap oscillation, flapping foil frequency (in addition to Strouhal number) and the number of flapping foils. Three-dimensional viscous non-linear theories are required to account for these effects.

When the present work was started, we were intrigued by the fact that the clapping motion of the wings of insects for propulsion is common in air, but is rare in water. On the other hand, the waving motion of the caudal fin of fish is common in water but is rare in air. Because clapping of wings in air produces both thrust and a large amount of lift force, it involves a complicated rotary motion of the wings as well. The ability of small insects to fly in the air remains a mystery. Quantitative experiments are required to ascertain the mechanisms involved. However, aquatic animals have separate means for handling the buoyancy forces and the thrust-producing role of the waving motion of the caudal fin is relatively better understood.

With aquatic animals, the main lacuna in our understanding is the element of drag. There is considerable uncertainty in the drag data of aquatic animals. This has led to much controversy in the past. Even our understanding of lift-based force generation is often based on inviscid non-linear theories. They do not adequately account for viscous effects, which influence the behavior in narrow Strouhal number ranges where optimum efficiency is reached. Careful laboratory experiments on simplified engineering models of aquatic animals and physical modeling might bring some clarity to the subject.

ACKNOWLEDGMENT

This research was funded by the Office of Naval Research (program managers J. Fein and Dr. T. McMullen) and the Naval Undersea Warfare Center Independent Research Program (program manager Dr. S. Dickinson). This support is gratefully acknowledged. The authors would also like to acknowledge the assistance of W. Nedderman, J. Castano, J. Dick, M. Zeiger, C. Straney, M. Savoie, and B. Doyle.

REFERENCES

1 Bandyopadhyay, P. R., Castano, J. M., Rice, J. Q., Philips, R. B., Nedderman, W. H., and Macy, W. K., "Low-Speed Maneuvering Hydrodynamics of Fish and Small Underwater Vehicles," J. Fluids Eng., *119*, 1997, pp. 136-144.

2. Jones, K. D., Dohring, C. M., and Platzer, M. F., "Wake Structures Behind Plunging Airfoils: A Comparison of Numerical and Experimental Results, Paper No. AIAA 96-0078, 1996.

3. "HSVA Towing Tests on a G7e Torpedo with SSR-Drive and with Normal Propeller Drive," PG/21600, translated by the British from the German, September 1944.

4. Gopalkrishnan, R., Triantafyllou, M. S., Triantafyllou, G. S., and Barrett, D., "Active Vorticity Control in a Shear Flow Using a Flapping Foil," J. Fluid Mech., *274*, 1994, pp. 1-21.

5. Hall, K. C., and Hall, S. R., "Minimum Induced Power Requirements for Flapping Flight," J. Fluid Mech., *323*, 1996, pp. 285-315.

6. Bandyopadhyay, P. R., "A Simplified Momentum Model of a Maneuvering Device for Small Underwater Vehicles," NUWC-NPT Technical Report 10,552, Naval Undersea Warfare Center Division, Newport, RI, 1996.

7. Ellington, C. P., "Unsteady Aerodynamics of Insect Flight," The Society of Experimental Biology," No. XLIX, pp. 109-129 (Eds. C. P. Ellington and T. J. Pedley), 1995.

8. Rayner, J. M., "Dynamics of the Vortex Wakes of Flying and Swimming Vertebrates," The Society of Experimental Biology, No. XLIX, 1995, pp. 131-155 (Eds. C. P. Ellington and T. J. Pedley).

9. Webb, P. W., Hydrodynamics and Energetics of Fish Propulsion, Bull. Fish. Res., BD., Canada, *190*, 1975, pp 1-158.

10. Lighthill, M., J., Mathematical Biofluidynamics, Philadelphia, SIAM, 1975.

11. Wu, T. Y., "Hydromechanics of Swimming Propulsion," J. Fluid Mech., *46*, 1971, pp. 337-355.

12. Webb, P. W., "Hydrodynamics: Nonscombroid Fish," in *Fish Physiology, Vol. VII*, eds., W. S. Hoar and D. J. Randall, Academic Press, 1978, pp. 189-237.

13. Gopalakrishnan, R., "Vortex-Induced Forces on Oscillating Bluff-Cylinders," Ph.D. Thesis, MIT, Cambridge, MA, 1993.

14. Schlichting, H., *Boundary-Layer Theory*, McGraw-Hill, New York, 1979.

15. Bandyopadhyay, P. R., and R. Balasubramanian, "Vortex Reynolds Number in Turbulent Boundary Layers," J. Theor. Comp. Fluid Dynamics, *7*, 1995, pp. 101-117.

16. Batchelor, G. K., *An Introduction to Fluid Dynamics*, Cambridge University Press, 1967.

17. Bandyopadhyay, P. R., Nedderman, W. H., Castano, J. M., and Donnelly, M., 1996, "A Small Maneuvering Device for Energetic Environment," NUWC-NPT Video, Naval Undersea Warfare Center Division, Newport, RI.

18. Zeiger, O. K. Rediniotis, Donnelly, M. J., and Telionis, D. P., "Temporal Evolution of the Flow Field Over a Pitching Tangent-Ogive Cylinder," AIAA Paper No. 95-0441, 1995.

19. Bainbridge, R., "The Speed of Swimming of Fish as Related to Size and the Frequency and Amplitude of the Tail Beat." J. Exp. Biol., *35*, 1963, pp. 109-133.

20. Kashin, S. and Greelner, S., "On the Generation of End Performance of Fish Swimming," in "Neurocontrol of Locomotion," (Eds. Stein, Greelner, and Stuart), 1976, pp. 81-102.

21. Kashin, S., "Fish Locomotion," Dr. Sci. Thesis, Inst. of Oceanology, Academia of Science of USSR, Lenin State Library, Moscow, 1985.

22. Chopra, M. G., "Hydromechanics of Lunate Tail Swimming Propulsion," J. Fluid Mech., *7*, 1977, pp. 46-69.

23. Triantafyllou, M. S., Triantafyllou, G. S., and Gopalakrishnan, R., "Wake Mechanics for Thrust Generation in Oscillating Foils," Phys. Fluids, *3*(12), 1991, pp. 2835-2837.

24. Triantafyllou, G. S., Triantafyllou, M. S., and Grosenbaugh, M. A., "Optimal Thrust Development in Oscillating Foils with Application to Fish Propulsion," J. Fluids and Structures, *7*, 1995, pp. 205-224.

25. Isshiki, H., and Murakami, M., "A Theory of Wave Devouring Propulsion," J. Soc. Naval Architects of Japan, *156*, 1984, pp. 102-114.

26. Fish, F., "Power Output and Propulsive efficiency of Swimming Bottlenose Dolphins (Tursiops Truncatus," J. Exp. Bio., *185*, 1983, pp. 179-193.

Modeling and Control of Biomimetic Aquatic Propulsion

Joel W. Burdick Richard M. Murray
Scott D. Kelly Richard J. Mason

Division of Engineering and Applied Science
California Institute of Technology

10 September 1997

Outline

I. Introduction and motivation

II. Geometric mechanics, control, and locomotion

III. Swimming without viscosity (irrotational flow)

IV. Swimming with vorticity

V. Summary and conclusions

Motivation and Goals

Traditional locomotion in fluids:

- Use propellers/thrusters with enough actuation to move in all directions
- Can be noisy due to motor noise, vibrations, cavitation, etc
- Not ideal for maneuvering in some situations (e.g. low speed)

Alternative locomotion mechanisms:

- Shape change: used at a variety of scales from amoeba to lamprey
- Fins: exploits vorticity effects (e.g. circulation/lift)
- May offer advantages in terms of noise, efficiency, *maneuverability*

Goals of this project:

- Apply and extend tools from geometric mechanics and nonlinear control to understand fundamental locomotion mechanisms and gaits
- Develop models for a large class of aquatic propulsion mechanisms
- Develop proof-of-concept experiments to validate models and concepts

Robotic Locomotion

Different types of robot locomotion systems:

- Wheeled mobile robots
- Snakelike (hyperredundant) robots
- Legged and walking robots, insect robots
- Underwater vehicles (low and high Re)

Common features in locomotion systems:

- Constraints: interaction with the environment restricts feasible velocities but not reachable positions
- Gaits: periodic motions of internal parts in proper phase generates motion

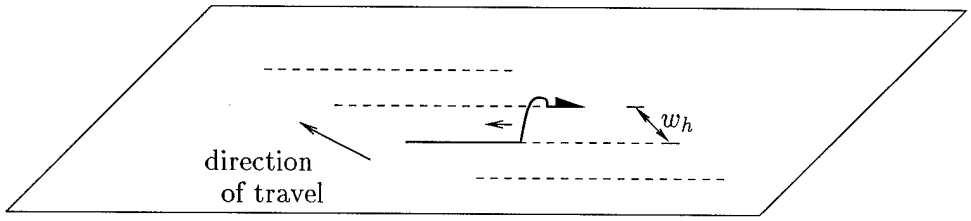

9/10/97

Modeling Locomotion using Geometric Phases

$r \in M$	robot shape (base)
$g \in SE(3)$	robot position (fiber)
$\Gamma : TQ \to \mathfrak{se}(3)$	Kinematic *connection*
	$\Gamma(q) \cdot \dot{q} = \mathrm{Ad}_g(g^{-1}\dot{g} + A(r)\dot{r}) = 0$

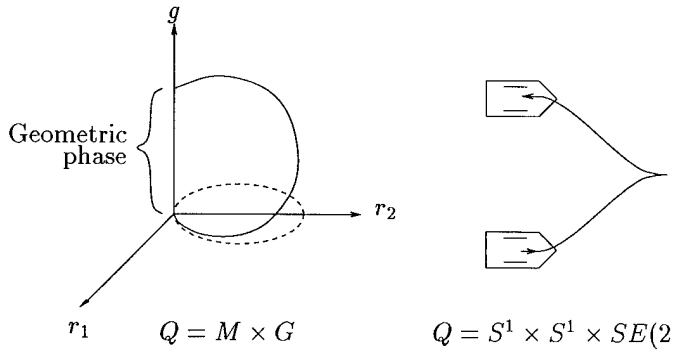

$Q = M \times G$ $Q = S^1 \times S^1 \times SE(2)$

Characterize controllability and gait behavior in terms of Γ and curvature of Γ

9/10/97

Example: Kinematic Car

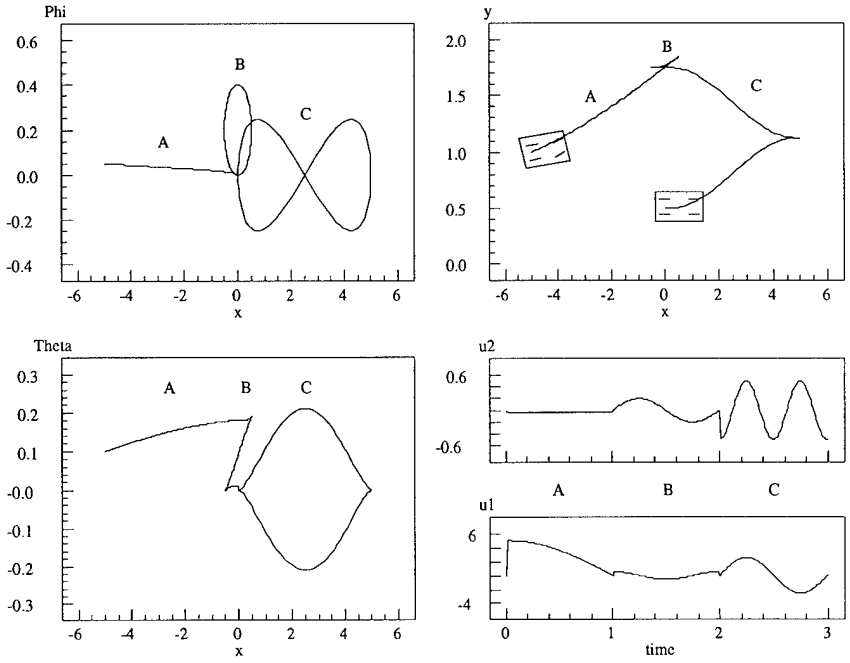

9/10/97

Locomotion in Incompressible, Inviscid, Irrotational Fluids

Simple example (Saffman, 1967):

- Simple planar body with shifting center of mass plus change of shape
- Exploit the fact that effective mass is a function of current shape

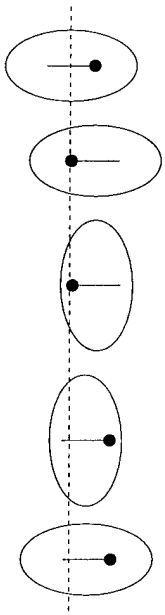

Modeling and control using *hydrodynamic* connection

- Potential flow formulation (Kirchhoff) gives kinetic energy of the form

$$K(g, r, \dot{g}, \dot{r}) = \dot{r}^T M_r(r)\dot{r} + \xi^T M_g(r)\xi$$

$$\xi = g^{-1}\dot{g} = \text{body velocity of vehicle}$$

- Standard Lagrangian setup $\Longrightarrow$ translational and rotational symmetry give conservation law

$$\frac{d}{dt}(\text{momentum}) = 0 \quad \Longrightarrow \quad \Gamma(q)\dot{q} = 0$$

9/10/97

"Squirming circles" Example

Low Reynolds number case: Blake 1971, Shapere & Wilczek 1988

- Viscous forces dominate $\Longrightarrow$ Stokes connection $\Longrightarrow$ $\Gamma_s \cdot \dot{q} = 0$
- Can use changes in shape to generate forward motion

Inviscid case: Saffman 1967, Miloh and Galper 1993

- No viscosity $\Longrightarrow$ conservation laws $\Longrightarrow$ $\Gamma_m \cdot \dot{q} = 0$
- Use control theory to figure out what "gaits" to use to generate motion in different directions.

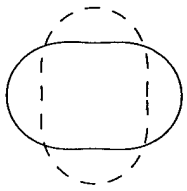

Mode 1
$\sin 2\theta$

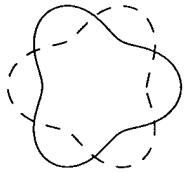

Mode 2
$\sin 3\theta$

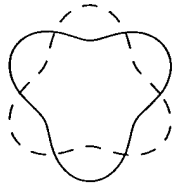

Mode 3
$\cos 3\theta$

Simulation Results using Squirming Circles

Modeling approach:

- Restrict perturbations to a finite dimensional set

$$r(t,\theta) = r_0(1 + \epsilon[k_1(t)\cos(2\theta) + k_2(t)\cos(3\theta) + k_3(t)\sin(3\theta)])$$

- Use perturbation expansion to solve for potential flow equations and shape-dependent inertial properties
- Use geometric control theory to predict motion for a given gait

1-1-1 gait: $k = (\cos t, -\sin t, -\sin t)$

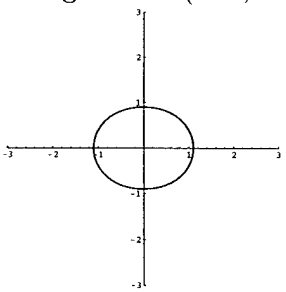

$t = 0$

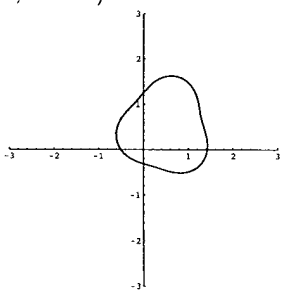

$t = 15.3$ cycles

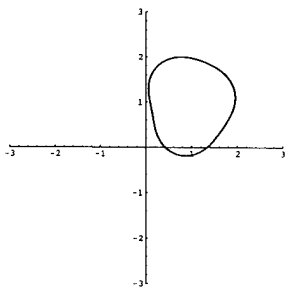

$t = 30.6$ cycles

Euler-Lagrange Formulation of Body/Fluid Equations

$SE(3)$	position and orientation of body
$\text{Diff}_{\text{vol}}(\mathcal{D})$	volume preserving diffeomorphisms on fluid domain $\mathcal{D}$
R	shape of body

Equations of motion evolve on $Q = SE(3) \times \text{Diff}_{\text{vol}}(\mathcal{D}) \times R$

- Lagrangian $L : TQ \to \mathbb{R}$ is left and right invariant

$$L(q, \dot{q}) = l(g^{-1}\dot{g}, \dot{\phi}\phi^{-1}, r, \dot{r}) \qquad \begin{array}{ll} g^{-1}\dot{g} = \xi & \text{body velocity} \\ \dot{\phi}\phi^{-1} = u(x) & \text{fluid velocity field} \end{array}$$

- Inviscid, irrotational case:

$$\begin{aligned} \frac{d}{dt}\frac{\partial l}{\partial \xi} + \text{ad}^*_\xi \frac{\partial l}{\partial \xi} = 0 \qquad & \text{body velocity} \\ \frac{d}{dt}\frac{\partial l}{\partial u} - \text{ad}^*_u \frac{\partial l}{\partial u} = 0 \qquad & \text{fluid motion} \\ \frac{d}{dt}\frac{\partial l}{\partial \dot{r}} - \frac{\partial l}{\partial r} = Bv \qquad & \text{internal shape} \end{aligned}$$

- Generalization of Euler equations and Kirchhoff equations.

9/10/97

Addition of vorticity

First cut: add circulation effects (lift + vorticity source term)

$$\begin{aligned} \frac{d}{dt}\frac{\partial l}{\partial \xi} + \text{ad}^*_\xi \frac{\partial l}{\partial \xi} = F = \rho U \Gamma \qquad & \text{lift} \\ \nabla \times \left(\frac{d}{dt}\frac{\partial l}{\partial u} - \text{ad}^*_u \frac{\partial l}{\partial u}\right) = Z = \dot{\Gamma}\delta_{\text{te}} \qquad & \text{vorticity} \end{aligned}$$

- For simple airfoil models, Kutta condition couples lift and vorticity
- Control problem: characterize gaits by studying different motions of fin/body system; somewhat similar form to previous problems
- Dissipation/drag can be added in similar way

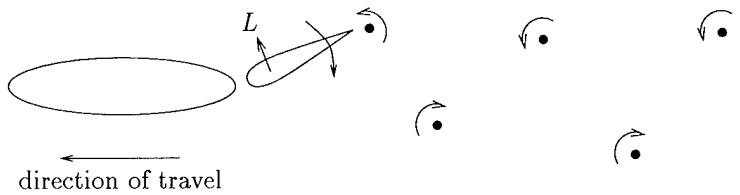

9/10/97

Experimental Apparatus

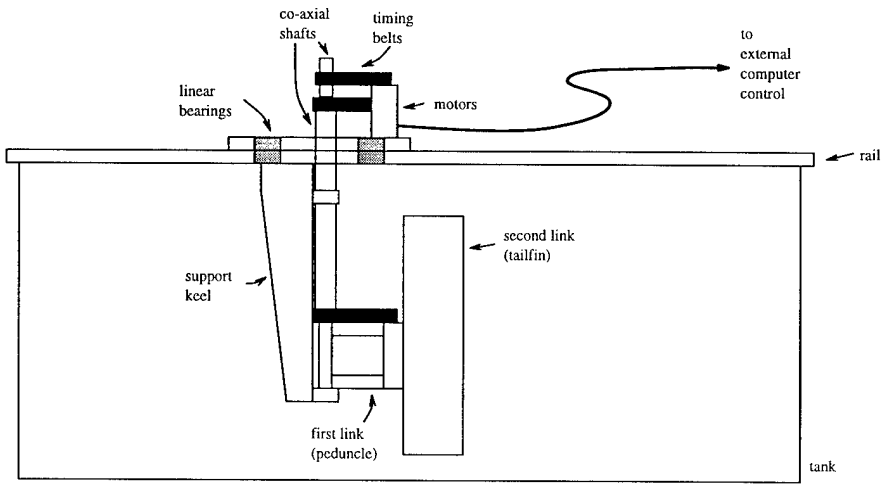

9/10/97

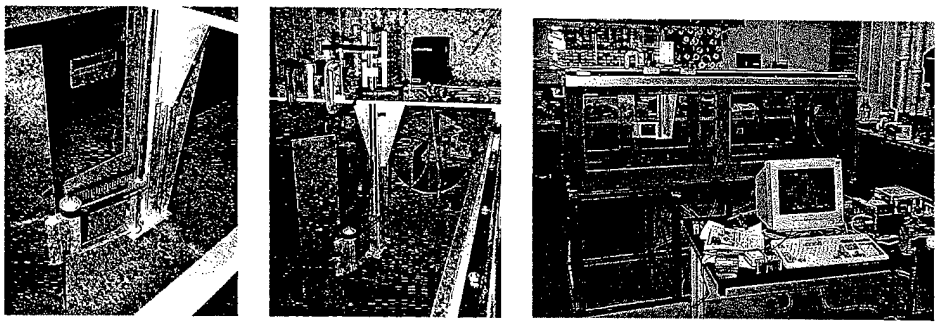

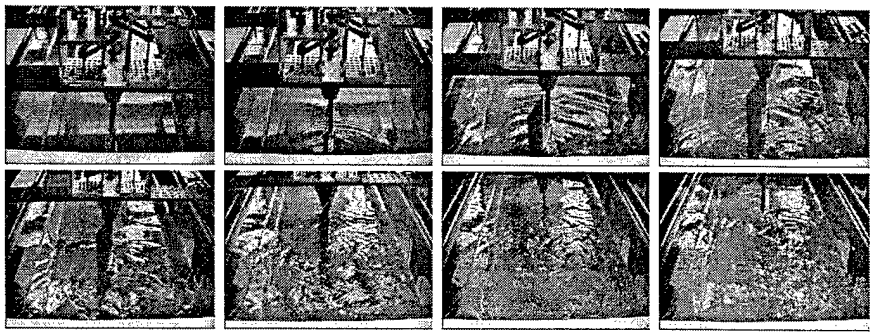

9/10/97

Initial Experimental Results

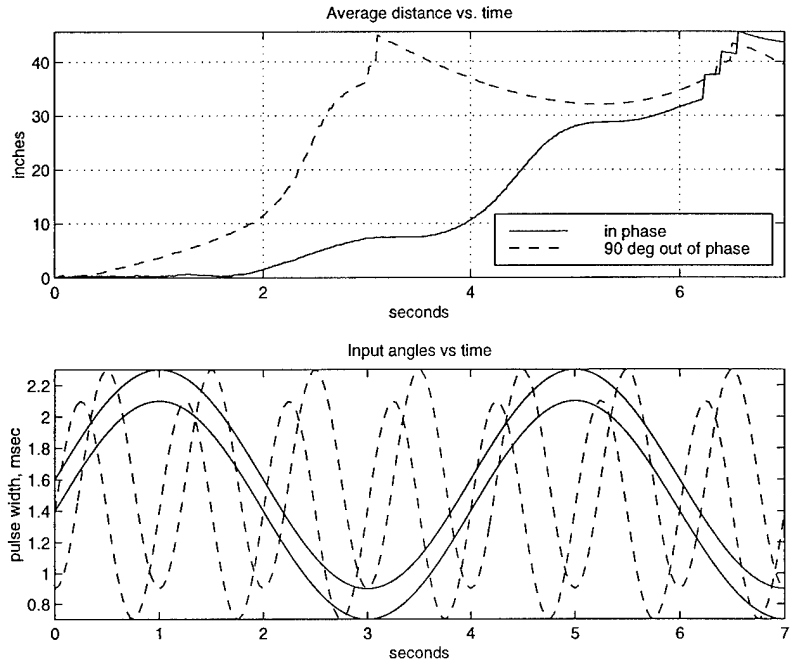

9/10/97

Conclusions

Geometric formulation of equations tuned to nonlinear control tools

- Utilize Euler-Lagrange formulation to allow use of recent tools from geometric mechanics and control
- External forces and dissipation are added after formulation of equations
- Many mathematical details left to work out (e.g., domain effects)

Derivation of control laws/gaits for underwater vehicles

- Substantial work available for use of holonomy in other locomotion systems
- Some extreme cases are already covered: low Re and inviscid/irrotational
- Just starting to study control properties of general body/fluid system

Experimental validation

- Simple experiments being used to test validity of models and assumptions
- Already see some interesting gaits (without application of control theory)

Further Information

S. D. Kelly, R. J. Mason, C. Anhalt, R. M. Murray, and J. W. Burdick, "Mechanics and Control of Self-Propulsion Through Fluids: Geometric Modeling and Experimental Validation", *American Control Conference*, 1998. In preparation.

R. M. Murray and S. Kelly, "Geometric Phases and Robotic Locomotion", *J. Robotic Systems*, Jun 95.

R. M. Murray, "Nonlinear Control of Mechanical Systems: A Lagrangian Perspective" *IFAC Symp. on Nonlinear Control Systems Design (NOLCOS)*, Jun 95. To appear, *Annual Reviews in Control.*

Copies of papers are available via the World Wide Web:

`http://avalon.caltech.edu/~murray`

Copies of these slides are available from

`http://avalon.caltech.edu/~murray/talks/auvi-sep97.ps`

9/10/97

SHAPE MEMORY ALLOYS IN AQUATIC BIOMIMETICS

OTHON K. REDINIOTIS
DEPARTMENT OF AEROSPACE ENGINEERING
TEXAS A&M UNIVERSITY
COLLEGE STATION, TEXAS

NORMAN W. SCHAEFFLER
AEROPROBE CORPORATION
BLACKSBURG, VIRGINIA

INTRODUCTION

The science of biomimetics attempts to study and apply nature's solutions to complex engineering problems, i.e. to mimic the successes of nature. Biological systems have, through millions of years of evolution, developed efficient mechanisms for locomotion and control. Fish and other aquatic animals do not swim by fins alone. Fish use the control and power of their entire bodies to maneuver sharply and propel themselves quickly. To generate these fast maneuvers and sharp accelerations, large amplitude motion of the entire body is needed. A man-made craft wishing to apply the lessons learned from nature must be continuously deformable along its entire length.

The present group has investigated the use of smart memory alloys (SMA) as actuators or "muscles" in a deformable hydrofoil. SMAs are materials that undergo a phase change under certain thermal and loading conditions. Specifically, the SMAs utilized here are in the form of wires that have been "trained" to contract when heated and expand when cooled. The heating of the wires can be achieved by passing an electric current through them. After the electrical heating ceases, especially when the wire is an environment conducive to high rates of heat convection, the wire will cool and thus expand. Therefore, complex actuation cycles can be achieved by controlling the flow of current through the wire and the rate of heat convection over the wire. If SMA wires are arranged in opposing (antagonistic) pairs, bi-directional muscles can be formed. The present team has developed such a muscle. A fully operational generic hydrofoil with a SMA actuator or "muscle" incorporated into the trailing edge of the hydrofoil has been developed. This SMA muscle was able to deflect the trailing edge $\pm$ 5° at rates as high as 1.5 Hz.

SMA MUSCLE - PRINCIPLE OF OPERATION

The principle of trailing edge actuation via the SMA muscle is shown in Figure 1. The muscle was applied to trailing-edge actuation of a hydrofoil as a precursor to lunate tail thrust generation. The main actuation elements are designed to be two sets of thin SMA wires (0.015" to 0.027") embedded into an elastomeric element that provides the main structural support. Controlled heating and cooling of the two wire sets can generate bi-directional bending of the elastomer, which in turn deflects (for quasi-static control) or oscillate (for thrust generation) the trailing edge of the hydrofoil. Towards this end, SMA wires were two-way trained and the market was searched for the elastomer with the right elastic properties. A flex sensor embedded inside the elastomer provided feedback on the muscle deflection.

SMA TRAINING AND PARTIAL ACTUATION EXPERIMENTS

Figure 2 presents an automated SMA training/modeling station developed by the present research team. The device performs repeated martensite-to-austenite (M to A) and austenite-to-martensite (A to M)

SMA transformation cycles and collects time records of SMA strain/displacement, load and temperature during each cycle. From the data, the SMA transformation behavior as well as behavior deterioration with number of transformation cycles are modeled.

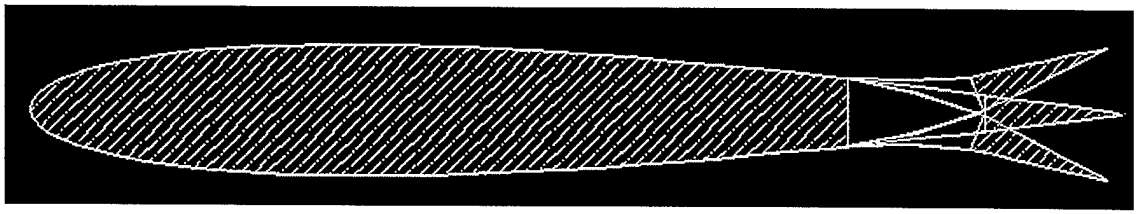

Figure 1. The SMA muscle (non-crosshatched section) deflects/oscillates the hydrofoil's trailing edge.

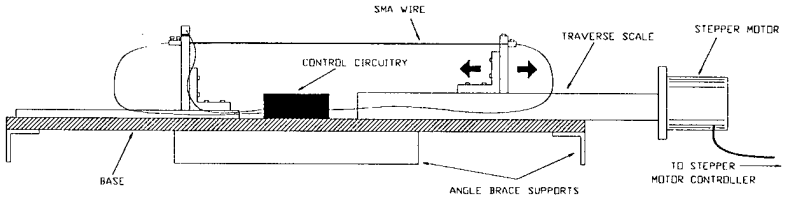

Figure 2. SMA training/modeling station.

It has been determined that rapid cooling directly affects the rate of response of the actuator. The higher the achieved heat transfer rates, the higher the achievable actuation or oscillation bandwidth. Furthermore, actuation frequency response can be improved by employing partial actuation at higher rates than would be achieved for full deflections. This technique can be implemented by employing partial transformation cycles. Preliminary tests of minor loops, or partial transformation loops, for a two-way wire have been performed and are shown in Figures 3 and 4. These tests show the shape of the hysteresis curves for minor loops with partial austenite to complete martensite transformations and vice versa. Figure 3 shows minor loops inside a major loop for a constant stress test with partial austenitic transformation on the heating cycle with complete transformation to martensite upon cooling. Figure 4 shows minor loops with partial martensite transformation on the cooling cycle with complete austenitic transformation upon heating.

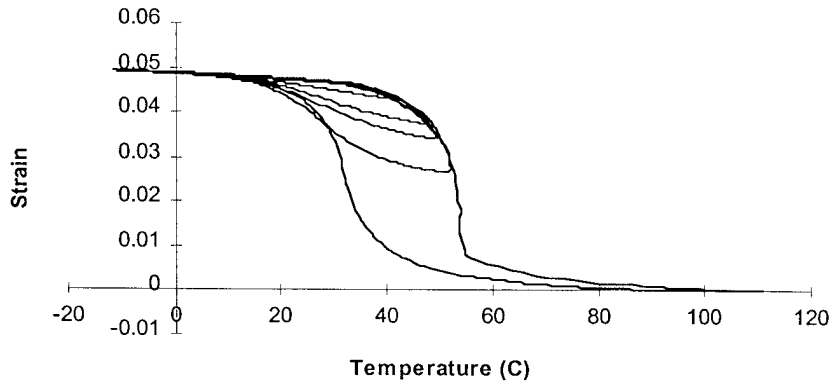

Figure 3. Strain vs. Temperature for a 2-way wire with partial austenite transformation from a fully martensitic state.

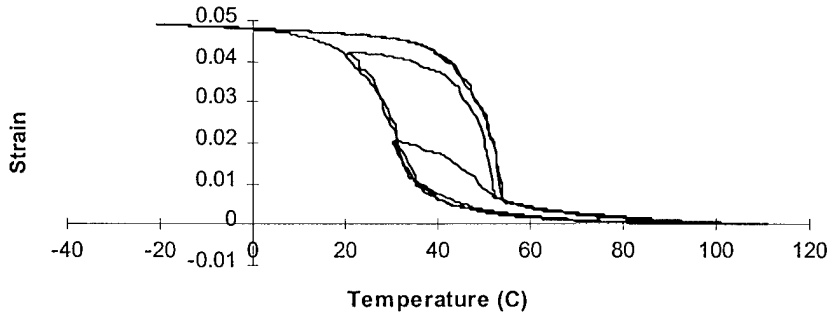

Figure 4. Strain vs. Temperature for a 2-way wire with partial martensitic transformation from a fully austenitic state.

SMA MUSCLE IMPLEMENTATION AND FEM MODELING

As discussed previously, control of the shape of the hydrofoil aft section was achieved by embedding small-diameter SMA wires/tubes into the body of the hydrofoil, specifically into the elastomeric part of an SMA muscle. Since the elastomer is a good thermal insulator, depending on the desired frequency response of the actuation, the distance of the embedded wires from the surface of the elastomer can vary. For high actuation frequencies (order or 1 Hz and higher), the wires were barely embedded or were even exposed to water. In the latter case a thin elastic electrically insulating coating covered each wire. Figure 5 presents our implementation of a first generation muscle and the latter actuation scheme. In this SMA muscle the wires were positioned very close to the elastomer surface but were totally exposed to water. One can distinguish the four SMA wires running longitudinally on the upper (Figure 5a) and lower (Figure 5b) surfaces. The SMA wires were two-way trained to 2.5% strain and had a diameter of 0.015". The function of the four long leads on the left of the Figures is to connect the two wire sets to an electric power source.

The performance of the device and its actuation bandwidth were very encouraging. The device was submerged in a water tunnel. The electric power source was a 20 Amp, 20 Volt, DC power supply. It provided the power necessary for the resistive heating of the wires and the martensite-to-austenite phase transformation. The austenite-to-martensite phase transformation was achieved by interrupting resistive heating, and allowing the water to conduct or convect the heat off the wires, thus cooling them down to their martensitic phase temperature. Conduction (water tunnel off) and convection (water tunnel on, water velocity variable up to 1ft/sec) tests were conducted. Continuous periodic actuation frequencies as high as 1.5Hz (full transformation cycles) were achieved. For water velocities larger than 1ft/sec, the specific power supply was unable (voltage limitations) to heat the wires up sufficiently and martensite-to austenite phase transformation was not possible.

These encouraging initial tests were capitalized on in the development of the second generation muscle. A 4" long (chordwise dimension), 3" wide (spanwise dimension) SMA muscle was fabricated and fully instrumented for testing. Instrumentation included a set of flex sensors, embedded inside the elastomer, properly calibrated to provide deflection feedback, one sensor for each bending direction and also a group of four thermocouples, distributed on the wires of the two SMA wire sets, to provide wire temperature feedback. Thermocouple redundancy warrants muscle functionality under partial

thermocouple failure conditions and provides information on thermal differences within each wire set. A schematic of the experimental hardware used in studying the muscle behavior is shown in figure 6.

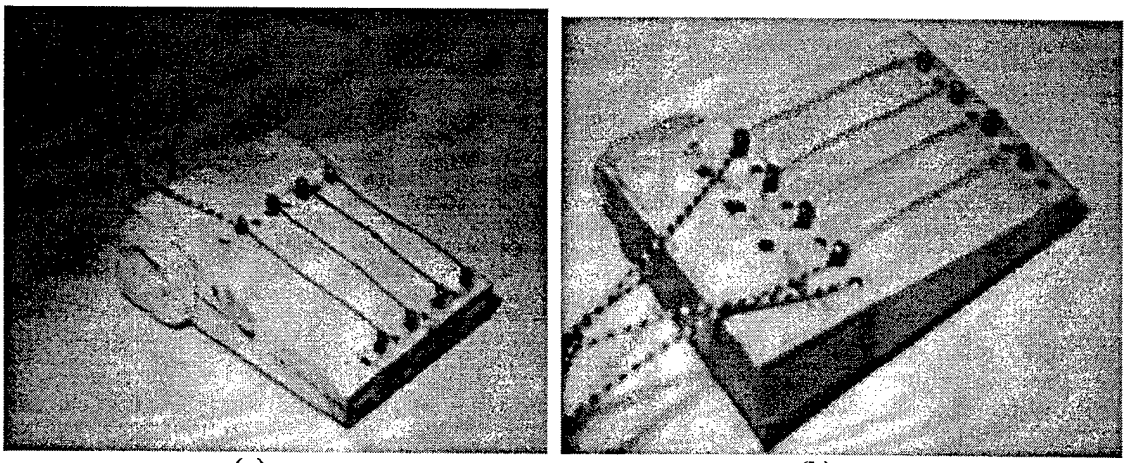

(a) (b)

Figure 5. Initial implementation of an SMA muscle.

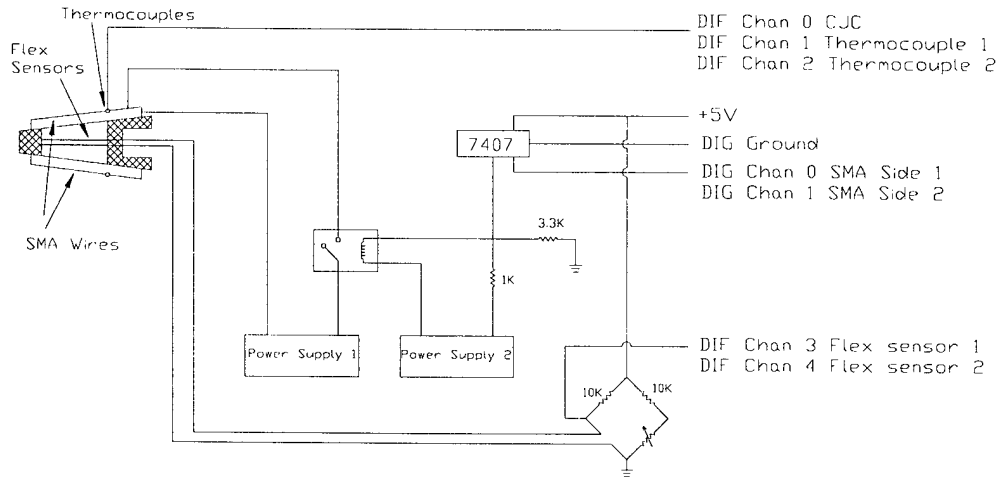

Figure 6. Schematic of SMA muscle instrumentation.

The modeling of deflected shapes as a function of input current has been carried out using a thermomechanical constitutive model for SMA coupled with the elastic response of the elastomer. An approximate structural analysis model, as well as detailed FEM analysis have been performed and the model predictions have been compared with experimental measurements. The constitutive model described above has been successfully integrated into the commercial Finite Element program ABAQUS. Using this model it is possible to model fully coupled thermomechanical problems as well as the mechanical response to a specified temperature variation. In the current analysis the temperature of the SMA is taken from experimental measurements in order to reduce computational time and simplify the model. Figure 7 shows the finite element model of the second generation muscle. A trailing edge is also shown in the figure to better illustrate muscle functionality. The model exploits the spanwise periodicity of the design to model only one cell (section between two adjacent SMA wires) of the muscle. The SMA wires are represented by one-dimensional truss elements rigidly fixed in all DOF and attached to planar elements representing the pins on the opposite end. The elastomer is represented by 20-node brick

elements. Also shown in figure 7 is the deflected muscle mesh at maximum deflection, with the bottom set of wires actuated. The results of a low frequency test are shown in figure 8, corresponding to muscle actuation in air, i.e. in the absence of hydrodynamic loading. The temperature profile shown (experimentally measured) was used as an input to the analysis. One set of wires was activated for this analysis. Prior to the application of the temperature profile the muscle was cooled to –20°C to assure an all martensite initial state. Based on previous characterization of the SMA wires the transformation temperatures and the amount of pre-strain were also used as input to the model. As is seen in the figure good agreement between the model and experiment was achieved.

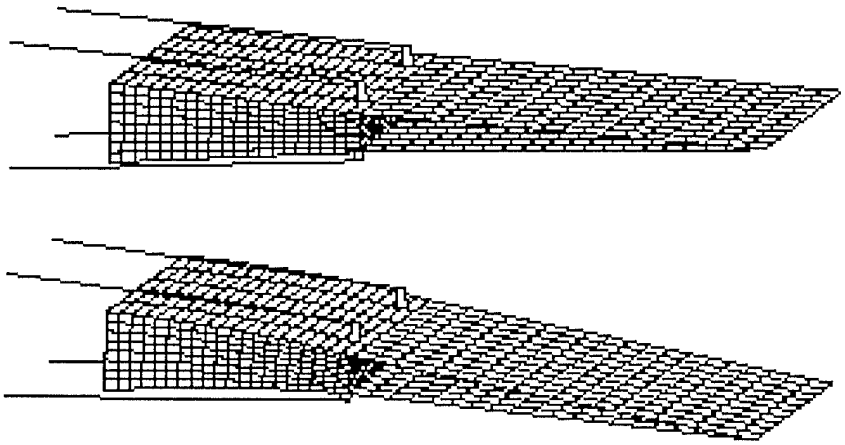

Figure 7. Finite Element mesh of muscle and the deformed mesh at maximum deflection.

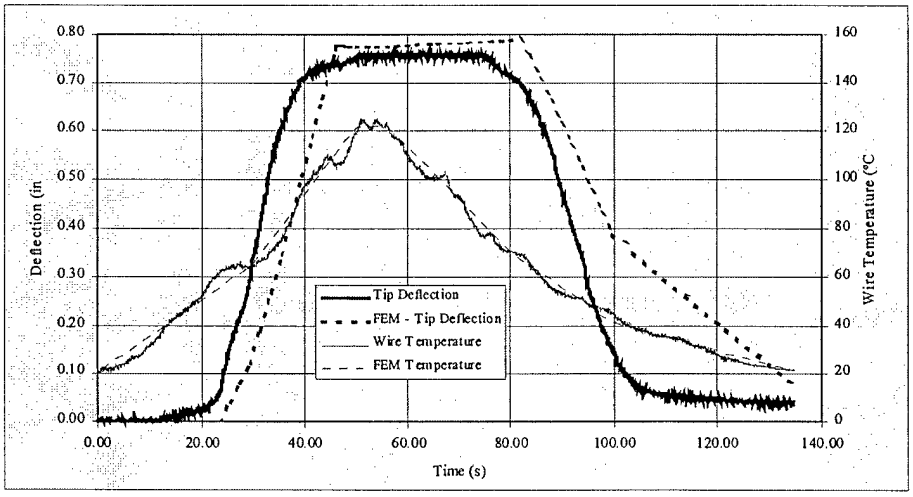

Figure 8. Experimental and numerical muscle (trailing edge) tip deflection and wire temperature versus time for quasi-static actuation in air.

THE ACTIVE HYDROFOIL MODEL

The hydrofoil model with the SMA muscle can be seen in Figure 9. The model is comprised of three sections. The leading edge section encompasses the front of the model and is constructed of foam and

fiberglass. This section is hollow to allow the mounting of the pitch sensor within the model. This section also has a shaft passing through it upon which the model is mounted in the water tunnel. The wires for the on-board flex sensors and thermocouples also pass through the leading edge section and then out of the model through the mounting shaft. Attached to the rear of the leading edge section is the SMA muscle. The elastomer can be seen, as can the SMA wires mounted across this section. The elastomer is mounted in a Plexiglas frame that is mechanically fastened to the leading-edge section. The trailing edge, which is also constructed out of fiberglass, is attached to the elastomer in a similar fashion. Figure 9a shows the entire hydrofoil model. The leading edge section can be seen as can the "muscle" section and the trailing edge. The reader can also distinguish the twelve upper-surface SMA actuator wires right above the elastomer. Figure 9b shows the compartment built in the leading-edge section to house equipment. Figure 9c shows how the wires are routed outside of the model. The bearings and the exit point on the shaft are waterproofed before the model is submerged. Finally, Figure 9d shows the hydrofoil model mounted in the water tunnel set-up. The shaft through the model is mounted into the bearings on the two vertical slides. This allows the model to plunge and pitch under its own trailing-edge control. In order for the model to be balanced about its pitch axis as well as neutrally buoyant, lead weights were added to the hollow area in the leading-edge section of the model.

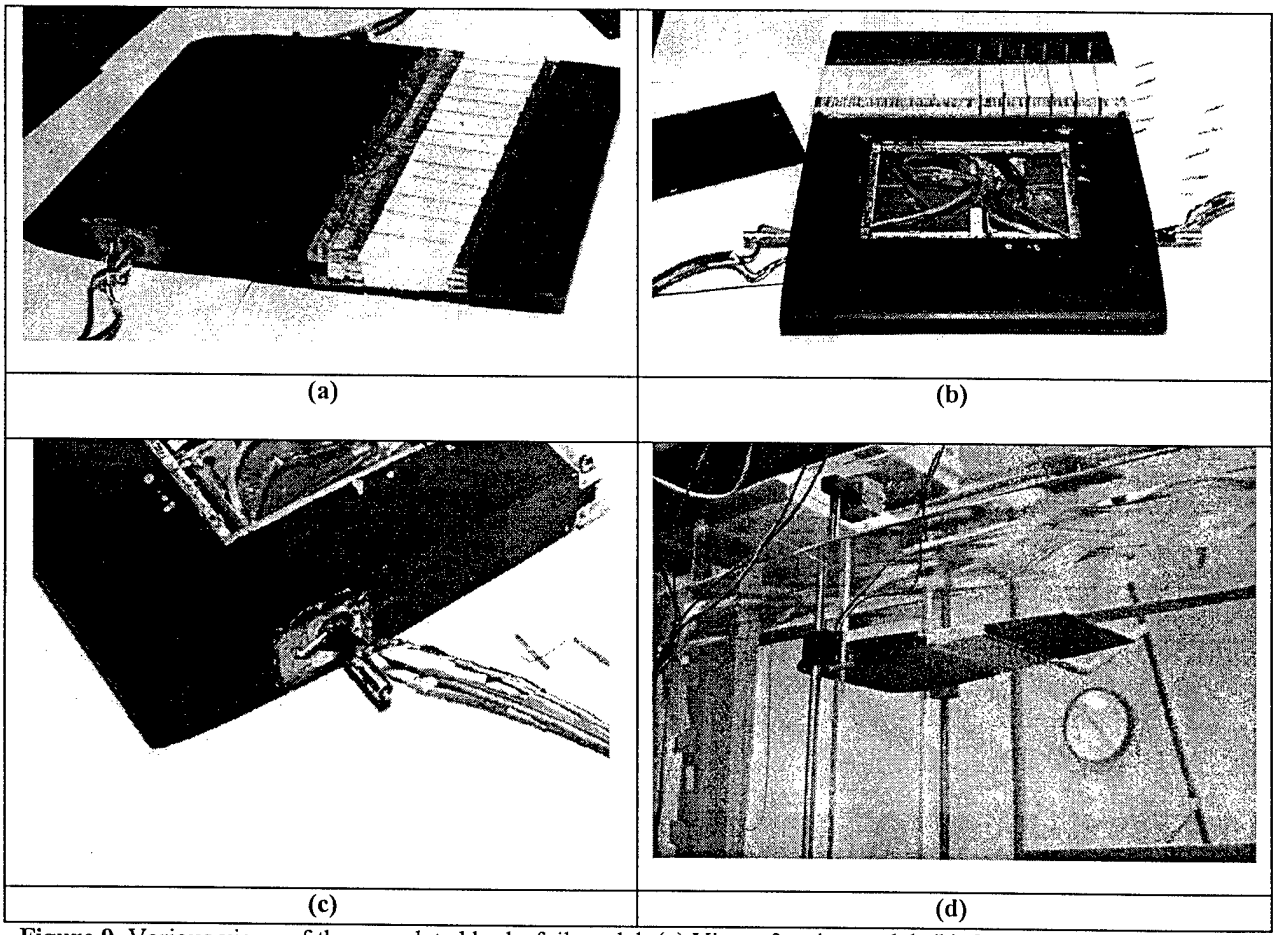

Figure 9. Various views of the completed hydrofoil model: (a) View of entire model, (b) Compartment within the leading-edge section of the model for instrumentation housing, (c) Exit point from the model of the wiring for the on-board instrumentation, (d) The water tunnel setup with the hydrofoil mounted in it.

Actuation tests were performed with the active hydrofoil in still air, still water and moving water at different speeds. The muscle was actuated and deflection and temperature data was collected in different heat convection and hydrodynamic loading conditions.

In order to model the coupling between the hydrodynamics and the mechanical problem successive iterations between a Smith-Hess potential flow code and the FEM model were performed. An iterative procedure was developed, whereby the hydrofoil is first loaded by the actuated SMA wires in the absence of hydrodynamic forces, which results in the maximum possible deflection imposed by the SMA wires. For this deflected shape, the hydrodynamic forces are evaluated for given flow parameters and are used to modify the loading boundary conditions for the mechanical problem. After the new deflected shape is evaluated by the modified FEM analysis, the hydrodynamic forces are computed again for the updated shape, and this iterative procedure is completed when the error for the maximum deflection between consecutive iterations becomes smaller than a given tolerance. Figure 10 shows the displaced upper and lower surfaces of the hydrofoil for a water freestream velocity of 1 ft/sec. The hydrofoil shapes shown are the undeformed case and each of the three iterations until convergence was reached.

Figure 11 shows deflection-temperature hysteresis loops for the hydrofoil in still air and still water. The relative shift of the two graphs is purely due to the zero offset of the deflection sensor. In these tests, the deflection sensor was a high precision, high repeatability Celesco stringpot. The original flex sensors did not meet our measurement repeatability standards. The fact that the loops do not close at their low ends is due to residual deflection when the muscle is unloaded (SMA wires cooled).

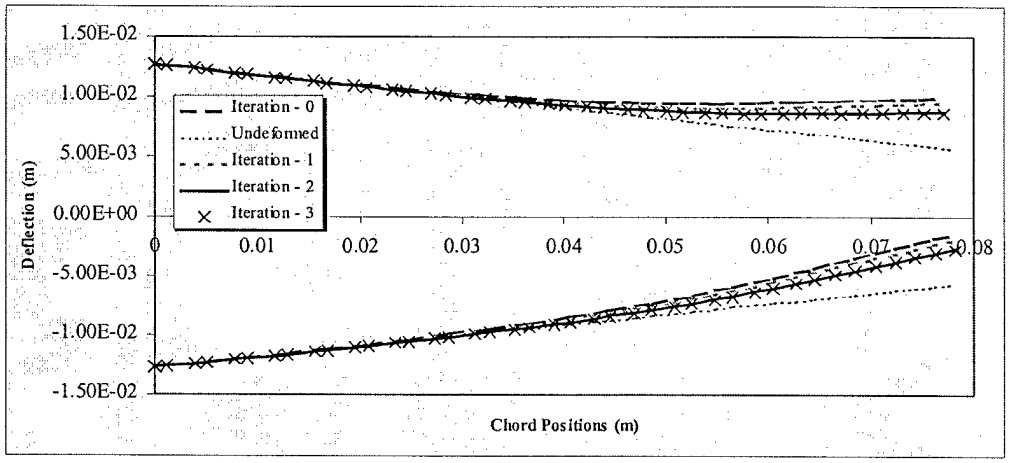

Figure 10. The upper and lower surfaces of the deflected hydrofoil muscle showing the progress towards convergence of successive iterations of the FEM and potential flow models.

Figure 12a shows experimental data on deflection and temperature time histories for the hydrofoil in moving water. During the experiments the undeflected (forward) section of the hydrofoil was fixed at zero angle of attack. Hydrodynamic loading developed on the flap as it deflected. Data at two different freestream values are presented. Figure 13 shows deflection-temperature hysteresis loops corresponding to the data of figure 12. The fact that the deflection magnitudes are similar for both experiments suggests that at these speeds, angle of attack and trailing edge deflections, the hydrodynamic loading does not reduce the maximum deflection achieved by the SMA muscle. We are currently replacing the thermocouple-based temperature measurement technique with a resistivity measurement technique which is expected to eliminate problem such as the noisy nature of the hysteresis loop corresponding to 2ft/sec.

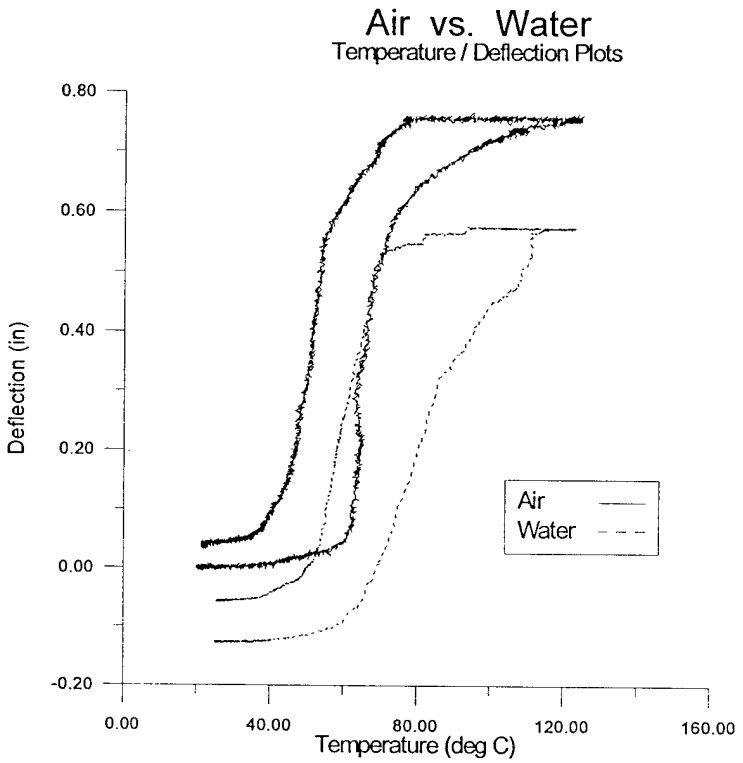

Figure 11. Deflection-temperature hysteresis loops for the hydrofoil in still air and still water.

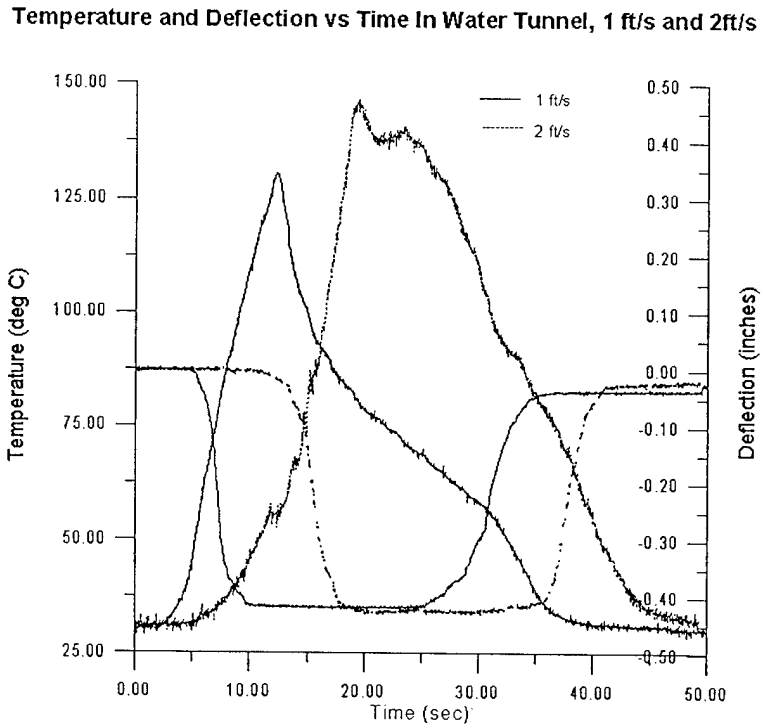

(a)

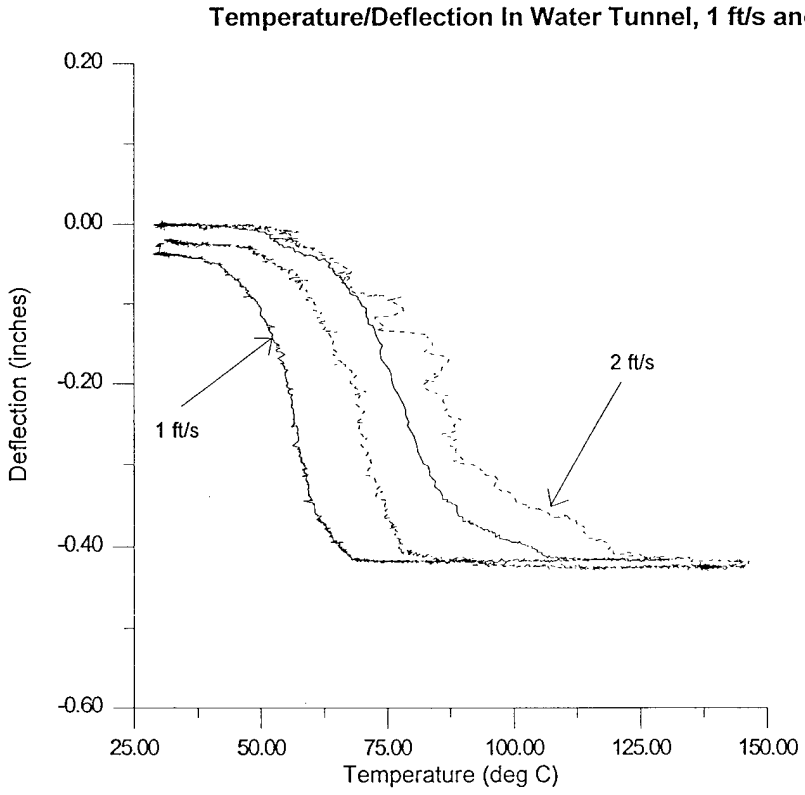

(b)

Figure 12. Experimental data for hydrofoil in water tunnel at two speeds: (a) deflection and temperature time histories and (b) deflection-temperature hysteresis loops.

RELATED CURRENT WORK

The present group is currently working, in collaboration with the Naval Surface Warfare Center (NSWC), on the development of a zero-stock-moment control surfaces for surface ships and submarines. Movable control surfaces in surface ships and submarines involve a fixed stock (pivot axis) about which the appendage rotates. A fundamental problem, causing early fatigue and increased probability of catastrophic failure, is that a parasitic and harmful hydrodynamic moment is created about the stock by the force-center being located some distance away from the stock centerline. Moreover, this force-center moves as the angle of attack changes. In this investigation, the objective is to actively position the center of pressure such that there is zero parasitic torque on the primary stock while getting the equivalent lift of a traditional appendage, by using a "smart flap" actuated through Shape Memory Alloy (SMA) technology.

The use of SMA actuators to effect the shape control can result in an all-electric actuation system without the noise associated with hydraulically moving mechanical components. Furthermore, optimal shape control will result in a hydrodynamically efficient control surface, delaying or avoiding boundary layer separation, a phenomenon associated with shear layer shedding in the wake, a process which is acoustically harmful. Figure 13 shows the design of the control surface. Active SMA cooling, motion amplification and Magneto-Rheological-Fluid (MRF) locking features can be distinguished. The accumulator provides, through valves, manifolds and channels around the SMAs, active SMA cooling, while SMA heating is electrical. Locking of the flap at selected deflections (thus reducing the time the

SMAs are active, in turn leading to longer SMA lifetimes) is achieved through Magneto-Rheological-Fluid dampers/couplers. The same design also provides amplification of the SMA deflections. Design flap deflections are +\- 30 degrees.

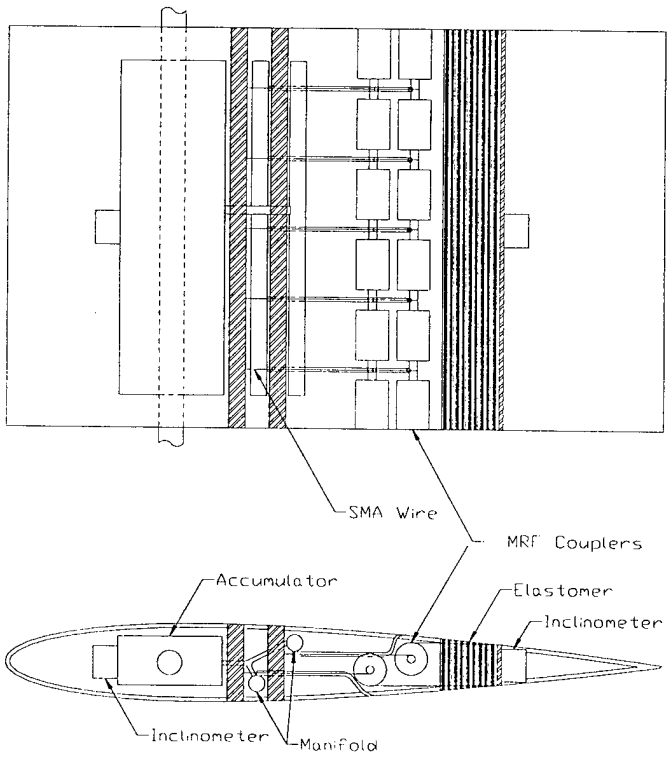

Figure 13. Design of a zero-stock-moment control surface, based on SMA-actuated trailing-edge flap deployment.

References

Bandyopadhyay, P. R., "Swimming and Flying in Nature," Naval Undersea Warface Center Division, NUWC-NPT Technical Memorandum 942080.

Jameson, A., "Optimum Aerodynamic Design Using CFD and Control Theory," AIAA Paper No. 95-1729-CP.

Lagoudas, D.C., Bo, Z., and Qidwai, M.A., 1996, "A Unified Thermodynamic Constitutive Model for SMA and Finite Element Analysis of Active Metal Matrix Composites," Mechanics of Composite Materials and Structures 4, pp. 153-179.

Bo, Z. and Lagoudas, D.C., 1997, "Thermomechanical Modeling of Polycrystalline SMAs Under Cyclic Loading, Part I, Part II, Part III," International Journal of Engineering Science, (submitted).

Rediniotis, O.K. and Lagoudas, D.C., "Theoretical and Experimental Investigation of an Active Hydrofoil with SMA Actuators," presented at the SPIE 1997 Smart Structures and Materials Conference, San Diego, CA, March 1997.

Ion-Exchange Polymer-Metal Composites As Biomimetic Sensors and Actuators- Artificial Muscles

Mohsen Shahinpoor
Artificial Muscles Research Institute
School of Engineering & School of Medicine
University of New Mexico, Albuquerque, NM 87131, USA

ABSTRACT

This paper discusses a number of recent findings in connection with ion-exchange polymer-noble metal composites (IPMC) as biomimetic sensors and actuators. These smart composites exhibit characteristics of both actuators and sensors. Strips of these composites can undergo large bending and flapping displacement if an electric field is imposed across their thickness. Thus, in this sense they are large motion actuators. Conversely by bending the composite strip, either quasi-statically or dynamically, a voltage is produced across the thickness of the strip between the two conducting electrodes attached. Thus, they are also large motion sensors. The output voltage can be calibrated for a standard size sensor and correlated to the applied loads or stresses. They can be manufactured and cut in any size and shape and in particular in the form of micro sensors and micro actuators for MEMS applications. In this paper first the sensing capability of these materials is reported by moving the tip end of a cantilevered sample and measuring the output voltage. The results were then plotted to get characteristic response of the composite for a given imposed tip displacement. The preliminary results shows the existence of a linear relationship between the output voltage and the imposed displacement for almost all cases. Furthermore, the ability of these ionic polymer-metal composites as large motion actuators and robotic manipulators is presented. Several muscle configurations are constructed to demonstrate the capabilities of these IPMC actuators. Further, the feasibility of using such smart composites as linear platform type actuators is discussed. A theoretical model is developed for such actuators and its predictions are compared to experimental results. This paper further identifies key parameters involving the vibrational and resonance characteristics of sensors and actuators made of IPMC's. When the applied signal frequency is varied, so does the displacement up to a point where large deformations are observed at a critical frequency called resonant frequency where maximum deformation is observed. Beyond which the actuator response is diminished. In this research paper, several samples of the actuators were made and tested with various dimensions to compare the vibrational behavior of the actuators. A data acquisition system was used to measure the parameters involved and record the results in real time basis. Finally reported in this paper are load characterization of such active polymer composites made with a noble metal such as platinum. A brief description of a proposed theory for this type of actuator was then discussed. The results showed that these actuators exhibit good force to weight characteristics in the presence of low applied voltages.

Keywords: Ionic Polymer-Metal Composite Sensor, Soft Actuator, Artificial Muscles, Biomimetic Sensor, Vibrations, Resonance.

2. INTRODUCTION

Ion-exchange polymer-metal composites (IPMC) are highly active actuators that show very large deformation in the presence of low applied voltage and exhibit low impedance. They operate best in a humid environment and can be made as a self-contained encapsulated actuators to operate in dry environments as well. They have been modeled as both capacitive and resistive element actuators that behave like biological muscles and provide an attractive means of actuation as artificial muscles for biomechanics and biomimetics applications. Grodzinsky[1], Grodzinsky and Melcher[2,3] and Yannas, Grodzinsky and Melcher[4] were the first to

present a plausible continuum model for electrochemistry of deformation of charged polyelectrolyte membranes such as collagen or fibrous protein and were among the first to perform the same type of experiments on animal collagen fibers essentially made of charged natural ionic polymers and were able to describe the results through electro-osmosis phenomenon. Kuhn[5] and Katchalsky[6], Kuhn, Kunzle, and Katchalsky[7], Kuhn, Hargitay, and Katchalsky[8], Kuhn, and Hargitay[9], however, should be credited to have been the first investigators to report the ionic chemomechanical deformation of polyelectrolytes such as polyacrylic acid (PAA), polyvinyl chloride (PVA) systems. Kent, Hamlen and Shafer[10] were also the first to report the electrochemical transduction of PVA-PAA polyelectrolyte system. Recently revived interest in these area with concentration on artificial muscles can be traced to Shahinpoor and co-workers and researchers [11-14, 22-49], Osada[15], Oguro, Asaka and Takenaka[16], Asaka, Oguro, Nishimura, Mizuhata and Takenaka[17], Guo, Fukuda, Kosuge, Arai, Oguro and Negoro[18], De Rossi, Parrini, Chiarelli and Buzzigoli[19] and De Rossi, Domenici and Chairelli[20]. More recently De Rossi, Chiarelli, Osada, Hasebe, Oguro, Asaka, Tanaka, Brock, Shahinpoor, Mojarrad[11-69] have been experimenting with various chemically active as well as electrically active ionic polymers and their metal composites as artificial muscle actuators.

Essentially polyelectrolytes possess many ionizable groups on their molecular chain. These ionizable groups have the property of dissociating and attaining a net charge in a variety of solvent medium. According to Alexanderowicz and Katchalsky[17] these net charge groups which are attached to network of macromolecules are called polyions and give rise to intense electric fields of the order of 10^{10} V/m. Thus, the essence of electromechanical deformation of such polyelectrolyte systems is their susceptibility to interactions with externally applied fields as well as their own internal field structure. In particular if the interstitial space of polyelectrolyte network is filled with liquid containing ions, then the electrophoretic migration of such ions inside the structure due to an imposed electric field can also cause the macromolecular network to deform accordingly. Shahinpoor[18,22,25,26,28,29,31,32,33,34,35,36] and Shahinpoor and co-workers[21,23,24,27,30] have recently presented a number of plausible models for micro-electro-mechanics of ionic polymeric gels as electrically controllable artificial muscles in different dynamic environments. The reader is referred to these papers for the theoretical and experimental results on dynamics of ion-exchange membranes -platinum composite artificial muscles. Most Ion exchange polymeric membranes swell in solvents and by and large are hydrophilic. This gives rise to ability of the membrane to swell in water which can be controlled in an electric field due to ionic nature of the membrane. Furthermore by placing two electrodes in close proximity of the membrane walls and applying a voltage, the forced transport of ions within a solution through membrane becomes possible at microscopic level. For a solvent such as water then local swelling and deswelling of membrane can be controlled depending on polarity of the electrode nearby more like the behavior of the bimorphic materials. This can be achieved by chemical or other possible means of plating of conductive materials on membrane surfaces. Platinum is one such conductor that can be deposited inside the network and on the outer surfaces of IPMC.

Also being ionic in microscopic structure, IPMC has the ability to shift its mobile ions of the same charge polarity within itself when it is placed in an electric field which results in ionic attraction or repulsion between the fixed charges of opposite polarity contained in the side groups within the polymer molecular chain. This leads to local collapse or expansion of the polymer membrane macroscopically. Physically this causes a stress gradient on opposite sides of the membrane causing it to bend. Therefore by applying an alternating signal at low voltage one can achieve membrane oscillation proportional to frequency and amplitude of the input signal. This bending oscillation can be utilized in various applications as in linear or platform type actuators.

The organization of this paper is such that it first discusses a number of recent findings in connection with ion-exchnage polymer-noble metal composites (IPMC) as biomimetic sensors and actuators. These smart composites exhibit characteristics of both actuators and sensors. Strips of these composites will undergo large bending and flapping displacement if an electric field is imposed across their thickness. Thus, in this sense they are large motion actuators. Conversely by bending the composite strip, either quasi-statically or dynamically, a voltage is produced across the thickness of the strip between the two conducting electrodes attached. Thus, they are also large motion sensors. The output voltage can be calibrated for a standard size sensor and correlated to the applied loads or stresses. They can be manufactured and cut in any size and shape and in particular in the form of micro sensors and micro actuators for MEMS applications. In this paper first the sensing capability of these materials is reported by moving the tip end of a cantilevered sample and measuring the output voltage. The results were then plotted to get characteristic response of the composite for a given imposed tip displacement.The preliminary results shows the existence of a linear relationship between the output voltage and the imposed displacement for almost all cases. Unlike strain gages where the output voltage needs to be conditioned and amplified by a factor of 1000 or more, these composite polymer sensors can produce up to a few millivolts output and sense large deformations in the presence of small amplifier gains of two order of magnitude less than conventional sensors.The most important advantage of these composites is the fact that they can be used both as large

motion sensors and actuators. This means that by using a simple feedback control scheme and double layers of the composite film, it will be possible to use these composites as self-contained robotic manipulators that do not need sophisticated sensor modules for full integration of intelligence.

Furthermore, the ability of these ionic polymer-metal composites as large motion actuators and robotic manipulators is presented. Ion-exchange-membrane-metal composites are highly active actuators that show very large deformation in the presence of low applied voltage and exhibit low impedance. A comparison between IPMC and the widely used transducing actuators shows that, while lagging in force delivering capability, these materials are superior in mass, power consumption and displacement levels. This produces an enabling technology of a new class of devices. Several muscle configurations are constructed to demonstrate the capabilities of these IPMC actuators. Further, the feasibility of using such smart composites as linear platform type actuators is discussed. In order to achieve linear motion from these typically bending type actuators, a series of muscles made from ion-exchange-membrane-metal composites were cut in strips and attached either end-to-end or to one fixed platform and another movable platform in a cylindrical configuration. A theoretical model is developed for such actuators and its predictions are compared to experimental results.

This paper further identifies key parameters involving the vibrational and resonance characteristics of sensors and actuators made of ion-exchange-polymer-metal composites. When the applied signal frequency is varied, so does the displacement up to a point where large deformations are observed at a critical frequency called resonant frequency where maximum deformation is observed. Beyond which the actuator response is diminished. In this research paper, several samples of the actuators were made and tested with various dimensions to compare the vibrational behavior of the actuators. A data acquisition system was used to measure the parameters involved and record the results in real time basis. This research was in support of active vibration suppression research for flexible structures using ionic polymers as active dampers. It also supported other applications in biomimetics research such as bird flight motion, artificial coral reefs and marine propulsion.

Finally reported in this paper are load characterization of such active polymer composites made with a noble metal such as platinum. Load characterization under oscillating voltage input on the resulting composite samples was then performed using a PC-platform data acquisition system, variable signal generator, amplifier and load cells. For fixed signal frequency, various shape signals at low voltage amplitudes were then applied and the corresponding induced forces measured by the load cells and recorded via the data acquisition setup. The applied input signals consisted of sinusoid, square, saw tooth, and triangular form in order to observe the difference in behavior and the resulting output forces of the actuators. A brief description of a proposed theory for this type of actuator was then discussed. The results showed that these actuators exhibit good force to weight characteristics in the presence of low applied voltages.

3-Biomimetic Sensing Capability of IPMC

3.1-Genral Considerations

Investigation of using ion-exchange-membrane metal composite (IPMC) materials as sensors can be traced to Sadeghipour, Salomon, and Neogi[21] where they used the composite membrane as a pressure sensor/damper in a small chamber which constituted a prototype accelerometer. Their research was involved with high frequency vibration sensing and suppression, and therefore much of their investigation involved higher bandwidth sensing.

In this paper the focus was on application of the IPMC sensor on quasi-static or dynamic displacement sensing where the response of the sensor against large imposed displacements was investigated. To get a better understanding of the mechanism of sensing, more explanation need to be given about the nature of the ionic polymers in general.

Most Ion exchange polymeric membranes swell in solvents and by and large are hydrophilic. This gives rise to ability of the membrane to swell in water which can be controlled in an electric field due to ionic nature of the membrane. Furthermore by placing two electrodes in close proximity of the membrane walls and applying a voltage, the forced transport of ions within a solution through membrane becomes possible at microscopic level. For a solvent such as water then local swelling and deswelling of membrane can be controlled depending on polarity of the electrode nearby more like the behavior of the bimorphic materials. This can be achieved by chemical or other possible means of plating of conductive materials on membrane surfaces. Platinum is one such conductor that can be deposited to make the Ion-Exchange Polymer Platinum Composite (IPPC). Also being ionic in

microscopic structure, IPMC has the ability to shift its mobile ions of the same charge polarity within itself when it is placed in an electric field which results in ionic attraction or repulsion between the fixed charges of opposite polarity contained in the side groups within the polymer molecular chain (Fig. 1). This leads to local collapse or expansion of the polymer membrane macroscopically. Physically this causes a stress gradient on opposite sides of the membrane causing it to bend.

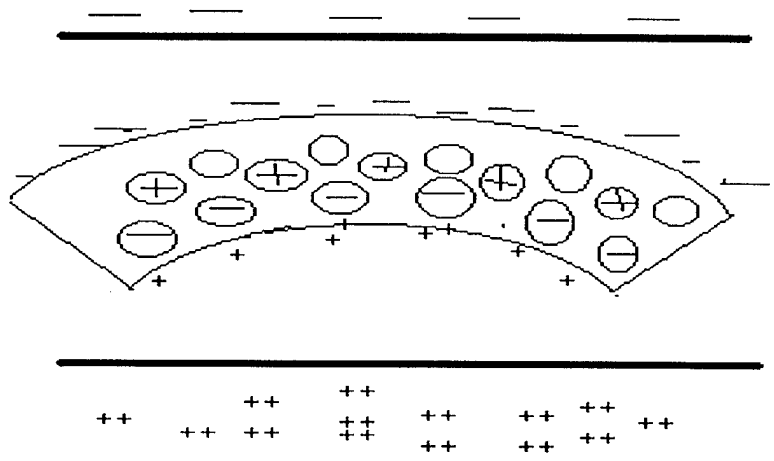

Figure 1. General redistribution of charges in ionic polymer due to imposed electric field.

Conversely by bending the material, shifting of mobile charges become possible due to imposed stresses. Consider Figure 2 where a rectangular strip of the composite sensor is placed between two electrodes. When the composite is bent a stress gradient is built on the outer fibers relative to neutral axis (NA). The mobile ions therefore will shift toward the favored region where opposite charges are available. The deficit in one charge and excess in other can be translated into a voltage gradient which is easily sensed by a low power amplifier and meter which is further explained in experimental procedure in the next section. Essentially polyelectrolytes posses many ionizable groups on their molecular chain. These ionizable groups have the property of dissociating and attaining a net charge in a variety of solvent medium. These net charge groups which are attached to network of macromolecules are called polyions and give rise to intense electric fields of the order of 10^{10} V/m. Thus, the essence of electromechanical deformation of such polyelectrolyte systems is their susceptibility to interactions with externally applied fields as well as their own internal field structure.

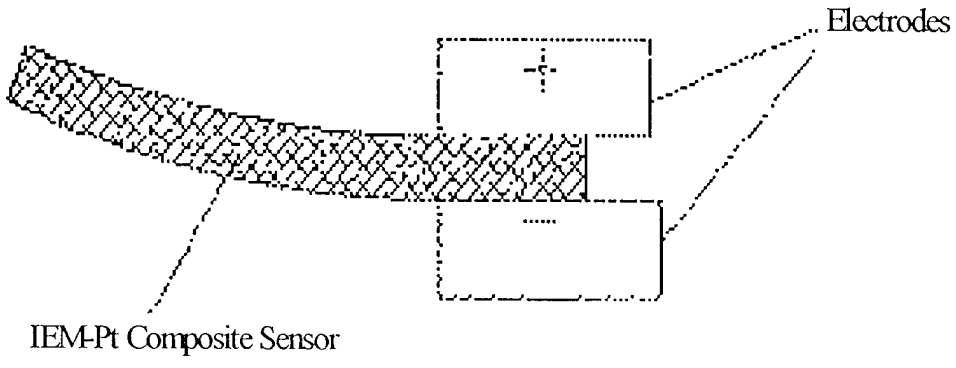

Figure 2. Simple IPPC sensor placed between two electrodes.

3.2- THEORETICAL ANALYSIS

In this section we propose a simple theory for deformation regimes of the composite sensor in a quasi-static or dynamic sense where the composite deformation is evaluated for loads at given deformation interval. The model is driven from geometry and nonlinear elasticity theory which applies for large deformations provided that no approximation is made to resulting differential equations describing the displacement field. The proposed theory in a sense uses rubber elasticity formulation for very large deformations as applied to our composite sensor.

Consider a simple cantilever beam with uniform rectangular cross section with an area A as shown in Figure 3. The beam is fixed at x=0 and assumed to have a concentrated load W at the free end where x=L and its deflection is measured in the y direction from unloaded neutral axis. The modulus of elasticity of the beam material is E. The relationship for displacement of the beam at any point along the beam and applied load can be obtained using a nonlinear elasticity theory similar to rubber elasticity. In this sense the stress is a nonlinear function of the deformation gradient as well as the applied electric field.

The stress in the material is given by:

$$\sigma = f(E, \varepsilon) \tag{1}$$

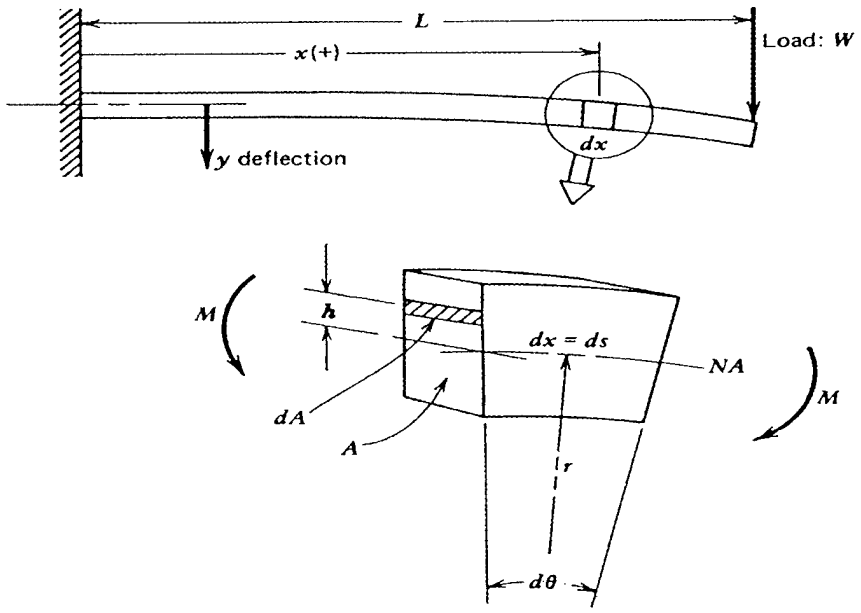

Figure 3. Simple cantilever beam configuration for IPMC sensor analysis.

The stress in the material layer dA, can be expressed in terms of strain ε, using above and knowing that strain is found by using arc length rdθ, according to:

$$\varepsilon = \frac{(r+h)d\theta - rd\theta}{rd\theta} = \frac{h}{r} \tag{2}$$

Where r is local radius of curvature. Substituting in (1) we get:

$$\sigma = f(E, \frac{h}{r}) \tag{3}$$

The differential moment dM, around the neutral surface line caused by load acting on dA, is given by:

$$dM = (\sigma dA)(h) \tag{4}$$

The total bending moment for the cross section A, is found by integrating the differential moment expression dM, over the area A.

$$M = \iint_A f(E, \frac{h}{r}) h dA \tag{5}$$

Note that the radius of curvature r, is given by:

$$r = \frac{\left[1 + (dy/dx)^2\right]^{3/2}}{d^2y/dx^2} \tag{6}$$

Also note that the moment applied by the load W at the free end is clockwise and thus we can write the following moment equation:

$$M = -W(L - x) \tag{7}$$

Combining equations (5) and (7) yields a nonlinear integro-differential equation for the static deflection of the beam as a function of x, in the following form:

$$-W(L - x) = \iint_A f\left[E, h\frac{d^2y/dx^2}{\left[1 + (dy/dx)^2\right]^{3/2}}\right] h dA \tag{8}$$

This is a second order nonlinear integro-differential equation with following boundary conditions:

$$\begin{cases} y = 0, & \forall\ x = 0 \\ y' = 0, & \forall\ x = 0 \end{cases} \tag{9}$$

The above integro-differential equation can be solved numerically using conventional techniques such as Runge-Kutta in combination with trapezoidal rule and knowing the beam properties and geometry.

Our experimental results showed that the tip displacement in the positive direction was linearly related to output voltage of the sensor. These results are described in detail in the next section.

3.3- EXPERIMENTAL PROCEDURES, RESULTS, AND DISCUSSION

Nafion-117™ (Du Pont Company) polymeric ion-exchange membrane was acquired from commercially available source. The membrane was about 0.17mm thick. The membrane was then chemically cleaned and treated with platinum to form a composite that is active under electric field of low voltage. The thickness after chemical plating was about 0.2mm. The membrane was then fully hydrated in pure water bath. It was then cut in standard size of 30mm×5mm which was measured to be 0.10 grams in weight. A digital micrometer (Mitutoyo, Digimatic) was used to incrementally bend the tip of the free end of the sensor in desired direction at 1mm interval. The other end was sandwiched between two platinum plates (Aldrich Chemical) of 0.1mm thickness each using a plastic forceps fixed to a stand. The effective length of the sensor was measured to be 25mm. The induced output voltage was sent to an amplifier (Crown, model 150A) before it was sent to an analog input data acquisition card (Labview model

AT-MIO-16XE-50) installed in a PC platform data acquisition system. The amplifier gain was set at maximum of 17.3 in order to get maximum sensitivity. Before each measurement the sample was completely wetted with pure water and initially the electrodes were discharged to prevent any charge buildup that might have been resulted in the sensor due to capacitive effect.

The experimental results showed that a linear relationship exists between the voltage output and imposed displacement of the tip of the IPMC sensor (Fig. 4). However the results were face sensitive while maintaining linearity, meaning the trend reversed itself when the sensor film was inverted (Fig. 5). This could be attributed to the fact that charges are built on the outer faces much like a capacitor which is then incrementally neutralized when the membrane sensor is inverted but same loading condition is applied.

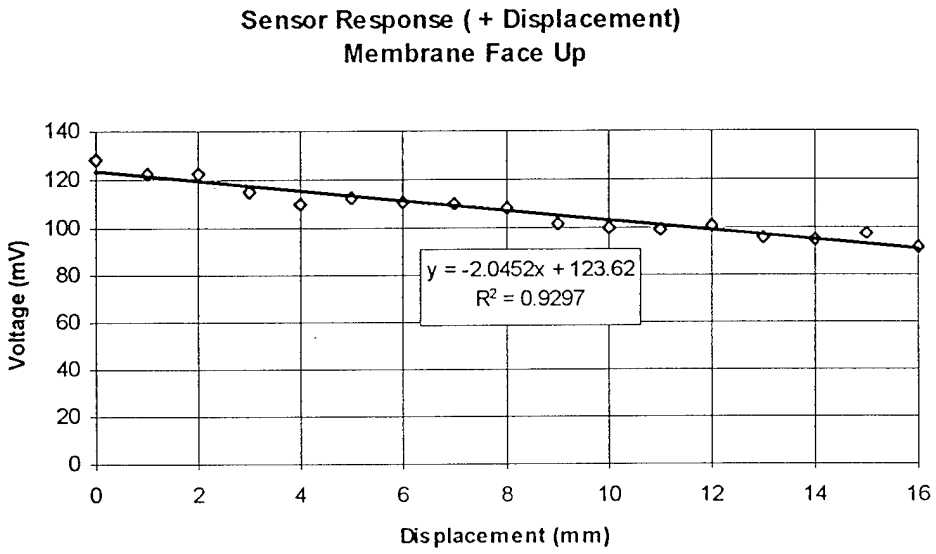

Figure 4. IPMC film sensor response for positive displacement input.

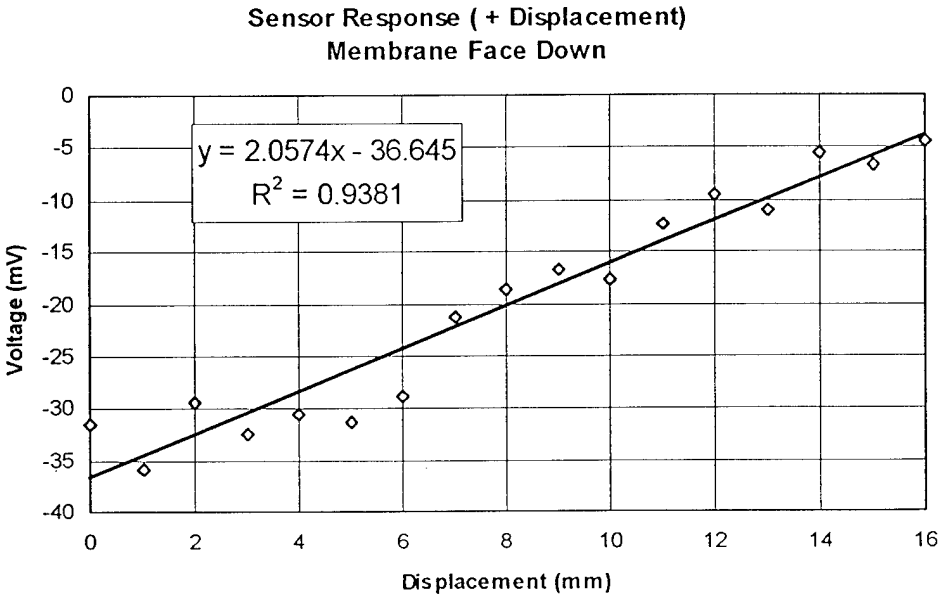

Figure 5. Inverted IPMC film sensor response for positive displacement input.

When tested for displacement in negative direction, starting at neutral or horizontal level and proceeding to -16mm displacement, higher order polynomial approximation was best describing the sensor behavior (Fig. 6). However the result would follow a clearly linear trend when a complete bending cycle was initiated. This was observed during evaluation of hysteresis curve for the film sensor (Fig. 7). As observed in this curve, the sensor shows a linear behavior in the first, second, and third quarter of bending cycle and finally follows a parabolic trend as the forth quarter is completed. Each quarter of the bending cycle forms a 16mm displacement as shown in the figures.

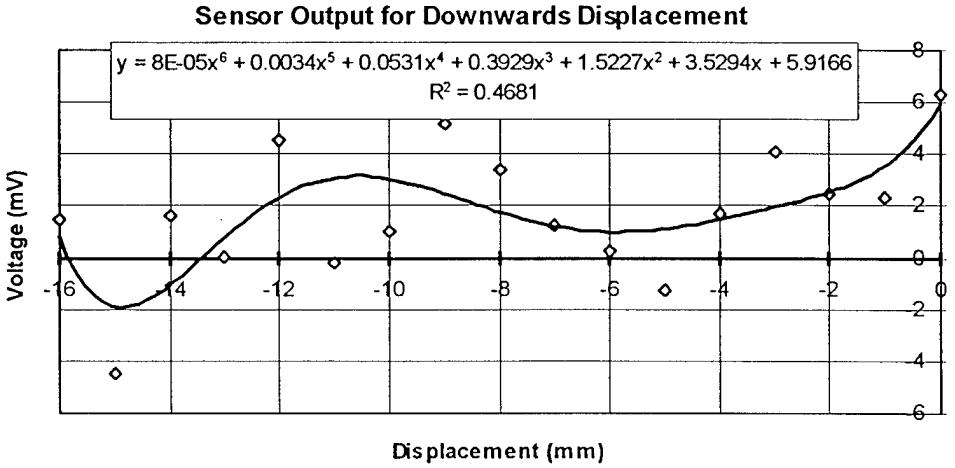

Figure 6. Response of IPMC sensor with downward bending imposition.

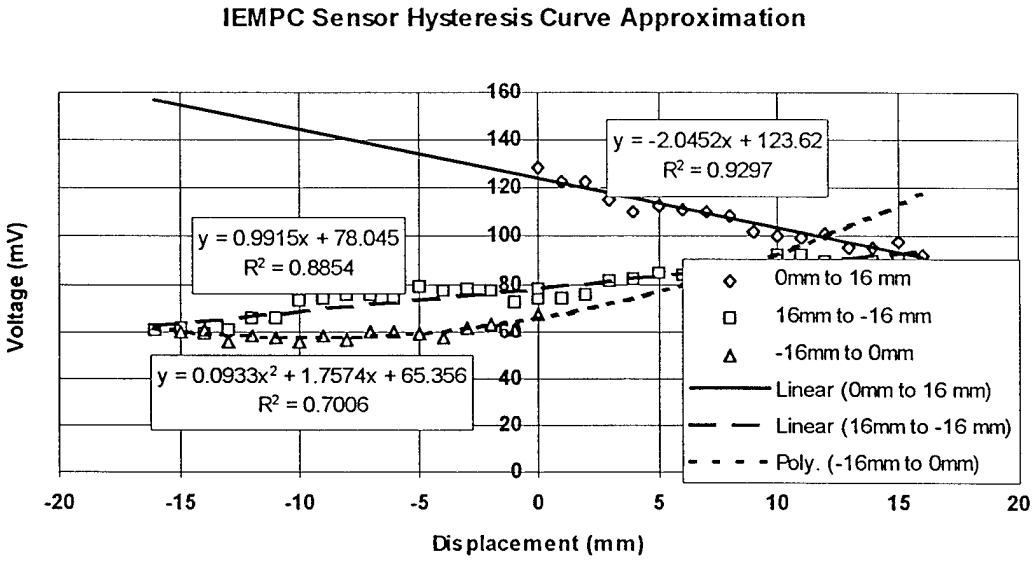

Figure 7. Hysteresis curve for IPMC sensor for one complete bending cycle.

3.4-DYNAMIC SENSING

When strips of IPPC are dynamically disturbed by means of a dynamic impact or shock loading, nicely damped electrical response is observed as shown in Figure 8 below. The dynamic response were observed to be highly repeatable with a fairly high band width to 100's of HZ. This particular property of IPPC's may find a large number of applications in large motion sensing

for a variety of industrial applications. Since these muscles can also be cut as small as one desires, they present a tremendous potential to micro-electro-mechanical systems (MEMS) sensing and actuation applications. Figure 9 displays micron size array of IPPC muscles cut in a laser microscope work station in our institute.

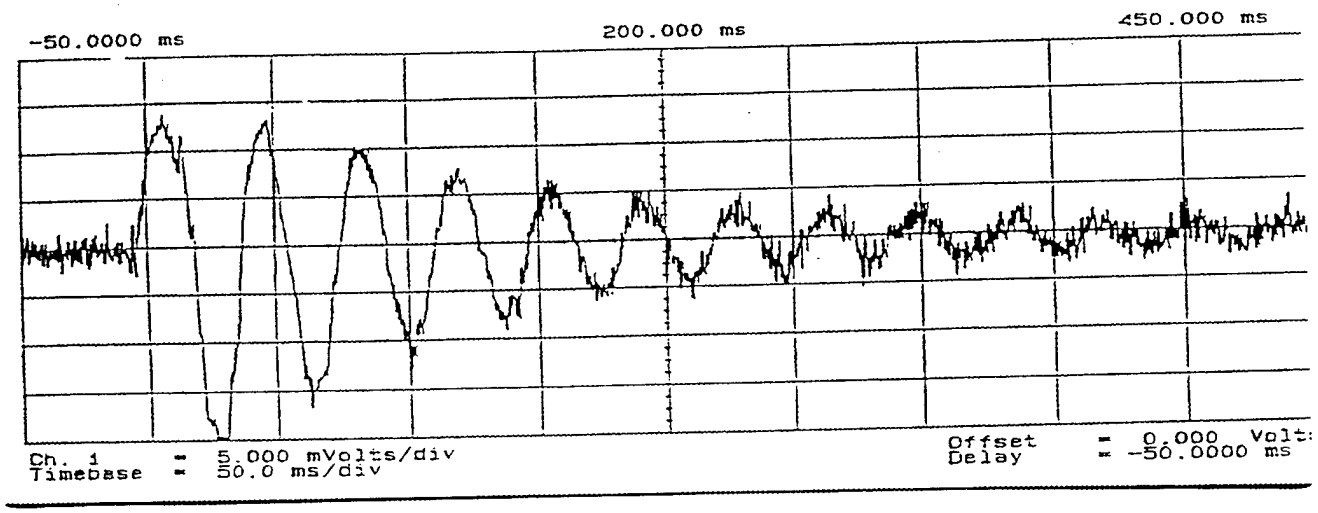

Figure 8- Dynamic sensing response in the form of output voltage of strips (40mmx5mmx0.2mm) of IPPC subject to a dynamic impact loading as a cantilever.

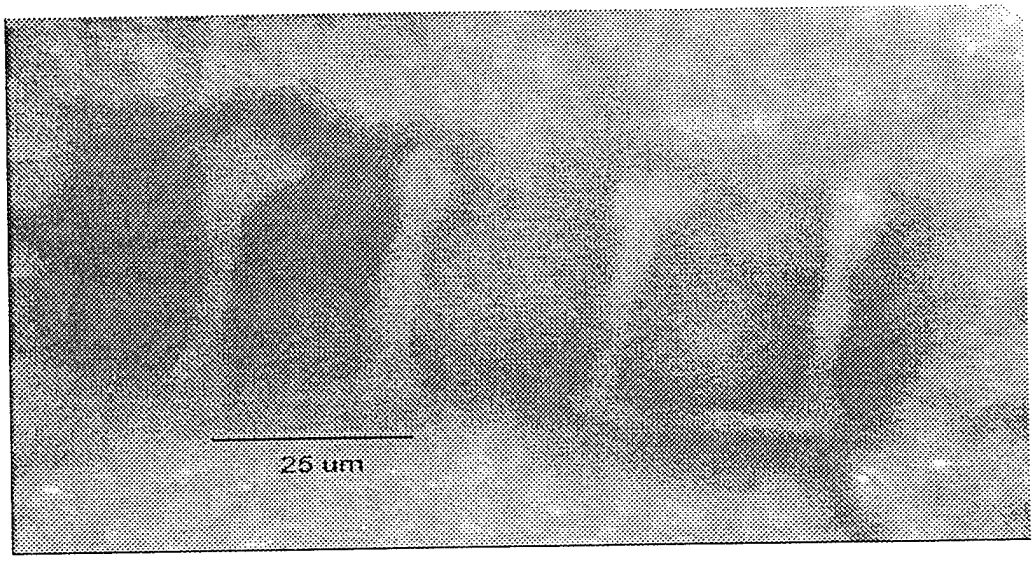

Figure 9- Assembly of micro-strips of IPPC cut in laser-microscope work station for micro-sensing and micro-actuation

3.5- CONCLUSIONS

Remarkable linear behavior of the membrane was observed specifically in the positive direction of travel for each complete bending cycle. The low amplification factor of 17.3 with no signal conditioning proved to be sufficient for our sample in use. The hysteresis curve showed a linear, followed by another linear and lastly a parabolic trend as the sensor was bent in a complete cycle. Higher order polynomial approximation seemed better describing the response of the sensor in negative displacement. It was also observed that the sensor was face sensitive due to capacitive nature of the sensor. Finally the use of ionic polymeric metal composites such as IPMC as sensor may be useful where simplicity and low cost are sought. However more research needs to be done to find out the effect of chemical treatment on sensor output. Highly Dynamic sensing characteristics of IPPC strips were remarkable in accuracy and repeatability and were found to be superior to existing motion sensors and micro sensors.

4-Biomimetic Actuation Properties of IPMC's

4.1- General Considerations

Generally, actuators are used to operate robotic devices that include robotic arms, rovers, fingers and systems. Other applications include release mechanisms, antenna and instrument deployment, positioning devices, aperture opening and closing devices, real-time compensation for thermal expansion in space structures, biomedical devices, heart, muscles and circulation assist devices equipped with soft actuators. Increasingly, there are requirements to reduce the size, mass, and power consumption of actuation devices, as well as their cost. Electroceramics (piezoelectric and electrostrictive) offer effective, compact, actuation materials to replace electromagnetic motors. A wide variety of Electroactive ceramics (EAC) materials are incorporated into motors, translators and manipulators, in such devices as ultrasonic motors and inchworms. In contrast to electroceramics, IPMCs are emerging as new actuation materials with displacement capabilities that cannot be matched by the striction-limited and rigid ceramics [1]. Table 1 shows a comparison between the capability of IPMC materials and both electroceramics and shape memory alloys. As shown in Table 1, IPMC materials are lighter and their potential striction capability can be as high as two orders of magnitude more than EAC materials. Further, their response time is significantly higher that Shape Memory Alloys (SMA). The authors' current study is directed towards taking advantage of these polymers' resilience and the ability to engineer their properties to meet robotic articulation requirements. The mass producability of polymers and the fact that electroactive polymer materials do not require poling (in contrast to piezoelectric materials) help producing them at low cost. IPMC materials can be easily formed in any desired shape and can be used to build MEMS-type mechanisms (actuators and sensors). They can be designed to emulate the operation of biological muscles [2-5] and they have unique characteristics of low density as well as high toughness, large actuation strain constant and inherent vibration damping.

TABLE 1: Comparison of the properties of IPMC, SMA and EAC

Property	Ionic polymer-Pt Composites (IPMC)	Shape Memory Alloys (SMA)	Electroactive Ceramics (EAC)
Actuation displacement	>40%	<8% short fatigue life	0.1 - 0.3 %
Force (MPa)	10 - 30	about 700	30-40
Reaction speed	μsec to sec	sec to min	μsec to sec
Density	1- 2.5 g/cc	5 - 6 g/cc	6-8 g/cc
Drive voltage	4 - 7 V	NA	50 - 800 V
Power consumption	watts	watts	watts
Fracture toughness	resilient, elastic	elastic	fragile

4.2- DEVELOPMENT OF MUSCLE ACTUATORS

The development of muscle actuators is based on an interdisciplinary effort using expertise in materials science, chemistry, electronics, robotics, etc. The initial effort concentrated on identifying IPMC with 10% actuation strain. This goal was set in reference to the capability of Shape Memory Alloys (SMA) that induce 8% maximum striction (at a relatively short fatigue life of 1K-cycle). Compared to EACs, which produce a fraction of a percent actuation, SMAs produce a relatively large displacement and they are increasingly being considered for space applications (e.g., pin-pullers). Two categories of IPMC actuators were investigated, including (a) Ionic Polymer Platinum) composites (IPPC), and (b) Linear IPMC actuators - employing electrostatically activated IPMCs. The emphasis of the current study is on the IPMC composites category, which displays a strong bending capability.

The IPMC muscle used in our investigation is composed of a Nafion® 117 (DuPont) film, i.e., a perfluorinated ion exchange membrane (IEM), which is chemically deposited platinum electrodes on its both sides. The thickness of the formed muscle actuator is 0.18-mm and it is cut in strips that is 1x0.125-inch in area and weighs 0.1 gram. To maintain the actuation capability the films need to be kept moist continuously. The commercially available Nafion has the following chemical formula,

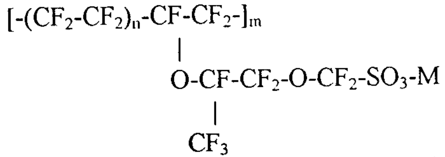

$$\begin{array}{l} [-(CF_2\text{-}CF_2)_n\text{-}CF\text{-}CF_2\text{-}]_m \\ \qquad\qquad\qquad\quad | \\ \qquad\qquad\qquad\quad O\text{-}CF\text{-}CF_2\text{-}O\text{-}CF_2\text{-}SO_3\text{-}M \\ \qquad\qquad\qquad\qquad\; | \\ \qquad\qquad\qquad\quad\; CF_3 \end{array}$$

where $n \sim 6.5$, $100 < m < 1000$, and M^+ is the counter ion (H^+, Li^+ or Na^+). The structure and properties of the Nafion membranes have been the subject of numerous investigations (see for example [6]). One of the interesting properties of this material is its ability to absorb large amounts of polar solvents, i.e. water. Platinum, Pt, metal ions, which are dispersed through out the hydrophilic regions of the polymer, are subsequently reduced to the corresponding metal atoms. This results-in the formation of a dendritic type electrodes. In Figure 10, a scanning electron micrographs are shows in two magnifications, with an order of magnitude difference. On the left, a view is give of the edge of an electroded Nafion® muscle, the Pt metal covers each surface of the film with some of the metal penetrating the subsurface regions of the material. A closer view with x10 magnification is shown in Figure 10 on the right.

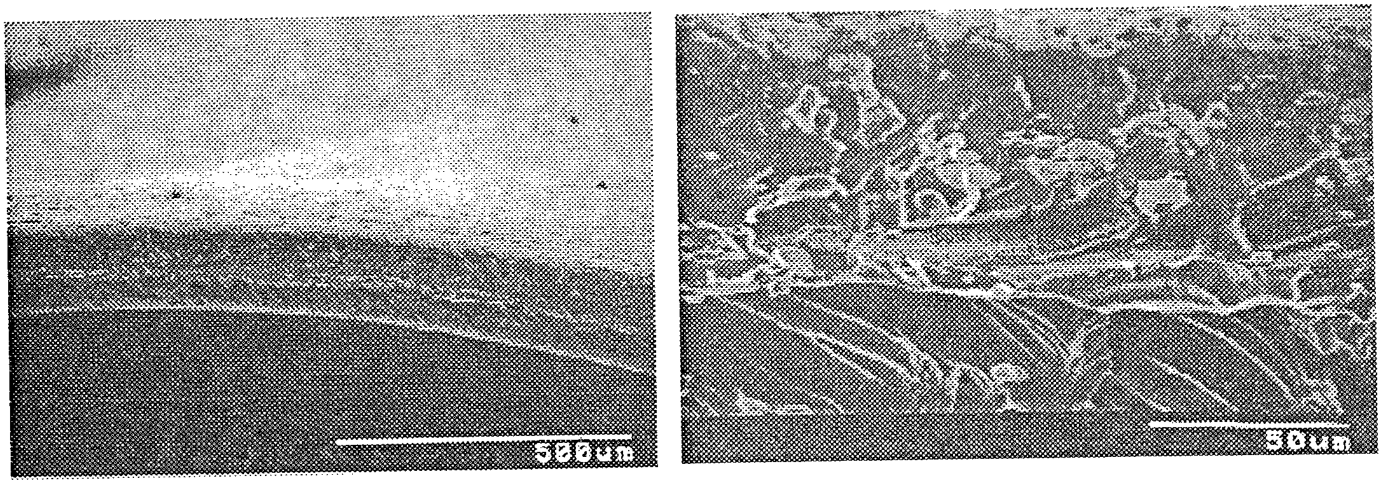

Figure 10: Scanning Electron Micrographs of the structure of Nafion®

When equilibrated with aqueous solutions these membranes are swollen and they contain a certain amount of water. Swelling equilibrium results from the balance between the elastic forces of the polymeric matrix and the water affinity to the fixed ion-exchanging sites and the moving counter ions. The water content depends not only on the hydrophilic properties of the ionic species inside the membrane but also on the electrolyte concentration of the external solution.

When an external voltage of 2 volts or higher is applied on a IPMC composite film, it bends towards the anode. An increase in voltage level (up to 6 or 7 volts) causes a larger bending displacement. When an alternate voltage is applied, the film undergoes movement like a swing and the displacement level depends not only on the voltage magnitude but also on the frequency. Lower frequencies (down to 0.1 or 0.01 Hz) lead to higher displacement (approaching 1 inch). Thus, the movement of the muscle is fully controllable by the applied electrical source. The muscle performance is also strongly dependent on the water content which serves as an ion transport medium and the dehydration rate gradient across the film leads to a pressure difference. The frequency dependence of the ionomer deflection as a function of the applied voltage is shown in Figure 11. A single film was used to emulate a miniature bending arm that lifted a mass weighing a fraction of a gram. A film-pair weighing 0.2-g was configured as a linear actuator and using 5V and 20 mW successfully induced more than 11% contraction displacement. Also, the film-pair displayed a significant expansion capability, where a stack of two film-pairs 0.2-cm thick expanded to about 2.5 cm wide (see Figure 12).

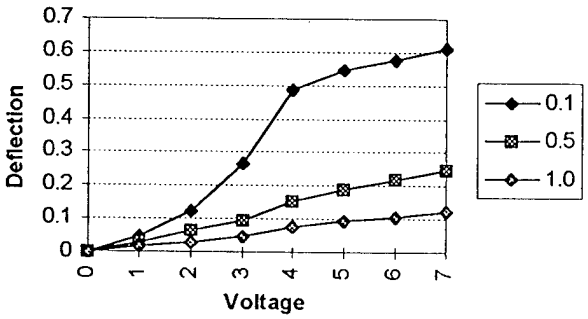

Figure 11: The deflection of a Nafion ionomer as a function of the frequency and the applied voltage.

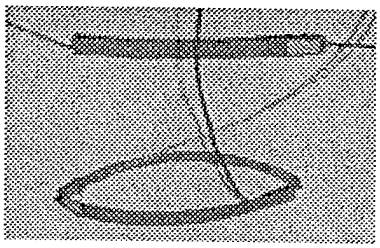

Figure 12: IPMC film-pair in expanded mode. A reference pair (top) and an activated pair (bottom).

4.3- MUSCLE ACTUATOR FOR ROBOTIC APPLICATIONS

IPMC films have shown remarkable displacement under a relatively low voltage drive, using a very low power. However these ionomers have demonstrated a relatively low force actuation capability. Since the IPMC composite films are made of a relatively strong material with a large displacement capability, we investigated their application to emulate fingers. In Figure 13, a gripper is shown that uses IPMC fingers in the form of an end-effector of a miniature low mass robotic arm.

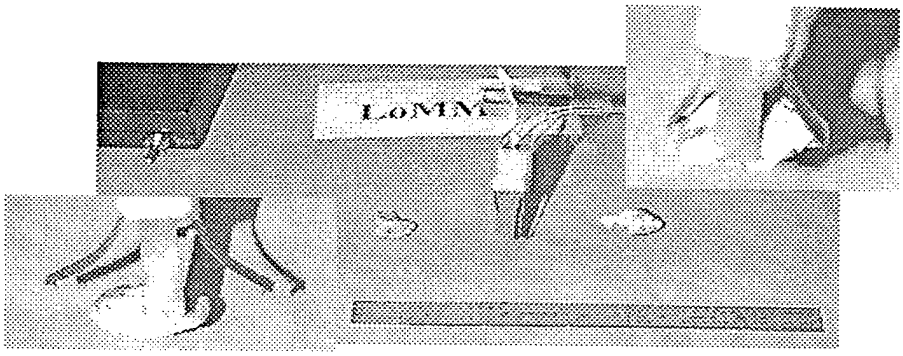

Figure 13: An end-effector gripper lifting 10.3-g rock under 5-V, 25-mW activation using four 0.1-g fingers made of perfluorinated ion-exchange membrane platinum composite.

The fingers are shown as vertical gray bars and the electrical wiring, where the films are connected back-to-back, can be seen in the middle portion of Figure 13. Upon electrical activation, this wiring configuration allows the fingers to bend either inward or outward similar to the operation of a hand and thus close or open the gripper fingers as desired. The hooks at the end of the fingers are representing the concept of nails and allow securing the gripped object that is encircled by the fingers.

So-far, multi-finger grippers that consist of 2- and 4-fingers were produced, where the 4-finger gripper shown in Figure 13 allowed to lift 10.3-g. This gripper prototype was mounted on a 5-mm diameter graphite/epoxy composite rod to emulate a light weight robotic arm. This gripper was driven by 5 volts square wave signal at a frequency of 0.1 Hz to allow sufficient time to perform a desirable demonstration of the capability of the Gripper -- opening the gripper fingers, bringing the gripper near the collected object, closing the fingers and lifting an object with the arm. The demonstration of this gripper capability to lift a rock was intended to pay the way for a future application of the gripper to planetary sample collection tasks (such as Mars) using ultra-dexterous and versatile end-effector.

To enhance the force actuation capability of IPMC composite actuators, techniques of producing thicker IPMC films are being developed. Further, we are seeking a better understanding of the actuation mechanism of ionomers as well as searching alternatives to Nafion as a base for ionomer actuators. Also, to protect the ionic constituents of IPMC composite films, encapsulation methods are being developed..

4.4- DESIGN OF LINEAR & PLATFORM TYPE ACTUATORS

For detailed dynamics description and analysis of the dynamic theory of ionic polymeric gels the reader is referred to Shahinpoor and co-workers (see the references). Since ionic polyelectrolytes are for the most part three dimensional network of macromolecules cross-linked nonuniformly, the concentration of ionic charge groups are also nonuniform within the polymer matrix. Therefore the mechanism of bending is partially related to migration of mobile ions within the network due to imposition of an electric field as shown in Figure 1. However, recent investigation by the author and hias co-workers point to a stronger effect due to surface charge interaction which will be reported later.

Figure 14 depicts the bending deformation of a typical strip with varying electric field, while Figure 15 displays the variation of deformation with varying frequency of alternating electric field.

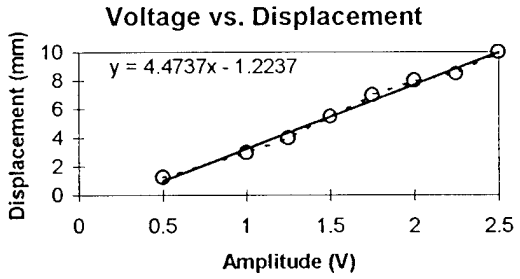

Figure 14-Bending Displacement versus Voltage for a typical strip of 5mmx0.20mmx20mm under a frequency of 0.5Hz.

Based on such dynamic deformation characteristics, linear and platform type actuators can be designed and made dynamically operational. These types of actuators are typically shown in Figures 16 and 17.

4.5-CONCLUSIONS

A new type of soft actuator and multi-fingered robotic hand were made from IPPC artificial muscles and were found to be quite superir to conventional grippers and multi-fingered robotic hands. The force capability, however, was observed to be still small while the robotic hands enjoyed large displacements with their multi-fingers. Encapsulation of the actuators to keep them moist appeared to be necessary for sustained actuation over a period of time. Efforts are underway to use the metal component in such composites to also play the role of encapsulants to keep the muscles moist and wet for long applications. Furthermore, In this section the feasibility of designing linear and platform type robotic actuators made with a polyelectrolyte ion

exchange membrane-metal composite artificial muscle were presented. In order to achieve linear motion from these typically bending type actuators, a series of muscles made from ion-exchange-membrane-metal composites were cut in strips and attached either end-to-end or to one fixed platform and another movable platform in a cylindrical configuration. By especially prepared electrodes embedded within the platforms one can convert the bending response of each strip into linear movement of the mobile platform. By applying a low voltage the movement of free end of the actuator could be calibrated and its response could be measured, accordingly. A theoretical model was developed and was compared to experimental results.

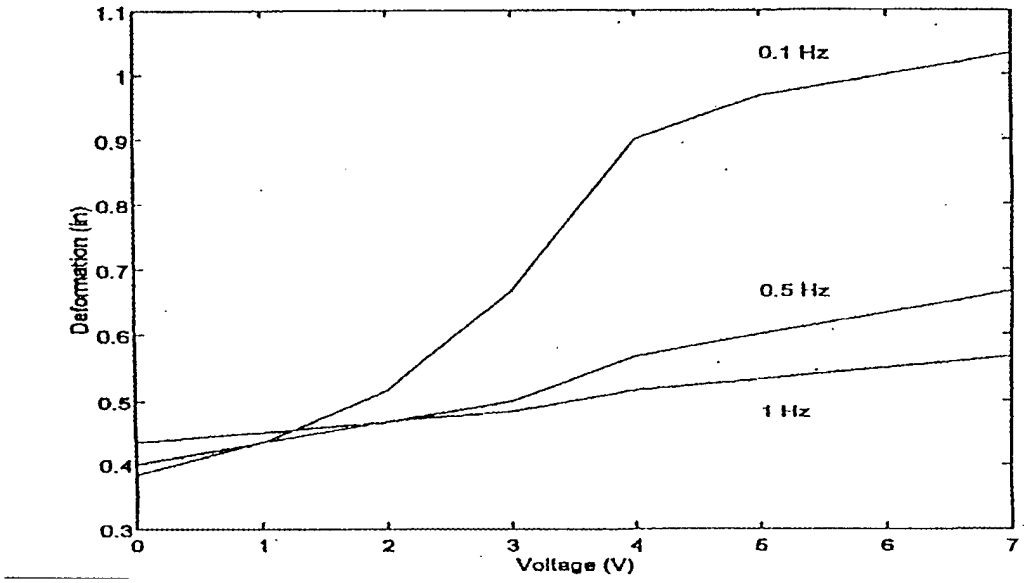

Figure 15-Frequency dependence of bending deformation of IPMC-Pt composite muscles

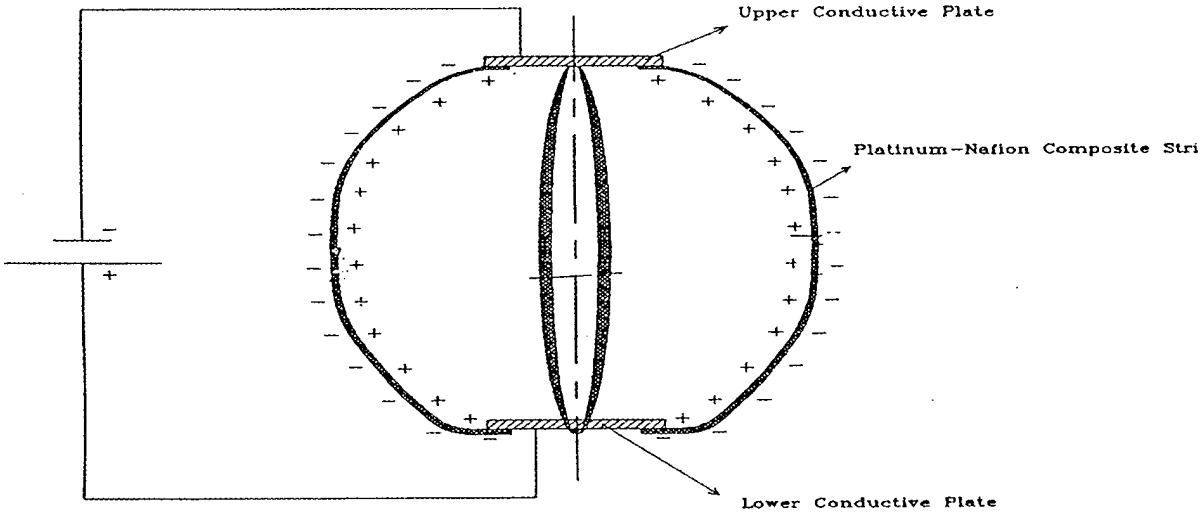

Figure 16- A typical linear-type robotic actuators made with IPMC-Pt composite legs

Figure 17 shows an assortment of such actuators made in our laboratory. The experimental results on the deformation of these actuators as depicted in Figure3 and 4 have been found to agree with the theoretical predictions as presented in references [16] through [34].

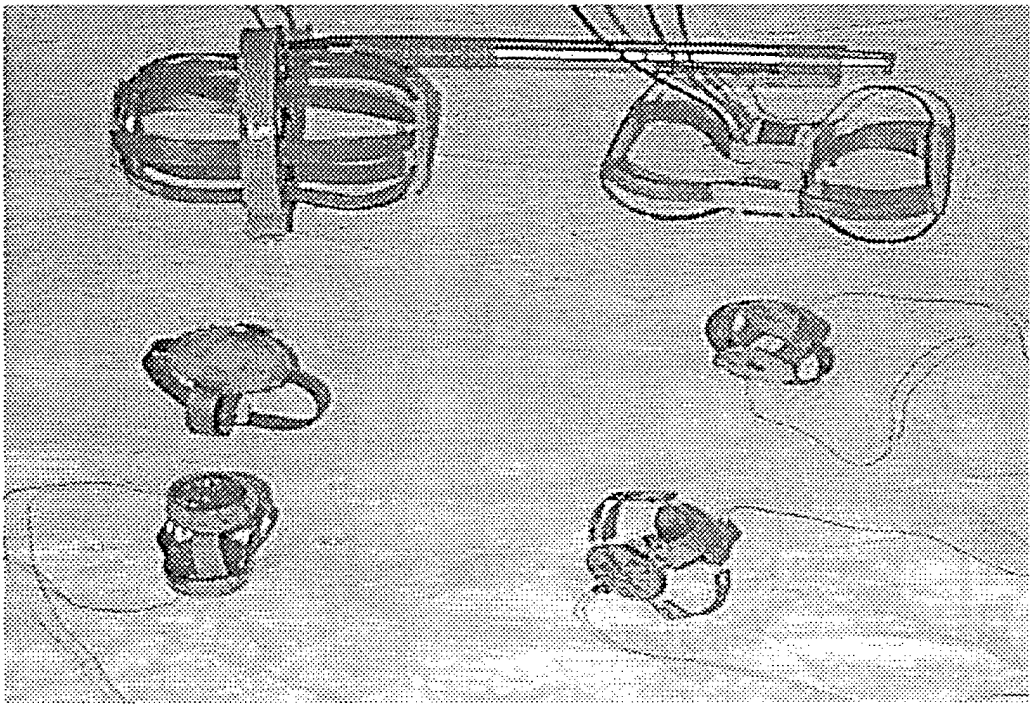

Figure 17- An assortment of linear and platform type actuators made in our laboratory.

5-Large Amplitude Vibrational Response of IPMC's

5.1-General Considerations

Strips of polyelectrolyte Ion-Exchange membrane (IPMC) were used to study the large amplitude vibration characteristics of ion-exchange-membrane-metal composites. The ion-exchange membrane strips were chemically plated with platinum. A small function generator circuit was designed and built to produce a variety of approximately ±4.0V amplitude alternating wave at varying frequency. In order to study the feasibility of using ion-exchange-membrane-metal composite artificial muscles as vibration damper, a series of muscles made from ion-exchange-membrane-metal composites were cut in strips and attached either end-to-end or to one fixed platform and another movable platform in a cantilever configuration. By applying a low voltage the movement of free end of the beam could be calibrated and its response could be measured, accordingly. Typical data for the frequency-dependence of amplitude of lateral oscillations of the muscle strips subjected to alternating voltages of various forms such as sinusoidal, rectangular, saw-tooth or pulsed is presented. Furthermore, additional data is presented on static deformation of the strip with voltage as well as the frequency dependence of deflection-voltage curves.

5.2-THEORETICAL MODEL

A simple one-dimensional model of electrically-induced dynamic deformation or vibration of a cantilever beam made with such IPMC-Pt composite artificial muscle strips is given by the following equations :

$$\sigma = (1/3)E(C_0, C_i)\,(\lambda - \lambda^{-2}), \tag{10}$$

$$F(x,t) = \kappa\,(C_0, C_i)\,E^{*2}(x,t), \tag{11}$$

$$\rho \frac{\partial^2 y}{\partial t^2} = \frac{\partial \sigma}{\partial x} + F\,(x, t), \tag{12}$$

$$\varepsilon = \varepsilon_c + \kappa_E \eta, \qquad -C<\eta<C, \tag{13}$$

$$\lambda = 1 + \varepsilon, \tag{14}$$

$$\lambda_+ - \lambda_- = 2\kappa_E C, \tag{15}$$

where σ is the stress, λ is the stretch, $E(C_0, C_i)$ is the corresponding Young's modulus of hyper-elasticity, C_0 is the polymer solid concentration, C_i, (i=1,2,....,N)'s are the molal concentration of various ionic species in the aqueous medium, κ (C_0, C_i) is an electromechanical coefficient , F is the body force per unit volume of the muscle, ρ is the density, ε is the strain, subscript c indicates values at the neutral axis of the cross-section of the strip, C is the distance of the outer-most remote fibers, κ_E is the local curvature due to an imposed electric field, η is a cross-sectional parameter, E* is the local electric field, x and t are axial location and time variables and subscripts + and -, respectively indicate the values of variable at the outermost remote fibers. Thus bending can occur due to differential contraction and expansion of outer most remote fibers of a strip if an electric field is imposed across its thickness. Numerical solutions to the above set of dynamic equations are presently underway and will be reported later. However, it must be mentioned that the governing equations (10)-(15) display a set of highly non-linear dynamic equations of motion for the IPMC-Pt composite muscles. Presently attempts are under way to establish existence and uniqueness of dynamic solutions to the above equations mathematically. However, experimental observations in our laboratory clearly indicate the non-linear motion characteristics of such muscles as well as unique vibrational response and resonance characteristics.

5.3--EXPERIMENTAL OBSERVATIONS

A 15cmx15cm piece of IPMC (Nafion 117, Du Pont Company) was chemically deposited with platinum to produce the IPMC-platinum composite artificial muscle. Then typical strips of about 2-4cmx4-6mm of membrane composite was cut and completely swollen in a suitable solution such as water or alcohol to swell . The IPMC-Pt composite muscle strip typically weighed 0.1-0.4 grams and its thickness measured about 0.2mm after platinum was deposited on its two surfaces and was swollen in water. The strip was then held by a clamping setup between two platinum plate terminals which were wired to a signal amplifier and generator apparatus driven by Labview software through an IBM compatible PC containing an analog output data acquisition board. The amplifier (Crown model D-150A) was used to amplify the signal output of a National Instrument data acquisition card (AT-AO-10). A software was written to produce various waveforms such as sinusoid, square, triangular and saw tooth signals at desired frequencies up to 100 Hz and amplitudes up to 10 volts. When a low voltage was applied, the membrane composite bent toward the anode side each time. So by applying an alternating signal we were able to observe alternating bending of the actuator that followed the input signal very closely up to 35 Hz frequency. At voltages higher than 2.0 volts, the electrolysis of water in the composite was observed which led to degradation of displacement output of the actuator. Another factor affecting membrane composite performance was the dehydration. Water act as single most important element for the composite bending by sequentially moving within the composite depending on the polarity of the electrodes. The side facing the anode dehydrated faster than the side facing the cathode leading to a differential stresses which ultimately leads to bending of the composite. So, prior to each experiment, the composite was completely swollen in water. The displacement of the free end of a typical 2cmx4mm composite membrane was then measured for frequency range of 0.1-35 Hz for sinusoid input voltage at 2.0 volts amplitude (Figure 18). Resonance was observed at about 20 Hz frequency where the associated displacement was observed to be 7.5mm. It should be noted that as the actuator dehydrates the resonance frequency and maximum displacement varies accordingly. By encapsulating the strips in a plastic membrane such as Saran, the deterioration in the amplitude of oscillation decreased with time. However, the initial amplitude of oscillation for the same level of voltage was smaller than the unwrapped case due to

increased rigidity of the strip. For our sample actuator the resonance occurred in the frequency range of 12 to 28 Hz for various swelling ratio.

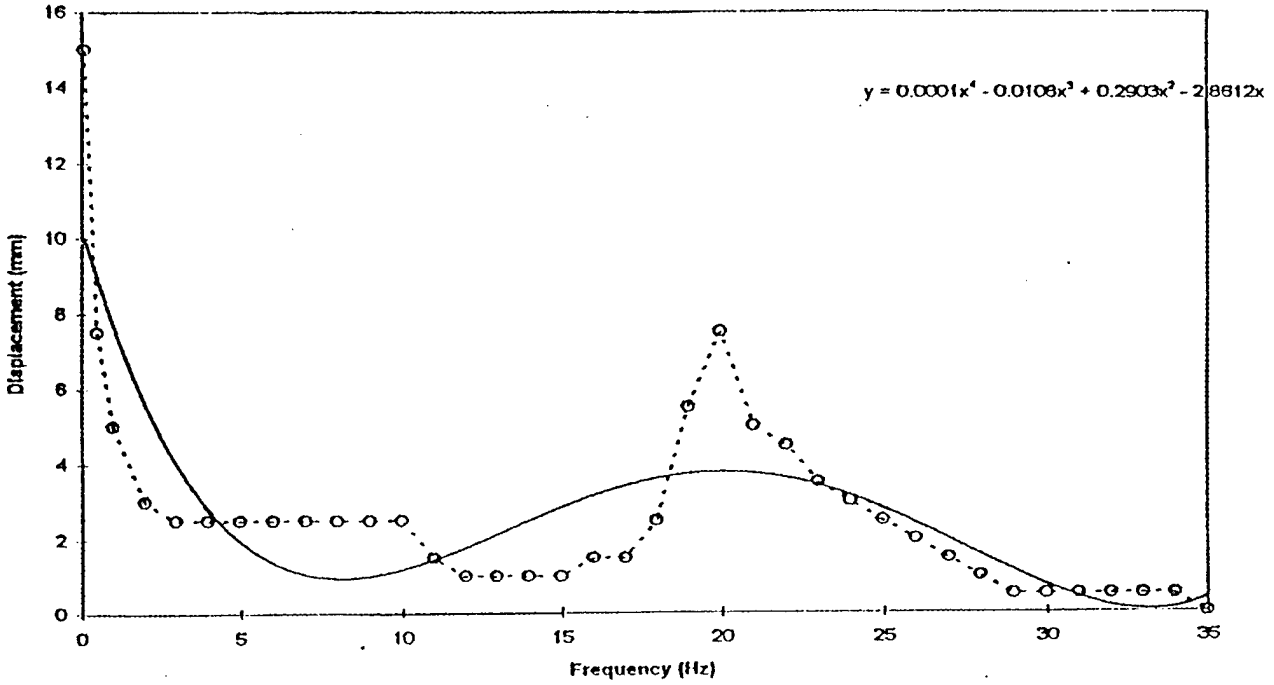

Figure 18- Amplitude of displacement versus the imposed frequency for a voltage of 2 volts for a 2cmx4mmx0.2mm sample

Based on such dynamic deformation characteristics, noiseless swimming robotic structures as shown in Figure 19 and cilia assembly-type robotic worlds, similar to coral reefs, as shown in Figure 20, were constructed and tested for collective vibrational dynamics. Furthermore, wing flapping flying machines, schematically shown in Figure 21, can be equipped with these muscles.

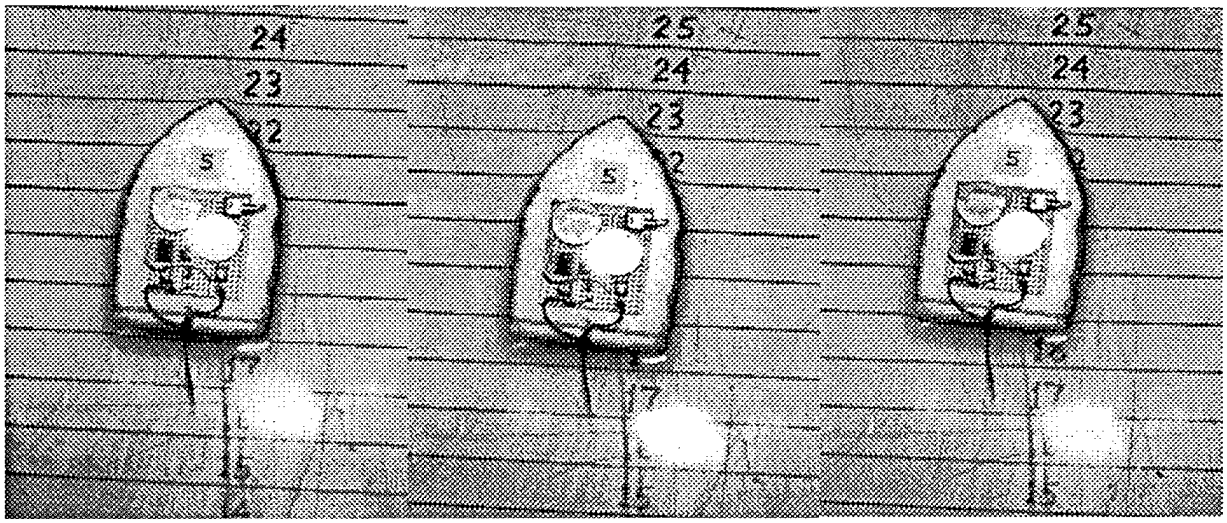

Figure 19. Robotic swimmer with muscle undulation frequency of 5 Hz (frame time interval, 1/3 second).

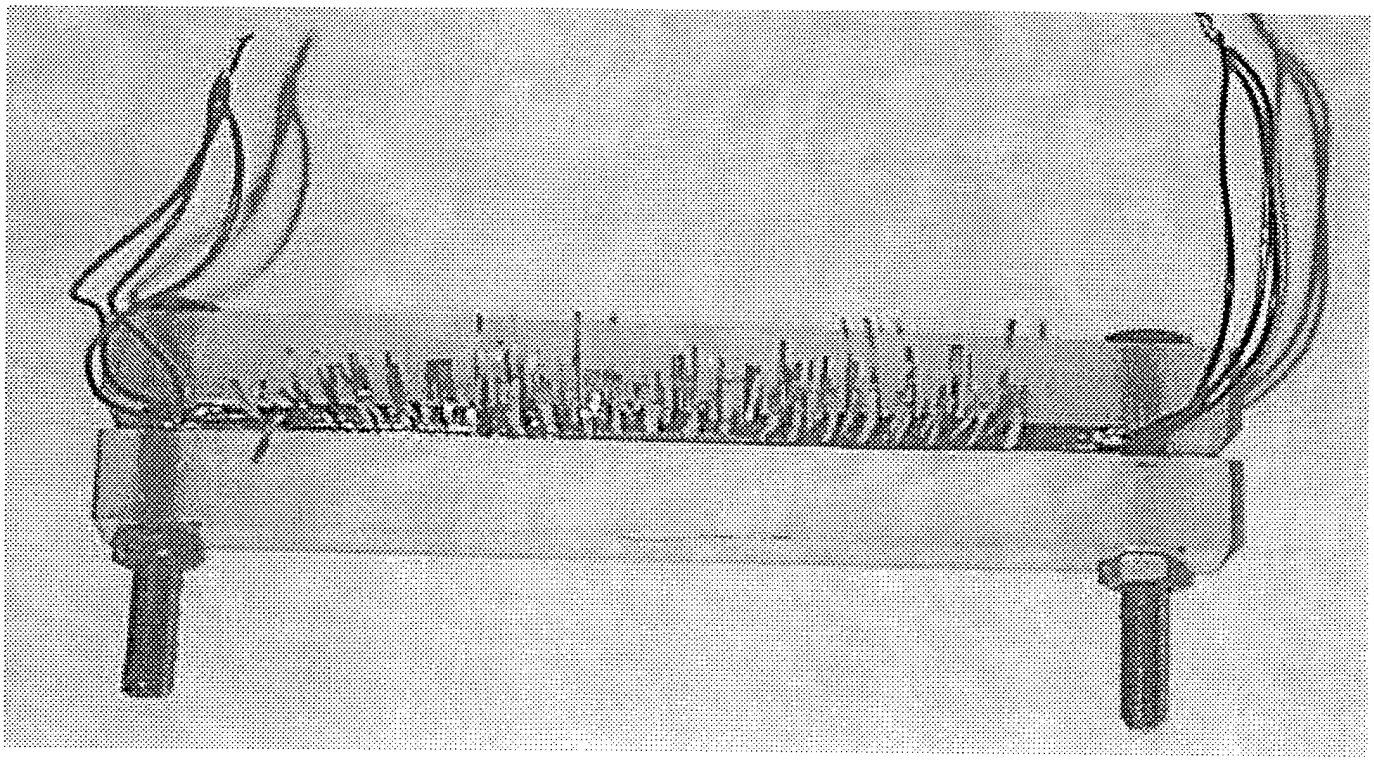

Figure 20--Cilia-Type assembly of IPMC-Pt Muscles Simulating Collective Dynamic Vibrational Response Similar to Coral Reefs and could create anti-biofouling surfaces

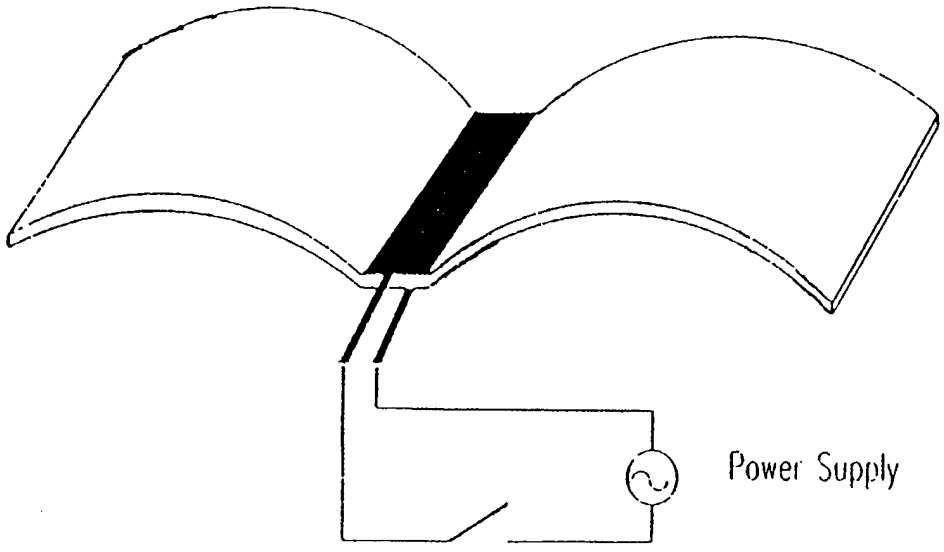

Figure 21-Wing-flapping flying machines design depicted schematically.

5.4- CONCLUSIONS

In this section the feasibility of designing dynamic vibrational systems of artificial muscles made with a polyelectrolyte ion exchange membrane-metal composite artificial muscle were presented. Our experiments confirmed that these types of composite muscles show remarkable bending displacement that follow input signal very closely. When the applied signal frequency is varied, so does the displacement up to a point where large deformations are observed at a critical frequency called resonant frequency where maximum deformation is observed. Beyond which the actuator response is diminished. Several samples of the actuators were made and tested with various dimensions to compare the vibrational behavior of the actuators. A data acquisition system was used to measure the parameters involved and record the results in real time basis. When a low voltage was applied, the membrane composite bent toward the anode side each time. So by applying an alternating signal we were able to observe alternating bending of the actuator that followed the input signal very closely up to 35 Hz frequency. At voltages higher than 2.0 volts, the electrolysis of water in the composite was observed which led to degradation of displacement output of the actuator. Another factor affecting membrane composite performance was the dehydration. Water act as single most important element for the composite bending by sequentially moving within the composite depending on the polarity of the electrodes. The side facing the anode dehydrated faster than the side facing the cathode leading to differential stresses which ultimately leads to bending of the composite. So, prior to each experiment, the composite was completely swollen in water. The displacement of the free end of a typical 2cmx4mm composite membrane was then measured for frequency range of 0.1-35 Hz for sinusoid input voltage at 2.0 volts amplitude. Resonance was observed at about 20 Hz frequency where the associated displacement was observed to be 7.5mm. It should be noted that as the actuator dehydrates the resonance frequency and maximum displacement varies accordingly. By encapsulating the strips in a plastic membrane (Saran) the deterioration in the amplitude of oscillation decreased with time. However, the initial amplitude of oscillation for the same level of voltage was smaller than the unwrapped case due to increased rigidity of the strip. For our sample actuator the resonance occurred in the frequency range of 12 to 28 Hz for various swelling ratio. Another measurement of the displacement of the free end was done by varying the amplitude of the sinusoid input voltage from 0.5-2.5 volts range at constant frequency of 0.5 Hz .

The observed remarkable vibrational characteristics of IPMC-Pt composite artificial muscles clearly point to the potential of these muscles for biomimetics applications such as swimming robotic structures, wing-flapping flying machines, slithering snakes, heart and circulation assist devices, peristaltic pumps and dynamic robotic cilia-worlds.

6-Load and Force Characterization of IPMC's

6.1-General Considerations

Polymeric ion-exchange membrane was acquired from commercially available source. This membrane is about 0.17mm thick and can be purchased as wide as one meter and any desired length. The membrane was then chemically cleaned and treated with platinum to form a composite that is active under electric field of low voltage. The thickness after chemical plating was about 0.2mm. The membrane was then fully hydrated in pure water bath. It was then cut in standard size of 20mm×5mm which was measured to be about 0.04grams in weight. A load cell (Transducer Techniques, model GS-30, 30 grams capacity) and corresponding signal conditioning module (Transducer Techniques, model TMO-1) together with a power supply was setup and connected to a PC-platform data acquisition and signal generation system composed of a 12-bit analog output board (National Instrument AT-AO-10) and a 16-bit multi-input-output board (National Instrument AT-MIO-16XE-50). A Nicolet scope was used to monitor the input and output waveform. Labview™ software was used to write a program to generate various waveform such as sinusoid, square, saw tooth, and triangular signals at desired frequency and amplitude (Fig. 3). Also a program was written to convert the output data from the load cell to force values and display on the monitor. The membrane actuator was then attached at one end to the load cell (load application point) and freed at the other end to be placed between two platinum electrode plates of 0.1mm thick (Aldrich Chemicals) which formed the jaws of a plastic forceps. Therefore the effective length of the membrane was 10mm when 10mm of the total length was placed between the electrodes. This made the effective weight of the muscle producing a force to be about 20 milligrams. A baseline was first established for each waveform with membrane actuator attached to load cell and electrodes to measure the initial pre-load and noise before actuation. Then a series of force data was generated by using a load cell correction factor of 0.255 and a constant frequency (0.5 Hz) signal input of 1.5, 2.0, 2.5, and 3.0 V rms amplitude voltages respectively. The resulting graphs were then adjusted for initial noise and pre-load and plotted over 5 seconds period (2.5 cycles). The force capability of these muscles , on the average was measured to be about 400 N/Kgm indicating that these muscles can lift almost 40 times their own weight

6.2- RESULTS AND DISCUSSION

The results showed that sinusoid and triangular wave form input to the IPMC-pt actuator generate more symmetric output forces, meaning they are relatively equal in either direction of travel (Fig. 22). The maximum forces were generated at higher input voltage amplitudes (3.0 V rms maximum) for most wave forms. The square and saw tooth input wave forms produced more nonuniform results in a sense that all or most of the generated forces were in one direction (Fig. 23). This can be attributed to the fact that there is insufficient time for ion travel to take place when the signal switches its polarity. However for the saw tooth signal, the voltage starts at zero and reaches a maximum in positive direction which results in force in one direction alone where in this case resulted in tension or downward movement of the IPMC-pt actuator. The next paragraph explains in details the effect of individual input waveform on the membrane actuator.

Sinusoid Input: This wave produced a uniform force in either direction of travel (tension and compression of the load cell). The output followed input best at 2.5 V amplitude. However the maximum forces were generated at 3.0 V input and reached 0.5 grams (10 times actuators mass) in either directions. This input shape appears to be more suitable for robotic controls where application of forces are involved for proper calibration and desired force response and command inputs.

Square Input: This wave generated the maximum output forces of all input wave forms reaching 1.25 grams (over 31 times actuators mass) in upward movement (load cell in compression) at 2.5 V amplitude. The reason for lower output at 3.0 V is not clear but square voltage causes sudden change of polarity which can attribute to rapid dehydration and heating of the membrane actuator all of which lead into increase in output in one direction only and may lead into actuator failure. At higher voltages, the generated forces appeared to shift toward negative (load cell in compression or upward movement).

Saw Tooth Input: This signal generated uniform forces in downward motion (load cell in tension) only reached a maximum of 0.65 grams (16 times actuators mass) at 3.0 V input.

Triangular Input: This wave form also produced a uniform force in both direction of travel and reached a maximum of 0.7 grams (17.5 times actuators mass) at 3.0 V in upward direction. However the best symmetry was observed to be at 1.5 V.

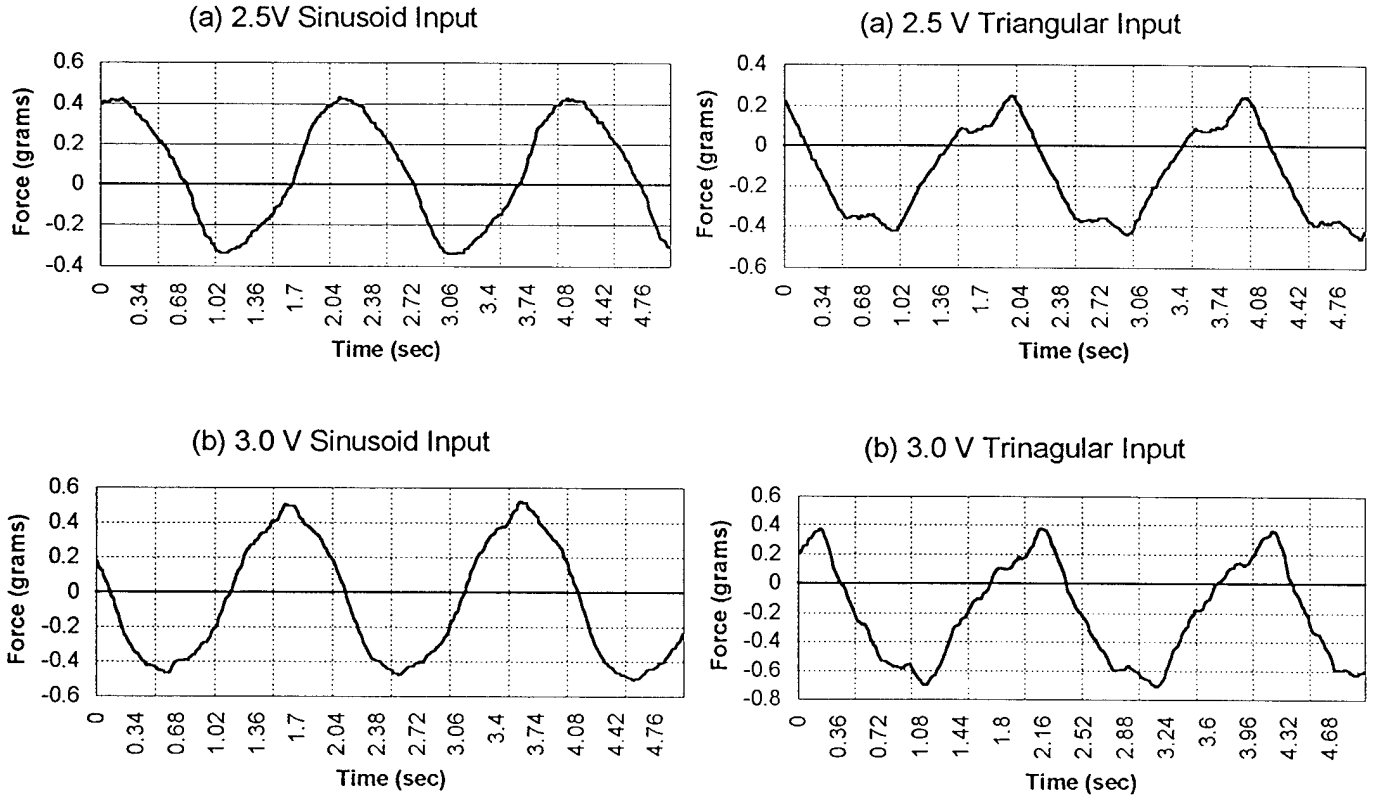

Figure 22. IPMC-Pt actuator response for sinusoid and triangular wave input at (a) 1.5, (b) 2.0, (c) 2.5, and (d) 3.0 Volts rms.

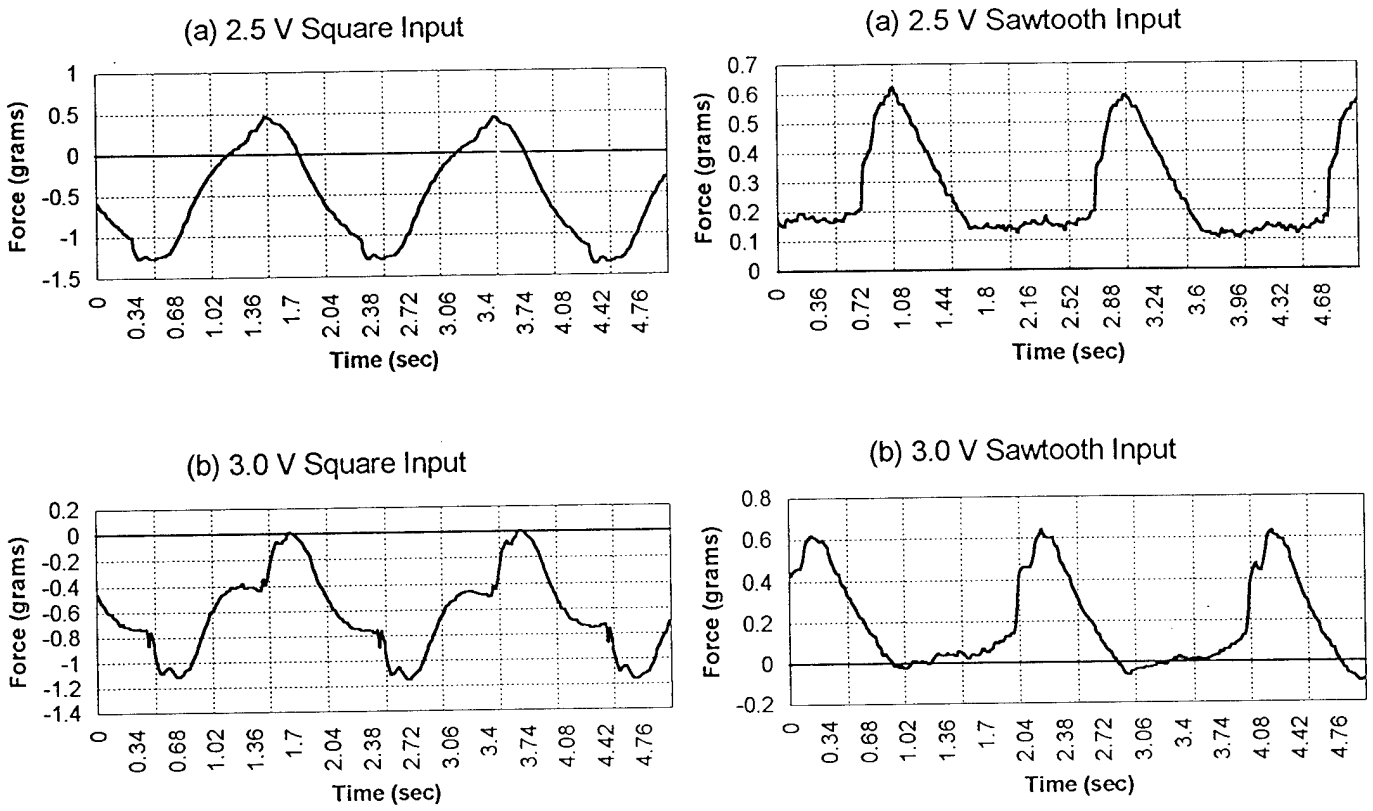

Figure 23. IPMC-Pt actuator response for square and saw tooth wave input at (a) 1.5, (b) 2.0, (c) 2.5, and (d) 3.0 Volts rms.

6.4- CONCLUSIONS

Polymer composite actuators such as IPMC-Pt proved to be practical for applications requiring large load and large motions as well as small load and micro-motion. These materials exhibit remarkable force to mass ratio (as high as 40 for these samples) and are inexpensive to manufacture. Depending on quality of manufacturing process control, actuators producing force in the order of over 50 times their mass have been observed previously in our laboratory. The experimental results showed that they are also sensitive to the shape as well as the amplitude of the applied input signal and result in different force responses accordingly.

For robotic controls, sinusoidal input at low amplitudes produce more uniform response but at low magnitudes. This will enable a simple controls circuitry requirement to integrate the IPMC-Pt actuator in a robotic system such as gripper.

7.0-ACKNOWLEDGMENT

This research was partially supported by NASA-JPL, Artificial Muscles Research Institute (AMRI), Albuquerque, NM., Artificial Muscles Research & Development, Inc. (AMRDI), Albuquerque, NM and Biomimetic Products, Inc, Albuquerque, Nm.Thanks are also to Dr. Jim Jalbert of AUSI and Dr. Teresa McMullen of ONR for inviting me to present this at their 10th. Int. Symposium on UUST.

8-REFERENCES

1. A.J. Grodzinsky, "Electromechanics of Deformable Polyelectrolyte Membranes", Sc.D. Dissertation, Dept. of Elec. Eng., MIT, Cambridge, June 1974.

2. A. J. Grodzinsky and Melcher, J. R., "Electromechanics of Deformable, Charged Polyelectrolyte Membranes", Proc. 27th Annu. Conf. Engineering in Medicine and Biology, Vol. 16, 1974, paper 53.2.
3. A. J. Grodzinsky, Melcher, J. R., "Electromechanical Transduction with Charged Polyelectrolyte Membranes", IEEE Transactions on Biomedical Engineering, Vol. BME-23, No. 6, pp421-433, November 1976.
4. Yannas, I. V., Grodzinsky, A., J., "Electromechanical Energy Conversion with Collagen Fibers in an Aqueous Medium", Journal of Mechanochemical Cell Motility, vol. 2, pp113-125, 1973.
5. W. Kuhn, Reversible Dehnung und Kontraktion bei Anderung der Ionisation eines Netzwerks Polyvalenter Fadenmolekulionen", Experientia, Vol. V, pp318-319, 1949.
6. A. Katchalsky, "Rapid Swelling and Deswelling of Reversible Gels of Polymeric Acids by Ionization", Experientia, Vol. V, pp319-320, 1949.
7. Kuhn, W., Kunzle, O., Katchalsky, A., "Verhalten Polyvalenter Fadenmolekelionen in Losung", Halvetica Chemica Acta, vol. 31, pp1994-2037, 1948.
8. Kuhn, W., Hargitay, B., Katchalsky, A., Eisenberg, H., "Reversible Dilation and Contraction by Changing the State of Ionization of High-Polymer Acid Networks", Nature, vol. 165, pp514-516, 1950.
9. Kuhn, W., Hargitay, B., "Muskelahnliche Kontraktion und Dehnung von Netzwerken Polyvalenter Fadenmolekulionen", Experientia, vol. VII, pp1-11, 1951.
10. Hamlen, R. P., Kent, C. E., Shafer, S. N., "Electrolytically Activated Contractile Polymer", Nature, Vol. 206, pp1149-1150, 1965.
11. Shahinpoor, M.,, "Continuum Electromechanics of Ionic Polymeric Gels as Artificial Muscles for Robotic Applications", Smart Material and Structures Int. J., Vol. 3, pp. 367-372, 1994.
12. Shahinpoor, M.,, "Microelectro-Mechanics of Ionic Polymeric Gels as Artificial Muscles for Robotic Applications", Proceeding of the IEEE Robotics & Automation Conf., vol. , pp. , 1993.
13. Shahinpoor, M., Mojarrad, M., "Active Musculoskeletal Structures Equipped with a Circulatory System and a Network of Ionic Polymeric Gel Muscles", Proceedings of the 1994 International Conference on Intelligent Materials, pp. 1079-1085, 1994.
14. Shahinpoor, M., Wang, G., Mojarrad, M., "Elctro-Thermo-Mechanics of Spring-Loaded Contractile Fiber Bundles with Applications to Ionic Polymeric Gel and SMA Actuators", Proceedings of the International Conference on Intelligent Materials" ICIM'94, Williamsburg, VA., pp. 1105-1116, 1994.
15. Osada, Y., "Electro-Stimulated Chemomechanical System Using Polymer Gels (An Approach to Intelligent Artificial Muscle System)", Proceeding of the International Conference on Intelligent Materials, pp155-161, 1992.
16. Oguro, K., Asaka, K., Takenaka, H., "Polymer Film Actuator Driven by Low Voltage", Proceedings of 4th International Symposium on Micro Machine and Human Science at Nagoya, pp39-40, 1993.
17. Asaka, K., Oguro, K., Nishimura, Y., Mizuhata, M., Takenaka, H., "Bending of Polyelectrolyte Membrane-Platinum Composites by Electric Stimuli. I. Response Characteristics to Various Waveforms", Polymer Journal, Vol. 27, No. 4, pp436-440, 1995.
18. Guo, S., Fukuda, T., Kosuge, K., Arai, F., Oguro, K., Negoro, M., "Micro Catheter System with Active Guide Wire Structure, Experimental Results and Characteristic Evaluation of Active Guide wire Using ICPF Actuator", Osaka National Research Institute, Japan, pp191-197, 1994.
19. De Rossi, D., P. Parrini, P. Chiarelli and G. Buzzigoli, " Electrically-Induced Contractile Phenomena In Charged Polymer Networks : Preliminary Study on the Feasibility of Muscle-Like Structures,", Transaction of American Society of Artificial Internal Organs, vol. XXXI, pp. 60-65, (1985)
20. De Rossi, D., C. Domenici and P. Chiarelli, " Analog of Biological Tissues for Mechanoelectrical Transduction : Tactile Sensors and Muscle-Like Actuators,", NATO-ASI Series, Sensors and Sensory Systems for Advanced Robots, vol. F43,, pp. 201-218, (1988)
21. Alexanderowicz, A.,Katchalsky, A., "Colligative Properties of Polyelectrolyte Solutions in Excess of Salt", Journal of Polymer Science, Vol. 1A, pp3231-3260, 1963.
22. Shahinpoor, M.,, "Nonhomogeneous Large Deformation Theory of Ionic Polymeric Gels in Electric and pH Fields", Proceedings of the 1993 SPIE Conference on Smart Structures and Materials, Feb. 1-4, Albuquerque, Vol. 1916, pp. 40-50, 1993.
23. Shahinpoor, M.,, "Micro-Electro-Mechanics of Ionic Polymeric Gels as Electrically Controlled Artificial Muscles," Proc. 1994 Int. Conf on Intelligent Materials, ICIM'94, June 1994, Williamsburg, VA, pp. 1095-1104, 1994
24. Shahinpoor, M., "Conceptual Design, Kinematics and Dynamics of Swimming Robotic Structures Using Ionic Polymeric Gel Muscles", Smart Materials and Structures Int. J., Vol. 1, pp. 91-94, 1992.

25. Segalman, D., Witkowsky, W., Adolf, D., Shahinpoor, M., "Electrically Controlled Polymeric Muscles as Active Materials used in Adaptive Structures", Proceedings of ADPA/AIAA/ASME/SPIE Conference on Active Materials and Adaptive Structures, Alexandria, VA, November 1991.
26. Shahinpoor, M.,, "Micro-Electro-Mechanics of Ionic Polymeric Gels As Electrically-Controllable Artificial Muscles,", Int. J. Intelligent Material Systems, vol. 6, no. 3, pp. 307-314, 1995
27. Mojarrad, M., and Shahinpoor, M., "Noiseless Propulsion for Swimming Robotic Structures Using Polyelectrolyte Ion-Exchange Membranes,", Proc. SPIE 1996 North American Conference on Smart Structures and Materials, February 27-29, 1996, San Diego, California, vol. 2716, paper no. 27, 1996
28. Shahinpoor, M., and M. Mojarrad, "Ion-Exchange Membrane-Platinum Composites As electrically Controllable Artificial Muscles,", Proc. 1996 Third International Conference on Intelligent Materials, ICIM'96, and Third European Conference on Smart Structures and Materials, Lyon, France, SPIE Publication No. ICIM'96 , pp. 1171-1184, June 1996
29. Shahinpoor, M.,, "Electro-Mechanics of Bending of Ionic Polymeric Gels as Synthetic Muscles for Adaptive Structures,", ASME Publication AD-Vol. 35, Adaptive Structures and Material Systems, edited by G.P. Carman and E. Garcia, Vol. AD-35, pp.11-22, 1993
30. Shahinpoor, M.,"Electro-Mechanics of Resilient Contractile Fiber Bundles with Applications To Ionic Polymeric Gel and SMA Robotic Actuators" Proc. 1994 IEEE International Conference on Robotics & Automation , vol. 2, pp. 1502-1508, San Diego, California, May 1994
31. Shahinpoor, M.,, "The Ionic Flexogelectric Effect" Proc. 1996 Third International Conference on Intelligent Materials, ICIM'96, and Third European Conference on Smart Structures and Materials, June 1996, Lyon, France
32. Shahinpoor, M.,, "Design and Development of Micro-Actuators Using Ionic Polymeric Micro-Muscles,", Proc. ASME Design Engn. Technical Conference, Boston, MA, September (1995)
33. Shahinpoor, M., and M.S. Thompson, "The Venus Flytrap As A Model For Biomimetic Material With Built-In Sensors and Actuators," J. Materials Science & Engineering, vol.C2, pp. 229-233, (1995)
34. Shahinpoor, M.,, "Design and Modeling of A Novel Spring-Loaded Ionic Polymeric Gel Actuator," Proc. SPIE 1994 North American Conference on Smart Structures and Materials ., February 94, Orlando, Florida, vol. 2189, paper no. 26, pp.255-264, (1994)
35. Shahinpoor, M.,, "Microelectro-Mechanics of Ionic Polymeric Gels As Synthetic Robotic Muscles," Proc. SPIE 1994 North American Conference on Smart Structures and Materials, February 94, Orlando, Florida, vol. 2189, paper no. 27, pp.265-274, (1994)
36. Shahinpoor, M.,, "Micro-Electro-Mechanics of Ionic Polymeric Gels as Electrically Controlled Synthetic Muscles,", Biomedical Engineering Recent Advances, Editor : J.Vossoughi, University of District of Columbia Press, Washington, D.C., April 1994, vol.1, pp.756-759, (1994)
37. Shahinpoor, M.,"Electro-Mechanics of Resilient Contractile Fiber Bundles with Applications To Ionic Polymeric Gel and SMA Robotic Actuators" Proc. 1994 IEEE International Conference on Robotics & Automation , vol. 2, pp. 1502-1508, San Diego, California, May (1994)
38. Shahinpoor, M.,, "Electro-Thermo-Mechanics of Spring-Loaded Contractile Fiber Bundles with Applications To Ionic Polymeric Gel and SMA Actuators," Proc. 1994 Int. Conf. on Intelligent Materials, ICIM'94, June 1994, Williamsburg, VA, pp. 1105-1116, (1994)
39. Shahinpoor, M., "A New Effect in Ionic Polymeric Gels : The Ionic "Flexogelectric Effect," Proc. SPIE 1995 North American Conference on Smart Structures and Materials, February 28-March 2, 1995, San Diego, California, vol. 2441, paper no. 05, (1995) .
40. Shahinpoor, M.,, "Active Polyelectrolyte Gels as Electrically-Controllable Artificial Muscles and Intelligent Network Structures,", Book Paper, in Active Structures, Devices and Systems, edited by H.S. Tzou, G.L. Anderson and M.C. Natori, World Science Publishing, Lexington, Ky., (1995)
41. Shahinpoor, M.,, " Ionic Polymeric Gels As Artificial Muscles For Robotic and Medical Applications, Int. Journal of Science & Technology vol. 20, no. 1, Transaction B, pp. 89-136, (1996)
42. Shahinpoor, M., and Y. Osada, "Heart tissue Replacement with Ionic Polymeric Gels" Proc. 1996 ASME Winter Annual Meeting, San Francisco, California, November 12-18, (1995)
43. Shahinpoor, M.,," Design, Modeling and Fabrication of Micro-Robotic Actuators with Ionic Polymeric Gel and SMA Micro-Muscles,", Proc. 1995 ASME Design Engineering Technical Conference, Boston, MA, September (1995)
44. Mojarrad, M., and Shahinpoor, M., "Noiseless Propulsion for Swimming Robotic Structures Using Polyelectrolyte Ion-Exchange Membranes,", Proc. SPIE 1996 North American Conference on Smart Structures and Materials, February 27-29, 1996, San Diego, California, vol. 2716, paper no. 27, (1996)

45. Salehpoor, K., Shahinpoor, M., and M. Mojarrad, "Electrically Controllable Ionic Polymeric Gels As Adaptive Lenses," , Proc. SPIE 1996 North American Conference on Smart Structures and Materials, February 27-29, 1996, San Diego, California, vol. 2716, paper no. 18, (1996)
46. Salehpoor, K.,Shahinpoor, M., and M. Mojarrad, "Electrically Controllable Artificial PAN Muscles,", Proc. SPIE 1996 North American Conference on Smart Structures and Materials, February 27-29, 1996, San Diego, California, vol. 2716, paper no. 07, (1996)
47. Shahinpoor, M., and M. Mojarrad, "Ion-Exchange Membrane-Platinum Composites As electrically Controllable Artificial Muscles,", Proc. 1996 Third International Conference on Intelligent Materials, ICIM'96, and Third European Conference on Smart Structures and Materials, pp. 1012-1017, June 1996, Lyon, France
48. Shahinpoor, M.,, "The Ionic Flexogelectric Effect" Proc. 1996 Third International Conference on Intelligent Materials, ICIM'96, and Third European Conference on Smart Structures and Materials, pp. 1006-1011, June 1996, Lyon, France
49. Shahinpoor, M., and M. Mojarrad, "Biomimetic Robotic Propulsion Using Ion-Exchange Membrane Metal Composite Artificial Muscles, ", Proceedings of 1997 IEEE Robotic and Automation Conference, Albuquerque, NM, April (1997)
50. Shahinpoor, M., , Salehpoor, K., and Mojarrad, M.," Some Experimental Results On The Dynamic Performance of PAN Muscles,", Smart Materials Technologies, SPIE Publication No. vol. 3040, pp. 169-173, (1997)
51. Shahinpoor, M.,, Salehpoor, K., and Mojarrad, M., "Linear and Platform Type Robotic Actuators Made From Ion-Exchange Membrane-Metal Composites,", Smart Materials Technologies, SPIE Publication No. vol. 3040, pp.192-198, (1997)
52. Shahinpoor, M. and Mojarrad, M.," Ion-Exchange-Metal Composite Sensor Films,", Proceedings of 1997 SPIE Smart Materials and Structures Conference, vol. 3042-10, San Diego, California, March (1997)
53. Shahinpoor, M. and Mojarrad, M.," Electrically-Induced Large Amplitude Vibration and Resonance Characteristics of Ionic Polymeric Membrane-Metal Composites,", Proceedings of 1997 SPIE Smart Materials and Structures Conference, vol. 3041-76, San Diego, California, March (1997)
54. Osada, Y., Hasebe, M., "Electrically Activated Mechanochemical Devices Using Polyelectrolyte Gels", Chemistry Letters, pp1285-1288, 1985.
55. Kishi, R., Hasebe, M., Hara, M., Osada, Y., "Mechanism and Process of Chemomechanical Contraction of polyelectrolyte Gels Under Electric Field", Polymers for Advanced Technologies, vol. 1, pp19-25, 1990.
56. Brock, D., Lee, W., Segalman, D., Witkowski, W., "A Dynamic Model of a Linear Actuator Based on Polymer Hydrogel", Proceedings of the International Conference on Intelligent Materials, pp210-222, 1994.
57. Mojarrad, M., Shahinpoor, M., "Ion-exchange-Metal Composite Artificial Muscle Load Characterization And Modeling", Smart Materials Technologies, SPIE Publication No. vol. 3040, pp. 294-301, (1997)
58. Sadeghipour, K., Salomon, R., Neogi, S., "Development of A Novel Electrochemically Active Membrane and 'Smart' Material Based Vibration Sensor/Damper", Smart Materials and Structures, Vol. 1, pp 172-179, 1992.
59. Tzou, H. S., Fukuda, T., "Precision Sensors, Actuators and Systems", Kluwer Academic Publishers 1992
60. Rieder, W. G., Busby, H. R., "Introductory Engineering Modeling Emphasizing Differential Models and Computer Simulations", Robert E. Krieger Publishing Company, Malabar, Florida, 1990.
61. Ugural, A. C., Fenster, S. K., "Advanced Strength and Applied Elasticity", Elsevier, New York, 1987.
62. Bar-Cohen, Y., T. Xue, B. Joffe, S.-S. Lih, Shahinpoor, M.,, J. Simpson, J. Smith, and P. Willis, " Electroactive polymers (IPMC) low mass muscle actuators, " Proceedings of 1997 SPIE Conference on Smart Materials and Structures, March-5, San Diego, California, (1997)
63. Shahinpoor, M., "Artificial Muscles," ERI Press, Albuquerque, New Mexico, Pending Publications, (1997)
64. Furukawa and J. X. Wen, "Electrostriction and Piezoelectricity in Ferroelectric Polymers," *Japanese Journal of Applied Physics*, Vol. 23, No. 9, pp. 677-679, 1984.
65. I. W. Hunter and S. Lafontaine, "A comparison of muscle with artificial actuators," *IEEE Solid-State Sensor and Actuator Workshop*, pp. 178-165, 1992.
66. Shahinpoor, M.,, "Continuum electromechanics of ionic polymeric gels as artificial muscles for robotic applications," *Smart Materials and Structures*, Vol. 3, pp. 367-372, 1994.
67. Kornbluh, K., R. Pelrine and J. Joseph, " Elastomeric dielectric artificial muscle actuators for small robots," *Proceeding of the 3rd IASTED International Conference*, June, 14-16, 1995.
68. Pelrine, R., R. Kornbluh, J. Joseph and S. Chiba, "Artificial muscle actuator," *Proc. of the First International Micromachine Sym.*, Nov. 1-2, pp. 143-146, 1995.
69. Heitner-Wirguin, C., "Recent advances in perfluorinated ionomer membranes: Structure, properties and applications," *Journal of Membrane Science*, V 120, No. 1, pp. 1-33, 1996.

Designs for Stability and Maneuverability in Aquatic Vertebrates: What can we learn?

Paul W. Webb,
University of Michigan,
School of Natural Resources and Environment
and Department of Biology,
Ann Arbor, MI 48109-1115.

email: pwebb@umich.edu

Abstract

Stability and maneuverability are mirror images of each other. Stabilizing systems detect perturbations from external and/or self-generated sources and make the necessary corrections. Maneuvering systems create perturbations to change direction, stop and start. Stability and maneuverability both involve acceleration of a resistive mass, a volume force $\propto L^3$. Altitude, posture, trajectory, and maneuvers are driven by hydrostatic forces, dynamic forces due to the passage of the body and control surfaces through the water and powered forces actively generated by propulsors. Drag and lift are area forces scaling with linear dimensions^2, as L^2, so that control performance relative to inertial resistance scales with L^{-1}. Lift and drag are also proportional to speed, u^2, so that it is easier to match control forces to inertial resistance at higher speeds. Acceleration reaction is especially important because muscle and propulsors oscillate at relatively high reduced frequencies. Acceleration reaction is a volume force, as is the inertial resistance to be stabilized and maneuvered and probably a major factor underlying the high maneuverability of aquatic vertebrates. Aquatic vertebrates use all axial and appendicular systems for dynamic and powered control and maneuvers. Flexibility of the body axis, muscle, and propulsor surfaces are especially important in generating large moments and supporting multi-task functionality. Stability is especially problematic at low speeds, when powered systems dominate but probably with high energy costs. Maneuvers can be executed using dynamic forces at high speeds, but the highest rates of maneuver are powered. Maintenance of high stability and maneuverability require chances in control system with size. Up to vehicle lengths of about 1 to 2 m, increases in acceleration and lift are sufficient, but at larger size, directional control of lift forces becomes essential. While the forces and mechanisms used for stability and maneuvering can readily be inferred, there are virtually no data on response characteristics of the neuro-muscular-propulsor systems involved. Consequently, it is not known if systems used by aquatic vertebrates are efficient *and* strong *while being* highly flexible.

Introduction

Stability and maneuverability superficially appear to be quite different phenomena. In reality, they are mirror images of each other. Stabilizing systems detect perturbations from desired set-points and make the necessary corrections. More stable systems rapidly self-correct with minimal perturbation or overshoot, and during locomotion, stable bodies track a trajectory with fidelity or remain at rest. Aquatic vertebrates control altitude (position in the water column), posture and trajectory. Maneuvering systems, in contrast, create perturbations in order to change direction, stop and start. More maneuverable systems make changes at higher rates in smaller volumes. Performance during maneuvers is usually quantified as minimum turning radius and maximum turning rate, as measured at the center of mass.

Perturbations from desired altitudes, postures, and trajectories occur in three planes and about three axes (Figure 1): the former are slip (sway) in the lateral direction, heave in the vertical direction, and surge in the longitudinal direction. Rotations are rolling about the longitudinal axis, yawing about the dorso-ventral axis, and pitching about the transverse axis.

Perturbations arise from a range of disturbances originating from external and/or self-generated sources (Table 1). A common source of external disturbances is turbulence due to currents and eddies, especially near surfaces, such as beaches, stream boundaries, and from current-swept protuberances, for example boulders, substratum ripples, woody debris, coral, and rooted macrophytes. External disturbances may also arise from other organisms, for example the wake of fish swimming nearby. Self-generated disturbances arise from gill ventilation currents and locomotor movements. Control errors are also sources of self-generated perturbations. Self-generated disturbances are not always undesirable. Given the complementarity of stability and maneuverability, self-generated forces from propulsors are used to maneuver in the same planes and axes about which stability is also sought.

Aquatic vertebrates mix good stability with high maneuverability, showing enviable control in all their locomotor activities. These animals track well, hold position on the bottom in flows, hover, change position at very high rates and do so with very small turning radii. Furthermore, aquatic vertebrates swim at high speeds. They perform all these feats over a wide range of turbulence regimes. However, research has historically focused on speed and Froude efficiency of fish and cetaceans, and in doing so has lost sight of how aquatic vertebrates achieve high performance simultaneously in so many tasks. In particular, the many ways aquatic vertebrates stabilize themselves during various activities and maneuvers has received little attention.

Evaluation of the design features of mechanisms used for stability and maneuvers is required if we are to learn from biological solutions with a view to realizing novel engineering opportunities: What forces are harnessed? What mechanisms develop these forces? How is performance affected by speed and organism size? What are the response characteristics of these systems? Because these areas have not received focused study, the following discussion is more a patchwork of scenarios demanding experimental testing. Changes and surprises are to be expected when formal study commences.

Forces in stability and maneuverability

Stability and maneuverability are united in physical terms. Both accelerate a virtual mass, the sum of body mass and the added mass of water of the system, which is returned to some desired position to achieve stability or accelerated to a new location in maneuvers. The inertial resistance to these corrections and maneuvers is a volume force, proportional ρV, or to L^3, where

ρ is the average density for the system being accelerated, and V is its volume. In both stability and maneuvers, high levels of performance require a control force that is large relative to the inertial resistance.

Four types of forces are involved in stabilizing and maneuvering the body (Table 1). First, hydrostatic forces due to body mass and upthrust are important in altitude control. These hydrostatic forces have been studied in considerable detail (Alexander, 1965, 1990, 1993; Gee, 1983; Webb & Weihs, 1994) and are not considered here.

Second, inertia damps disturbances. This appears to be especially important in controlling trajectory because most swimming modes self-generate disturbances which result in recoil (Bainbridge, 1958). Inertial damping has been studied in detail for the self-generated disturbances in caudal fin propulsion (Lighthill, 1977; Webb, 1988b). Lighthill (1977) has shown that the lateral force component in fish causes yawing recoil perturbations. Tail-generated disturbances are damped by the anterior body mass plus the added mass of the water entrained by the body and anterior median fins. Similar self-generated recoil and damping occur with all single-mode propulsors, especially oscillatory propulsors, for example pectoral fin swimmers (Webb, 1973; Geerlink, 1983; Drucker & Jensen, 1996; Westneat, 1996). However, while inertia helps stabilize trajectories, it is also the major resistance to maneuvers.

The other two control forces are hydrodynamic in origin. First, forces arise from the flow over the body and appendages due to external currents or translocation of the body. These are generally described as dynamic forces, which promote dynamic stability and dynamic maneuvers. Dynamic control forces have been a major focus of research and design for human-engineered vehicles (von Mises, 1945; Hoerner, 1965, 1975; Marchaj, 1988), and not surprisingly, most research on aquatic vertebrates has concentrated on the same phenomena (Aleyev, 1977; Weihs, 1989, 1993; Bandyopadhyay et al., 1997). The second group of hydrodynamic forces is those actively generated by propulsive movements. These forces or a force component are actively oriented by the propulsor in a direction necessary to stabilize or maneuver the body. I refer to these as powered forces.

Dynamic and powered forces for stability and maneuver may be lift-based or resistance-based, the latter being drag and acceleration reaction. Lift and drag are both areal forces, proportional to propulsor area. Therefore, they scale with linear dimensions^2, as L^2. However resistance is a volume force scaling with L^3. Performance is the ratio of thrust to the resistance force and as a result decreases with increasing size, scaling with L^2/L^3, or L^{-1}. Therefore, it is not possible to match areal forces to inertial resistance over a large size range. Lift and drag are also proportional to speed, u^2, so that it is easier to match control forces to inertial resistance at high speeds. Drag is primarily used for braking (Breder, 1926; Geerlink, 1986), but fins may also be extended on the inside of a turn to increase centripetal acceleration and reduce turning radius. Lift, being larger per unit surface area of a propulsor than drag, is more commonly used for control, including steering.

Acceleration reaction is the product of an added mass of water and the acceleration given to it. It is always present in vertebrate propulsion because muscles are reciprocating engines. Consequently, propulsive elements oscillate, and there is always a phase in a propulsor beat where acceleration occurs. The importance of acceleration reaction relative to other force components is indicated by the reduced frequency parameter, $\sigma = \omega L/u$, were ω is the radian frequency and u is the mean forward speed. Acceleration reaction has a significant effect on forces when $\sigma > 0.1$, and values for aquatic vertebrates are characteristically greater than 0.2 (Daniel, 1984; Daniel & Webb, 1987; Webb, 1988a).

Acceleration reaction is a volume force. Thus the added mass per unit length is proportional to the square of the propulsor span, or to L^2 and the hence integral of added mass

along a fin is proportional to L^3. Furthermore, because of the density of water is similar to that of a typical animal body, added mass is large and acceleration reaction can be very large compared with inertial resistance. The use of acceleration reaction is probably a major factor underlying the high maneuverability of aquatic vertebrates. It also contributes to stability, as shown by its role in damping tail-generated recoil.

Stability and Maneuver Mechanisms

Effective stability and maneuverability are based on hydrostatic, dynamic and powered forces. A variety of mechanisms are involved in generating and modulating these forces, and these originated early in the evolution of chordates and fishes (Figure 2).

One diagnostic trait of the chordates is a post-anal tail, supported internally by the notochord. The tail apparently arose among chordates from mutations in perhaps a single gene (Jeffery, 1997). It is believed to have been selected through evolutionary time because a flexing tail provided greater power for swimming and maneuvering, thereby facilitating dispersal and settlement of larvae over current-swept surfaces (Clark, 1964). Hence the need for good stability and maneuverability is undoubtedly ancient indeed. Body flexibility permits the generation of very large moments. This is probably a second major factor underlying the high maneuverability of aquatic vertebrates.

Early fish lacked additional control surfaces. Therefore all propulsion and directional control had to be provided by the post-anal tail supported by the notochord. The notochord is a remarkable structure (Symmons, 1979). As a hydrostatic skeleton it provides rigidity to withstand compression forces associated with transmission of the locomotor force to the body (Wainwright, 1983, 1988). However, the notochord is also flexible so that the tail can orient control forces in many directions to stabilize altitude, posture, and trajectory and to maneuver in all planes.

Strengthening the notochord through the subsequent evolution of centra and vertebral arches is characteristic of vertebrates. These structures in fish are also used to restrict the degrees of freedom of the vertebral column, making it rigid in most planes other than the beat plane of the caudal propulsor (Hebrank et al., 1990; Long et al., 1994; Long, 1995; Long et al., 1997). However, these changes occurred after additional control surfaces appeared. However, in spite of the adequacy of tail-based powered control to stabilize and maneuver the body, this was apparently not very effective in most situations. Thus numerous additional structures arose among early fishes (Figure 2) which undoubtedly functioned to provide greater control and maneuverability at higher speeds and larger sizes in frequently hostile environments.

Among these early control devices was armor (Figure 2). At this time, the tail was relatively small and often pointed. The axial skeleton was relatively poorly reinforced. Therefore swimming forces were probably small (Webb, 1982). Under these circumstances, the armored head and anterior body probably provided inertial damping of both external and self-generated disturbances, similar to modern anuran tadpoles (Wassersug, 1989; Liu et al., 1996).

Lateral structures appeared, probably as extensions of armor (Jarvik, 1965; Figure 2). Some were elongated folds extending laterally along much of the body (e.g. *Jamoytius*). Others were extensions to head shields (e.g. *Heterocyclaspis*), probably precursors to pectoral fins. Head shields and lateral control surfaces are believed to have been essential for dynamic stability and altitude control. The latter has been studied in considerable detail. Early armored fishes were undoubtedly negatively buoyant and regulating swimming depth must have depended on hydrodynamic lift forces. Lift was generated by the anterior control surfaces and a downward thrust component from the tail (Bunker & Machin, 1991; Ferry & Lauder, 1996). The anterior

and posterior lift forces generated opposing moments about the center of mass, and these must have been balanced to control posture. Thus the head and paired anterior appendages generated a positive pitching moment balanced by a negative pitching moment at the tail. It is worth noting that the moment arm of the tail about the center of mass was much smaller than that of the pectoral appendages. As a result, the pectoral appendages generated the larger lift force, and only a small portion of the tail thrust was necessary to control pitch (Bunker & Machin, 1991). This illustrates a common theme in the design of control system among aquatic vertebrates, the simultaneous use of dynamic and powered control for stability and maneuvers.

In addition to lateral control surfaces, various median fin configurations arose. Initially, numerous dorsal fins and spines were common (e.g. *Jamoytius, Climatius*). The most diverse group of fishes, the bony fishes, radiated about a fin plan with a dorsal fin and an anal fin. Elasmobranchs, which are generally much larger than bony fishes but are less maneuverable, radiated around a form with two dorsal fins and an anal fin. Both groups, however, converged on two pairs of lateral control surfaces, the pectoral and pelvic fins. Originally, all these surfaces probably had little mobility, but undoubtedly greatly improved dynamic control of stability. The motive power was provide by the tail which also controlled surge.

Armor was not retained by the majority of fishes (Moy-Thomas & Miles, 1971). Loss of armor probably increased maneuverability by reducing inertial resistance at a time when jawed fishes were becoming more common, shifting the balance in predator-prey interactions from defense to flight. At the same time, there was a concomitant expansion of the caudal fin span (Webb & Smith, 1980) of the order of 2 to 4 times. This would have increased acceleration reaction by 4 to 16 times. With the loss of armor, the increased tail force could have created a major recoil problem and an extremely unstable platform for cephalic sensory systems. However, the loss of armor was associated with more prominent dorsal fins and often increased body depth (Figure 2). This would have resulted in a compensatory increase in the anterior virtual mass, increasing inertial damping of tail-generated recoil (Lighthill, 1977).

The loss of armor also made it easy to achieve neutral buoyancy with small low density inclusions. Neutral buoyancy is critical to hovering and swimming at low speeds, adaptations which have been exploited by fish as platforms for scanning the environment for food and predators (O'Brien et al., 1986), ambushing prey, and refuging. (Moyle & Cech, 1996). However, like the loss of armor, acquisition of neutral buoyancy could have created a stability problem (W. W. Schultz, personal communication). This is because a streamlined neutrally buoyant body is directionally unstable when released in a uniform inviscid flow. The instability is due the vortical wake. Thus, if the body receives a clockwise disturbance as it traverses from right to left, a clockwise body vorticity is required to satisfy the Kutta-condition at the new tail location. From Kelvin's theorem, a counter-clockwise vortex must be released behind the tail. This vortex slows the fluid atop the tail, and hence increases the pressure (Bernoulli's theorem). This high pressure at a distance far from the center of mass applies a strong clockwise torque that supports the initial angular perturbation. Schultz has shown that this potential stability problem is not realized because aquatic vertebrates use an oscillating tail as their major means of propulsion. This confers directional stability because powered swimming is known to reverse the sign of the wake vorticity, hence allowing stable swimming.

Subsequent evolution among aquatic vertebrates built on the basic patterns established early among fishes. In many situations, control surfaces have been diminished or lost. Then, like the earliest fishes, powered forces produced by the tail are solely responsible for control and maneuvers. This is seen in many orders of fishes, anurans, and reptiles, but usually in circumstances where predation risk is mitigated by poisons (e.g. sea snakes), or refuges in space (e.g. burrowing eels) and time (e.g. tadpoles as founder species in temporary ponds).

Many modern fishes are negatively buoyant and use dynamic and powered forces to balance weight, using principles to achieve altitude and postural stability that are fully comparable to those of early fishes (Alexander, 1993; Bunker & Machin, 1991). However, in contrast to the probably slow and clumsy early fishes, many modern negatively buoyant fishes, notably many sharks and tunas, are fast continuous swimmers. Under these circumstances, dynamic and powered control of altitude is more economical than using hydrostatic forces (Alexander, 1990).

The greatest evolutionary innovations leading to modern fishes primarily related to the magnitudes of dynamic and powered forces. These in turn depended on changes in the dimensions and strength of supporting structures, and perhaps propulsor beat frequencies driven by faster muscles (Alexander, 1969; Bone, 1977, 1978; Webb, 1982). Thus there is a trend towards strengthening the centra and vertebral arches, increasing the magnitude of locomotor forces which could be transmitted to the body (Webb, 1982). Various innovations occur in fin-ray structure and skeletal supports increasing force magnitudes as well as the ability to direct these as needed for control and maneuvers. For example, single fin rays articulate with each basal supporting structure of the median fins in the Neopterygii (Lauder & Liem, 1983). This apomorphy is believed to have promoted fin flexibility, presumably improving thrust and the precision in orienting control forces. Similarly, the development of the hypochordal longitudinalis and ventral flexor muscles in the Ginglymodi, and subsequently interradialis and supracarinalis muscles in Halecostomes improved control of the caudal fin shape (Lauder, 1989). Major trends in the evolution of teleosts have occurred in the caudal skeleton. Not only has the strength the caudal fin blade support been increased, but so has flexibility of the fin web (Lauder & Liem, 1983; Webb, 1982; Gibb et al., 1994; Gosline, 1997). Thus another feature underlying the stability and maneuvering abilities of fish is the combination of flexibility with strength in support and force transmission systems.

Another trend among bony fishes has been an increase in the number of propulsors. This is associated with a reduction in the dominance of the tail for routine swimming in many highly maneuverable fishes, such as many littoral freshwater and marine species. In addition, long based fins have arisen several times in which relatively independent motion of propulsive elements is possible within the fin length (e.g. mormyrids). These single fins are also essentially multiple propulsors. Fish using multiple propulsors achieve extremely smooth trajectories when swimming, apparently with little or no recoil. It may be no coincidence that these fishes are very economical swimmers (Gordon et al., 1989).

Stability and Speed

The effectiveness of stabilizing mechanisms varies with speed (Marchaj, 1988). Dynamic forces vary with u^2. The mass to be moved in making a correction, however, remains proportional to mass, independent of speed. Therefore, as speed decreases, dynamic forces also decrease relative to required stabilizing forces. Consequently, stability is more difficult at low speeds, as every bicycle rider, sailor, or pilot knows from experience.

Some fish may increase the area of control surfaces as speed decreases (Videler, 1993; Bone et al., 1995), but eventually a point is reached when dynamic lift cannot support the weight in water. One alternative for fish is to stop swimming and rest on the substratum. Currents present problems, and fish in currents, for example selachians, salmonids, gadids, and cyprinids, use their pectoral fins to create a lift force oriented towards the substratum. This adds to the weight of the fish, increasing the friction force to help resist displacement (Arnold & Weihs, 1978; Arnold et al., 1991).

The second common response to declining dynamic forces at low speeds is a shift to powered control. As speed decreases, fish make more frequent and more pronounced fin

movements (Harris, 1937a,b), generating higher thrust than would be expected to overcome drag at these speeds (Videler, 1993; Webb, 1993). This can create problems of surge, which is controlled by postural changes, called tilting, which increases drag to balance thrust (He & Wardle, 1986; Webb, 1993; 1997). A shift to powered control at low speeds generally requires a flexible fin web supported by skeletal elements capable of independent movement. Selachians and cetaceans lack flexible fins and as a result do not swim at very low speeds (Webb, 1997).

Although powered control forces become the only option for control at low speeds, their use carries a high energy cost. In particular, induced drag is proportional to $1/u^2$, and hence becomes large at low swimming speeds, and especially during hovering (Hoerner, 1965, 1975; Blake, 1979).

Stability is more readily accomplished as speed increases. Dynamic forces become large and propulsive movements of median and paired fins decline as speed increases. As a result powered control becomes less important with savings in induced drag (Alexander, 1990). Furthermore, dorsal, anal, pectoral, and paired fins are frequently furled to minimize drag, exposing to the flow only the minimum area necessary for control (Bone et al., 1995). The caudal fin, of course, is typically expanded fully to maximize thrust.

Maneuverability and Speed

Maneuverability is also affected by speed. As with stability control, dynamic forces decrease at low speeds and become insufficient for maneuvering. Therefore, aquatic vertebrates again tend to shift to powered maneuvers. At zero speed, hovering fish can rotate, turning about the dorso-ventral axis with zero turning radius (Blake, 1978, 1980), and hence with no slip or surge. However, the relatively small mass of muscle and small size of propulsors compared with the tail generally preclude turning at high rates during low speed swimming.

The smallest turning radii and highest turning rates occur in fast-start turns (Webb, 1994; Harper & Blake, 1990; Domenici & Blake, 1991, 1993; Jayne & Lauder, 1993). These harness the large acceleration reaction and large turning moments of the tail (Weihs, 1972, 1973). Thus in fast-start turns from rest, the center of mass turns with a radius of less than 10% of the body length, accelerating at rates in excess of 10 G, to reach speeds of the order of 1 to 2 $m.sec^{-1}$ after 100 to 150 msec.

At cruising and sprint speeds, dynamic forces acting on control surfaces become large enough for steering. However, the highest turning rates still require powered control forces generated by fast-starts (Jayne & Lauder, 1993). In both dynamic and powered maneuvers, turning radius is proportion to body length and independent of speed (Howland, 1974; Webb, 1976, 1983).

Indirect evidence has recently been obtained which suggests there is a substantial energy cost associated with maneuvers of fish. The Froude efficiency of fast-starts is only 10 to 20 % compared with over 90% in cruising and sprints (McCutcheon, 1971; Webb, 1979). Furthermore, maneuvers dominate routine swimming (Nursall, 1958) and elevate energy costs by over an order of magnitude compared to rectilinear propulsion at the same mean speed (Webb, 1991; Boisclair & Tang, 1993; Krohn & Boisclair, 1994).

Maneuverability and Size

Aquatic vertebrates span six orders of magnitude from free swimming larvae of ≥3 mm to blue whales ≥22 m in total length. In spite of the large size range, vertebrates generally swim at Reynolds Numbers where inertial forces are significant (Webb & Weihs, 1986; Jordan, 1992;

Bone et al., 1995), the exception being fish larvae at routine speeds (Fuiman & Webb, 1988). A common geometric design cannot provide stability and maneuverability over such a large size range because performance scales with L^{-1} (Daniel & Webb, 1987; Webb, 1988a). As a result, design changes are necessary as size increases.

The smallest aquatic vertebrates, fish larvae, generate resistance-based forces by undulation of the body and tail (Lighthill, 1975; Daniel et al., 1992). The areas of the propulsive surfaces are increased by an extensive fin fold. Small larvae lack additional control surfaces and hence are entirely power controlled. As larvae grow, paired and median fins differentiate, and as they develop, they increase in aspect ratio (Webb & Weihs, 1986). Then lift forces become important, and because these are large compared to resistance forces, some compensation is achieved for increased mass. Fin spans also increase to help match added mass to body inertia (Webb, 1976).

A variety of mechanisms are involved in maintaining control performance at larger sizes. One may be found in selachians, a group of fish which are typically large (Moyle & Cech, 1996). Bones and ligaments transmit propulsive forces to the body. Their cross-sectional area scales with L^2 compared to inertial resistance scaling with L^3. Therefore, the strength of the transmission system could become limiting to performance at larger body sizes. Selachians use hydrostatic pressure within the non-compliant skin to help transmit muscle forces to the body from the tail propulsor (Wainwright et al., 1978). This may be a way of overcoming possible limiting areas of bones and ligaments when matching control forces to inertial resistance. Thus the internal hydrostatic pressure is distributed over an internal skin area proportional to L^2, with a skin thickness scaling with L. Thus the volume of the skin resisting expansion scales with L^3. The use of septa internal to the myotomal muscle (Westneat et al., 1993) might also aid in offsetting effects of increasing size on stability and maneuvering.

The largest fish and cetaceans achieve the highest recorded absolute speeds. Indeed, most of these animals share suites of characteristic increasing power and thrust, and minimizing resistance. These include endothermy, large amounts of oxidative muscle, low resistance body shapes, a reinforced vertebral column and use of septa to facilitate force transmission, and perhaps store energy between propulsive beats (Alexander, 1988; Webb & de Buffrenil, 1990; Westneat et al., 1996), and high aspect ratio lift-based propulsors and control surfaces. The high speeds achieved by these fishes and their efficient lift-based propulsors provide some compensation for control at increased body mass. In spite of these adaptations, however, turning radii of large fish and cetaceans are two to three times larger than those of smaller species in proportion to total length (Webb & Keyes, 1981; Domenici & Blake, 1993; Fish, 1996). In addition, the design of fins of large fish and cetaceans for efficient lift-based prolusion and control preclude fin flexibility. As a result, these animals cannot hover or swim at very low speeds, and they do not frequent highly turbulent flow regimes.

Maneuvering poses special problems for cetaceans, not only because of their large size, but also because the plane of the tail beat is normal to the axis of yawing turns. Cetaceans have fewer control surfaces than fish but yawing maneuvers are important when moving near the water surface and in capturing fish prey. Cetaceans have a single dorsal fin and paired pectoral fins, while fish have dorsal and anal median fins and the paired lateral pectoral and pelvic fins. However, cetaceans may have increased the range of bending and twisting of the vertebral column to compensate. In contrast to the well developed neural and hemal arches of fishes, locked together to provide a dorso-ventral plate limiting excursions laterally (Hebrank, 1982; Hebrank et al., 1990; Long, 1992), the caudal centra of cetaceans tend to be simple ellipses, with similar major and minor axes (P. W. Webb, unpublished observations). This probably allows substantial freedom to rotate the caudal peduncle supporting the tail flukes. Observations of turning cetaceans shows their flukes can rotate through angles as high as ±45° (F. E. Fish and P. W. Webb, unpublished observations). Coupled with rolling of the body, twisting of the peduncle

allows the flukes to be rotated as necessary to maneuver in all planes. Thus cetaceans show increased dependence on powered control than the most derived fastest fishes.

Response Characteristics

The ultimate key to understanding the design features of systems used by aquatic vertebrates for stability and maneuvering is through the response characteristics as they correct disturbances and drive maneuvers. It is possible to infer much about the forces and mechanisms involved, but design characteristics must be measured. There are virtually no such measurements. It is known that it takes some 50 to 150 msec for a fast-start to acquire high speeds. Although the rate of turn is high during this period, the displacement of the center of mass is small, and grows rapidly only after the fast-start (Webb, 1994a). Rotation rates are also slow, as are rolling and yawing maneuvers at low speeds in the absence of fast-starts (Webb et al., 1996; Schrank, 1997)

Dynamic control can, to a large extent, be self-correcting (Weihs, 1989, 1993), but the frequency response of fine tuning is unknown. Powered control is dependent on small latencies of sensory-motor systems to anticipate, detect and correct perturbations. Long response latencies can result in an attempted correction amplifying a perturbation, with a loss of control known as [pilot] induced error. The dorsal nerve chord, a chordate apomorphy, and probably metameric segmentation, undoubtedly played an important role in reducing response times (Gans et al., 1997). Again, the amplitude and frequency response of powered control is unknown, but indirect evidence suggests response characteristics may be limiting to the radiation of fish into some turbulent flow conditions common in streams. For example, chub have well developed dynamic control and entrain on cylinders from 13 to 23 C over a wider range of current speeds and cylinder diameters (Figure 3). In contrast, bass make greater use of powered control. This species only entrains at 23 C when the well known temperature effects on biological processes would minimize response latencies (P. W. Webb, unpublished observations). Turbulence also affects the ability of fish to negotiate obstacles (Fletcher, 1990) and reduces swimming speed (Pavlov, 1982; Shtaf, 1983). There are insufficient data to determine if differences in the use of dynamic and powered stability effect performance in such flow regimes.

There are currently no empirical measures of energy costs associated with aquatic vertebrate solutions to control. Thus, it is not known if the high stability and maneuverability of aquatic vertebrates comes with a cost which might make designs impractical for human engineered systems. Therefore, measuring response characteristics of design features from the sensory and integrating components, muscle linear actuators, control mechanisms and the forces they generate, to whole organism responses, performance and energetics is essential.

Biological and Human Designs

As sources for design ideas for stable but maneuverable engineered vehicles, the mechanisms used by aquatic vertebrates show both similarities and differences from current human engineered vehicles (Table 2). These similarities primarily occur at a high level of organization where both aquatic vertebrates and engineered vehicles:

- improve engine design and size (Alexander, 1969; Fetcho, 1987).
- use dynamic control surfaces at high speeds where they are most effective. Observations on fishes show that lift-based dynamic control is used on vehicles as small as 10 to 15 mm in total length (Weihs & Webb, 1986).

- replace dynamic control with powered control systems at low speeds when dynamic forces become small (Alexander, 1989; Webb, 1994b).

- use specialized designs for specific tasks, but at a cost to versatility. Vehicles with high performance in an area have a limited task (gait) range. Vertebrate example include thunniform vertebrates swimming at high speed, eels adept at penetrating high density complex structures) *versus* multi-tasking littoral bony fishes (Webb, 1994b).

- maximize performance relative to payload. In animals, volume affects how much muscle can be carried, the size of digestive systems, and gamete production (Vogel, 1994; Webb et al., 1996).

Aquatic vertebrates largely part company with human engineering when specific mechanisms are explored for low speed stability and maneuvering. Humans tend to use specialized devices for individual tasks. For example a bow thruster might be used for low speed maneuvers, but to perform only this task. In contrast, most fish have multitask devices which simultaneously function as propulsors, stabilizers, and drive maneuvers. At such, control surfaces and propulsion systems are not usually separate, and dynamic and powered control are fully integrated.

The integrated control/propulsion systems of fish reflect differences in the construction elements of animals *versus* human devices. Organisms are built around flexing materials, materials which will bend but not break, that allow bodies to mold to complex contours and to assimilate remarkable amounts of damage with little loss in functionality. Flexing of propulsors occurs on many scales from orienting the propulsor/controller device (e.g. by caudal peduncle bending and torsion) to local camber of the fin web (McCutcheon, 1971; Videler, 1975; Gibb et al., 1994). A distributed nervous system provides both local and central integration in space and time. Smart materials may begin to erode the advantage of biological designs for local shape modulation of control surfaces, but efficient, strong, highly flexible drives are not a common part of the engineering lexicon. On the other hand, it is not known if systems used by aquatic vertebrates are efficient *and* strong *while being* highly flexible.

It is clear, however, that the use of muscle is especially important for the soft, flexible form of organisms. Furthermore, the properties of muscle have far reaching consequences for the way animal propulsors work and for differences between nature and engineering. Muscles are composed of numerous linear actuators (sarcomeres) arranged in both series and parallel. As such, force and power are readily modulated by recruiting variable numbers of fibers. Muscles do not follow Hooks law, and a given tension can be generated over a wide range of muscle lengths. However, muscles are an expensive way of holding a desired posture or position, and engineering practices such as cams-and-pins, hydraulics, worm-gears and springs have a clear advantage. Indeed, convergent designs are often found where animals lock joints (e.g. catfish spines).

A consequence of using muscles is that the elements of the propulsive systems oscillate. This is true even when the body or fin undulates, for undulation is an emergent property of numerous oscillating elements closely coupled together. As a result of propulsor oscillation, acceleration reaction affects the force balance in all circumstances. Furthermore, changes in shape and size of propulsors have occurred often to increase the acceleration reaction force component. Engineering practice usually seeks to avoid large and sudden accelerations.

It is relatively easy to make acceleration reaction large over a wide range of small sizes, perhaps in vehicles up to about 1 m in length, the size of the largest adult salmonids. Coupled with the flexibility of the body, this allows the generation of forces and moments that are very large compared with the inertial resistance. This combination of a large mass of myotomal muscle, a flexible body, and harnessing acceleration reaction powers maneuvers at high rates of

turning with small radius that make yawing maneuverability of fishes (and pitching maneuverability of mammals) so enviable.

Acceleration reaction appears to be of lesser importance in larger animals, >1 to 2 m in overall length. However, it appears that body flexibility then becomes more important to proved large powered control forces, plus high speeds that generate large dynamic control forces.

All vehicles, whether animal or engineered, have safety factors built in which reflect the frequency and magnitude of environmental stresses and strains. Both animals and vehicles may experience environments where loss or damage from attack is high. Sometimes, therefore, damage occurs. Both organisms and engineering practice build in some redundancy, but this seems especially well developed in aquatic vertebrates. At a fine scale, redundancy occurs in the construction of muscle from multiple sarcomeres, organized in series as fibers and with fibers bundled in parallel. Control of muscle also involves both local control (e.g. via the force-velocity relationship; McMahon, 1984) and distributed neural inputs (e.g. polyneuronal innervation; Fetcho, 1987).

At the propulsor level, ray-finned webs are multi-element devices which can sustain substantial damage. Indeed this is the basis for using fin clipping as a marker by management agencies, as well as allowing fish to assimilate the common loss of fin surface due to disease and predators. Maintenance of propulsor functionality in the face of damage is also facilitated by the use of multiple propulsors with overlapping roles in both control and propulsion. Finally, forces generated by propulsors include resistance and lift components, providing greater versatility to compensate for damage.

The development of multiple propellers allows fish to swim with very smooth trajectories. Such smoothness is unusual because oscillating systems usually create incompletely damped recoil forces. Indeed, energy losses associated with such motions are believed to be a major contributor to the high cost of transport in many aquatic vertebrates (Casey, 1992). Here engineering systems easily provide stable platforms. However, the multiple propulsors of fish create a large number of degrees of freedom in which an animal can suddenly destabilize itself and hence rapidly initiate a high performance maneuver.

Both aquatic vertebrates and engineered vehicles depend on rapid and appropriate response to a disturbance. This is especially critical when powered control is emphasized. Some fish appear to be near the response limits of the musculo-skeletal system. Although computing power can provide very short latencies for data integration and decision making, response time of engineered vehicles may still be limited when large lift-based forces must be generated by control surfaces to maneuver relatively large masses. There are no adequate data here to compare nature and engineering.

Conclusions

Aquatic vertebrates are designed around systems that have passed the test of natural selection. However, this does not mean that designs for propulsion, stability, and maneuverability are optimal, let alone desirable. Rather, they are sufficient - adequate - compared with alternatives expressed by competitors. In addition, observed designs have not been selected from among all possibilities. Instead, the variability on which natural selection operates is restricted by history in terms of materials used by ancestors and by developmental patterns. Finally, chance disasters are not uncommon. These arbitrarily cull both superior and less effective systems and the survivors are simply lucky. Human engineered designs must pass the same tests in a real world as do animals, but humans face a level playing field in being able to chose from among many alternative designs. Thus it is far from clear that vertebrate solutions are superior, or the

circumstances under which they have promise, and the compromises which might have to be made in their use. For example, high control and maneuver performance derives in large part from mixed dynamic and powered control devices based on oscillating flexible propulsors generating high acceleration reaction forces. A consequence of this is a high cost of transport. We do not know how to couple the advantages of traditional human engineering where they out-perform fish in translocation with maneuverability where vertebrates have the edge.

Yet informed decision making on the use of vertebrate designs rests on knowledge of system response characteristics. It is not known if systems used by aquatic vertebrates are efficient *and* strong *while being* highly flexible because response characteristics and trade-offs have not been studied in any detail for control and maneuver systems. Knowing response characteristics of aquatic vertebrate stability and maneuver systems is fundamental to determining the utility of borrowing designs for engineering application.

Acknowledgements

Much of this review is based on research performed with support from the National Science Foundation, grant number DCB-9017817.

References

Alexander, R. McN. (1965). The lift produced by the heterocercal tails of Selachii. J. exp. Biol. 43:131-138.

Alexander, R. McN. (1969). The orientation of muscle fibres in the myomeres of fishes. J. mar. biol. Ass. UK 49;263-290.

Alexander, R. McN. (1988). *Elastic mechanisms in animal movement*. Cambridge University Press, Cambridge, England.

Alexander, R. McN. (1989). Optimization and gaits in the locomotion of vertebrates. Physiol. Rev. 69;1199-1227.

Alexander, R. McN. (1990). Size, speed and buoyancy adaptations in aquatic animals. Amer. Zool. 30;189-196.

Alexander, R. McN. (1993). Buoyancy. In *The Physiology of Fishes*, (ed. D.H. Evans). pp. 75-97. CRC Press, Boca Raton, FL.

Aleyev, Y. G. (1977). *Nekton*. Junk, The Haque.

Arnold, G. P. and Weihs, D. (1978). The hydrodynamics of rheotaxis in the plaice (*Pleuronectes platessa*). J. exp. Biol. 75:147-169.

Arnold, G. P., Webb, P. W. and Holford, B. H. (1991). The role of the pectoral fins in station-holding of Atlantic salmon parr (*Salmo salar*). J. exp. Biol. **156**: 625-629.

Bainbridge, R. (1958). The speed of swimming of fish as related to size and to the frequency and the amplitude of the tail beat. J. exp. Biol. 35;109-133.

Bandyopadhyay, P. R., Castano, J. M., Rice, J. Q., Philips, R. B., Nedderman, W. H. and Macy, W. K. (1997). Low-speed maneuvering hydrodynmaics of fish and underwater vehicles. Trans. Amre. Soc. Struct. Mech. Engin. 119;136-144.

Blake, R. W. (1978). On balistiform locomotion. J. mar. biol. Ass. UK 58:73-80.

Blake, R. W. (1979). The energetics of hovering in the mandarin fish (*Synchropus picturatus*). J. exp. Biol. 82,25-33.

Blake, R. W. (1980). Undulatory median fin propulsion of two teleosts with different modes of life. Can. J. Zool. 58;2116-2119.

Boisclair, D. and Tang, M. (1993). Empirical analysis of the swimming pattern on the net energetic cost of swimming in fishes. J. Fish. Biol. 42;169-183.

Bone, Q. (1977). Muscular and energetics aspects of fish swimming. In *Swimming and Flying in Nature* (eds. T. Y. Wu., C. J. Brokaw and C. Brennen), pp. 493-528. Plenum Press, New York, NY.

Bone, Q. (1978). Locomotor muscle. In *Fish Phsyiology vol VII*, (eds W.S. Hoar and D.J. Randall), pp. 361-424. Academic Press, New York, NY.

Bone, Q., Marshall, N. B. and Blaxter, J. H. S. (1995). Biology of Fishes. Chapman and Hall.

Breder, C. M. (1926). The locomotion of fishes. Zoologica 4:159-297

Bunker, S. J. and Machin, K. E. (1991). The hydrodynamics of cephalaspids. Soc. Exp. Biol. Seminar Ser. 36;113-129.

Casey, T.M. (1992). Energetics of locomotion. Adv. Comp. Environ. Physiol. 11;251-275.

Clark, R. B. (1964). Dynamics in Metazoan Evolution. Oxford Univ. Press, Oxfored, England.

Daniel, T. L. (1984). Unsteady aspects of aquatic locomotion. Amer. Zool. 24;121-134.

Daniel, T. L. and Webb, P. W. (1987). Physics, design and locomotor performance. In *Comparative Physiology: Life in Water and on Land* (eds. P. Dejours, L. Bolis, C. R. Taylor and E. R. Weibel), pp. 343-369. Liviana Press, Springer-Verlag, NY.

Daniel, T. L., Jordan, C. and Grunbaum, D. (1992). Hydromechanics of swimming. Adv. Comp. Environ. Physiol. 11;17-49.

Domenici, P. and Blake, R. W. (1991). The kinematics and performance of the escape response of the angelfish (*Pterophyllum eimekei*). J. exp. Biol. 156;187-205.

Domenici, P. and Blake, R. W. (1993). Escape trajectories in angelfish (*Pterophyllum eimekei*). J. exp. Biol. 177;253-272.

Drucker, E. G. and Jensen, J. S. (1996). Pectoral fin locomotion in the striped surfperch. I. Kinematic effects of swimming speed and body size. J. exp. Biol. 1999;2235-2242.

Ferry, L. A. and Lauder, G. V. (1996). Heterocercal tail function in leopard sharks: a three dimensional kinematic analysis of two models. J. exp. Biol. 199;2253-2268.

Fetcho, J.R. (1987). A review of the organization and evolution of motoneurons innervating the axial musculature of vertebrates. Brain Res. Rev. 12;243-280.

Fish, F. E. (1996). Comparative turning performance of odontocete cetaceans. Am. Zool. 36: 90A.

Fletcher, R.I. (1990). Flow dynamics and fish recovery experiments: Water intake systems. Trans. Am. Fish. Soc. 119;393-415.

Fuiman, L. A. and Webb, P. W. (1988). Ontogeny of routine swimming activity and performance in zebra danios (Teleostei: Cyprinidae). Anim. Behav. 36;250-261.

Gans, C., Gaunt, A. S. and Webb, P. W. (1997). Vertebrate Locomotion. In *Handbook of Physiology* (Ed. W. H. Dantzler), pp. 55-213. American Physiological Society, Oxford University Press, Oxford, UK.

Gee, J. H. (1983). Ecological implications of buoyancy control in fish. In Fish Biomechanics (eds P. W. Webb and D. Weihs), pp.140-176. Praeger, New York.

Geerlink, P.J. (1983). Pectoral fin kinematics of *Coris formosa* (Teleostei, Labridae). Neth. J. Zool. 33;515-531.

Geerlink, P.J. (1986). Pectoral fins. Aspects of propulsion and braking in teleost fishes. PhD Thesis, University of Groningen.

Gibb, A. C., Jayne, B. C. and Lauder, G. V. (1994). Kinematics of pectoral fin locomotion in the bluegill sunfish *Lepomis macrochirus*. J. exp. Biol. 189;133-161.

Gordon, M. S., Chin, H.G. and Vojkovich, M. (1989). Energetics of swimming in fishes using different modes of locomotion: I. Labriform swimmers. Fish. Physiol. Biochem. 6;341-352.

Gosline, W. A. (1997). Functional morphology of the caudal skeleton in teleosten fishes. Ichthyol. Res. 44;137-141.

Harper, D. G. and Blake, R. W. (1990). Fast-start performance of rainbow trout *Salmo gairdneri* and northern pike *Esox lucius*. J. exp, Biol. 150;321-342.

Harris, J. E. (1937a) The mechanical significance of the position and movements of the paired fins in the teleostei. Papers Tortugas Lab., Carnegie Inst. 31;173-189.

Harris, J. E. (1937b) The role of fin movements in the equilibrium of fish. Ann. Rep. Tortugas Lab., Carnegie Inst. 11936-37; 91-93.

He, P. and Wardle, C. . (1986). Tilting behavior of the Atlantic mackerel, *Scomer scombrus*, at low swimming speeds. J. Fish. Biol. 29 (Suppl. A);223-232.

Hebrank, M. R. (1982). Mechanical properties of fish backbones in lateral bending and in tension. J. Biomech. 15;85-89.

Hebrank, J. H., Hebrank, M. R., Long, J. H, Block, B. A. and Wainwright, S. A. (1990). Backbone mechanics of the blue marlin *Makaira nigricans* (Pisces, Istiophoridae). J. Exp. Biol. 148;449-459.

Hoerner, S. F. (1965). *Fluid-dynamic Drag*. Hoerner Fluid Dynamics, Brick Town, NJ.

Hoerner, S. F. (1975). *Fluid-dynamic Lift*. Hoerner Fluid Dynamics, Brick Town, NJ.

Howland, H. C. (1974). Optimal strategies for predator avoidance: the relative importance of speed and manoeuverability. J. Theor. Biol. 47:333-350.

Jarvik, E. (1965) On the origin of girdles and paired fins. Israel Journal of Zoology 14();141-172

Jayne, B. C. and Lauder, G. V. (1993). Red and white muscle activity and kinematics of the escape response of the bluegill sunfish during swimming. J. comp. Physiol. 173A;495-508.

Jeffery, W. R. (1997). Evolution of ascidian development. BioSci. 47;417-425.

Jordan, C.E. (1992). A model of rapid-start swimming at intermediate Reynolds number: Undulatory locomotion in the chaetognath *Sagitta elegans*. J. exp. Biol.163;119-137.

Krohn, M. M. and Boisclair, D. (1994). Use of a stereo-video system to estimate the energy expenditure of free-swimming fish. Can. J. Fish. Aquat. Sci. 51;1119-1127.

Lauder, G.V. (1989). Caudal fin locomotion in ray-finned fishes: Historical and functional analysis. Amer. Zool. 29;85-102.

Lauder, G.V. and Liem, K. F. (1983). The evolution and interrelationships of the actinopterygian fishes, Bull. Mus. Comp. Zool. Harvard Univ. 150: 95-197.

Lighthill, J. (1975). Mathematical Biofluiddynamics. Society for Industrial and Applied Mathematics, Philadelphia, PA.

Lighthill, J. (1977) Mathematical theories of fish swimming. In *Fisheries Mathematics*, (ed. J.H. Steele), pp. 131-144. Academic Press, New York, NY.

Liu, H., Wassersug, R. J. and Kawachi, K. (1996). A computational fluid dynamics study of tadpole swimming. J. exp. Biol. 199;1245-1260.

Long, J. H. Jr. (1992). Stiffness and damping forces in the intervertebral joints of blue marlin (*Makaira nigricans*). J. exp. Biol 162;131-155.

Long, J. H. Jr. (1995). Morphology, mechanics, and locomotion: the relation between the notochord and swimming motions in sturgeon. Environ. Biol. Fishes 44;199-211.

Long, J. H. Jr., McHenry, M. J., and Boetticher, N. (1994). Undulatory swimming: how traveling waves are produced and modulated in sunfish (*Lepomis gibbosus*). J. exp. Biol. 192;129-145.

Long, J. H., Jr., Pabst, D. A., Sheperd, W. R., and McLellan, W. A. (1997). Locomotor design of dolphin vertebral columns: bending mechanics and morphology of *Delphinus delphis*. J. exp. Biol. 200: 65-81.

Marchaj, C. (1988). Aero-Hydrodynamics of sailing. International Marine Publishing, Camden, Maine.

McCutcheon, C. W. (1971). Froude propulsive efficiency of a small fish, measured by wake visualization. In *Scale Effects in Animal Locomotion* (ed. T. J. Pedley), pp. 339-363. Academic Press, New York, NY.

McMahon, T. A. (1984). *Muscles, Reflexes, and Locomotion*. Princeton Univ. Press, Princeton, NJ.

Moy-Thomas, J. A. and Miles, R. S. (1971). *Palaeozoic Fishes*. Saunders, Philadelphia, PA.

Moyle, P. B. and Cech, J. J. (1996). Fishes: an introduction to ichthyology. Prentice Hall, Upper Saddle River, NJ.

Nursall, J. R. (1958). A method of analysis of the swimming of fish. Copeia 1958;136-141.

O'Brien, W.J., Evans, B.I. and Howick, G.L. (1986). A new view of the predation cycle of a planktivorous fish, white crappie (*Pomoxis annularis*). Can. J. Fish. Aquat. Sci. 43:1894-1899.

Pavlov, D.S., Skorobagatov, M.A., & Shtaf, L.G. (1982). The critical current velocity of fish and the degree of flow turbulence. Rep. USSR Acad. Sci. 267;1019-1021.

Schrank, A. L. (1997). Maneuverability of fish traversing tubes. MS Thesis, University of Michigan, School of Natural Resources and Environment, Ann Arbor, MI.

Shtaf, L.G., Pavlov, D.S., Skorobogativ, M.A. and Baryekian, A.S. (1983). Fish behaviour as affected by the degree of flow turbulence. Voprosy Ikhtiologii 3;307-317.

Symmons, S. (1979). Notochordal and elastic components of the axial skeleton of fishes and their function in locomotion. J. Zool. (Lond.) 189;157-206.

Videler, J. J. (1975). On the interrelationships between morphology and movement in the tail of the cichlid fish *Tilapia nilotica* L. Neth. J. Zool. 25;144-194.

Videler, J. J. (1993). *Fish Swimming*. Chapman & Hall, New York.

Vogel, S. (1994). *Life in Moving Fluids*. Princeton Univ. Press, Princeton, NJ.

Von Mises, R. (1945). *Theory of Flight*. Dover, New York, NY.

Wainwright, S. A. (1983). To bend a fish. In *Fish Biomechanics* (eds. P. W. Webb and D. Weihs)., pp. 68-91. Praeger, New York, NY.

Wainwright, S. A. (1988). *Axis and Circumference*. Harvard Univ. Press, Cambridge, MA.

Wainwright, S. A., Vosburgh, F. and Hebrank, J. H. (1978). Shark skin: function in locomotion. Science 202;747-749.

Wassersug, R. J. (1989). Locomotion in amphibian larvae (or "Why aren't tadpoles built like fishes?"). Amer. Zool. 29;65-84.

Webb, P. W. (1973). Kinematics of pectoral-fin propulsion in *Cymatogaster aggregata*. J. Exp. Biol. 59; 697-710.

Webb, P. W. (1976). The effect of size on the fast-start performance of rainbow trout (*Salmo gairdneri* Richardson) and a consideration of piscivorous predator-prey interactions. J. Exp. Biol. 65; 157-177.

Webb, P. W. (1979). Mechanics of escape responses in crayfish (*Orconectes virilis*, Hagen). J. Exp. Biol. 79; 245-263.

Webb, P. W. (1982). Locomotor patterns in the evolution of actinopterygian fishes. Amer. Zool. 22;329-342.

Webb, P. W. (1983). Speed, acceleration and manoeuverability of two teleost fishes. J. Exp. Biol. 102:115-122.

Webb, P. W. (1988a). Simple physical principles and vertebrate aquatic locomotion. Amer. Zool. 28;709-725.

Webb, P. W. (1988b). "Steady" swimming kinematics of tiger musky, an esociform accelerator, and rainbow trout, a generalist cruiser. J. Exp. Biol. 138;51-69.

Webb, P. W. (1991). Composition and mechanics of routine swimming of rainbow trout, *Oncorhynchus mykiss*. Can. J. Fish. Aquat. Sci. 48;583-590.

Webb, P. W. (1992). Is the high cost of body/caudal fin undulatory propulsion due to increased friction drag? J. exp. Biol. 162;157-166.

Webb, P. W. (1993). Is tilting at low swimming speeds unique to negatively buoyant fish? Observations on steelhead trout, *Oncorhynchus mykiss*, and bluegill, *Lepomis macrochirus*. J. Fish. Biol. 43;687-694.

Webb, P. W. (1994a). Exercise performance of fish. In *Advances in Veterinary Science and Comparative Medicine* (ed. J. H. Jones), 38B; p. 1-49. Academic Press, Orlando.

Webb, P. W. (1994b). The biology of fish swimming. In *Mechanics and Physiology of Animal Swimming*, (eds L. Maddock, Q. Bone, and J.M.V. Rayner), pp. 45-62. Cambridge University Press, Cambridge, UK.

Webb, P. W. (1997). Swimming. In *The Physiology of Fishes, 2nd. edition,* (Ed. D.D. Evans). CRC Press, Marine Science Series, Boca Raton, FL. *In press.*

Webb, P. W. and de Buffrenil, V. (1990). Locomotion in the biology of large aquatic vertebrates. Trans. Amer. Fish. Soc. 119;629-641.

Webb, P. W. and R. S. Keyes. (1981). Division of labor between median fins in swimming dolphin fish. Copeia 1981; 901-904.

Webb, P. W. and Smith, G. R. (1980). Function of the caudal fin in early fishes. Copeia 1980; 559-562.

Webb, P. W. and Weihs, D. (1986). Functional locomotor morphology of early life history stages of fishes. Trans. Amer. Fish. Soc. 115:115-127.

Webb, P. W. and Weihs, D. (1994). Hydrostatic stability of fish with swimbladders: Not all fish are unstable. Can. J. Zool. 72;1149-1154.

Webb, P. W., LaLiberte, G. D. and Schrank, A. J. (1996). Does body and fin form affect the maneuverability of fish traversing vertical and horizontal slits? Environ. Biol. Fish. 46;7-14.

Weihs, D. (1972). A hydrodynamic analysis of fish turning manoeuvers. Proc. R. Soc. Long. 182B:59-72.

Weihs, D. (1973). The mechanism of rapid starting of slender fish. Biorheology 10:343-350.

Weihs, D. (1989). Design features and mechanics of axial locomotion in fish. Amer. Zool. 29:151-160.

Weihs, D. (1993). Stability of aquatic animal locomotion. Contemp. Math. 141;443-461.

Wesneat, M. W., Hoesse, W., Pell, C. A., and Wainwright, S. A. (1993). The horizontal septum: mechanics of force transfer in locomotion of scombroid fishes (Scombridae: Perciformes). J. Morph. 217;183-204.

Westneat, M. W. (1996). Functional morphology of aquatic flight in fishes: kinematics, electromyography, and mechanical modeling of labriform locomotion. Amer. Zool. 36;582-98

Legends

Figure 1. Classification of linear and rotational perturbations. Slip or sway is a perturbation in the lateral direction, heave in the vertical direction, and surge in the longitudinal direction. Rolling is a rotational perturbation about the longitudinal axis, yawing about the dorso-ventral axis, and pitching about the transverse axis.

Figure 2. Basic propulsion and control surfaces arose early in the evolution of chordates and vertebrates. Amphioxus has many features that are believed to have been shared with a vertebrate ancestor, a flexible yet incompressible notochord supporting a post-anal tail which is responsible for all prolusion and control. Additional, initially multiple control surfaces and armor arose among agnathans, such as the heterostracans *Hemicyclaspis, Jamoytius, Anglaspis* and *Pteraspis* and the arthrodire *Climatius*. Early actinopterygians have radiated around an un-armored body, with a deep caudal fin, single dorsal fin and single anal fin, and paired pectoral and pelvic fins. These fish propulsors are also characterized by highly flexible fin webs with both self cambering and active fine control features. These are illustrated by the chondrosteans *Moythomasia, Phanerosteon, Pyritocephalus* and *Aedulla* and the holostean *Acentrophorus*.

Figure 3. The proportion of fishes from two species entraining on 19 mm diameter horizontal cylinders, similar in diameter to typical branches and root structures in their natural stream habitats. Observations were made at three temperatures. Performance by river chub (*Nocomis micropogon*) is independent of temperature. That of smallmouth bass (*Micropterus dolomieui*) is strongly temperature dependent, and comparable with chub only at 23 C. At this temperature, response latencies for powered control would be smallest. Similar results are found with 6.5, 13, and 25 mm diameter cylinders for chub, and for 13 mm diameter cylinders with bass. Bass would not entrain on 6.5 and 25 mm cylinders. The ability to entrain on cylinders in currents is a simple and effective assay for the fish stability performance.

Table 1. A summary of stability and maneuverability problems for aquatic vertebrates and general strategies for control.. Stability, or control of altitude, posture, and trajectory, uses hydrostatic lift, and dynamic and powered forces to correct perturbations. Maneuvers are self-generated perturbations driven primarily by dynamic and powered forces.

Control Problem	Perturbation	Correction or driving forces	Problems
Stability			
External perturbations			
Self-generated perturbations			
Altitude control	Depth changes (heave).	Hydrostatic lift	System is unstable: a) Gas inclusions in complaint chambers follow the ideal gas laws. b) Non-gaseous alternatives are energetically expensive. c) Center of mass usually below center of buoyancy.
Posture control	Heave, slip and surge. Roll, pitch and yaw.	Hydrostatic lift plus Dynamic forces Powered forces	
Trajectory control	Heave, slip and surge. Roll, pitch and yaw.	Inertial damping Dynamic forces Powered forces	Minimize response time to maximize rate of motor response. Match control forces to: a) inertia of virtual mass. b) over a range of speeds. c) for a range of sizes.
Maneuver			
Self-generated perturbations	Controlled perturbation	Dynamic forces Powered forces	

Table 2. A summary of design features of aquatic vertebrates used for stability, posture control and maneuvering, compared with common features of human engineered underwater vehicles.

	Aquatic Vertebrates	Engineered Vehicles
Engine	Highest performance powered by myotomal muscle mass.	Increase engine size to increase performance.
	Muscles = numerous linear actuators in series and parallel. Propulsive elements oscillate.	Rotary drives. Control surfaces oriented with worm and hydraulic drives.
Propulsor Forces	Reduced frequency >0.2 when acceleration reaction always affects thrust production.	Reduced frequency <<0.2 when acceleration reaction not important.
	Similar tissue and water densities result in large acceleration reaction relative to inertial resistance.	
	Lift commonly used for control and most important control force for larger, faster animals.	Lift usual force used for prolusion and control.
	Drag used for thrust and generated for braking.	Drag avoided (except for row boats).
Dynamic Control	Fins of all axial and appendicular systems and body shape.	Rudders, hydroplanes.
	Most commonly used and economical self-correcting system at moderate to high speeds.	
Powered Control	Fins of all axial and appendicular systems.	Rudders in propeller wash, bow thrusters, auxiliary tugs etc.
	Multiple propulsors provide stable trajectories.	Hull design major contributor to platform stability.
	Powered control used at low speeds and is essential to achieve the high maneuverability.	
Dynamic and Powered Control	Simultaneous use of dynamic and powered devices for stability, posture and maneuverability.	Control and propulsion systems usually separate.
	Largest control and turning moments derive from flexibility of body	Rigid structures usual.
Redundancy:	Multiple muscle fibers crossing several joints.	
	Oscillatory fins generate volume and areal forces.	
	Multiple propulsors and control surfaces.	
	Each propulsors functions as both variable aspect thrust and control generators.	Control and propulsion systems usually separate.
Specialization	Specialized designs used for narrow ranges of tasks.	
Volume	Design performance characteristics with respect to volume/mass/payload of body	
Response latency:	Actual latencies may limit the distribution of powered control systems to less turbulent situations.	Rapid response systems available.

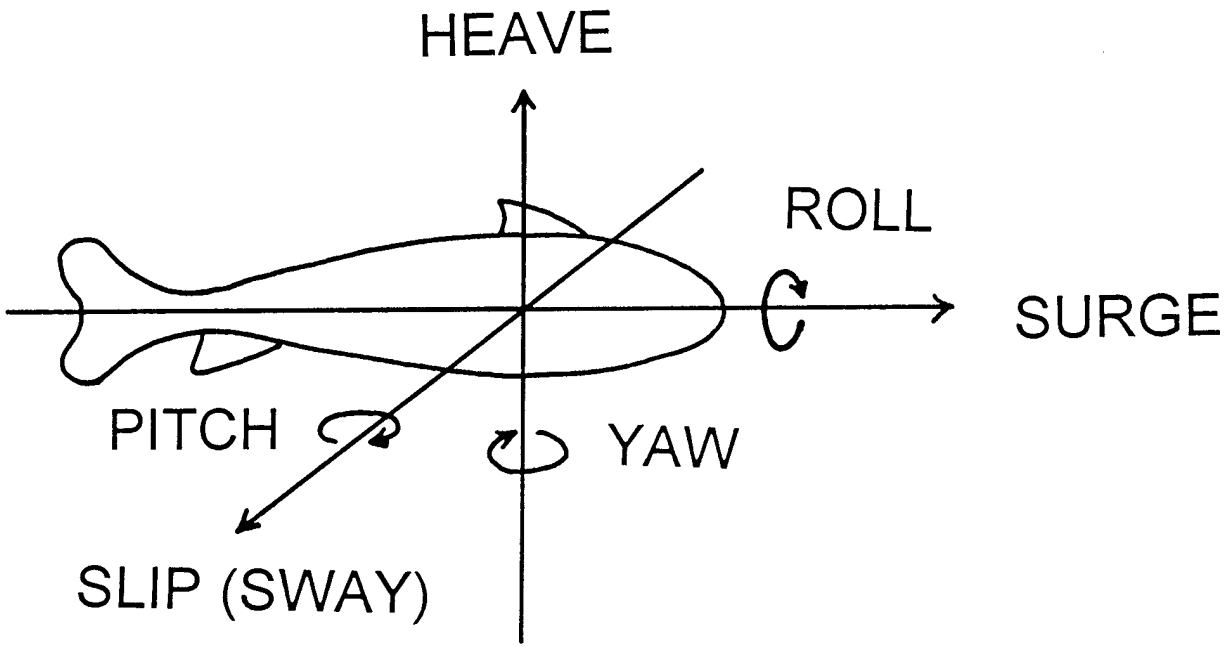
HEAVE
ROLL
SURGE
PITCH
YAW
SLIP (SWAY)

amphioxus

Hemicyclaspis

SILURIAN

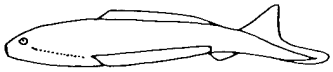

Jamoytius

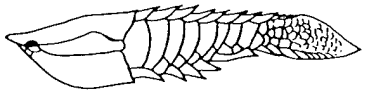

Anglaspis

Climatius

DEVONIAN

Pteraspis

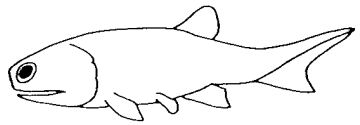

Moythomasia

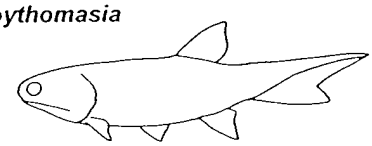

Phanerosteon

CARBONIFEROUS

Pyritocephalus

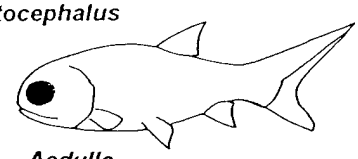

Aedulla

PERMIAN

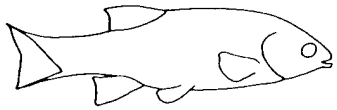

Acentrophorus

BIOLOGICAL DESIGNS FOR ENHANCED MANEUVERABILITY: ANALYSIS OF MARINE MAMMAL PERFORMANCE

Frank E. Fish

Department of Biology
West Chester University
West Chester, PA 19383 USA

Abstract - Maneuverability is critical to the performance of autonomous underwater vehicles (AUV) and fast swimming marine mammals which use rapid turns to catch prey. Overhead video records were analyzed for seven cetacean species (29-4536 kg) and sea lions (88-138 kg) turning in the horizontal plane. Powered and unpowered turns were executed by body flexion in conjunction with use of control surfaces, including flukes, flippers, dorsal fin, and caudal peduncle. Banking was used in powered turns and in unpowered turns where major control surfaces were horizontally oriented. Turning radius was dependent on body mass and swimming velocity. Relative minimum radii were 9-17% of body length and were equivalent for pinnipeds and cetaceans. However, *Zalophus* had smaller turning radii at higher speeds than cetaceans. Rate of turn was inversely related to turn radius. The highest turn rates were observed in *Lagenorhynchus* at 453 deg/s and *Zalophus* at 690 deg/s. Centripetal acceleration measured over 3 *g* for small cetaceans and 5.1 *g* for *Zalophus*. While cetaceans are configured for stability, otariid pinnipeds use their relatively large area flippers to produce increased instability with greater turning performance. This work was supported by the Office of Naval Research.

INTRODUCTION

An important consideration in the performance of autonomous underwater vehicles (AUV) is the ability to maneuver or turn. Rapid turns with small radii while maintaining speed are paramount to quickly locating objects, avoiding obstructions in confined and complex environments, and maintaining stability. Animal performance in terms of maneuverability can be superior to manufactured underwater vehicles [1]. Animals, therefore, can serve as effective model systems in exploring body and control surface designs which can be introduced into the design of AUVs to foster increased maneuverability.

Animals rarely move continuously in straight lines. This is especially true in instances where potential prey must out-maneuver a predator or the reverse for a predator to turn fast enough to catch its prey [2, 3]. In addition, the search patterns employed by animals use continuous turning maneuvers. Even the largest of all animals, whales, display considerable proficiency in their maneuverability [4]. Various morphologies within animal lineages have evolved which foster maneuverability. Within the marine mammals there are divergent body designs that suggest differences in turning performance. Of the fastest swimming marine mammals, the pinnipeds (e.g., sea lions, seals) and cetaceans (e.g., whales, dolphins) display considerable variation in both their morphology and propulsive mode [5].

To understand how variation in the morphology of marine mammals can affect maneuverability, consideration should be given to parameters associated with stability. In that maneuverability represents a controlled instability, the possession of morphological characters that deviate from a

design which maintains stability is expected to enhance turning performance. Based on analysis of aerodynamics, the following features are associated with stability [6, 7]:

1. Control surfaces located far from the center of gravity

2. Concentration of control surface area posterior of center of gravity

3. Anterior placement of center of gravity

4. Dihedral of control surfaces

5. Sweep of control surfaces

6. Reduced motion of control surfaces

7. Reduced flexibility of body

If we compare the placement and design of control surfaces on sea lions and cetaceans (Fig. 1), we see marked differences between the two groups. The control surfaces of sea lions are represented by fore- and hindflippers with the larger foreflippers near the center of gravity. Because of the high mobility of the foreflippers, both the sweep and the dihedral of the flippers is variable. For the cetaceans, the flippers, flukes, dorsal fin, and caudal peduncle are the control surfaces with the more mobile surfaces distance from the center of gravity. The flippers, flukes, and dorsal fin, when present, can be highly sweep, particularly in the faster species.

Flexibility in the body of cetaceans is generally constrained [8]. In comparison, pinnipeds display significant axial flexibility [9].

Comparison of the morphology between pinnipeds and cetaceans suggests the whales and dolphins have a more stable design than marine mammals such as sea lions. Therefore, it is predicted that pinnipeds will be more highly maneuverable compared to cetaceans.

MATERIALS AND METHODS

To study variation in maneuverability based on differing body and control surface morphologies and propulsive modes, I examined the turning performance of eight species of marine mammals (seven cetaceans, one pinniped) with different swimming capabilities. All were captive animals which were maintained in pools at various research and zoological facilities including Sea World, Pittsburgh Zoo, and Long Marine Laboratory of the University of California Santa Cruz.

For the cetaceans, these included the bottlenose dolphin (*Tursiops truncatus*), killer whale (*Orcinus orca*), Commerson's dolphin (*Cephalorhynchus commersonii*), Pacific white-sided dolphin (*Lagenorhynchus obliquidens*), false killer whale (*Pseudorca crassidens*), beluga (*Delphinapterus leucas*), and Amazon river dolphin (*Inia geoffrensis*). *Orcinus* was the largest cetacean with one individual of 4536 kg; whereas the smallest at 29 kg was *Cephalorhynchus*. *Pseudorca* and *Lagenorhynchus* are regarded generally as fast swimmers; whereas, *Delphinapterus* and *Inia* are considered to be slow swimmers. *Delphinapterus* and *Inia* are different from the other cetaceans by possessing mobile necks and flippers. *Inia* is capable of a notable degree of lateral flexion. In addition, the dorsal fin is reduced in *Inia* or absent in *Delphinapterus*. The cetaceans all use oscillations of the caudal flukes in the vertical plane for propulsion [4, 5]. Analysis of maneuverability has not been performed previously.

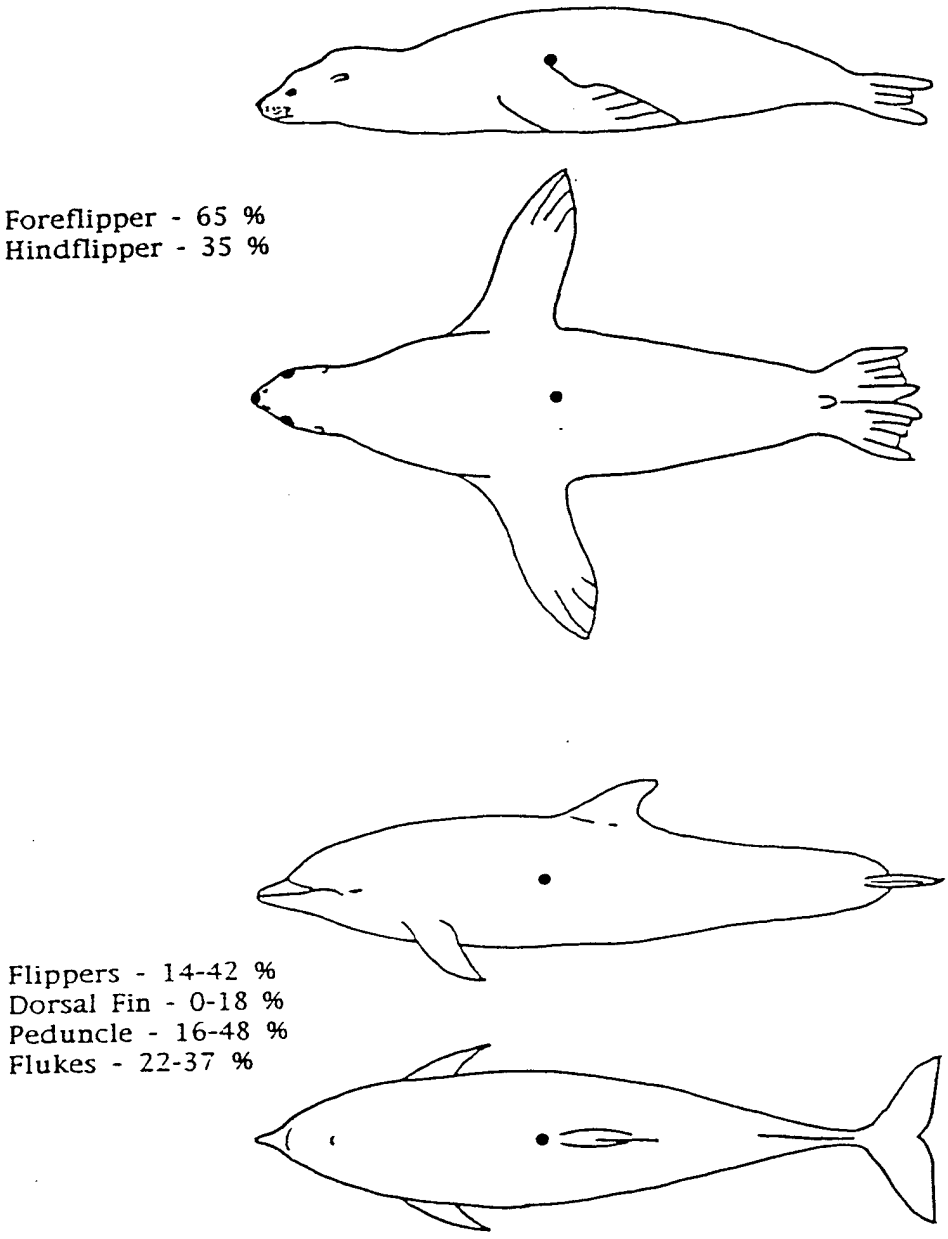

Fig. 1. Dorsal and lateral outlines of a pinniped (*Zalophus californianus*) and a cetacean (*Tursiops truncatus*) comparing the position, design and planar area of the control surfaces (e.g., flippers, flukes, dorsal fin, caudal peduncle). Percentage of area control surface area is provided. Percentage ranges are given for cetaceans examined in this study. The black circle on each drawing indicates the position of the center of gravity.

The single pinniped species was represented by the California sea lion (*Zalophus californianus*). This animal swims by oscillations of the paired foreflippers [5]. Analysis of turning performance was restricted previously to descriptions of gross movements of the body and appendages during turning [10, 11], but no data were collected on performance capabilities.

Animals were videotaped with a camcorder (Panasonic DV-510) as they executed turning maneuvers at or near the water surface under the direction of their trainers. These maneuvers were observed through a glass wall for a lateral view underwater to detail the motion of the control surfaces. To collect data on turning performance (e.g., radius, turning rate), a dorsal view of the turn was recorded by positioning the video camera above the animal's pool. Distance above the pool varied with the physical layout of the facility and size of the animal. Vertical distance of the camera and observer over the water surface ranged from approximately 2 m to 10 m. Prior to swimming trials, animals were measured and marked with zinc oxide dots, which served as reference points and scale. One marker was placed at the approximate position above or lateral to the center of gravity.

Video records of the dorsal view were analyzed frame-by-frame at 30 Hz with a video recorder (Panasonic AG-7300). Only those records were used in which the animal's body remained horizontal through the turn. The sequential positions of the center of gravity marker were recorded onto transparencies from the video monitor. The center of rotation of the turn was determined geometrically. This technique allowed for determination of the trajectory of the center of gravity, despite distortion in observing the actual position of the marker due to refraction from surface waves. Turning radius, r, and average velocity, v, were measured, and centripetal acceleration, a_C, in gs was computed according to:

$$a_C = v^2/r\ 9.8. \qquad (1)$$

Angular displacement was used to calculate the turning rate in deg/s.

RESULTS

Observations of cetaceans showed two turning patterns: powered and unpowered. Powered turns were defined as turns in which the animal was continuously propelling itself by the dorso-ventral oscillations of the flukes; whereas in unpowered turns, the animal glided through the turn without apparent use of the caudal propulsor. Turns were initiated from the anterior of the animal with lateral flexion of the head and rotation of the flippers into the turn. The flippers also were adducted. During unpowered turns, substantial lateral flexion of the peduncle was observed in addition to twisting at the base of the flukes. The twisting action depressed the inner fluke tip. Some inward banking was observed during unpowered turns. Oscillation around the longitudinal axis occurred during powered turns that were associated with the propulsive fluke motions and produced a rolling movement.

Both *Inia* and *Delphinapterus* proved to be exceptions to the general cetacean turning pattern. *Inia* showed no tendency to bank during turns, instead using its flexible body to produce the turn. *Delphinapterus*, without a dorsal fin, would bank 90° with its ventral surface facing into the turn.

Zalophus used only unpowered turns. As previously described [11], The anterior end of the animal initiates the turn as the sea lion rolls 90° so that the ventral (abdominal) surface faces the outside of the turn. The body is flexed dorsally. The fore- and hindflippers are abducted and held in the vertical plane. This maneuver brings the full area of the flippers into use. In addition, the position of the foreflippers is set to execute a power stroke and accelerate the sea lion as it comes out of the turn.

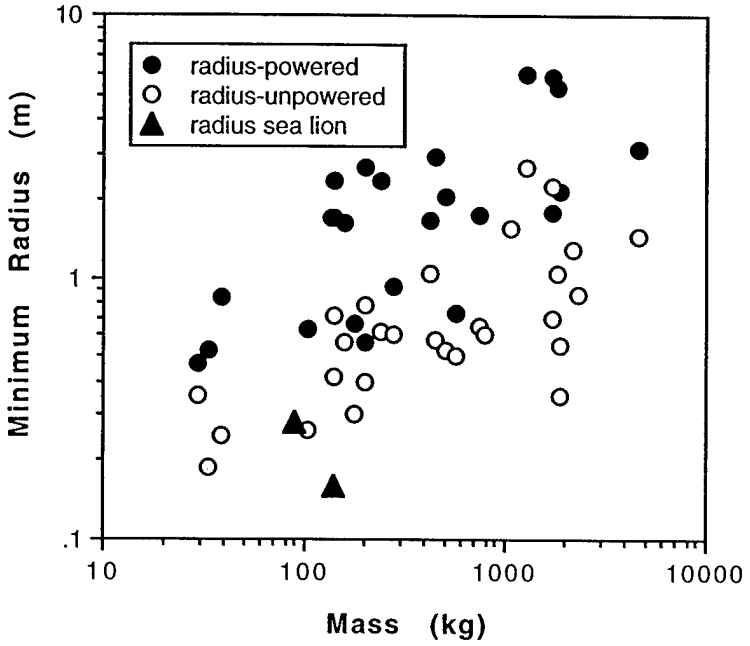

Fig. 2. Minimum turning radius plotted against body mass for individuals. Circles represent cetaceans for powered and unpowered turns and triangles represent *Zalophus*.

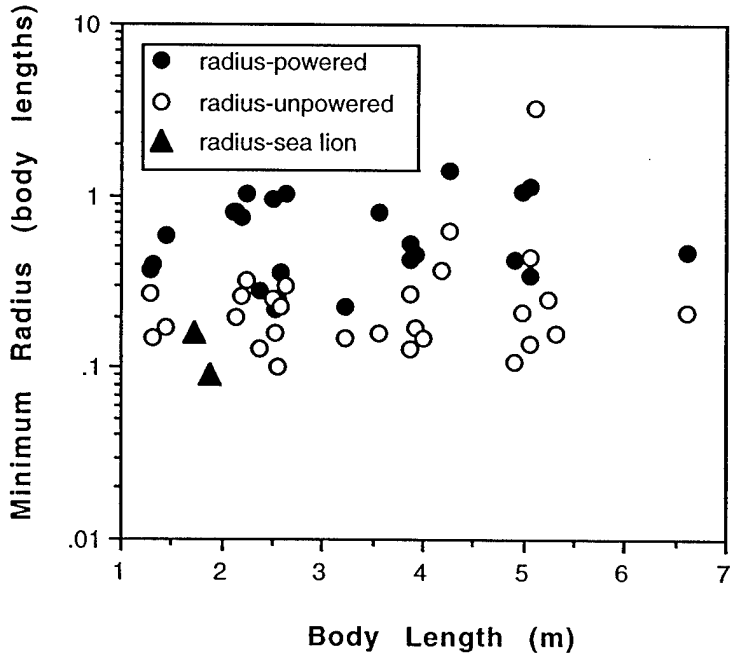

Fig. 3. Minimum length-specific turning radius plotted against body length for individuals. Circles represent cetaceans for powered and unpowered turns and triangles represent *Zalophus*.

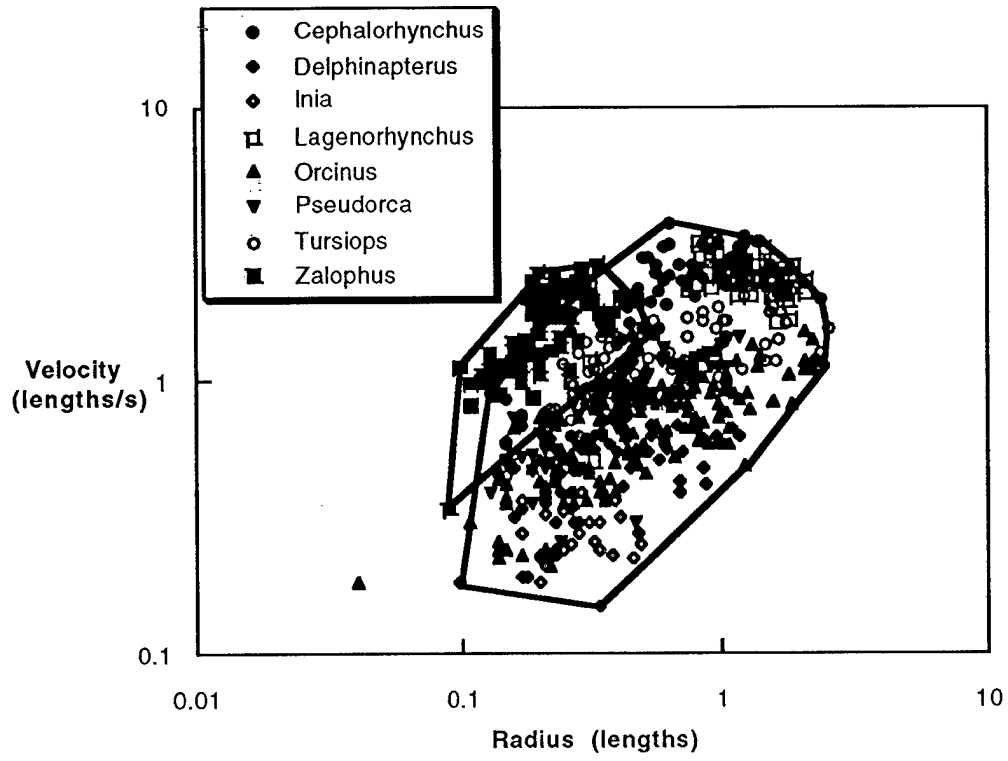

Fig. 4. Average length-specific velocity in relation to length-specific turning radius. Polygons are drawn around data for cetaceans and around data for *Zalophus*. The single point outside the cetacean polygon represents a 1725.2 kg, 5.05 m *Orcinus* which was able to produce a turn radius of 4 % of body length by ventrally flexing the posterior half of the body The flukes were used to pivot the animal around its longitudinal axis.

The force necessary to maintain a curved trajectory of a given radius is directly related to the square of the velocity and the mass of the body [12]. Indeed, minimum turning radius plotted for individuals was associated with body mass (Fig. 2). Unpowered turns for cetaceans had smaller minimum radii than powered turns for the same individuals. When scaled to body length, cetaceans generally demonstrated minimum unpowered turning radii of < 50% of body length (Fig. 3). Minimum radii within each species ranged from 11 to 17% of body length. These results are comparable to maneuvers by fish and penguins [1, 3, 13, 14].

Minimum unpowered turn radii for the two individuals of *Zalophus* were 0.16 and 0.28 m, representing 9 and 16% of body length, respectively. While the length-specific radii were small, they were not substantially different from similar values for cetaceans (Fig. 2, 3).

However, different levels of performance between species were indicated when all the data for turning radius were plotted as a function of velocity (Fig. 4). The cetaceans displayed varying capabilities. *Inia* and *Delphinapterus* produced low-speed, small radius turns. Faster speed but larger radius turns were performed by *Lagenorhynchus* and *Cephalorhynchus* and intermediate performance was displayed by *Orcinus*, *Pseudorca* and *Tursiops*. *Zalophus* was able to make small radius turns while at high speed (up to 4.5 m/s).

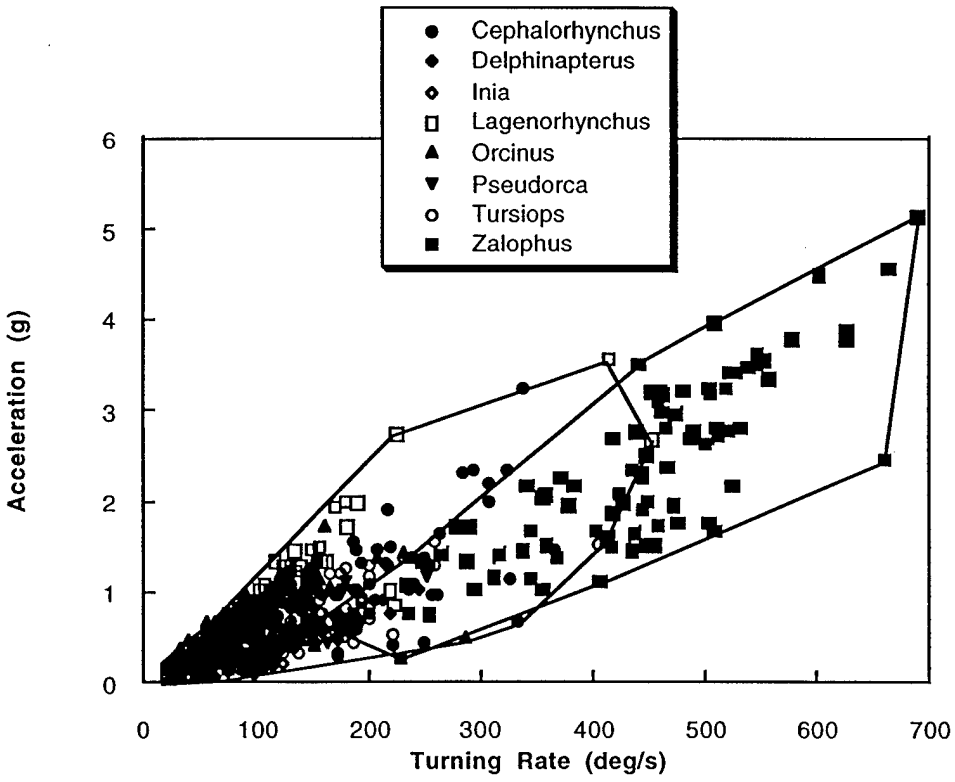

Fig. 5. Relationship between centripetal acceleration and turning rate. Polygons are drawn around data for cetaceans and around data for *Zalophus*.

The performance limits for turning are illustrated in Fig. 5 by a plot of centripetal acceleration and turning rate. Most data for cetaceans is clustered at accelerations < 1.5 *g* with turning rates < 200 deg/s. Individuals of *Cephalorhynchus* and *Lagenorhynchus* were able to exceed these lower values for cetaceans with *Lagenorhynchus* displaying the maximum performance with an acceleration of 3.6 *g* and turning rate of 453 deg/s during unpowered turns. However, *Zalophus* typically exceeded even these maximal performances by cetaceans. One animal was able to execute a 5.13 *g* turn at 690 deg/s.

With the exception of high-performance aircraft (e.g., F-15, F-16) marine mammals meet or exceed the centripetal accelerations of manufactured devices (Fig. 6). However, *Zalophus* was able to achieve an acceleration greater than that experienced during lift-off on the space shuttle, whereas, *Lagenorhynchus* and *Cephalorhynchus* with maximum centripetal accelerations of approximately 3 *g* were equivalent. Other cetaceans exhibited generally lower performance, although still higher than small underwater vehicles [1]. The lowest centripetal accelerations occurred in *Inia* followed by *Delphinapterus* which both swam slowly during testing.

Marine mammals generally show a high level of performance with regard to turning. This performance, however, varies between species and between major taxonomic groups relating to the ecology and the morphology of the animals. Maneuverability by marine mammals is dependent on body size, body stiffness and use of control surfaces. The body stiffness and position and size of the control surface, in particular, determine the stability of the animal when swimming. The sea lion, *Zalophus*, exhibits few adaptations for stability and is able to execute tighter turns at higher rates than cetaceans. The highly flexible body and mobile control surfaces (e.g., fore- and hindflippers) aid in rapidly producing instability for turning. The large area of the flippers aid during the turn by preventing side-slip [11].

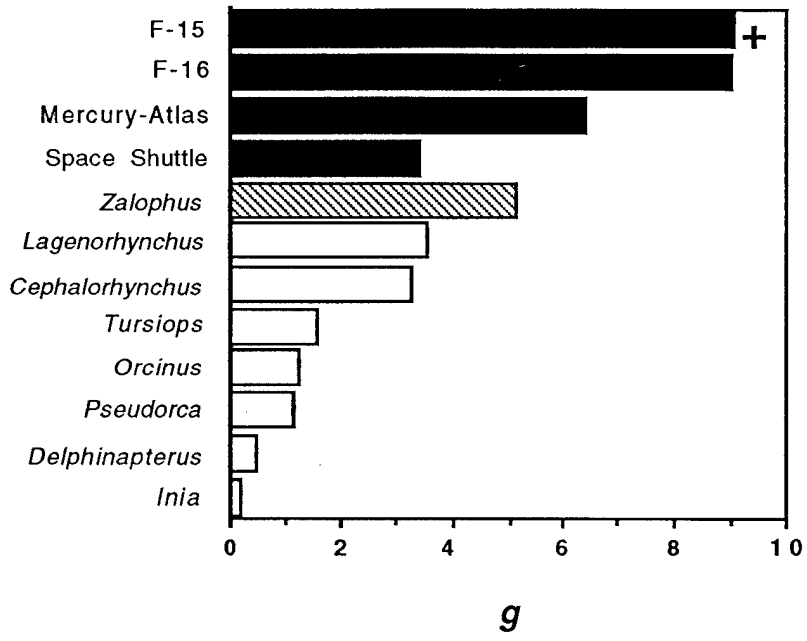

Fig. 6. Comparison of centripetal accelerations, *g*, of high-performance crafts and marine mammals.

Conversely, cetaceans have a morphology that enhances stability thereby constraining turning performance. Cetaceans with flexible bodies and mobile flippers (e.g., *Inia, Delphinapterus*) sacrifice speed for maneuverability, whereas species with more restricted morphologies (e.g., *Lagenorhynchus, Cephalorhynchus*) produce faster but wider turns. The dual function of the caudal appendages for both turning and propulsion presents a restriction to simultaneously maintain high speed during tight turns. To produce a small turn radius, cetaceans must use unpowered maneuvers which uncouples the control surfaces from thrust production and limits speed and acceleration after the turn. During unpowered turns, the peduncle and flukes are diverted from their propulsive orientation and used like a rudder.

The enhanced maneuverability of sea lions thus allows them to operate in restricted, in-shore waters with complex environments, whereas the more stable design of cetaceans limit these animals to swimming and foraging in more pelagic habitats. In addition, the limitations of the cetacean design may be a causative reason for the use of cooperative foraging behaviors by whales and dolphins.

The potential scientific and technological significance of this research is an understanding of the basic turning performance by large aquatic organisms and the use and design of control surfaces. The morphology and turning performance displayed by marine mammals suggest future avenues for the design of faster and more highly maneuverable autonomous underwater vehicles (AUV).

ACKNOWLEDGMENT: I gratefully acknowledge the cooperation and assistance of the personal associated with this project from Sea World, University of California Santa Cruz, Pittsburgh Zoo, Smithsonian Institution, Brown University, and West Chester University. This work was sponsored by ONR under grant #N00014-95-1-1045.

REFERENCES

[1] Bandyopadhyay, P. R., J. M. Castano, J. Q. Rice, R. B. Philips, W. H. Nedderman, and W. K. Macy. 1997. Low-speed maneuvering hydrodynamics of fish and small underwater vehicles. Trans. ASME 119: 136-144.

[2] Howland, H. C. 1974. Optimal strategies for predator avoidance: The relative importance of speed and manoeuvrability. J. theor. Biol. 47: 333-350.
[3] Webb, P. W. 1983. Speed, acceleration and manoeuvrability of two teleost fishes. J. exp. Biol. 102: 115-122.
[4] Fish, F. E., and J. M Battle. 1995. Hydrodynamic design of the humpback whale flipper. J. Morph. 225: 51-60.
[5] Fish, F. E. 1996. Transitions from drag-based to lift-based propulsion in mammalian swimming. Amer. Zool. 36: 628-641.
[6] Weihs, D. 1993. Stability of aquatic animal locomotion. Cont. Math. 141: 443-461.
[7] Smith, H. C. 1992. Illustrated Guide to Aerodynamics. McGraw-Hill, Blue Ridge Summit, PA.
[8] Long, J. H., Jr., D. A. Pabst, W. R. Shepherd, and W. A. McLellan. 1997. Locomotor design of dolphin vertebral columns: Bending mechanics and morphology of *Delphinus delphis*. J. exp. Biol. 200: 65-81.
[9] Gal, J. M. 1993. Mammalian spinal biomechanics. I. Static and dynamic mechanical properties of intact intervertebral joints. J. exp. Biol. 174: 247-280.
[10] English, A. W. 1976. Limb movements and locomotor function in the California sea lion (*Zalophus californianus*). J. Zool., Lond. 178:341-364.
[11]Godfrey, S. J. 1985. Additional observations of subaqueous locomotion in the California Sea Lion (*Zalophus californianus*). Aqu. Mamm. 11:53-57.
[12] Weihs, D. 1981. Effects of swimming path curvature on the energetics of fish motion. Fish. Bull. 79: 171-176.
[13] Domenici, P, and R. W. Blake. 1991. The kinematics and performance of the escape in the angelfish (*Pterophyllum eimekei*). J. exp. Biol. 156: 187-205.
[14] Hui, C. A. 1985. Maneuverability of the Humbolt penguin (*Spheniscus humboldti*) during swimming. Can. J. Zool. 63: 2165-2167.

Manueuverablity and Reversible Propulsion: How Eel-Like Fish Swim Forward and Backward Using Traveling Body Waves

John H. Long, Jr.[1], William Shepherd[2], and Robert Root[3]

[1]Department of Biology, Vassar College, Poughkeepsie, NY 12604, USA.
[2]Steinhart Aquarium, California Academy of Sciences, San Francisco, CA 94118, USA.
[3]Department of Mathematics, Lafayette College, Easton, PA 18042, USA.

Abstract

Anguilliform, or eel-like, swimmers can reverse the direction of their axial undulatory wave and swim backward. The goals of this work were to (1) compare the kinematics of forward and backward swimming and to (2) determine how these maneuvers are controlled by the axial musculature. We used high-speed video (500 images per second) to record forward and backward maneuvers in the American eel. Quantitative analysis of the motion of the reconstructed axial midline revealed that backward swimmers increase the lateral displacement and the midline flexion throughout the body. Increased midline flexion suggests that the body is able to lower its flexural stiffness when swimming backward. We tested the ability of the caudal musculature to control these changes by sinusoidally bending freshly-killed eels, stimulating their muscles, and measuring changes in the body's flexural stiffness, damping, and work. The muscles can triple the body's flexural stiffness and can generate seven times the work needed to bend the body alone. A dynamic model relating flexural stiffness and muscle work predicts that changes in the relative timing of the onset of muscle activity and local muscle strain would permit the eel to reduce body stiffness as required to swim backward.

Introduction

Anguilliform, or eel-like, fishes use most of the length of their slender bodies for propulsion and, in doing so, display a remarkable range of locomotor maneuvers, all of which are modulated by changes in the body's axial wave of bending. For example, American eels, *Anguilla rostrata*, migrate long distances, feed by spinning about their long axis, move over land, burrow, and swim forward and backward. The latter behavior — forward and backward swimming — is the focus of this study, since understanding how it is produced mechanically gives us insight into the design and control of reversible propulsion and translational maneuverability. Thus, we have two goals: (1) to quantify the undulatory motions of steady forward and backward swimming, and (2) to determine how locomotor muscles operate within the body to modulate bending properties and mechanical power output in order to reverse direction.

In locomoting vertebrates, our view of muscle function has been altered by examining dynamic, time-dependent mechanical behaviors. For example, from measurements of muscle activity patterns (electromyography, "emg") during flight, wing muscles in doves are now believed to operate as accelerators and decelerators, rather than as elevators and depressors (Dial, 1992). Furthermore fish activate the axial muscles as they lengthen, which suggests that these muscles produce negative mechanical work (Altringham et al., 1993; Johnson et al., 1994; Johnston et al., 1995). By forcefully resisting changes in shape, negative work can function to dynamically alter body stiffness (Long & Nipper, 1996), and such changes can alter the motions of undulatory swimming as predicted by mechanical theory (Long et al., 1996; McHenry et al., 1995).

Using whole-body work loops, a technique in which a freshly dead and intact fish is bent while its muscles are electrically stimulated *in situ*, active muscle increased the body stiffness of a largemouth bass by 6 %, a value that likely underestimates the capacity for change since only parts of several myomeres were being stimulated (Long &

Nipper, 1996). Greater change is expected on the basis of mechanical theory: fish should use their muscles to increase body stiffness several-fold with increasing swimming speeds in order to match their body's natural frequency to the higher tail-beat frequency needed to increase the hydrodynamic rate of working (Long & Nipper, 1996). Evidence that the mechanics of swimming are influenced in a manner consistent with this theory comes from experimental changes in the passive (without muscle stimulation) body stiffness of swimming sunfish models (McHenry et al., 1995), swimming sunfish bodies driven by electrically-stimulated muscles (Long et al., 1994), and live gar swimming with surgically-altered skin (Long et al., 1996).

Understanding the possible mechanical functions of muscle within the intact body is necessary for accurate modeling of undulatory swimming. *In vitro* single-fiber experiments (Josephson, 1985), in which individual fibers or small bundles of fibers are removed from the animal and strained and stimulated as measured *in vivo*, have demonstrated that the mechanical performance of isolated muscle fibers of fish varies with changes in strain, strain rate, stimulus pattern, fiber type, acclimation temperature, and body position (Altringham & Johnston, 1990; Altringham et al., 1993; Coughlin & Rome, 1996; Coughlin et al., 1996; Curtin & Woledge, 1993a; 1993b; Johnson & Johnston, 1991; Johnson et al., 1994; Johnson et al., 1993; Johnston et al., 1995; Rome & Swank, 1992; Rome et al., 1993). Missing is how the performance of these fibers would be altered, if at all, when operating as part of the whole body, with its complex muscle architecture (Spierts et al., 1996; Westneat et al., 1993), intra-muscular pressure (Wainwright et al., 1978), variable neural activation patterns (Jayne & Lauder, 1993, 1994, 1995 a & b, 1996), and serial and parallel elastic structures such as backbone (Long, 1992, 1995), skin (Hebrank, 1980; Long *et al.* 1996), and myotomes (Westneat et al., 1993). Theoretically, in swimming animals the stiffness and arrangement of elastic elements should determine the output of various patterns of muscle activity (Alexander, 1988; Bennett et al., 1987; Blickhan & Cheng, 1994; Ettema, 1996; Jordan, 1996; Pabst, 1996).

Methods

Experimental animals

We used American eels for these experiments because they, their European congeners, *Anguilla anguilla*, or other eel-like swimmers have been the focus of studies on undulatory kinematics (Gillis, 1996; Gray, 1933; Williams et al., 1989), neural control of muscle activity (Gray 1936a, 1936b, Grillner & Kashin, 1976), hydrodynamics (for review see Lighthill, 1975), and swimming mechanics (Bowtell & Williams, 1991; Hebrank, 1980). Furthermore, during steady swimming it appears that both red and white muscle are simultaneously active (Grillner & Kashin, 1976), a pattern easily mimicked in our whole-body work loop experiments by direct and simultaneous electrical stimulation of left- and right-sides of the body musculature. Female eels were captured in traps in the freshwater region of the Hudson River at the Norrie Point Environmental Site in October and November, 1995. They were held indoors in aquaria for one year with a 12:12 hour light:dark cycle and water temperatures fluctuating from 18 to 22° C. All experiments were conducted at 20° C. Eels were fed live fish, a diet which required active foraging, thus ensuring daily exercise. Individuals were tested once grown to a size amenable for these experiments (Table 1).

Table 1. *Morphological features of the eels used in the bending experiments.*

Feature	Mean (± s.d.)
L_b, total length (m)	0.28 (0.063)
Total weight (kg)	0.03390 (0.02515)
Position of section (% L_b)	0.70 (0.010)
Myomeres in test section	3
Joints in test section	4
L, test section length (m)	0.0065 (0.00227)
Test section width (m)	0.0070 (0.00280)
Test section height (m)	0.0119 (0.00355)
Max. midline curvature (m^{-1})	25.4 (10.99)
Max. bending, each joint (°)	1.06°
Transverse area ($m^2 \times 10^{-5}$)	7.09 (4.141)
Section volume ($m^3 \times 10^{-7}$)	5.24 (3.826)
ε, maximal muscle strain	0.079 (0.0064)

All procedures in this study were approved by the Institution Animal Care and Use Committee of Vassar College.

Swimming kinematics

Swimming sequences in both directions were captured at 500 images per second using a high speed video system (Kodak Ektapro model 1000E). The ventral surface of each fish was filmed through the glass bottom of a still-water tank. The tank was backlit by a 500 W halogen light directed through a sheet of 0.5 cm white acrylic in order to make clear, high contrast images. A 10 x 10 cm square grid was placed in the video field for calibration of the digitized image. We analyzed only those swimming sequences where fish swam in a straight line at constant velocity for at least two complete tailbeat cycles.

Digital video images were downloaded to super VHS videotape. Midlines of the fish were digitized from the video by overlaying a paused video image (Sony model SVO-9500-MDR-1 SHVS video deck) onto a computer screen (Apple model Macintosh Iifx) via a video genlock (Digital Vision model Televeyes Pro). From within a software program (NIH Image), a series of twenty points on the fish's midline was manually plotted for twenty frames per tailbeat cycle. For each midline, a custom cubic spline routine (Jayne & Lauder, 1993) was used to construct a backbone of 19 segments of equal length. From each series of reconstructed midlines, we measured swimming velocity (body lengths, L_b, per second), tailbeat frequency (Hz), lateral amplitude ($\%L_b$), propulsive wavelength ($\%L_b$), and flexion (°) at each of 18 intervertebral joints.

To calculate the swimming speed, we computed the mean x and y points of the twenty digitized coordinates for each time frame. The displacement of the mean x and y through time yielded the average displacement of the fish, from which average velocity could be computed. Tailbeat frequency was defined as the number of complete left-right-left cycles of the tail tip occuring per second. Maximum lateral amplitudes were calculated at the head and tail tip and at four of the eighteen joint positions — 3, 7, 12, and 16. These positions were chosen for the following reasons: we can compare anatomical positions between forward and backward swimming or we can compare hydrodynamic positions; *e.g.*, point 3 forward corresponds to point 16 backward; point 7 forward to point 12 backward. One half of the maximum side-to-side motion was taken as the amplitude. Maximum midline flexion was calculated at each of these four joints (3, 7, 12, 16) as the angular deviation from a straight line.

Muscle experiments

We conducted whole-body work loop experiments (Long & Nipper, 1996), a method which combines techniques from the half-myotome stimulation (Johnsrude and Webb, 1985) and *in vitro* work loop (Josephson 1985) procedures. Each of three eels was anaesthetized with tricaine (1:10,000 dosage); each then had its spinal cord transected below the medulla in order to avoid static undulatory posture (Gray, 1936a). The body was mounted so that a small section of the mid-caudal region — midway between the cloaca and the posterior margin of the caudal fin at a relative axial position of 70.0 % (± 0.26, S.E.M.) total body length, L_b, from the tip of the rostrum — was left free to bend laterally. The mid-caudal region was chosen because the muscles in this region may generate negative work in some species (Wardle et al., 1995) and because, in eels, it is one position from which muscle activity patterns were measured (at 72.4 % L in a 41.1 cm L eel, Grillner & Kashin, 1976; and at 75 % L by Gillis, pers. comm.). The mounts were made of aluminum pipe of 1.56 cm inner diameter; the anterior and posterior sections of the eel's body, relative to the targeted bending mid-caudal section, was inserted into each pipe and held in place by a pin inserted through holes in each pipe and then through the eel. Lateral movement of the eel was restricted by inserting, between the eel and the pipe walls, air-injected styrene particles (packing material). The styrene, if compressed while inserted, would expand and hold the eel snugly in place with the gripping force evenly distributed circumferentially and axially.

The two mounts were clamped to the oscillating and stationary sections of the dynamic

bending machine; the anterior margin of the bending section was aligned with the bending axis. This configuration approximates that of a cantilevered beam with a bending couple at one end. At static equilibrium, the flexural stiffness, EI (Nm^2), of the beam is given by the following formula (Stevens, 1987):

$$EI = \frac{CL}{\theta_{max}} \quad (1)$$

where θ is the angular deflection (° or rad), C is the bending couple (Nm), L is the length of the beam (m), E is the Young's modulus (Nm^{-2}), and I is the second moment of area (m^4). The two latter terms represent the contributions of material and shape, respectively, and are often measured as the composite, EI, for anisotropic, heterogeneous structures.

The body section was bent sinusoidally at a frequency of 3 Hz, which corresponded in similarly sized eels to tailbeat frequencies used during steady swimming. Collinear with the lateral bending axis at the anterior margin of the bending section was an angle sensor (RVDT, rotary variable differential transducer, Shaevitz model R30D); the bending moment, M (Nm) transmitted through the test section was transduced using two foil strain gauges (Omega Engineering, 120 Ω) mounted on the cantilevered steel support of the stationary grip. This half-bridge configuration was excited at 5 VDC using a 40 kHz bridge amplifier (Omega Engineering, model DMD-520). The bending moment transducer was calibrated by inputting a series of known static moments. The accuracy of the dynamic measurements (explained below) produced by the machine was always greater than 90 %, as tested using a homogeneous beam (polyvinyl chloride) of known mechanical properties.

In all experiments, we adjusted the testing conditions to maintain a maximal linear strain, ε (ratio of final to resting length), of approximately ± 8 % for the superficial muscle on both sides of the eel's body (Table 1). A maximal ε of ± 8 % has been used in studies of superficial red muscle (Swank et al. 1997), is within the maximum range estimated for white muscle during unsteady swimming (Franklin and Johnston, 1997; Johnston et al., 1995; Johnson et al., 1994), and is only slightly greater than the value of ± 6 % used to model *in vivo* swimming power in posterior white muscles (Rome et al. 1993). To produce ε of ± 8 % for eels of different size, given a constant angular strain θ ± 4.25° in the bending machine, the test section length, L, was adjusted, so that the smallest eel had the shortest absolute L. While this kept ε constant across individuals, the resulting maximal midline curvature, κ (m^{-1}), the inverse of the radius of curvature, r_c (m), ranged from 38, 20, to 18 m^{-1}. The bending sections in all three eels included four intervertebral joints (± 1.06° per joint), three full myomeres (and part of an anterior and posterior myomere), as determined by inspection of the muscle.

Once mounted, the left and right sides of the eel's body were implanted with a pair of platinum stimulating electrodes possessing tips of 1.1 cm in length (Grass Instruments, model E2). On each side the cathode and anode were separated by the maximal distance allowed by the test section length (Table 1), were oriented parallel to the vertical septum, and provided a linear electrode exposure to the muscle equal to approximately the dorso-ventral height of that section of the body. Preliminary experiments showed that this electrode arrangement, compared to others, produced maximal bending moments. Furthermore, current leakage to surrounding myomeres stimulated adjacent myomeres on a given side; this current leakage is responsible for the two full cycles of supra-maximal stimulation required to achieve a stable and fully potentiated functional state (Fig. 2). To provide the current density necessary to produce supra-maximal stimulations of the myomeres, the contra-lateral electrode pairs were supplied independently by two 300 milliamp stimulators (Grass Instruments, S48). Each stimulator was externally triggered, alternately, by a two-channel, digital stimulator (Grass, S11B) with quartz timing circuits. The stimulator was in turn externally triggered by a pulse generator (Data Dynamics, 5113) which was triggered by the voltage from the RVDT attached to the bending axis.

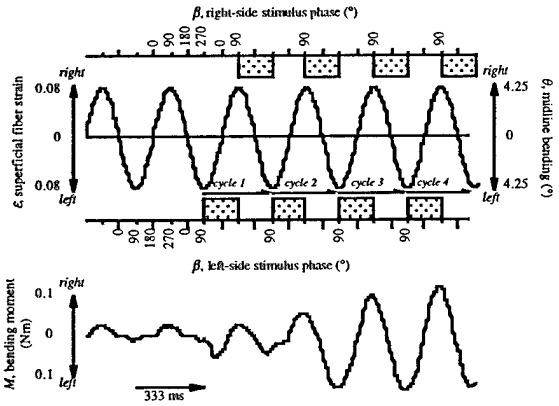

Fig. 1. Typical dynamic signals generated during a whole-body work loop experiment. At a frequency of 3 Hz (333 ms per cycle), a θ of ± 4.25° of the body's midline strains superficial fibers ± 8 %. Electrical stimuli (stippled rectangles) are applied alternately to the left and right sides for 50 % of a given bending cycle. The stimulus phase, ϑ, is 90°. Stimulation causes the bending moment, M, to increase. By the third stimulus cycle, a relatively stable mechanical signal has been generated by the fully potentiated muscle system.

Myomeric muscle, including all of the red and white fibers, on each side of the body was alternately stimulated for 50 % of the bending cycle with an 80 Hz train of electrical pulses of 2 msec duration. The duty cycle of 50 % was chosen from those reported for European eel; it is the maximum value measured (Grillner & Kashin, 1976); single-fiber work loop studies have used similar train pulses (Johnston & Johnson, 1991). Voltage of the stimulus was varied from 2 to 40 VDC to maintain supra-maximal contraction. The primary independent variable was stimulus phase, β (°), which indicates the timing of the onset of the electrical stimulus relative to the axial body strain on that side of the body (Fig. 2). Following the convention of single-fiber studies (see Johnston & Johnson, 1991), β = 0° represents the relative time in the dynamic bending cycle (a full cycle = 360°) when the electrical stimulation of the muscle begins ("onset") as the muscle is at its resting length and is lengthening; β = 90° represents the time when the onset occurs as the muscle is at its minimum length; β = 180° represents the time when the onset occurs when the muscle is at resting length and is shortening; β = 270° represents the time when onset occurs when the muscle is at its maximum length.

Because the muscle fatigued within one hour, and sometimes sooner, the experiments were performed in two stages, with the most important experiments first. In stage one, we measured the isometric properties of the right- and left-side myomeres at supra-maximal voltage with the body held straight. This was immediately followed by sinusoidal bending of the body with electrical stimulation of the muscles at β of 0, 90, 180, and 270°, with the order of the β randomized for each eel in order to avoid artifacts of test order. In stage two, the new supra-maximal voltage, required because of gradual muscle fatigue, was determined and a second isometric test was performed. This was immediately followed by sinusoidal bending of the body with electrical stimulation of the muscles at β of 45, 135, 225, and 315°, with the order of the phases randomized for each eel in order to avoid artifacts of test order.

Two replicates were measured from each experiment. Experiments consisted of either unstimulated or stimulated bending at a given β. Total sample size was 96 (two replicates, three individuals, and two stimulus states at each of eight β). Those replicates were the third and fourth stimulus cycles; these cycles were chosen because between one and two stimulus cycles were required to achieve a stable, fully potentiated state (Fig. 1). Stimulation was discontinued as soon as possible after the fourth stimulus cycle in order to prolong the experimental life of the whole-body preparation.

For a dynamically bending beam, the instantaneous external bending moment, M (Nm), transmitted through the test section is balanced by the internal moments caused by stiffness, damping, and change in angular momentum (Den Hartog, 1956; Denny, 1988):

$$M = k\theta_0 \sin(\omega t - \delta) + c\omega\theta_0 \cos(\omega t - \delta) - N\omega^2\theta_0 \sin(\omega t - \delta) \qquad (2)$$

where k is the angular stiffness (Nm rad^{-1}), ω is the angular frequency (rad s^{-1}), t is the time

(s), δ is the phase advance of M relative to θ (rad), c is the damping coefficient (kg m^2 rad^{-2} s^{-1}), and N is the moment of inertia (kg m^2 rad^{-3}). Since the moment gauge is mounted on the cantilevered side of the bending machine, the tip of which oscillates at maximum of ± 1 mm (Fig. 1B), moments due to angular acceleration are negligible, with maximal values of 3.4 x 10^{-5} Nm (when the effective N = 1.28 x 10^{-6} kg m^2 for the largest eel, ω = 18.85 rad s^{-1}, and θ_0 = 0.074 rad). Hence, Eq. 2 simplifies to

$$M = k\theta_0 \sin(\omega t - \delta) + c\omega\theta_0 \cos(\omega t - \delta). \quad (3)$$

Given the sinusoidal nature of M with t,

$$M = M_0 \sin(\omega t), \quad (4)$$

where M_0 is the amplitude, which was measured from the digitized transducer record (1000 Hz sample rate) for each experiment (a given β, stimulus state, and individual). In addition, the phase advance, δ (rad), was measured as the relative timing of the peaks of the M and θ records. To solve for k, a time, t, was found when

$$\cos(\omega t - \delta) = 0, \quad (5)$$

and

$$\sin(\omega t - \delta) = 1, \quad (6)$$

such that the damping term (Eq. 3) was 0, and Eq. 3 was combined with Eq. 4 to yield

$$k = \frac{M_0 \sin(\omega t)}{\theta_0}. \quad (7)$$

To normalize for the different sizes of eels, we substituted Eq. 7 into Eq. 1, since k is the ratio of M and θ, and replaced the bending couple, C (Nm), with the bending moment, M (Nm). This yielded the flexural stiffness, EI (Nm^2), which takes the subscript "ext" to denote that the bending machine measured the external moment working to bend the eel :

$$EI_{ext} = kL, \quad (8)$$

where L is the length of the test section. To solve for c, a time, t, was found when

$$\sin(\omega t - \delta) = 0, \quad (9)$$

and

$$\cos(\omega t - \delta) = 1, \quad (10)$$

such that the stiffness term (Eq. 3) was 0, and Eq. 3 was combined with Eq. 4 to yield

$$c = \frac{M_0 \sin(\omega t)}{\omega\theta_0}. \quad (11)$$

To normalize for different sizes, we divided c by L, since increases in L will increase the lateral velocity of the test section and c is inversely proportional to velocity (Eq. 10):

$$c_{ext} = \frac{c}{L}. \quad (12)$$

Finally, the external work done by the machine on the test section was calculated as a function of the phase advance, δ (Den Hartog, 1956):

$$W = \pi M_0 \theta_0 \sin\delta. \quad (13)$$

To normalize for the different muscle masses, m_m (kg), of the various test sections (estimated from test section volume assuming a muscle density of 1000 kg m^3, Table 1), the following mass-specific work was computed:

$$W_{ext} = \frac{W}{m_m}. \quad (14)$$

Two additional indices of each response variable were calculated. To isolate the absolute contribution of the stimulated muscle to the fully potentiated state, the difference between the values for the stimulated and unstimulated states was calculated for each β and individual (denoted by EI_{diff}, c_{diff}, and W_{diff}). To determine the relative contribution of the stimulated muscle, the ratio of the difference value, EI_{diff} *e.g.*, to the unstimulated value, EI_{ext}, was calculated for each β and individual (denoted by EI_{rel}, c_{rel}, and W_{rel}).

During cyclic bending experiments, changes in β were expected to produce sinusoidal changes in net muscle work (Johnson & Johnston, 1991) and hence in all of the dependent variables. Using the mean value of each relative response variable at a given β (n = 8, pooled across individual), a sinusoidal, least-squares regression line was produced which maximized the coefficient of determination (r^2 value). Sinusoidal regressions of were generated (Wilkinson, 1989):

$$y = b + a\sin(x + \delta) \qquad (15)$$

where y is the response variable, b is the grand mean of the y values (baseline), a is the amplitude, x is the stimulus phase, β, and δ is the phase advance.

In order to understand the dynamic, non-linear relationship between the muscularly-generated changes in flexural stiffness, EI_{rel}, and mechanical work, W_{rel}, the sinusoidal functions for the two properties were combined in a parametric plot, with β as the parameterized independent variable. In order to compare the muscular power output of the eel to that using different species and measurement techniques, the externally measured W_{diff} was converted to muscular power output, P_m, (W kg^{-1}) as the product of W_{diff} and the bending frequency (3 Hz). In order to signify that the power being produced by the muscle, and not the external power required to bend the eel, the sign of W_{diff} was reversed.

In the isometric tests, the body was held straight and stationary while being stimulated on the right side. The supra-maximal stimulus was identical to that used in the dynamic tests at a bending frequency of 3 Hz. The activation delay (ms), from the onset of the electrical stimulus to the onset of detectable M, was measured, as was the time to the maximal M, M_{max}, and the relaxation time to 50% of M_{ma}. The sample size was three, with one trial used from each of the three eels.

Results

Swimming kinematics

Eels swam forward and backward (Fig. 2) over a range of steady swimming speeds.

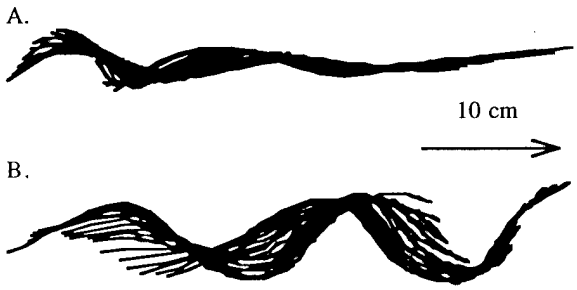

Fig. 2. Reversible propulsion in eels. Reconstructed midlines for a complete tailbeat cycle. A. Forward swimming, head to right. B. Backward swimming, head to left. Arrow indicates scale and direction of swimming.

To swim steadily backwards, eels required greater tailbeat frequency (Fig. 3). To increase speed while swimming backward, eels increased lateral amplitude (yaw) of the head, which is, during that maneuver, the trailing edge (Fig. 4). To swim backward, eels also required greater lateral displacement

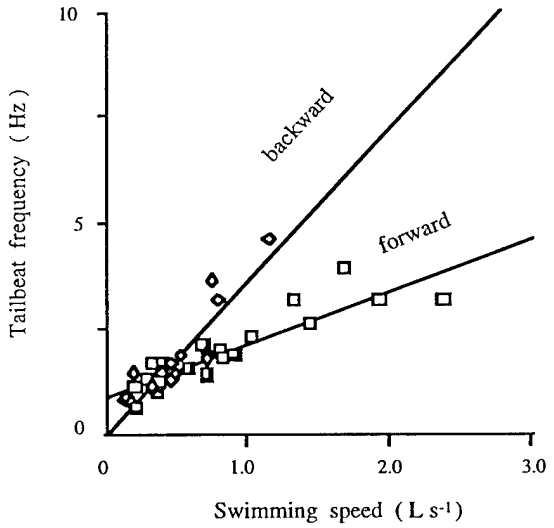

Fig. 3. Swimming speed is controlled, in part, by tailbeat frequency in both backward and forward swimming directions (n = 40).

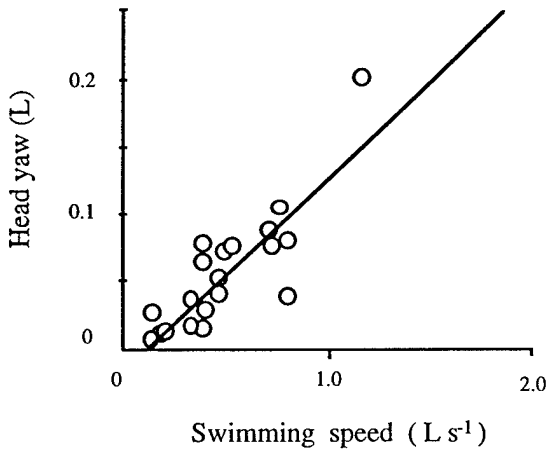

Fig. 4. Backward swimming eels increase swimming speed by increasing the yaw of the head (trailing edge). Forward swimming eels so no such pattern (n = 20).

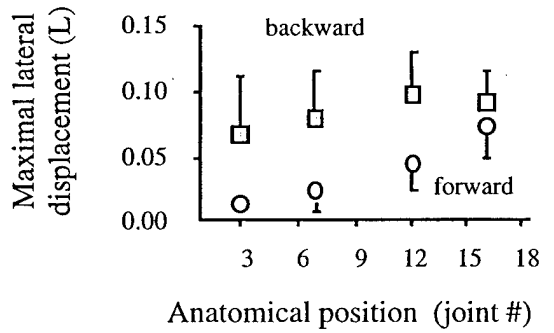

Fig. 5. Lateral displacement increases during backward swimming (n =20 for each mean value, ± s.e.m.). Means pooled across individual and trial.

along all points of the body (Fig. 5). A similar pattern was seen for the maximal midline curvature, which increased along the entire length of the body during backward swimming (Fig. 6). This increased curvature can be interpreted in one of two ways: (a) the net bending load on the body is constant but the body has reduced its stiffness, or (b) the net bending load on the body has increased, causing greater curvature on a body of constant stiffness. We believe the former to be most likely, since eels swimming backward do so at slower speeds (Fig. 3), and hydrodynamic loads, and the internal loads required to overcome the hydrodynamic resistance, should be proportionally lower.

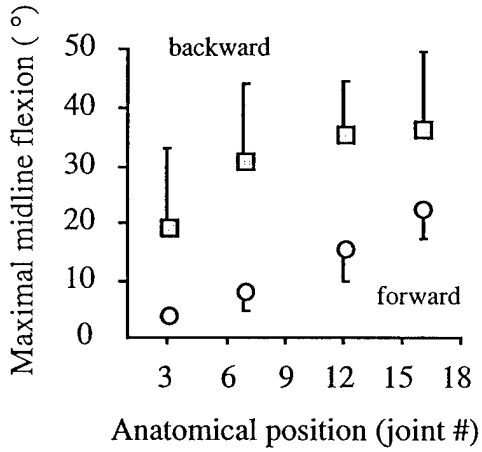

Fig. 6. Midline flexion increases during backward swimming (n = 20 for each mean, ± s.e.m.).

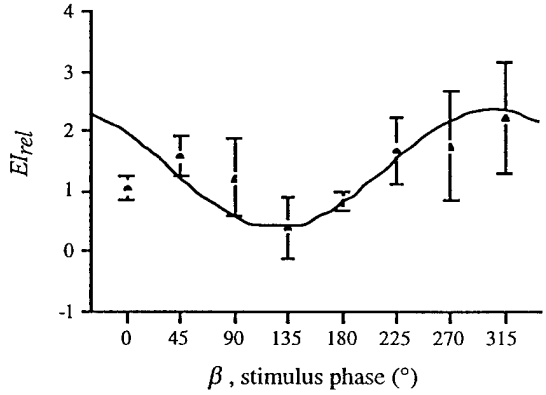

Fig. 7. Flexural stiffness, EI, varies with stimulus phase, β. Changes in EI_{diff} relative to the unstimulated EI_{est} are given as the ratio of the two, EI_{rel}. The line is a least-squares, sine wave regression (Eq. 16).

Muscle mechanics

The sinusoidal fit of the means of the flexural stiffness, EI_{rel} to β (Fig. 7), yielded the equation (n = 8, $r^2 = 0.716$, p = 0.023):

$$EI_{rel} = 1.347 + 1.00\sin(\beta + 143°). \quad (16)$$

The greatest value of EI_{rel} occurs at a β of 315°, and represents a tripling of the body's stiffness relative to that when the muscle is not stimulated. The sinusoidal fit of the means of c_{rel} to β (Fig. 8), yielded the equation (n = 8, $r^2 = 0.779$, p = 0.008):

$$c_{rel} = -1.33 + 5.13\sin(\beta + 304°). \quad (17)$$

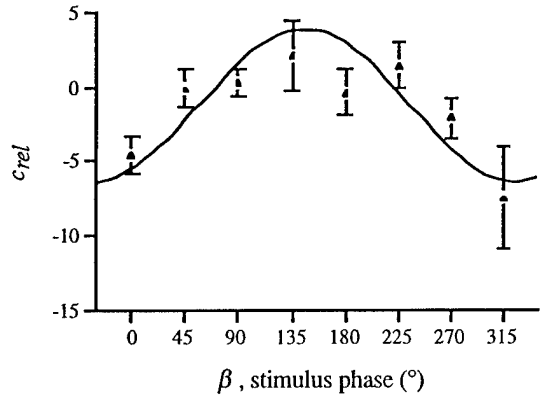

Fig. 8. Damping coefficient, c, varies with stimulus phase, β. Changes in c_{diff} relative to the unstimulated c_{ext} are given as the ratio of the two, c_{rel}. The line is a least-squares, sine wave regression (Eq. 17).

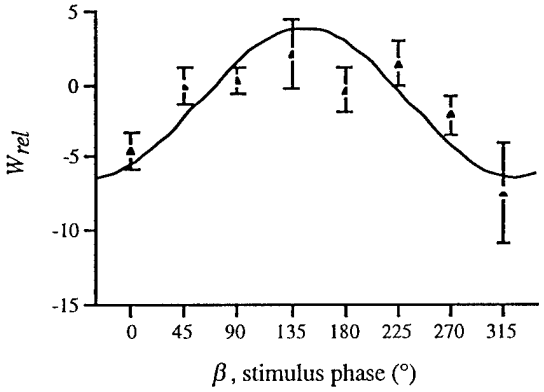

Fig. 9. Mechanical work, W, varies with stimulus phase, β. Changes in W_{diff} relative to the unstimulated W_{ext} are given as the ratio of the two, W_{rel}. The line is a least-squares, sine wave regression (Eq. 17).

The sinusoidal fit of the means of W_{rel} to β (Fig. 9), yielded the equation (n = 8, r^2 = 0.779, p = 0.008):

$$W_{rel} = -1.33 + 5.13\sin(\beta + 304°). \quad (18)$$

Note that since these values represent the work required by the machine to bend the eel's body, negative values of W_{rel} mean that the stimulated muscles were performing positive work internally.

To understand the relation between EI_{rel} and W_{rel}, the two sinusoidal functions (Eqs. 16 & 18) were combined in a parametric plot (Fig. 10). A maximal EI_{rel} of 2.3 occurred at a β of 307°, and a minimal EI_{rel} of 0.3 occurred

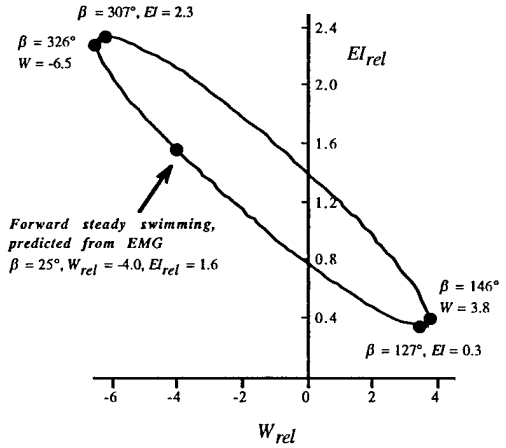

Fig. 10. Dynamics of the whole-body muscle preparation and predicted *in vivo* mechanics. A parametric plot of the sinusoidal function of flexural stiffness, EI_{rel} (Eq. 16) against that of the mechanical work, W_{rel} (Eq. 18). During steady swimming at 1 L_b s^{-1} (35-40 cm total length), caudal muscle (0.75 L) is activated at a β of 25° (G. Gillis, pers. com.). Change in swimming direction speed may be modulated by increasing or decreasing β.

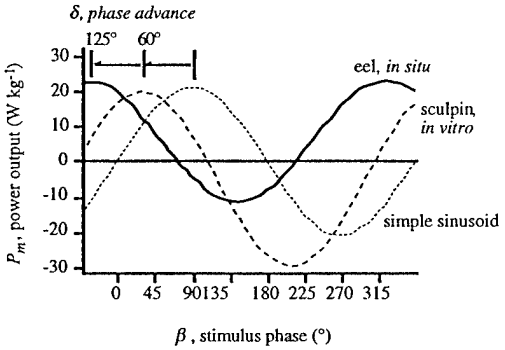

Fig. 11. Muscle power output. The eel *in situ* curve (Eq. 19) is derived from measurements using the whole-body work loop technique. Maximal P_m occurs when β = 325° (δ = 125°). The sculpin *in vitro* curve is derived from measurements using the single-fiber work loop technique (Eq. 20) on isolated white muscle bundles of sculpin (Johnson & Johnston, 1991). Maximal P_m occurs when β = 30° (δ = 60°). The simple sinusoid (Eq. 21) assumes that positive P_m can only by generated during muscle shortening.

at a β of 127°. A maximal W_{rel} of 3.8 occurred at a β of 146°, and a minimal W_{rel} of -6.5 occurred at a β of 326°. Thus maximal EI_{rel} is expected when W_{rel} is nearly minimal. When W_{diff} is converted to muscular power output, P_m, (W kg^{-1}), a

sinusoidal curve fit of the form (n = 8, r^2 = 0.644, p = 0.070), is generated (Fig. 11):

$$P_m = 5.64 + 17.50\sin(\beta + 125°). \quad (19)$$

For comparison with *in vitro*, single-fiber values, we estimated the sinusoidal function of sculpin white muscle from reported values of β at which maximal and minimal net P_m occurred (see Fig. 3A of Johnson & Johnston, 1991):

$$P_m = -5 + 25\sin(\beta + 60°). \quad (20)$$

Both functions were compared to a sinusoidal function with an amplitude intermediate to those in Eqs. 19 and 20:

$$P_m = 21.25\sin(\beta). \quad (21)$$

Inspection of these equations reveal two functionally significant differences: (1) The maximal net P_m of eel muscle *in situ* occurs at a δ more than twice that of the maximal net P_m of sculpin muscle *in vitro*; (2) in spite of a lower amplitude of the net P_m function of eel muscle *in situ* compared to than that of sculpin muscle *in vitro* (17.50 v. 25 W kg^{-1}), the maximal net P_m of eel is greater than that for sculpin (23.14 v. 20 W kg^{-1}).

Table 2. *Isometric muscle properties of the whole-body preparation with 167 ms tetantic stimulus.*

Variable	Mean	St. Error
Activation delay, detectable *M*	17 ms	± 0.0
Time to M_{max}	139 ms	± 34.6
Relaxation time, to 50 % M_{max}	330 ms	± 42.4
M_{max}	0.02 Nm	± 0.008

Sample size = 3 for each value.
All times relative to the onset of the electrical stimulus.
Electrical stimulus was supra-maximal.

Discussion

For eels, a seemingly simple aquatic maneuver — reversing the direction of steady undulatory swimming (Fig. 2) — requires modulation of lateral body displacements and midline flexion. Particularly intriguing is the greater midline flexion seen during backward swimming (Fig. 6). Since the speed of backward swimming was on average slower than that of forward swimming, it is unlikely that the greater midline flexion is caused by increased internal or external bending loads. Instead, we propose that the body becomes more flexible in order to swim backward. The corollary of this assertion is that the body is stiffer during forward swimming.

Our experiments demonstrate a possible internal mechanism for controlling body stiffness and hence maneuverability — the mid-caudal myomeric muscles of eel, when maximally stimulated during sinusoidal bending, can triple the body's flexural stiffness, EI_{rel}, relative to the body's stiffness when the muscle is unstimulated (Fig. 7). Dynamic changes in EI_{rel} are predicted by changes in the net muscle work, W_{rel} (Fig. 10). Combined with *in vivo* muscle activity patterns, whole-body work loops predict that live eels use their caudal locomotor muscle to increase EI_{rel} and to decrease W_{rel} at steady swimming speeds (Fig. 10). Compared to results from *in vitro* single-fiber work-loop studies, stimulation earlier in the muscles' lengthening phase (stimulus phases, β, of 325° vs. 30°) is required to produce maximal positive power output (Fig. 11), suggesting the presence of series elastic elements. With the external load provided by the kinetic energy of the traveling undulatory wave, elastic elements on one side of the caudal region of the body could be engaged by activated muscle lengthened by an external load, a process that would store elastic energy for release as positive work during the first half of the shortening cycle (Fig. 12).

Altering body stiffness and swim direction

One way to assess the likelihood that muscles are actively increasing EI_{rel} during swimming is to examine emg patterns. Gillis (pers. com.) measured emg patterns of American eel from different axial positions and at different swimming speeds. At the location closest to the axial position (75 % L_b) that we used for whole-body work loops (72 % L_b), Gillis measured a β of 25° for both red and white

muscle in 35 to 40 cm long eels swimming at 1 L_b s^{-1}. Using this β , the results of this present study predict that live, steadily swimming eels use their caudal musculature to increase EI_{rel} by a factor of up to 1.6 (Fig. 10). The dynamic model of *in situ* muscle function also predicts that the caudal musculature may increase the muscular work output, the negative of W_{rel}, by a factor of up to 4.0 during swimming (Fig. 10). The precise increase in stiffness or muscle work would depend on the number of motor units actually recruited during swimming. It is important to keep in mind that all of the white (fast) and red (slow) muscle fibers on one side of the body are stimulated with the supra-maximal voltages used in the whole-body work loop experiments. While eels appear to be unusual in stimulating both fiber types at all speeds (Grillner & Kashin, 1976), it is unlikely that they recruit all of the fibers of each type at low speeds. More likely is a scenario in which more motor units are recruited as speed increases (Jayne & Lauder, 1996).

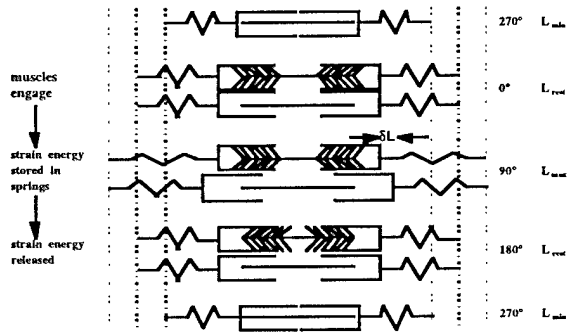

Fig. 12. An elastic energy model for undulatory swimmers. The caudal muscles of eel may use elastic energy to power bending and stiffen the body simultaneously. In the absence of local muscle activity (contractile elements figured without cross-bridges), the wave of bending, generated by muscles anteriorly, will propagate down the body, transmitting kinetic energy and causing undulatory motion in this caudal region. When caudal muscles are active (figured with cross-bridges attached) with a duty cycle of 50%, they can produce maximal work by engaging their cross-bridges at a time of 0° (muscle at resting length and lengthening). The muscle, lengthening under the external load (traveling wave) with cross-bridges engaged, generates high negative force (1.75 times that of shortening) as it resists lengthening; it thus engages the serial elastic elements, straining them and storing elastic energy. At 90° (maximal muscle length), the strain in the system, and hence the stored elastic energy, is maximal; the extra strain added by the active muscles is indicated (δL). At the next moment, the muscle begins to contract, keeping the springs engaged, and releasing the strain energy. At 180° (muscle at resting length and shortening), the muscle should be inactive, since the elastic elements will have released the stored energy and will be shortening passively because of the traveling wave of bending.

In order to swim backward, this model predicts that eels would increase β , causing the body to be more flexible. At faster swimming speeds, β could decrease and, according to the model (Fig. 10), permit greater muscle power, P_m, and EI_{rel} to be produced. To swim slowly, the model predicts that β would increase.

How muscle alters body stiffness

From results of *in vitro* work loops on small bundles of the white caudal muscle of saithe, Altringham et al. (1993) predicted that those muscles, when activated while lengthening *in vivo*, would generate maximal force, resulting in negative work locally and internally (a positive W_{ext} or W_{rel}). This local negative work would stiffen the muscles, permitting them to transmit, as functional tendons, mechanical power from the anterior muscle to the caudal propulsive elements (Videler, 1993; Wardle et al. 1995). Thus, we were initially surprised to find the opposite result in the *in situ* whole-body work loop experiments — increased body stiffness correlated with increased net positive muscle work (a negative W_{rel} in Fig. 10). In fact, de-coupling of stiffness and work has been found in other, non-axial systems (Luiker & Stevens, 1991). The unexpected mechanical behavior in the eel whole-body preparation might be understood by comparing the results from *in vitro* and *in situ* experiments with those predicted by a model of simple muscle contraction and work production (Fig. 11).

In the simplest case, myomeric muscles should produce maximal power, P_m, when they are electrically activated at their maximum length ($\beta = 90°$) and forcefully shorten for 50 % of the cycle (simple sinusoid in Fig. 11). Activation at 90°, however, does not account for the delay between the onset of the stimulus and the actual contraction, which is

17 ms (Table 2). Thus, for cyclic bending at 3 Hz, maximal P_m would require a compensatory phase advance, δ, in stimulus onset of 18°, yielding a prediction of maximal P_m at $\beta = 72°$. *In vitro* measurements of isolated white caudal muscle fibers, however, show production of maximal net muscle work at $\beta = 29°$ in sculpin (bending frequency of 5 Hz; Johnston et al. 1993), and 36° in dogfish (bending frequency of 3.3 Hz; Curtin and Woledge, 1993a). We chose the sculpin's value of approximately 30° to represent bony fish (Fig. 11). This β yields a δ of 60° relative to the maximal work predicted by the simple contraction model. Given the 18° needed to engage the contractile elements, that still leaves 42° of muscle activity before shortening begins. By activating the muscles as they are lengthened, this "pre-stretch" period is thought to permit fibers to generate greater force during shortening; longer periods of pre-stretch, *i.e.*, further advances in β, reduce maximal P_m by increasing the amount of negative work generated locally (Johnson & Johnston, 1991; Johnston, 1991; but see Lombardi et al., 1995 for alternative explanation). *In situ* measurements of white and red caudal muscle using the whole-body work loop technique, show a pattern different from that of either the simple contraction or *in vitro* models; eel muscle produces maximal P_m at $\beta = 325°$, a δ of 125° (Fig. 11).

An elastic energy model

The whole-body preparation produces maximal net P_m when it is stimulated as the segment is being lengthened, a result that suggests that the body stores energy in serial elastic elements strained during lengthening that is released during shortening. The fact that maximal net P_m is produced during lengthening ($\beta = 325°$, see Fig. 11), and that caudal muscle is activated early during lengthening in swimming eels (emg $\beta = 25°$, see Fig. 10), indicates that our notion of how the muscle functions in eels, and perhaps other anguilliform swimmers, needs to be revised. Videler (1993) suggested that anterior myomeres produce a large amount of positive net P_m that is transferred to the propulsive elements by caudal muscle stiffened by activation during lengthening caused by a load external to that muscle, a situation that produces local negative work (Altringham et al., 1993; Cheng & Blickhan, 1994; Hess & Videler, 1984; Johnson et al., 1994; Van Leeuwen et al., 1990). This model is not supported by findings that caudal muscle fibers in scup when tested by *in vitro* work loop techniques using *in vivo* stimulation parameters, produce primarily positive work throughout the bending cycle (Coughlin et al., 1996; Coughlin & Rome, 1996; Rome et al. 1993; Rome & Swank, 1992). While *in vitro* single-fiber studies predict maximal stiffening associated with local negative work produced by stimulated muscle lengthening under an external load (Altringham & Johnson, 1990; Altringham et al., 1993; Johnson et al. 1994), in this study it is positive — not negative — muscle work (the opposite of the externally measured W_{ext}) that is associated with increased *EI* (Figs. 7 and 9). How can this be?

The caudal muscle of eel may store energy in serial elastic elements (SEE), resulting in maximal P_m when stimulated during lengthening. We propose that the caudal muscle in eels generates positive P_m not by simple contraction (forceful shortening) but by loading the SEE as the muscle lengthens under an external force, which, in the case of an undulating fish, is provided by the kinetic energy of the traveling wave of bending (Fig. 12). As long as the active contractile elements are stiffer than the SEE (Alexander, 1988), the SEE could then release the strain energy during the shortening phase, and the local segments would produce a net positive P_m cycle even though the muscles had been activated during a large portion of their lengthening cycle. In this model, muscles function as *dynamic springs*, increasing the stiffness of the body and at the same time causing elastic energy to be stored in elastic elements, energy that is then released during shortening of that side of the body. At the same time, it is unclear which structures function as the SEE. The myotomes are arranged serially (Westneat et al., 1993) and are activated sequentially (Jayne & Lauder, 1995a), a situation that might provide the requisite mechanical properties. Other candidates include the skin (Hebrank, 1980; Long et al., 1996; Wainwright et al., 1978)

and the axial skeleton (Long, 1992, 1995), both of which are sites of myotomal muscle attachment.

How might the predictions of the elastic energy model be tested? While the whole-body work loop results on eel suggested the model in the first place, they permit me to demonstrate a simple test of internal consistency. According to the elastic energy model (Fig. 12), We can predict the following. With a duty cycle of 50%, muscle should be active (cross-bridge activity) at β = 0°, since activity before then will merely pull on SEE that are slack. Furthermore, the muscle should stay active until 180°, since release before that will not allow SEE to transfer stored strain energy to surrounding structures. To predict optimal emg β, one must know the delay between electrical onset and cross-bridge activity. Eel muscles measured isometrically have a contraction delay of 17 ms (Table 2), which, at a bending frequency of 3 Hz, is 5% of the period of the bending cycle, or 18° of 360°. Thus, we would predict that eels would produce maximal P_m at β = 342° (360° - 18°). We found maximal P_m at a closely-corresponding β = 325° in the whole-body work loop experiments (Fig. 11). Thus both theoretical and measured values of β that produce maximal P_m predict that emg onset would occur early in the lengthening portion of the bending cycle. The model can be independently tested using emg data in live eels. At relatively slow swimming speeds of 1.0 L_b s^{-1}, β = 25° in the mid-caudal muscles (Gillis, pers. com.), suggesting the following testable prediction — during faster steady swimming, or vigorous unsteady swimming, when more P_m and higher EI are required, emg β should decrease from 25° towards 342°, as predicted by the model. Shifts in the opposite direction would refute the model.

Because this is first time, to our knowledge, that a specific elastic energy mechanism has been proposed for undulatory swimmers, it is important to consider potential problems with this model. The reader should keep in mind that the experiments conducted in this study included only a single bending frequency (3 Hz), a single muscle strain (± 8 %), a single body position (72 % L_b), and a single temperature (20° C). All four of these variables significantly alter dynamic muscle properties in *in vitro* single-fiber experiments. Thus, extensions of the elastic energy model, and results of the *in situ* whole-body experiments in general, should be done cautiously. Conservatively, the implications of this work apply only to the caudal muscles of eels swimming with a tail-beat frequency of 3 Hz in water at 20° C.

(1) Why should muscles use elastic energy when they can generate power directly, thus avoiding viscous losses? Given that elastic tissues dissipate some of the stored strain energy (Alexander, 1988), why not avoid losing that energy and produce positive power directly? The mechanical "reason" to store elastic energy by using the traveling wave of bending to lengthen the muscle as it is activated is that caudal muscle can produce 1.75 times the force of shortening as it is caused to lengthen (Altringham et al., 1993; also see McMahon, 1985). The "pay-off" threshold for elastic return would therefore be efficiencies (ratio of energy returned to energy stored) greater than 57 % (ratio of forces during shortening and lengthening). The efficiency of the tendon in wallaby is about 93 % (Ker et al., 1986); the efficiency in bending of the intervertebral joints of blue marlin is over 90 % as well (Long, 1992). While the functional SEE in eel have not been identified, it is clear that vertebrate connective tissues can have efficiencies that would render feasible the elastic energy model of caudal muscle function. If the caudal muscles use elastic energy to produce greater amounts of P_m than they could do by simple shortening, it leaves us with the intriguing possibility that this mechanism compensates for the reduced muscle mass as the body tapers caudally. The elastic energy mechanism might also compensate for P_m production limitations that would constrain actively shortening muscle to operate at ratios of contraction velocity to maximal contraction velocity near 0.2 to 0.3 (see Rome et al., 1988); caudal muscle fibers could specialize in high force production without compromising production of positive work.

(2) What provides the load needed to strain activated muscle and SEE? In a terrestrial, limbed vertebrate, the load needed to strain SEE is provided, in part, by gravitational force, which, in the form of potential energy, is exchanged for kinetic energy which, in turn, is converted to strain energy (*e.g.*, Farley et al., 1991; McMahon, 1985). On the other hand, neutrally-buoyant swimming vertebrates have no external force which might load elastic elements; any energy used in lengthening muscle and elastic elements must be provided by P_m from other muscles. The P_m used for lengthen would be unavailable for hydrodynamic power and, considering losses during transmission, a substantial benefit would be needed to compensate. While some compensation might be provided by the greater forces generated as muscle is lengthened (see question 1), those greater forces require greater antagonistic force in turn. My counter argument is this: the "external" loading could be supplied, in part, by the kinetic energy transferred from anterior myomeres by the traveling wave of bending. This propulsive wave will travel rearward without input from the caudal muscles (Blight, 1977; Long et al., 1994; Wassersug and Hoff, 1985), propagating by exchanging strain and kinetic energy in elastic structures (McHenry et al., 1995). *The traveling wave of bending and its kinetic energy is thus the undulatory analogue to gravity and its potential energy.* The elastic elements and the caudal muscle harness this propagating energy to strain tissues and lengthen muscle. In turn, the newly loaded body section transfers its P_m to rearward segments and to the surrounding fluid. Kinetic and strain energy are thus cyclically exchanged in a manner partially analogous to that seen in the limbed locomotion of vertebrates.

(3) Do the experimental conditions accurately mimic those seen in life? We used a procedure that stimulated all of the red and white muscle simultaneously. While this pattern may be realistic for steadily swimming eels (Grillner & Kashin, 1976), it has been described in other species only during unsteady kick-and-glide and fast-start behaviors (see Jayne & Lauder, 1996). In the worst case, the elastic energy model might only operate during behaviors that use all or most of the myomeric musculature. Another potential problem is that direct electrical stimulation of the muscles may have also stimulated afferent neural pathways that were not destroyed in the whole-body preparation; these pathways could provide feedback to the central pattern generators in the spinal cord which could, in turn, stimulate motor units independently (see Fetcho, 1987; Fetcho and Faber, 1988). Gray (1936a, 1936b) found that spinally transected eels, such as the ones used in this study, were inhibited from muscle contractions in response to tactile stimulation by strong restraint of the body, which is a condition similar to that imposed by the bending grips in the experimental machine. It is possible, although untested, that this inhibitory mechanism may have effectively blocked the response to afferent stimulation at the level of the central pattern generator or motor pathway. Another potential problem is how closely the bending apparatus mimicked the internal and external loading conditions during swimming. While the machine imposed a sinusoidal bend that approximates the external motion seen in a small section of the swimming eel's body, the interaction of internal and external forces in undulatory swimmers is complex (Jordan, 1996), but since it has not been modeled comprehensively in fish, we cannot determine how closely the grips match the conditions seen in live eels.

Our understanding of how eels swim is changing. While it is still likely that anterior myomeres use forceful *shortening* to produce positive mechanical work that drives local body bending, the caudal muscles generate force as they are *lengthened* to produce, simultaneously, positive mechanical work and increased body stiffness. The dual function of caudal muscle as a body bender and dynamic stiffener is made possible by the use of elastic energy to store and release muscle work. Increases in body stiffness will increase the speed of the traveling wave of bending and make bending itself less mechanically costly at higher tail-beat frequencies. By examining dynamic, time-dependent behaviors of the muscles operating within the intact body, an integrated view emerges — of function at different structural

levels, from single sarcomeres to contiguous blocks of myomeres and their associated elastic elements — a perspective unanticipated from any single level.

Acknowledgements

Karen Nipper was instrumental in helping to design the whole-body work loop technique, the inspiration for which was originally provided by conversations with Ted Goslow and Thelma Williams. John Hermanson provided neurobiological advice. Wayne Gilchrest graciously provided the eels. Gary Gillis kindly shared his unpublished data on eel swimming kinematics and electromyography. Bruce Jayne, Robert Suter, and Matt McHenry critiqued earlier versions of this manuscript. This work was funded by grant number N00014-97-1-0292 to J.H.L. and R.R. from the Office of Naval Research.

References

Alexander, R. M. 1988. *Elastic mechanisms in animal movement.* Cambridge U. Press, New York.

Altringham, J.D. and I.A. Johnston. 1990. Scaling effects on muscle function: power output of isolated fish muscle fibers performing oscillatory work. *J. exp. Biol.* 151: 453-467.

Altringham, J.D., C.S. Wardle and C.I. Smith. 1993. Myotomal muscle function at different locations in the body of a swimming fish. *J. exp. Biol.* 182: 191-206.

Bennett, M.B., R.F. Ker & R.M. Alexander. 1987. Elastic properties of structures in the tails of cetaceans (*Phocoena* and *Lagenorhynchus*) and their effect on the energy cost of swimming. *J. Zool., Lond.,* 211:177-192.

Blickhan, R. and J.-Y. Cheng. 1994. Energy storage by elastic mechanisms in the tail of large swimmers — a re-evaluation. *J. theor. Biol.* 168: 315-321.

Blight, A.R. 1977. The muscular control of vertebrate swimming movements. *Biol. Rev.* 52: 181-218.

Bowtell, G. and T. Williams. 1991. Anguilliform body dynamics: modeling the interaction between muscle activation and body curvature. *Phil. Trans. R. Soc., Lond. B.* 334: 385-390.

Cheng, J.-Y. and R. Blickhan. 1994. Bending moment distribution along swimming fish. *J. theor. Biol.* 168: 337-348.

Coughlin, D.J. and L.C. Rome. 1996. The roles of pink and red muscle in powering steady swimming in scup, *Stenotomus chrysops. Am. Zool.* 36(6): 666-677.

Coughlin, D.J., G. Zhang and L.C. Rome. 1996. Contraction dynamics and power production of pink muscle of the scup (*Stenotomus chrysops*). *J. exp. Biol.* 199: 2703-2712.

Curtin, N.A. and R.C. Woledge. 1993a. Efficiency of energy conversion during sinusoidal movement of white muscle fibres from the dogfish *Scyliorhinus canicula. J. exp. Biol.* 183: 137-147.

Curtin, N.A. and R. C. Woledge. 1993b. Efficiency of energy conversion during sinusoidal movement of red muscle fibers from the dogfish *Scyliorhinus caniculua. J. exp. Biol.* 185: 195-206.

Den Hartog, J.P. 1956. *Mechanical vibrations.* 4th edn. McGraw-Hill, New York.

Dial, K.P. 1992. Activity patterns of the wing muscles of the pigeon (*Columbia livia*) during different modes of flight. *J. Exp. Zool.* 262: 357-373.

Ettema, G.J.C. 1996. Mechanical efficiency and efficiency of storage and release of series elastic energy in skeletal muscle during stretch-shorten cycles. *J. exp. Biol.* 199(9): 1983-1997.

Farley, C.T., R. Blickhan, J. Saito and C.R. Taylor. 1991. Hopping frequency in humans: a test of how springs set stride frequency in bouncing gaits. *J. Appl. Physiol.* 71(6): 2127-2132.

Fetcho, J.R. 1987. A review of the organization and evolution of motoneurons innervating the axial musculature of vertebrates. *Brain Res. Rev.* 12(1987): 243-280.

Fetcho, J.R. and D.S. Faber. 1988. Identification of motoneurons and interneurons in the spinal network for escapes initiated by the mauthner cell in goldfish. *J. Neurosci.* 8(11): 4192-4213.

Franklin, C.E. and I.A. Johnston. 1997. Muscle power output during escape responses in an Antarcttic fish. *J. exp. Biol.* 200: 703-712.

Gillis, G.B. 1996. Undulatory locomotion in elongate aquatic vertebrates: anguilliform swimming since Sir James Gray. *Am. Zool.* 36(6): 656-665.

Gray, J. 1933. Studies in animal locomotion. I. The movement of fish with special reference to the eel. *J. exp. Biol.* 10: 88-104.

Gray, J. 1936a. Studies in animal locomotion. IV. The neuromuscular mechanism of swimming in the eel. *J. exp. Biol.* 13: 170-180.

Gray, J. 1936b. Studies in animal locomotion. V. Resistance reflexes in the eel. *J. exp. Biol.* 13: 181-191.

Grillner, S. and S. Kashin. 1976. On the generation and performance of swimming in fish. In R.M. Herman, S. Grillner, P.S.G. Stein and D.G. Stuart (eds.). *Neural control of locomotion.* Pp 181-201 Plenum Press, New York.

Hebrank, M.R. 1980. Mechanical properties and locomotor functions of eel skin. *Biol. Bull.* 158: 58-68.

Hess, F. and J.J. Videler. 1984. Fast continuous swimming of saithe *(Pollachius virens)*: a dynamic analysis of bending moments and muscle power. *J. exp. Biol.* 109: 229-251.

Jayne, B.C. and G.V. Lauder. 1993. Red and white muscle activity and kinematics of the escape response of the bluegill sunfish during swimming. *J. Comp. Physiol. A.* 173: 495-508.

Jayne, B.C. and G.V. Lauder. 1994. How swimming fish use slow and fast muscle fibers: implications for models of vertebrate muscle recruitment. *J. Comp. Physiol. A.* 175: 123-131.

Jayne, B.C. and G.V. Lauder. 1995a. Are muscle fibers within fish myotomes activated synchronously? Patterns of recruitment within deep myomeric musculature during swimming in largemouth bass. *J. exp. Biol.* 198: 805-815.

Jayne, B.C. and G.V. Lauder. 1995b. Red muscle motor patterns during steady swimming in largemouth bass: effects of speed and correlations with axial kinematics. *J. Exp. Biol.* 198: 1575-1587.

Jayne, B.C. and G.V. Lauder. 1996. New data on axial locomotion in fishes: how speed affects diversity of kinematics and motor patterns. *Am. Zool.* 36(6): 642-655.

Johnson, T.P. and I.A. Johnston. 1991. Power output of fish muscles fibres performing oscillatory work: effects of acute and seasonal temperature change. *J. exp. Biol.* 157: 409-423.

Johnson, T.P., D.A. Syme, B.C. Jayne, G.V. Lauder and A.F. Bennett. 1994. Modeling red muscle power output during steady and unsteady swimming in largemouth bass. *Am. J. Physiol.* 267: R481-R488.

Johnsrude, C.L. and P.W. Webb. 1985. Mechanical properties of the myotomal musculo-skeletal system of rainbow trout, *Salmo gairdneri. J. exp. Biol.* 119: 71-83.

Johnston, I.A., C.E. Franklin and T.P. Johnson. 1993. Recruitment patterns and contractile properties of fast muscle fibres isolated from rostral and caudal myotomes of the short-horned sculpin. *J. exp. Biol.* 185: 251-265.

Johnston, I.A., J. L. Van Leeuwen, M.L.F. Davies and T. Beddow. 1995. How fish power predation fast starts. *J. exp. Biol.* 198: 1851-1861.

Jordan, C.E. 1996. Coupling internal and external mechanics to predict swimming behavior: a general approach? *Am. Zool.* 36(6): 710-722.

Josephson, R.K. 1985. Mechanical power output from striated muscle during cyclic contractions. *J. exp. Biol.* 114: 93-512.

Ker, R.F., N.J. Dimery and R. M. Alexander. 1986. The role of tendon elasticity in hopping in a wallaby *(Macropus rufogriseus). J. Zool., Lond. A.* 208: 417-428.

Lighthill, M.J. 1975. *Mathematical Biofluiddynamics.* Res. Conf. Nat. Sci. Found., 1973, New York Soc. Ind. Appl. Math. SIAM.

Lombardi, V., G. Piazzesi, M.A. Ferenczi, H. Thirlwell, I. Dobbie and M. Irving. 1995. Elastic distortion of myosin heads and repriming of the working stroke in muscle. *Nature* 374: 553-555.

Long, J.H., Jr. 1992. Stiffness and damping forces in the intervertebral joints of blue marlin *(Makaira nigricans). J. exp. Biol.* 162: 131-155.

Long, J.H., Jr. 1995. Morphology, mechanics and locomotion: the relation between the notochord and swimming motions in sturgeon. *Env. Biol. Fishes* 44: 199-211.

Long, J.H., Jr., M.E. Hale, M.J. McHenry and M.W. Westneat. 1996. Functions of fish skin: the mechanics of steady swimming in longnose gar, *Lepisosteus osseus. J. exp. Biol.* 199: 2139-2151.

Long, J.H., Jr., M.J. McHenry and N.C. Boetticher, N.C. 1994. Undulatory swimming: how traveling waves are

produced and modulated in sunfish (*Lepomis gibbosus*). *J. exp. Biol.* 192: 129-145.

Long, J.H., Jr. and K.S. Nipper. 1996. The importance of body stiffness in undulatory propulsion. *Am. Zool.* 36(6): 678-694.

Luiker, E.A. and E.D. Stevens. 1991. Effect of stimulus frequency and duty cycle on force and work in fish muscle. *Can. J. Zool.* 70: 1135-1139.

McHenry, M.J., C.A. Pell & J.H. Long, Jr. 1995. Mechanical control of swimming speed: stiffness and axial wave form in undulating fish models. *J. exp. Biol.* 198(11): 2293-2305.

McMahon, T.A. 1985. The role of compliance in mammalian running gaits. *J. exp. Biol.* 115: 263-282.

Pabst, D.A. 1996. The role of elastic energy storage in aquatic locomotion. *Am Zool.* 36(6): 723-735.

Rome, L.C., R.P. Funke, R.M. Alexander, G. Lutz, H. Aldridge, F. Scott and M. Freadman. 1988. Why animals have different muscle fibre types. *Nature* 335: 824-827.

Rome, L.C. and D. Swank. 1992. The influence of temperature on power output of scup red muscle during cyclic length changes. *J. exp. Biol.* 171: 261-281.

Rome, L.C., D. Swank & D. Corda. 1993. How fish power swimming. *Science* 261: 340-343.

SAS Institute Inc. 1985. *SAS User's Guide: Statistics,* version 5. SAS Institute Inc., Cary, North Carolina.

Spierts, I.L.Y., H.A. Akster, I.H.C. Vos & J.W.M. Osse. 1996. Local differences in myotendinous junctions in axial muscle fibres of carp (*Cyprinus carpio* L.). *J. exp. Biol.* 199: 825-833.

Stevens, K.K. 1987. *Statics and strength of materials.* 2nd. Ed. Prentice-Hall, Englewood Cliffs, New Jersey.

Swank, D.M., G. Zhang & L.C. Rome. 1997. Contraction kinetics of red muscle in scup: mechanism for variation in relaxation rate along the length of the fish. *J. exp. Biol.* 200: 1297-1307.

Timoshenko, S., D.H. Young & W. Weaver, Jr. 1974. *Vibration problems in engineering.* 4th edn. John Wiley and Sons, New York.

Van Leeuwen, J.L., M.J.M. Lankeet, H.A. Akster and J.W.M. Osse. 1990. Function of red muscles of carp (*Cyprinus carpio*): recruitment and normalized power output during swimming in different modes. *J. Zool. Lond.* 220: 123-145.

Videler, J.J. 1993. *Fish swimming.* Chapman and Hall, New York.

Wainwright, S.A., F. Vosburgh & J.H. Hebrank. 1978. Shark skin: function in locomotion. *Science* 202: 747-749.

Wardle, C.S., J.J. Videler & J.D. Altringham. 1995. Tuning in to fish swimming waves: body form, swimming mode and muscle function. *J. exp. Biol.* 198(8): 1629-1636.

Wassersug, R.J. & K.v.S. Hoff. 1985. The kinematics of swimming in anuran larvae. *J. exp. Biol.* 119: 1-30.

Westneat, M.W., W. Hoese, C.A. Pell & S.A. Wainwright. 1993. The horizontal septum: mechanisms of force transfer in locomotion of scombrid fishes (Scombridae, Perciformes). *J. Morph.* 217: 183-204.

Wilkinson, L. 1989. *SYSTAT: the system for statistics.* SYSTAT, Inc., Evanston, IL.

Williams, T.L., S. Grillner, V.V. Smoljaninov, P. Wallen, S. Kashin & S. Rossignol. 1989. Locomotion in lamprey and trout: the relative time of activation and movement. *J. exp. Biol.* 143: 559-566.

A CASE FOR BUILDING INTEGRATED MODELS OF AQUATIC LOCOMOTION THAT COUPLE INTERNAL AND EXTERNAL FORCES

Stephen L. Katz
CMBB-MBRD-0204, Scripps Inst. of Oceanography, La Jolla, Ca 92092-0204 USA

and

Chris E. Jordan
Dept. of EPO Biology, Univ. of Colorado, Boulder, CO 80309 USA

SUMMARY

To swim requires two things, (i) deforming the body or propulsive surfaces (fins, flukes, flippers) to generate propulsive waves, and (ii) pushing against the fluid surroundings to generate thrust. Although these may seem to be the same thing, they are two fundamentally different mechanical aspects of a single behavior. The former concerns the internal mechanics of a swimming organisms, while the latter, the external mechanics. Each follows its own set of governing rules (e.g. force-velocity relationships of muscle, resistive and reactive fluid force relationships), but they are mechanically coupled since any motion of the body must result in a displacement of the surrounding fluid. The governing rules are also coupled in that the external forces act as loads for the internal forces, and the external environment provides the equal and opposite reaction for every internally generated action. A fish out of water is more than just helpless, it is a substantially different mechanical system than in its submerged state. Thus, to understand the mechanics of swimming, we must both account for the internal and external mechanics, as well as their interactions. This paper focuses on the mechanical coupling between the internal and external forces, and the constraints this coupling imposes on the design, behavior, and performance of swimming organisms.

INTRODUCTION

There is a long tradition of human engineers applying biological design principles to man-made devices. To be successful, such an attempt must incorporate an appreciation of the complexities inherent in biological designs and the uniqueness of the design process itself. Biological designs are constructed around compromises between the potentially competing design objectives of locomotion, feeding, reproduction and homeostasis. In addition, the design process that results from evolution is fundamentally different from that commonly adopted by human engineers. Evolution by natural selection is a trial and error process of experimental success and failure constrained to modifying existing designs, rather than the invention of designs *de novo*. An important example of this design limitation is the complete absence of rotating propellers in macroscopic biological propulsion designs - whereas they are

ubiquitous in human engineered designs for aquatic propulsion.

The design process aside, some biological systems are credited with high performance - tuna are thought to be capable of bursts of speed in the range of 40 knots and maintenance of 3 to 6 knots for 30 to 40 years. This type of performance exceeds current man-made designs by a substantial margin and at least suggests that a critical analysis of tuna design performance in the context of vehicle design is appropriate. However, the multifactorial design objectives in something like a swimming tuna suggest that one will not be able to effectively implement biological principles in a man-made device without a complete understanding of the design features of the fish. Of concern are the potentially contentious choices that one makes in defining a strategy for analyzing the mechanical problem in a way that gets at the key design issues without missing anything important. In this paper we will attempt to review some of the key issues that must be addressed in generating a synthetic understanding of axial undulatory propulsion--with special reference to the tuna--in a way that will facilitate the application of biological design principles to human-engineered swimming devices.

Thinking of a swimming organism as a mechanical system, we can describe its component parts in terms of their mechanical properties. That is to say, muscle, soft tissue, and skeletal elements can be thought of as active and passive materials that have characteristic properties that determine how they will react to being dynamically loaded. In addition, we can think of the entire body-form of the swimmer, and how it interacts with its fluid surroundings, as another mechanical system, this time dominated by the physical properties of the fluid. Given these two classes of components, internal and external, we can describe swimming behavior emerging from their interaction as determined by the form of their coupling. Considerable experimental work, both biological and engineering, has been focused on the internal and external mechanics of swimming, however, much less effort has been applied to their interactions.

However, answering questions of this sort requires an understanding of swimming mechanics beyond the current state of the field. To move in this direction requires a mechanistic framework reflecting the internal and external architecture of aquatic locomotors. In this paper we present some preliminary mathematical models that attempt the coupling of internal and external forces. In addition, we present some information on force generation and force transmission in swimming fish to illustrate the importance of the rigorous mechanistic understanding of internal force dynamics required to produce predictive models of aquatic locomotion.

WHY IS THIS AN INTERESTING QUESTION?

Questions about the design for aquatic locomotion are potentially of interest to many biologists because a complex behavior that requires a tight integration of morphology, physiology and kinematics could not have arisen suddenly, rather it would have evolved over time from a less 'adept' ancestral form. In fact, swimming is a ubiquitous locomotory mode with much of biology (some insect and angiosperms excepted) needing to swim, and swim well, at some point in their lives. Swimming organisms span 8 orders of magnitude in size, and a billion years of common ancestry, yet we know precious little about the design constraints on swimming imposed by either the physical environment, biological materials or phylogenetics. By developing a

biomechanical understanding of the determinants of swimming performance it may be possible to tease apart the critical aspects underlying a behavior common to such a wide range of biological diversity.

There are two primary reasons why it is necessary to know how the components of the swimming-system interact to predict swimming performance. Firstly, the coupled nature of the mechanical system means that studying any one component in isolation neglects the feedback inherent in the system as a whole. This feedback can take at least two forms, mechanical and sensory. Both are lost when, for example, a muscle bundle is dynamically tested *in vitro*, or when a model fin is undulated in a flow tank. This fact does not escape most experimentalists, and as a result tests on isolated components are designed to mimic *in situ* conditions (*e.g.* periodic loading of muscle fibers as opposed to isometric or isotonic loading, running physical models under non-steady state flow conditions). However, this points to the second motivation for our approach: the strongly non-linear nature of coupling between the internal and external components. The non-linearities arise from several sources. At the scale of most swimming fishes and man-made underwater vehicles the fluid-body interactions are governed by the highly non-linear relation between the viscous and inertial fluid stresses. At the level of the organism's tissues, the mechanics are dominated by the non-linear visco-elastic nature of biological materials, as well as the strain, strain rate, frequency and excitation phase dependence of force output from the swimming musculature. The implications of these non-linearities are manifold. Of highest importance is the explicit unpredictability of the system's behavior under novel situations. As we noted above, *in vitro* experiments must be performed under *in vivo-like* conditions in order to capture the component's appropriate behavior. However, due to the coupled non-linear nature of the component's interactions, it is difficult, if not impossible, to guess what the *'in vivo-like* conditions' would be for a situation other than the normal behavior of the system. That is to say, with experimental techniques alone it is possible to completely describe the function of an observed swimming-system, but it is not possible to develop predictive relationships without a mechanistic understanding of the components's interactions.

There are many questions that we would like to address on the mechanics of swimming. These questions reflect our approach to the field of aquatic locomotion, and express the sorts of objectives that biologists have in exploring questions that relate to the mechanics of swimming.

(i) How do the morphology and physiology of the organism interact to determine swimming behavior? We think of a swimming organism as a mechanical system, where each component (e.g., muscles, skeleton, body shape) can be characterized in isolation, but only when all the parts are connected can the system's behavior be recovered.

(b) What is the effect of variation in the organism's morphology and physiology on swimming behavior and performance? In other words, how well tuned is this mechanical system? There is natural variation in everything biological, but how does an interconnected mechanical system incorporate, or compensate for this variation? Or does it need to?

(3) What are the most effective parameters of the swimming system to change, and in what way, to 'optimize' the design for swimming? Organisms swim for a variety of reasons (e.g., feeding, predation escape, place holding,

migration), each with its corresponding performance criterion (stealth, acceleration, maneuverability, efficiency). How is an organism built to accomplish these varied tasks? Are there tradeoffs in the design for swimming to maximize a single performance criterion, or is it possible to be a generalist?

A MECHANISTIC FRAMEWORK: THEORY

We are using a predictive mathematical model (Jordan, 1996) to explore design issues in aquatic locomotion. The model is based on the body architecture of an axial swimmer. It has skeletal elements connected by active and passive tissues housed in a body shape for fluid-body interactions. The model takes as its only input a pattern of swimming muscle activation. Life-like swimming behavior emerges as a property of the morphological and physical properties of its component parts.

The fundamental governing equations for the preliminary model are the equations of motion for a body segment in 2-dimensions (dorso-ventral and anterior-posterior axes). Ignoring the third dimension assumes left-right symmetry and saves computational time since including the third dimension would increase the complexity of the system at least as N^2, where N is the number of state equations.

For a body free to translate and rotate in 2 dimensions the equations of motion say that the sum of forces in the x and y directions equal the object's mass times the acceleration in the x and y directions, and that the sum of the moments is balanced by the angular acceleration times the moment of inertia. Therefore, the position in space of a body through time is given by the solution to the resulting system of 2^{nd} order ordinary differential equations.

In this simple 2-D model, an organism's body is represented by n rigid elements (generally 10), each with mass, connected by hinges that transmit force, but not moments. The hinges are spanned by a material with the active and passive mechanical properties of muscle and connective tissue. Internal forces are generated by the deformation of this material, and external forces are generated by the movement of each segment in the surrounding fluid. For example, exciting a ventral muscle segment may result in dorso-ventral bending, stretching tissue dorsally and displacing adjacent segments. In this case, muscle forces act to rotate adjacent segments, while the passive tissue forces act to resist that rotation. In addition, tissue connections to up and down-stream segments transmit forces, resulting in rotations and translations. Any motion of a segment is also opposed by the fluid around the body relative to the shape of the segment as well as its velocity and acceleration. All of these interactions are instantaneous and interdependent. Thus, the only way to determine the effect of exciting a muscle segment on the entire body it so simultaneously solve the equations of motion for each segment (a system of $3n$ 2^{nd} order ordinary differential equations in $3n$ unknowns, position and orientation of each element). This means that the forces and moments that are summed over each body segment arise directly from the morphology and physiology of each segment and the swimming behavior, from their mechanical coupling. Therefore, to model a swimming organism in this fashion, we need to describe the mechanical properties of each segment, and allow them to interact *via* the system of governing equations presented above.

At present, body-fluid interactions are included in the model in the form of sectional force coefficients. The fluid forces are approximated by the linear superposition of local resistive and reactive forces. This method assumes that each section of the organism 'sees'

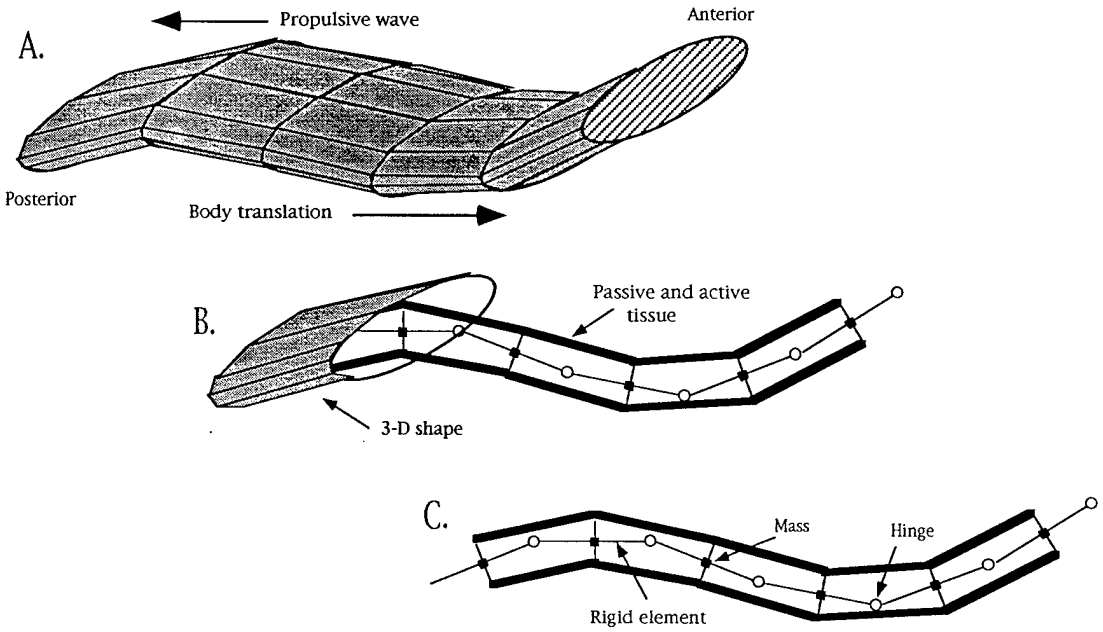

Figure 1. The geometry of the 2-dimentional mathematical model. A. The overall shape to the model is that of an elliptical solid. B. The backbone of the model is spanned by tissue with the mechanical properties of active and passive soft tissue. C. The backbone consists of ridig elements with mass joined by hinges.

undisturbed fluid, and that the force exerted on each section is the sum of the fully-developed drag and added-mass forces given the instantaneous velocity and acceleration of the section. The obvious limitations of this approach are the neglected segment-segment interactions through the fluid, the assumption of fully-developed flow over each segment, and the linear combination of resistive and reactive components. None the less, under some circumstances these assumptions are not bad (Williams 1994a&b, Jordan 1992), and the ease of implementation makes the approach very attractive.

One of the primary limitations to the coefficient approach is the lack of information regarding the magnitude of sectional resistive and reactive force coefficients in non-rectilinear flow for non-engineering shapes (with the exception of rough circular cylinders in harmonic cross-flow, Sharpkaya and Storm 1985). To overcome some of the limitations inherent in the coefficient based approach, sectional fluid forced could be measured directly from a translating and undulating body. Coefficients determined in this manner explicitly relax the assumptions of no up- and down-stream interactions, and thus represent a marked

improvement over present applications of force coefficients.

Unfortunately, the 2-dimensional force balance outlined above is not sufficient to describe the mechanical structure of all axial locomotors. The 2-dimensional description may be inadequate due to extensive changes in body length (e.g. a soft bodied organism), or, despite the presence of an axial skeleton, pressure or local volume changes may be mechanically important (Videler 1993, Wilson et al. 1996). In either case, a 3-dimensional force balance would be required to capture all mechanical interactions. It is possible to represent a 3-dimensional structure with a framework of extensible elements joined by hinges that encloses a constant volume (Niebur and Erdos 1991, Wadepuhl and Bevin 1989). Such a construct would be capable of representing a highly deformable body but is very computationally intensive. In addition, no refinements of the fluid-body interaction are gained from this method. Therefore, we also describe a coupling of the internal and external mechanics *via* a novel numerical representation of fluid-body interactions; the immersed boundary method (introduced by Peskin 1977 to model blood flow in the heart).

In the immersed boundary method, the organism is represented by a distribution of forces applied to the fluid. This approach is analogous in spirit to the distribution of Stokeslets used to model the hydrodynamics of flagellar propulsion (Gray and Hancock 1955). However, there is no restriction to zero Reynolds number flow. Moreover, unlike Gray and Hancock's theory, individual segments of the organism do interact through the fluid dynamics. The lack of a material representation of the organism overcomes the primary hurdle to solving the full incompressible Navier-Stokes equations for arbitrary motions at arbitrary sizes, that of time dependent boundary conditions. In the immersed boundary method, the full incompressible Navier-Stokes equations are solved numerically on a uniform grid in an infinite (periodic) fluid domain. Thus, the layer of force that represents the organism results in fluid motion (solution of the N-S equations at each time step), and the representation of the organism moves with the velocity and acceleration of the fluid points corresponding to its boundary (no-slip condition).

A number of swimming organisms have been modeled by the immersed boundary method (Fauci & Peskin 1988, Fauci 1990, 1993, 1996). In these models the organisms are represented by elastic filaments which contain the point sources of force being applied to the fluid. A target configuration of these points as a function of time is supplied to the model (in a sense a prescribed motion), but due to the elasticity of the filaments, the target configuration may not be reached. Herein lies the overwhelming advantage of this approach; an inherent coupling between the mechanical properties of the immersed boundary and the surrounding fluid. Such a coupling results in either computational intractability for models of organisms as time dependent material-fluid boundaries, or critical assumptions of fluid realm (zero or infinite Reynolds number), organism shape (spheres, infinite cylinders, flat plates and Joukowski airfoils), or motions (harmonic or rectilinear) in order to solve the full Navier-Stokes equations.

We have constructed a 2-D undulating body consisting of point masses joined by visco-elastic elements that have the active and passive mechanical properties of leech body wall. The next step will be to couple the internal body mechanics, with the external fluid mechanics calculated from numerical solutions to the equations of fluid motion. As described above, the internal and external mechanics are inherently coupled by the immersed boundary

method. The elastic filaments traditionally used to connect the material points of the immersed boundaries will be replaced with a visco-elastic material that has the active and passive properties of connective tissue and the swimming-muscles. As in all of our modelling efforts, instead of prescribing the motion of the model organism, we will prescribe the pattern of muscle activation, and predict the swimming motion.

WHERE DO INTERNAL FORCES REALLY COME FROM?

The notion of internal forces relies on two important components that are themselves coupled - force generating mechanisms and force transmission systems. In fish for example, the force is generated by muscle which possesses a complex anatomical geometry and the trajectories of forces from production at the muscle to application to the surrounding fluid are not always obvious as a result. Indeed, it is only recently that there has been an appreciation of the role of a force transmission system composed of collagenous connective tissues that is at work in the axial swimming of fish.

At the beginning of the last century the aerodynamicist Sir George Cayley performed a preliminary analysis of the source of undulations in swimming trout and deduced that the swimming muscle amounted to a series of blocks that ran down both sides of the vertebral midline, one connected directly to the next (Bone *et al.*, 1995). Undulations of the body during swimming resulted from the sequential activation of blocks of muscle and that a wave of undulation would proceed down the body. Integral to this vision are two important components. Firstly, muscle is attached to muscle and the trajectory of their forces must therefore pass one to the next down the body. Thus, the wave of undulation down the body is a manifestation of the history of muscle activity down the body. The second important issue is that muscles act locally - that is to say that the movement produced by a muscle is manifest at approximately the same location on the body as the muscle itself.

Importantly, undulatory swimming in fish is powered by laterally placed myotomes that are highly folded rather than appearing as cubic solids. Each myotome is separated from adjacent myotomes by a myoseptal sheet composed of collagen fibers that serves as an attachment point for the muscle fibers within the myotomes. Myotomes appear to be activated sequentially on each side to produce a propulsive wave that increases in amplitude toward the tail. Superimposed on the complex myotomal anatomy is an additional anatomical distinction in that swimming muscle consists of two main fiber types that are recruited differentially: red being used for low intensity, sustained swimming and white for high intensity, short duration bursts. In the majority of fishes the red muscle is located in a lateral wedge of tissue close to the skin. Exceptions to this include tunas and some lamnid sharks that contain an additional large loin of red fibers located in a medial position within the myotomes that in other fish would be exclusively white fibers. It has been suggested that this arrangement is an adaptation for high performance swimming, but this hypothesis remains to be rigorously validated. At the very least, however, the distribution of red muscle in tunas will have mechanical consequences that need to be examined.

Critically, as a mechanical tissue, skeletal muscle does several jobs: it actuates a dimensional change (i.e. shortens), it generates force, it does work (force x distance) and generates mechanical power (force x shortening velocity). Importantly, the intrinsic characteristics of muscle prevent it from

simultaneously doing all of these jobs maximally. Therefore, understanding the way in which muscles are utilized in this fish is fundamentally important to understanding the swimming mechanics of the fish. Modeling the power output of cyclically shortening muscle is problematic because the muscle shortening velocity continually changes during the power stroke. In addition, force may be developed as the muscle is being lengthened or shortened. Traditional estimates of power output using *in vitro* force-velocity curves derived from isotonic shortening experiments are inappropriate for modelling fish swimming muscle because these measurements only consider force produced during shortening, and will overestimate the *in vivo* power output (Swoap et al., 1993).

Recent use of the oscillatory work-loop technique addresses many of these limitations. Isolated muscle fibers are subjected to sinusoidal length changes and phasic stimulation, mimicking the cyclic *in vivo* loading conditions (Rome *et al.*, 1990, 1992a&b). Thus, the work-loop technique is highly appropriate for determining realistic values of power output and efficiency of fish muscle (Altringham and Johnston, 1990a,b; Johnson and Johnston, 1991; Anderson and Johnston, 1992; Johnson *et al.*, 1991; Moon *et al.*, 1991; Rome and Swank, 1992; Altringham et al, 1993; Rome *et al.*, 1993).

Attempts to map *in vitro* experiments on isolated muscle samples onto the whole animals have used body curvature to estimate local muscle strain patterns and EMG to estimate local patterns of muscle activation. Using curvature as an index of muscle strain, studies on carp and saithe white muscle (Hess and Videler, 1984; Van Leeuwen et al., 1990, Altringham et al., 1993) suggest that in these fish the anterior muscles are activated with the appropriate phase to produce maximal positive work. In contrast, more posterior muscles are actively stretched (*i.e.*, do negative work) during an increasing proportion of the cycle, thus acting as transmission elements for the power from more rostral contractions. The most caudal muscles are predicted to do entirely negative work, thus functioning essentially as tendons rather than actuators. An alternative view is that of Rome et al (1993) who proposed that for superficial red muscle in scup, the posterior fibers generate the majority of the power for swimming, by virtue of their larger strain, and relatively earlier activation compared to the anterior fibers.

It is important to remember that if local body curvature does not specifically define the phase and amplitude of muscle strain at the same anatomical location, then the mapping of *in vitro* muscle experiments to *in vivo* dynamics will not accurately model muscle work output during swimming. Recent work on the mackerel, *Scomber japonicus* using x-ray videography indicates that in these fish local curvature is, in fact, a very reliable indicator of local red muscle strain (Shadwick *et al.*, 1997). Radio-opaque, gold beads were surgically introduced into the muscle of the fish who were then allowed to swim in a small flume that was placed in the beam of a video-radiography apparatus. Local changes in muscle length, indicated by the distance between gold beads, were correlated in time with estimates of muscle strain deduced from local body curvature and thickness - the estimation of strain from curvature amounts to treating the bending body of a fish as a continuous, homogeneous beam. This observation has also been made in scup by Caughlin *et al.* (1996) using sonomicrometry and high speed videography.

These observations suggest that in spite of the complex geometry of the myotomes, it may be possible to model analytically the

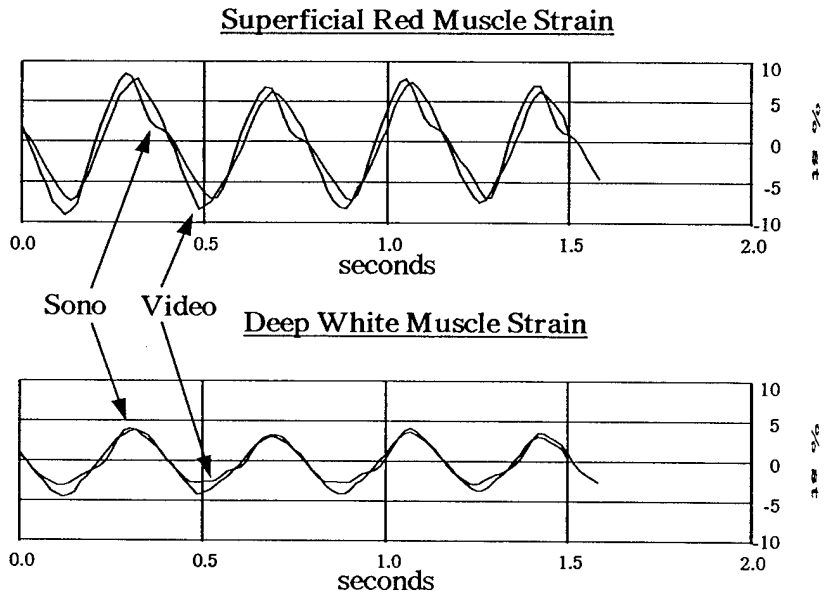

Fig. 2 Plot of muscle strain estimates from videography compared from direct measures of muscle segment strain from sonomicrometry in swimming milkfish (Channos channos) swimming at 2.34 L/s. The sonomicrometry crystals were located at 0.53L at the skin surface and deep at a point halfway between the backbone and the skin in the epaxial myotomes.

myotomes as a homogeneous continuum. In tunas the result is somewhat different. One of us (SLK) has recently completed work on the mechanics of red muscle of skipjack and yellowfin tuna while steadily swimming in a water tunnel treadmill. We compared estimates of local muscle shortening deduced from measurements of local curvature of the body midline calculated from video images with direct measurements of dimensional change made with sonomicrometry. (Fig. 2) Sonomicrometry is a technique that amounts to measuring the time it takes a series of ultrasound pulses to travel between two piezoelectric crystal elements that are implanted in the muscle (Covell *et al.*, 1991; Ohmens *et al.*, 1993). The product of the travel time and the speed of sound in muscle is the distance between the crystals. The emitted sound is in the ultrasound frequency range and the travel times are very short, thus the distance can be sampled very frequently and the temporal resolution of length changes is quite high (5 KHz). Looking first at the wedge of red muscle that is adjacent to the skin we have observed that the muscle length changes are quite well estimated by local curvature. However, the internal loin of red muscle does not shorten in phase with local body curvature. Indeed, at the approximate midpoint of the body of yellowfin muscle length changes are almost 30 degrees

later in time (= phase within one tail beat period) than the local body bending. (Fig. 3) A consequence of this observation is that some mechanical shear must occur in the inactive white muscle between the loin of deep red muscle and the skin. The energetic losses that result from this shear consume some of the force generated by the muscles and in effect form a force trajectory in addition to the that which results in momentum transfer to the surrounding fluid. The relative magnitude of this force trajectory to any other remains a complete unknown. In any event, the results from tuna suggest that the geometric features of red muscle distribution in these fish impart mechanical performance that will likely turn out to be important when attempting to implement biomimetic design ideas gleaned from scombrids in human-engineered designs.

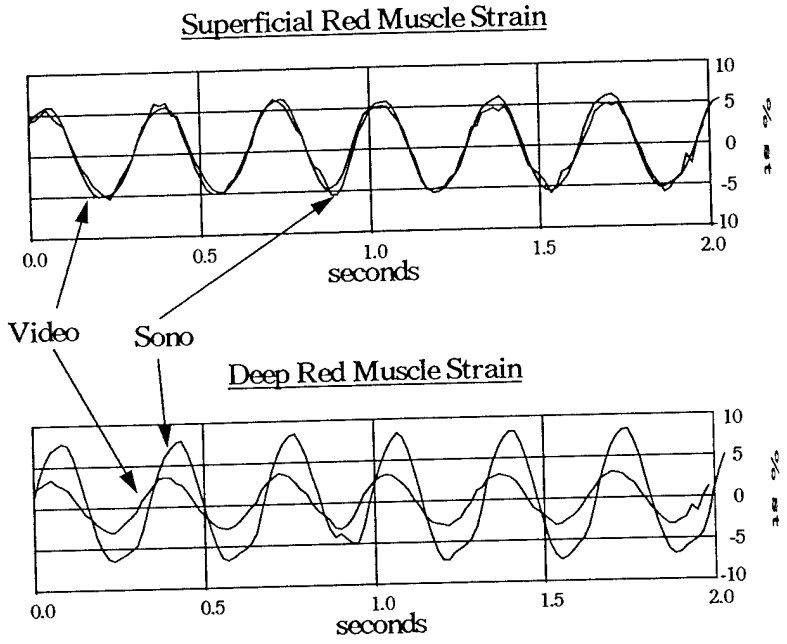

Fig. 3 Plot of muscle strain estimates from videography compared from direct measures of muscle segment strain from sonomicrometry in swimming yellowfin tuna (Thunnus albacares) swimming at 1.8 L/s. The sonomicrometry crystals were located at 0.46 L at the skin surface and deep at a point halfway between the backbone and the skin in the epaxial myotomes.

WHERE DOES THE FORCE GO?

Recently a number of researchers have drawn attention to the presence of highly ordered connective tissue elements located within the axial musculature. Perhaps most significantly, Westneat *et al.* (1993) in analysizing connective tissue functional morphology previously described by Kishinouye (1923), Kafuku (1950) and Fierstine and Walters (1968) arrived at a model for the action of organized tendons within the mid lateral septum of scombrid fishes. In brief, red muscle fibers that lie above or below the mid-lateral septum attach to collagen fibers that coalesce into a tendon near the skin. The path of the tendon travels obliquely and medially down and inserts onto the vertebral column several vertebrae caudal to the location of the muscle fibers. The suggested mechanical role of these oblique tendons is an important departure from Cayley's vision in that myotomal muscle is attached to tendons which subsequently attach to bone. This anatomical force trajectory from muscle to bone is also important in that it suggests that muscle is acting over a distance of perhaps several vertebrae - rather than strictly at the same anatomical position as the muscle fibers themselves. Despite being parsimonious and satisfying from the point of view that all other locomotor muscle systems in vertebrate animals consist of muscle-tendon-bone linkages, this model remains untested. Indeed, the technical and surgical requirements of testing this hypothesis - introducing force transducers into the midlateral septum of otherwise intact fish - are quite daunting.

It should be pointed out that although described for scombrid fishes, the oblique tendon system is nearly ubiquitous in fishes and if its mechanical role proves true for scombrids it will likely prove to work in other fishes as well. What does make scombrids, and in particular tunas, distinct from other fishes in this regard, is the progressive replacement of the most caudal myotomes with tendon (Fierstine and Walters, 1968). The great lateral tendon is formed from the collagenous myoseptal sheets that separate myotomes in the caudal portion of the body. These tendons run from the caudal myotomes, across the caudal peduncle and insert on the hypural bones of the caudal fin. The mechanical role of these tendons has been explored by Knower *et al.* (1997) in a couple of species of tuna swimming in a water tunnel. The tension in the tendon is transduced by a steel tendon force buckle after the design of Biewener *et al.* (1988). Briefly, the tendon force buckle is a three tyned fork through which the tendon is woven. When under tension, the tendon deflects the tynes of the fork. A small, resistive strain gauge is bonded to the middle tyne of the fork. The strain gage forms one arm of a Weatstone bridge and changes in voltage potential across the bridge are correlated with loads on the tendon. This work has shown that

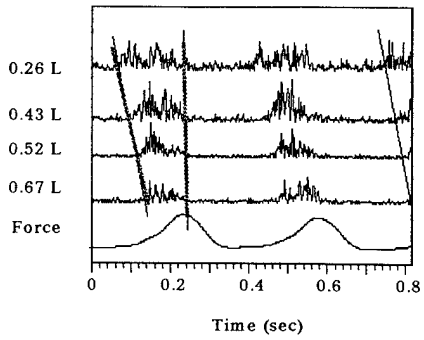

Fig. 4 Plot of electromyography data for four longitudinal positions on the body of a steadily swimming yellowfin tuna swimming at 1.8 L/s compared with simultaneous measurements of force in the caudal tendons. The EMG data were collected at locations 0.26 L, 0.43 L, 0.52 L, and 0.67 L. This figure is based on data from Knower et al. (1997).

during steady swimming these tendons are substantially loaded. More significantly than the magnitudes of the loads, perhaps, is the observation that tension in the tendon starts to rise when myotomes in only the most anterior one third of the body are active, as indicated with simultaneous electromyographic recordings. This indicates that force generated in these most anterior myotomes is somehow transmitted along the length of the fish, across otherwise inactive muscle, during swimming. In scombrid fishes this is an additional and important trajectory of force transmission from the force generating machinery to the tail blade and subsequently the surrounding fluid.

Fish skin contains collagen fibers that form crossed helical layers around the body. Fish skin has been recognized as an important mechanical component in the musculoskeletal system by many investigators (Motta, 1977; Hebrank, 1980; Videler, 1993; Wainwright, 1983; Long *et al.*, 1996) and its importance as an external "body tendon" was demonstrated in sharks. Mechanical tests on teleost skin, including skipjack tuna (Hebrank and Hebrank, 1986) indicated a relatively low stiffness in the longitudinal direction. This does not mean that the skin is not suitable for longitudinal force transmission because if the shortening muscle bulges laterally it will expand the skin in the dorsoventral direction and cause it to shorten longitudinally. This has been proposed as a force transmission mechanism (Wainwright, 1983; Videler, 1993) and tested in preliminary work by Muller and Blickhan (1991) on trout. The helical layering of collagen fibers in the skin means that each fiber connects a point on one edge of the sheet of skin (*i.e.* on the dorsal or ventral midline) with a more posterior point on the opposite edge (Videler, 1993), also suggesting that loading of the skin would likely transmit forces longitudinally.

Other anatomical evidence suggesting a mechanical role for the skin includes the observation that in tuna the skin is firmly attached to the myosepta of the lateral muscles above and below the region of the superficial red muscle. This suggests that while the medial anterior pointing muscle and myoseptal cones link to the backbone *via* the oblique tendons, the posterior pointing cones, which are situated more dorsally and ventrally, link to the skin. In addition, the skin is well fused to the superficial lateral caudal tendon (called the subdermal sheath by Westneat *et al.*, 1993) which inserts directly onto the caudal fin rays, suggesting that forces transmitted to the skin *via* the myosepta could be applied directly to the tail.

Preliminary results of dynamic, biaxial mechanical tests of salmon skin (Katz and Gosline, unpublished results) reveal previously undescribed mechanical behavior of the skin. Because the angle the collagen fibers make with the antero-posterior axis of the fish is greater than 45°, as it also is in tuna skin, strain in the dorsoventral direction causes longitudinal shortening in the central region of the test piece even though the margins of the test piece are subjected to simultaneous tensile strain. This interesting phenomenon probably arises as a function of the crossed fiber structure, and thus skin from other fish (*e.g.* tuna) with fibers > 45° should behave similarly, but obviously this needs to be investigated directly. The significance of the preliminary findings is that the fish skin has appropriate mechanical properties to transmit forces along the body if loaded by lateral thickening of the underlying muscle.

The model used in previous mechanical analyses of fish skin stiffness assumes effective transfer of force between collagen fibers, and a limited ability of the fibers to re-orient under load (*i.e.* a rigid, fiber reinforced material). If one considers a network of relatively mobile fibers in a soft matrix where there is relatively poor transmission of force from fiber to fiber

(*i.e.* the matrix is much more compliant than the fibers), one observes substantially different behavior than in either rigid composite or homogeneous elastic materials. Figure 5 illustrates the performance of fiber-reinforced sheets of material tested in biaxial tension. Significantly, if the skin fiber angles are 45° and the test piece is square, then at most one fiber in each orientation will traverse the entire test piece from grip to grip. If the test piece is square and fiber angles are greater than 45° (or if fiber angles are greater than 45° but the test piece is rectangular), then many fibers may traverse the test piece in one orientation, but no single fiber will traverse the sample in the opposite direction. In this case there will be a central portion of the test piece that must transmit all of the tension in that orientation *via* inter-fibrillar connections and the material stiffness one observes in this orientation is largely determined by the stiffness of the matrix. The size of this central area that relies on matrix stiffness will increase with increasing fiber angle. A situation like this will produce apparent differences in stiffness in the two primary orientations that are functions of the testing protocol rather than a function of fiber orientation in the intact tissue.

Unfortunately, there is no detailed description of the relationship between fiber angle and aspect ratio in the test pieces used in the mechanical tests of skin from skipjack tuna reported by Hebrank and Hebrank (1986). It is difficult, therefore, to rely on their conclusions that the skin is not capable of transmitting force longitudinally down the animal from anterior myotomes to posterior locations. Indeed, uniaxial tensile tests of the skin of aquatic salamanders - which contain a collagen cross-fiber network in a compliant, dermal matrix - produced exotic values of Poisson's ratio (Frolich *et al.*, 1994). These results suggest that such a network can impart at least unexpected mechanical performance, if not important locomotor performance as an element in the force trajectory from muscle to fluid.

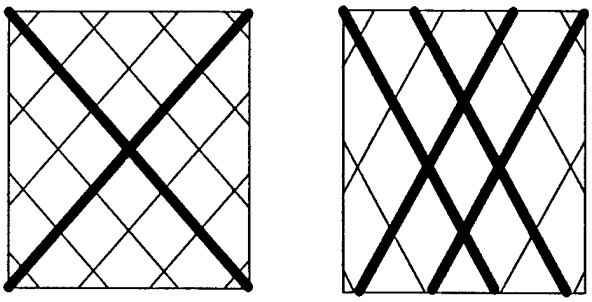

Fig. 5. Cartoon representation of the effect of the relationship between test sample aspect ratio and distribution of fibers in a compliant composite sheet. The left hand panel shows a square test piece with fibers oriented at 45 ° to the lateral axis. The right hand panel shows a square test piece with fibers oriented > 45 ° to the lateral axis. Fibers that traverse the entire test piece are shown in bold. See text for other details.

So we have a number of force trajectories to balance in constructing a synthesis of how the internal forces are generated: muscles pull on other muscles across myoseptal sheets, muscles apply force locally to the backbone via oblique tendons, muscles pull directly on the caudal fin via lateral tendons, viscous losses in shearing inactive muscle that surrounds the active medial red muscle of scombrids. A complete synthesis of the mechanics of internal force generation in fishes will, of necessity, await the elucidation of the relative importance of these various pathways of force transmission. We may be able to generate a clear picture of the amount of force generated by one particular block of muscle, but until we know what fraction of that force is applied locally to the body segment, how much is transmitted along the body for some distance and how much is lost in shearing adjacent, inactive muscle we will know nothing about

how that block of muscle is coupled to external forces and ultimately contributes to thrust production.

CONCLUSIONS

Our primary goal is to understand the mechanics of aquatic locomotion such that we predict the effect of morphology and physiology on swimming performance. To do so we need to know how the component parts of a swimming organism behave in the context of the entire dynamical system. Knowing this requires a detailed description of the mechanical coupling between components within the body, as well as between the body and the fluid. However, as we have demonstrated, the internal mechanics of force production can be extremely complex in a device that has the structure like a scombid fish. As a result, the swimming performance implications of these morphological complexities cannot be assessed until a full description of the linkages is known and represented mathematically in a mechanistic model.

This work represents a major advance for the field of aquatic locomotion in that it relaxes the assumptions inherent in exisiting approaches to the study of swimming. To do so, this appoach embraces the physical coupling between the internal and external mechanics of a swimming organism. As a result, we do not rely on prescribed body kinematics, nor can we generate mechanically or physiologically unrealistic conditions since the physical and biological constraints on a swimming organism are the framework of our methods. In a broader context, the development of an approach to address size and scale effects in aquatic locomotion has implications beyond biological studies of swimming mechanics. We are explicitly determining the critical design parameters required for any aquatic locomotor, biological or man-made.

ACKNOWLEDGEMENTS

This paper has resulted from the 10th International Symposium on Unmanned, Unteathered Submersible Technology Conference, the author's attendance at which was dependant on the generosity of the Autonomous Undersea Systems Institute, in particular Jim Jalbert as well as the Office of Naval Research. For this we are grateful. The included data on tuna represents some of the work of Torre Knower and Robert Skadwick, withwhom SLK collaborates. The Physiological data on tuna was funded by the National Science Foundation (IBN95-14203).

LITERATURE CITED

Altringham, J. D. and Johnston, I. A. (1990a). Modelling muscle power output in a swimming fish. J. exp. Biol. 148: 395-402.

Altringham, J. D. and Johnston, I. A. (1990b). Scaling effects on muscle function: power output of isolated fish muscle fibers performing oscillatory work. J. exp. Biol. 151: 453-467.

Altringham, J. D., Wardle, C. S. and Smith, C. I. (1993). Myotomal muscle function at different locations in the body of a swimming fish. J. exp. Biol. 182: 191-206.

Anderson, M. E. and Johnston, I. A. (1992). Scaling of power output in fast muscle fibers of the Atlantic cod during cyclical contractions. J. exp. Biol. 170: 143-154.

Biewener, A. A., Blickhan, R., Perry, A. K., Heglund, N. C., & Taylor, C. R., (1988). Muscle forces during locomotion in kangaroo rats: force platform and tendon buckle measurements compared. J. exp. Biol. 137(1):191-206.

Bone, Q., Marshall, N. B., and Blaxter, J. H. S., (1995). Biology of fishes (2nd Ed.). Blackie Academic & Professional. Glasgow Scottland. pp. 332.

Coughlin D. J., Valdes, L., and Rome, L. C., (1996). Muscle length changes during swimming in Scup: Sonomicromtry verifies the anatomical high-speed cine technique. J. exp. Biol. **199**:459-463.

Covell, J. W., Smith, M., Harper, D. G., and Blake, R. W. (1991). Skeletal muscle deformation in the lateral muscle of the intact rainbow trout *Oncorhynchus mykiss* during fast start maneuvers. J. exp. Biol. 156: 453-466.

Fauci, L. J., (1990). Interaction of oscillating filaments: A computational study. J. Comput. Phys. 86:294-313.

Fauci, L. J., (1993). Computational modeling of the swimming of biflagellated algal cells. Contemp. Math. 141:92-101.

Fauci, L. J., (1996). Computational modeling of unsteady flow from undulatory motions. Amer. Zool. 36(6).

Fauci, L. J. and Peskin, C. S., (1988). A computational model of aquatic locomotion. J. comput. Phys. 77(1):85-101.

Fierstine, H. L. and Walters, V. (1968). Studies in locomotion and anatomy of scombroid fishes. Mem. of the S. Calif. Acad. Sci. 6: 1-31.

Frolich, L. M., LaBarbera, M. and Stevens, W. P., (1994). Poisson's ratio of a crossed fibre sheath: the skin of aquatic salamanders. J. Zool., Lond. **232**:231-252.

Gray, J. and HAncock, G. J., (1955). The propulsion of sea-urchin spermatozoa. J. exp. Biol. 32:802-814.

Hebrank, M. R. (1980). Mechanical properties and locomotor functions of eel skin. Biol. Bull., 158: 58-68.

Hebrank, M. R. and Hebrank, J. H. (1986). The mechanics of fish skin: lack of an "external tendon" role in two teleosts. Biol. Bull. 171: 236-247.

Hebrank, J. H., Hebrank, M. R., Long, J. H., Jr., Block, B. A., and Wainwright, S. A. (1990). Backbone mechanics of the blue marlin *Makaira nigricans* (Pisces, Istiophoridae). J. exp. Biol. 148: 449-459.

Hess, F. & Videler, J. J. (1984). Fast continuous swimming in the saithe (*Pollachius virens*): a dynamic analysis of bending moments and muscle power. J. exp. Biol. 109: 229-251.

Johnson, T. P. and Johnston, I. A. (1991). Power output of fish muscle fibers performing oscillatory work: effects of acute and seasonal temperature change. J. exp. Biol. 157: 409-424.

Johnson, T. P., Johnston, I. A., and Moon, T. W. (1991a). Temperature and the energy cost of oscillatory work in teleost fast muscle fibers. Pflgers. Arch. 419: 177-183.

Jordan, C. J., (1996). Coupling internal and external mechanics to predict swimming behavior: A general approach? Amer. Zool. 36:710-722.

Kafuku, T., (1950). "Red muscle" in fishes. I. Comparative anatomy of the scombroid fishes of Japan. Gyoruigaka Zasshi 1:89-100.

Kishinouye, K., (1923). Contributions to the comparative study of the so-called scombroid fishes. J. Coll. Agric. Tokyo Imp. Univ. 8:293-475.

Knower, T., Shadwick, R. E., Katz, S. L., Graham, J. B., and Wardle, C. S., (1997). Red muscle activation patterns in yellowfin (Thunnus albacares) and skipjack (Katsuwonus pelamis) tunas during steady swimming. (In Prep.).

Long, J. H., Hale, M. E. , McHenry, M. J., and Westneat, M. W., (1996). Functions of fish skin: Flexural stiffness and steady swimming of longnose gar *Lepisosteus osseus*. J. exp. Biol. 199:2139 - 2151.

Moon, T. W., Altringham, J. D., and Johnston, I. A. (1991). Muscle energetics and power output of isolated fish fast muscle performing oscillatory work. J. exp. Biol. 158: 261-273

Motta, P. J. (1977). Anatomy and functional morphology of dermal collagen fibers in sharks. Copea 1977: 454-464.

Muller, U. K. and Blickhan, R. (1991). New functional aspects of fish skin during locomotion.. J. Mar. Biol. Ass. U. K. 71: 738.

Niebur, E. and Erdos, P., (1991). Theory of locomotion in nematodes: Dynamics of undulatory progression on a surface. Biophys. J. 60:1132-1146.

Ohmens, J. H., MacKenna, D. A. and McCulloch, A. D. (1993). Measurement of strain and analysis of stress in resting rat left ventricular myocardium. J. Biomechanics 26:665-676.

Peskin, C. S., (1977). Numerical analysis of blood flow in the heart. J. comp. Physiol. 25:220.

Rome, L. C. and Swank, D. (1992). The influence of temperature on power output of scup red muscle during cyclical length changes. J. exp. Biol. 171: 261-281.

Rome, L. C., Choi, I. H., Lutz, G., and Sosnicki, A. (1992). The influence of temperature on muscle function in the fast swimming scup. 1. Shortening velocity and muscle recruitment during swimming. J. exp. Biol. 163: 259-279.

Rome, L. C., Funke, R. P., and Alexander, R. McN. (1990). The influence of temperature on muscle velocity and sustained performance in swimming carp. J. exp. Biol. 154: 163-178.

Rome, L. C., Swank, D., and Corda, D. (1993). How fish power swimming. Science 261: 340-343.

Shadwick, R. E., Steffensen, J. F., Katz, S. L., and Knower T., (1997). Muscle dynamics in fish during steady swimming. Am. Zool. In Press.

Swoap, S. J., Johnson, T. P., Josephson, R. K., and Bennett, A. F. (1993). Temperature, muscle power output and limitations on burst locomotor performance of the lizard *Dipsosaurus dorsalis*. J. exp. Biol. 174: 185-197.

Van Leeuwen, J. L., Lankheet, M. J. M., Akster, H. A., and Osse, J. W .M. (1990). Function of red axial muscles of carp (*Cyprinus carpio*) recruitment and normalized power output during swimming in different modes. J. Zool. 220: 23-145.

Videler, J. J. (1993). Fish swimming. London: Chapman and Hall. [Fish and Fisheries series 10].

Wadepuhl, M. and Bevin, W.-J., (1989). Computer simulations of the hydrostatic skeleton. The physical equivalent, mathematic and application to worm-like forms. J. theor. Biol. 136:379-402.

Waiwright, S. A. (1983). To bend a fish, in Fish Biomechanics, (Eds. P. W. Webb and D. Weihs), Praeger, N. Y., pp. 68-91.

Waiwright, S. A., Vosburgh, F. and Hebrank, J. H. (1978). Shark skin: function in locomotion. Science 202: 747-749.

Westneat, M. W., Hoese, W., Pell, C. A., and Wainwright, S. A. (1993). The horizontal septum: mechanisms of force transfer in locomotion of scombrid fishes [Scombridae: perciformes]. J. Morph. 217: 183-204.

Williams, T. A., (1994a). Locomotion in developing *Artemia* larvae: Mechanical analysis of antennal propulsors based on large-scale models. Biol. Bul. 187(2):156-163.

Williams, T. A., (1994b). A model of rowing propulsion and the ontogeny of locomotion in *Artemia* larvae. Biol. Bul. 187(2):164-*et seq.*

Wilson, R. J. A., Skierczynski, B. A., Meyer, J. K., Blackwood, S., Skalak, R. and Kristan Jr., W. B., (1996). Mapping motor nueron activity to overt behavior in the leech:Internal pressures produced during locomotion. J. exp. Biol. 199:1415-1428.

Applied aspects of mechanical design, behavior, and performance of pectoral fin swimming in fishes

Mark W. Westneat and Jeffrey A. Walker
Department of Zoology, Field Museum of Natural History, Roosevelt Road at Lake Shore Drive
Chicago, IL 60605, 312-922-9410 x451, westneat@fmppr.fmnh.org, walker@fmppr.fmnh.org

Abstract

Many fishes use the pectoral fins to generate thrust across a broad range of speeds and to perform complex maneuvers. Analysis of the biomechanics of labriform locomotion provides several kinds of data that can be applied to the design of autonomous underwater vehicles (AUVs), including morphology, kinematics, and swimming performance. Data are presented here on pectoral fin locomotion in *Gomphosus varius*, a labrid fish that uses the pectoral fins at speeds of 1-8 total body lengths per second. First, the swimming performance of labrid fishes is assessed, including measures of critical swimming speed. Swimming performance of aquatic flyers is comparable or greater than performance of undulatory swimmers, suggesting that fin-based propulsion in AUVs may provide appropriate thrust as well as maneuvering capability. Second, the morphological structure of the fin suggests engineering features of flapping wings for aquatic propulsion that could be incorporated into AUV propulsors. A biomechanical model of the pectoral fin is proposed in which fin morphometrics and computer simulations allow predictions of fin kinematics in three dimensions. Third, three-dimensional kinematic data for the pectoral fins of *G. varius* are presented. Using video at 60Hz, we reconstructed the 3D motion of the center of mass, the fin tip, and two fin chords. We computed hydrodynamic parameters (Reynolds number, Strouhal number, and reduced frequency parameter) to define the hydrodynamic regime. Fin-beat frequency, stride length, stroke plane angle, stroke angle, and stroke area were also calculated. We measured the velocity and acceleration of the fish's center of mass in anteroposterior and dorsoventral directions, velocity and acceleration of the fin tip, leading edge, and trailing edge, morphological and hydrodynamic angles of attack at both fin chords, and the phase lag in positional angle between leading and trailing edges. This allowed us to construct a hydrodynamic hypothesis of the fin beat. At slow speeds, thrust and upward forces occur during both abduction and adduction while at higher speeds thrust is associated with downward forces during adduction. The reduced frequency suggests that unsteady effects are important in *G. varius* aquatic flight, especially at low speeds. Detailed kinematic data such as these are critical for AUV designs that attempt to mimic behaviors that have been optimized in fishes.

INTRODUCTION

Most fishes use their pectoral fins in some way for steady swimming, turning, braking, or balance. For many species, pectoral fin propulsion is the primary mode of swimming. Recent literature on pectoral fins includes several studies on the kinematics (Webb 1973; Blake 1979; Geerlink 1983; Archer and Johnston 1989; Gibb et al. 1994; Drucker and Jensen 1996; Walker and Westneat 1997), morphology (Blake 1981a; Geerlink 1989; Westneat 1996), and hydrodynamics (Blake 1981b; 1983a; 1983b) of pectoral fin locomotion. These studies identified the major levels of design in pectoral fin systems that relate to the mechanics and evolution of this mode of propulsion. However, few fish species that use pectoral fin propulsion have been studied, and only recently has research provided a detailed, quantitative analysis of labriform swimming biomechanics across a broad range of speeds.

The design of Autonomous Underwater Vehicles (AUVs) may benefit from the use of design principles learned from the study of fish biomechanics (Kato and Furushima 1996; Bandyopadhyay et al. 1997). We identified three areas of our research program that are of potential use for AUV technology; (1) the swimming performance and efficiency of labriform swimmers, (2) mechanical design of pectoral fins, and (3) kinematics of labriform propulsion. Thus, the objective of this paper is to summarize new data on the functional morphology of locomotion in the labrid fishes, the group for which labriform locomotion is named. Particularly detailed analysis is available for *Gomphosus varius*

(the bird wrasse), a high performance labriform swimmer at speeds up to 8 body lengths per second. The first section of the paper considers the performance and efficiency of fin locomotion. A central concern of AUV design is thrust efficiency of the propulsors. For fishes, this parameter can be explored by examining the swimming performance of species that use different swimming behaviors. Few pectoral fin swimmers have previously been tested for performance, and labriform locomotion has not previously been considered to be a high-performance mode of locomotion. New data is presented that suggests that pectoral fin locomotion may be an efficient mode of transport suitable for bioengineering applications in AUVs.

The second area of applied labriform locomotion involves the anatomy of pectoral fins and outlines a biomechanical model of these structures (Westneat 1996). This research asks the question: what is the musculoskeletal mechanism of pectoral propulsion? It is likely that future aquatic vehicle designs will mimic fin shape and perhaps internal fin architecture to acheive maximal thrust performance.

Finally, we present a detailed data set on fin kinematics (Walker and Westneat 1997). Studies of pectoral fin kinematics may provide the most important biological data for applied AUV technology, because mimicry of precise fin motions may produce the most efficient thrust for AUVs. Recent research has demonstrated the complexity of the motion of pectoral fins during labriform locomotion. Our goal has been to determine the 3-dimensional motions of the pectoral fin during the locomotor stroke. Pectoral kinematics are variable due to thrust requirements across a range of speeds, but general patterns useful for AUV design are summarized.

Mechanics of generating thrust in labriform locomotion.

In his classic monograph on fish locomotion, Breder (1926) recognized two modes of oscillatory pectoral fin propulsion, rowing and flapping. Rowing, according to Breder, is a largely fore-aft movement in which the pectoral fin is brought "forward almost edgewise and [forced] back broadside." By contrast, flapping is a largely dorsoventral fin motion. A recent detailed kinematic analysis of the flapping fin in the bird wrasse, *Gomphosus varius*, showed that large changes of pitch occurred throughout its motion (Walker and Westneat 1997).

Rowing and flapping employ different mechanisms for generating thrust (Blake 1983a; Vogel 1994). During the power stroke of rowing, the fin is pulled back broadside to the flow of water. The resistance to moving the fin against the local flow creates a large pressure drag at the fin, which, being directed anteriorly, is felt as thrust at the body's center of mass (Blake 1979). In addition to this drag-based thrust, a rowing fin probably generates substantial thrust during the power stroke from the acceleration reaction. As the fin is rapidly pulled back at the onset of adduction, the fin accelerates a large mass of water in the caudal direction. This causes a reaction force in the opposite direction that is felt as thrust at the center of mass. The acceleration reaction should also contribute a small thrust component during the end of abduction as the fin slows down (thus having caudally directed acceleration) in order to reverse its direction (Daniel 1984). As the magnitude of the acceleration reaction is proportional to the projected fin area orthogonal to the path of fin motion, the contribution of the acceleration reaction to the latter part of abduction should be small because the fin is feathered during this portion of the stroke cycle. Finally, it has also been suggested that the rapid closure of the space between the fin and the body at the end of adduction creates a jet reaction force that contributes to thrust (Blake 1979; Geerlink 1983; Daniel & Meyhofer 1987).

During steady forward swimming using a flapping stroke, the oscillation of the fin creates a vertical component to the flow over the fin. By maintaining the fin at a small angle to this local flow, a net circulation around the fin is generated, causing a lift force normal to the flow. The component of lift in the direction of swimming is felt as thrust at the center of mass (Webb 1973; Blake 1983a, b). Until recently, unsteady effects due to a rapidly oscillating fin were thought to decrease lift (Daniel and Webb 1987) due to the time it takes for circulation to rebuild following each half stroke. On the contrary, recent studies from flapping insect wings have shown that unsteady effects can greatly enhance lift (Dickinson 1994; Van den Berg and Ellington 1997a,b). Two unsteady mechanisms of enhanced lift production that could potentially

be employed by fish or AUVs include the fling and delayed stall. In insects, the fling is the rapid opening of a space between the previously closed wings during the start of the downstroke. Movement of water into this void creates a large vortex (Spedding and Maxworthy 1986) that allows instantaneous development of circulation. For fish, or a similarly designed AUV, the fins would not open from each other but from the vehicle's body. Delayed stall occurs when the translating fin accelerates following stroke reversal at a large angle of attack, creating a leading edge vortex due to separation of the flow over the fin. This vortex incresaes flow velocity over the wing, similar to a wing with increased camber (Van den Berg and Ellington 1997a,b).

Vogel (1994) recently argued that rowing and flapping operate most effectively at different swimming speeds. Resistance during the power stroke in rowing is proportional to the speed of the fin moving backwards relative to the speed of the fish moving forward. This ratio is greatest when the body is not moving at all and, for a constant oscillation frequency, declines with increasing swimming speed. By contrast, in a lift-based stroke, lift increases with the speed of the water over the fin and, therefore, with the speed of the fish. At a given oscillation frequency, however, thrust increases only to a point. The eventual decrease in thrust with increasing swimming speed reflects the point at which the horizontal component of lift begins to decrease, despite an increase in length of the lift vector in general, due to the increasingly vertical orientation of the vector.

Vogel modeled the magnitude of thrust generated over a range of speeds but the mechanical effiency of the mechanism over the same range of speeds may be more important for a fish or AUV. Blake (1979; 1980) computed a mechanical efficiency of 0.16 for the rowing stroke used by *Pterophyllum eimekei* (length = 0.08m) swimming at 0.04 $m \cdot s^{-1}$ while Webb (1973) estimated an efficiency of between 0.6 and 0.65 for the flapping stroke of *Cymatogaster aggregata* (length = 0.143 m) swimming at 0.55 $m \cdot s^{-1}$. These data support the generally held view that lift-based flapping is a more efficient mechanism than drag-based rowing, at least at their preferred speeds. In addition, there is a tendency for fishes that maneuver slowly within structurally complex habitats to have paddle or fan shaped fins, which are better designed for drag-based mechanisms (Blake 1981a) while fishes that swim at higher speeds have more wing-shaped fins, which are better designed for lift-based mechanisms.

Performance of labrid fishes.

The efficiency of thrusters is a critical criterion for AUVs due to limited power supply. The use of fish-like fins for generating thrust and maneuverability must therefore meet with stringent criteria for thrust performance. As mentioned above, this performance will likely vary depending upon whether high speed is desirable or lower speeds and high maneuverability are required. An important consequence of Vogel's hypothesis for both fishes and AUVs with different locomotor requirements is that a vehicle employing a flapping stroke should be able to achieve and maintain higher pectoral-fin-powered speeds than one employing a rowing stroke.

We tested this idea by comparing the association between pectoral fin kinematics and maximum speed achieved and maintained using only pectoral-fin based locomotion. We compared several species pairs that differed in the degree to which they used a rowing or a flapping stroke. In the first pair, *Gomphosus varius*, a flapper, and *Halichoeres bivittatus*, a rower, are members of the tribe Julidinae. In the second pair, *Cirrhilabrus rubripinnis*, a flapper, and *Pseudocheilinus octotaenia*, a rower, are members of the tribe Cheilininae. We used two different types of increasing velocity tests to measure performance. In the first design, which followed traditional protocol for establishing critical swimming speed, we started individuals at 2.0 $BL \cdot s^{-1}$ and increased the flow rate 0.25 to 0.33 $BL \cdot s^{-1}$ at 15 minute intervals. We noted the time the fish first supplemented pectoral fin propulsion with body and caudal fin propulsion but allowed the trial to continue until the individual reached exhaustion and could not be forced to swim (Ucrit). In the second design, we started the fish at 2.0 BL/s and increased the flow by 0.25 to 0.33 $BL \cdot s^{-1}$ increments but at 20 second intervals (20 second intervals were used because this is the lower limit of prolonged swimming). A trial ended when the fish could not maintain position in the flow using only its pectoral fins (Upc).

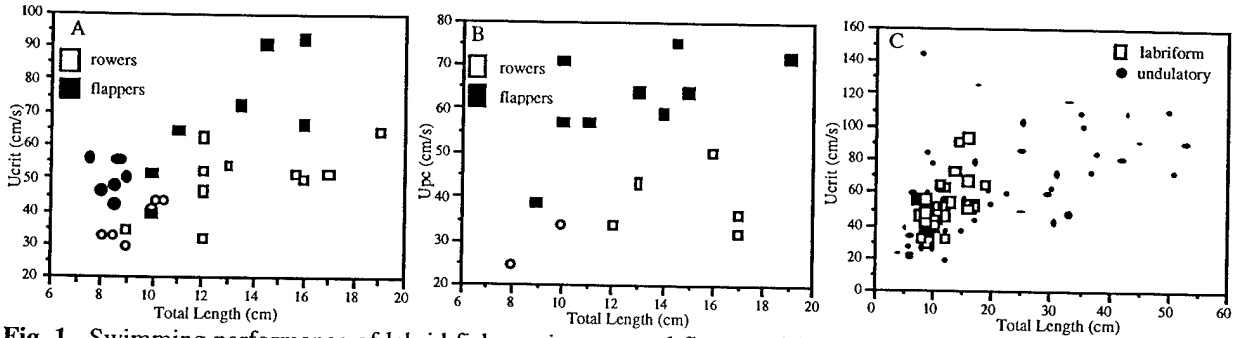

Fig. 1. Swimming performance of labrid fishes using pectoral fin propulsion. (A) Critical swimming speed (Ucrit) as a function of body size. Two species are rowers (open symbols) and two are flappers (closed symbols). (B) Critical pectoral fin- caudal fin swimming speed (Upc) in the same fishes. (C) Labrid performance data (open squares) compared to similar performance data for a range of undulatory swimming fishes (points).

We found that species that use a flapping stroke have a greater Ucrit and Upc, relative to body length, than species employing a rowing stroke (Fig. 1a, 1b). These data support our hypothesis that fishes employing a flapping stroke should be able to achieve and maintain higher steady swimming velocities, relative to fishes employing a rowing stroke, using only pectoral fins as propulsors. In addition to this within-wrasse comparison, we have compared swimming performance in wrasses to that of other fishes using an undulatory body-caudal fin mode of swimming (Fig. 1c). The non-wrasse data were collected from the literature and represent fishes with diverse ecologies, including stalking predators (*Esox*), generalized piscivores (*Micropterus*), anadromous fishes (*Onchorhynchus*), and marine pelagic piscivores (*Scomber*). Because of differences in methodology, as well as fish condition, water temperature and condition, etc, Fig. 1c should not be used to compare specific species but to explore general trends. The trend that has some importance for the design of AUVs is the relatively high size-specific swimming performance of wrasses that employ a flapping stroke, suggesting that pectoral fin propulsion is an effective alternative to body and caudal fin propulsion for steady swimming behavior.

Morphology and mechanical design of fin propulsors.

If AUVs are to use paired oscillating fins for propulsion, there may be design features that could be copied from of external and internal fin morphology. The morphological basis of pectoral propulsion has been described in the cichlid *Sarotherodon niloticus* (Geerlink 1979), and two labrid fishes in the genus *Coris* (Geerlink 1989). The muscle origins and insertions and the attachments of tendons to the bases of fin rays allow two axes of rotation for pectoral fin rays: motion in an anteroposterior plane and a dorsoventral plane. The leading edge fin ray articulates with the scapula in a saddle-shaped joint, which also allows biaxial motion of the fin ray.

Recently, we proposed a biomechanical model of the pectoral fin flapping mechanism in *Gomphosus varius* (Westneat 1996). Mechanical modeling of this system uses morphometric data on pectoral design and lever mechanics to generate a predictive model of fin motion. The pectoral girdle (Fig. 2A) is the anchor upon which the pectoral muscles originate. The anteroventral surfaces of the cleithrum, both laterally and medially, as well as scapula and coracoid, are the sites of attachment for abductor and adductor musculature (Fig.2B, 2C). The first pectoral fin ray is a short, thick ray that articulates with the scapula in a synovial joint. The first and second pectoral rays are tightly connected by connective tissues to form a single rotational element that forms the leading edge of the pectoral fin (Fig. 2A). Pectoral rays 2-16 in *G. varius* have their bases imbedded in a fibrous pad that separates them from the underlying radials. Pectoral fin shape is determined largely by relative fin ray length: the anterodorsal rays of *G. varius* are the longest and the rays taper in length from dorsal to ventral to form a wing-shaped fin.

Six major pectoral muscles actuate the fin during locomotion. Three muscles form the abductor complex that abducts the fin in the downstroke. The abductor superficialis and

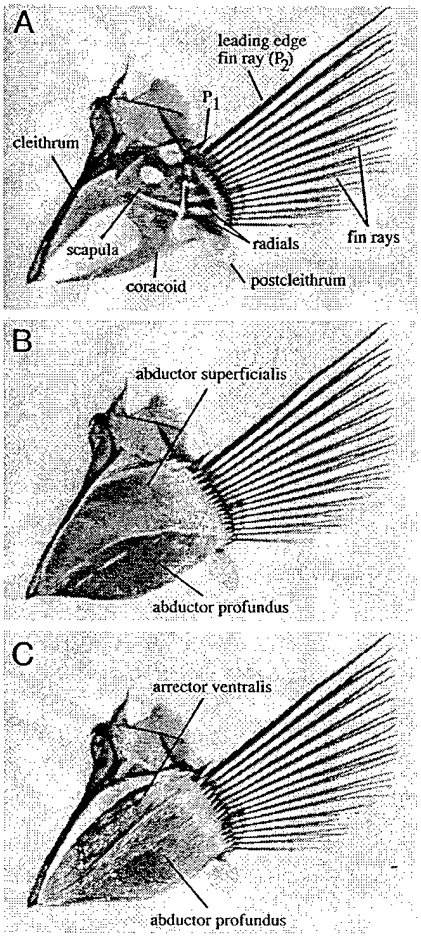

Fig. 2. Morphology of the pectoral fin of *G. varius*. (A) Lateral view of the pectoral girdle, radials, and fin rays. (B) Lateral view of the abductor superficialis profundus muscles, illustrating their origin on the cleithrum, and insertion via tendon onto the fin ray bases. (C) Lateral view of the abductor musculature with the abductor superficialis removed to reveal the arrector ventralis and its insertion onto the P1 ray.

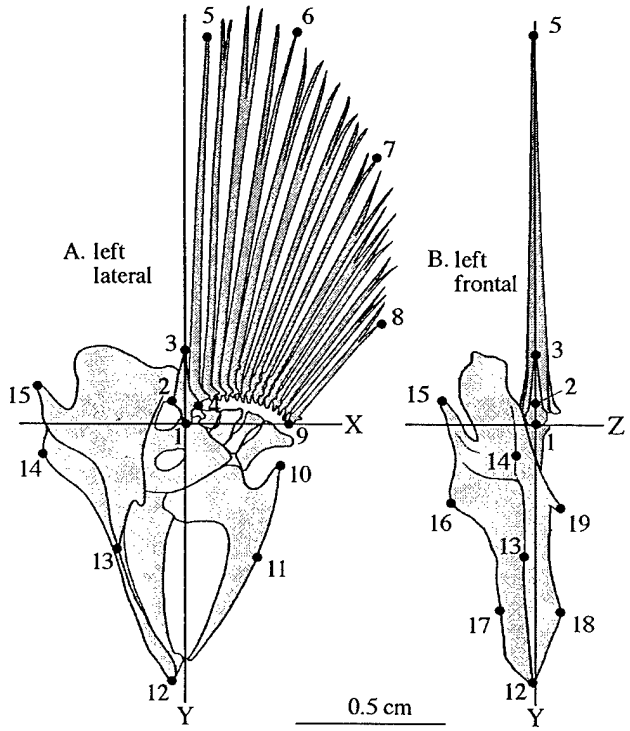

Fig. 3. Morphometric data from lateral and frontal views used as input to a 3-dimensional mechanical model of fin motion. (A) Left lateral view showing morphometrics of 1st fin ray (1-4), fin rays (5-9), and pectoral girdle shape (10-15). (B) Frontal view showing morphometrics of 1st fin ray (1-3), fin tip (5), and pectoral girdle shape (12-19). Points with same number in both views are identical, allowing triangulation in X, Y, and Z planes.

abductor profundus (Fig. 2B) are broad, flattened muscles that originate on the anterolateral face of the cleithrum and insert via the abductor tendons onto pectoral rays 2-16. The arrector ventralis (Fig. 2C) also attaches along the anterolateral edge of the cleithrum, lying medial to the abductor superficialis. The arrector ventralis inserts onto the anterior base of the first pectoral ray by a stout tendon. The adductor complex (not illustrated) is composed of three major muscles and two smaller muscles. The adductors superficialis and profundus originate on the anteromedial surface of the cleithrum and insert via adductor tendons onto pectoral rays 2-16. These muscles are antagonists to the abductors superficialis and profundus. The arrector dorsalis originates anteroventrally on the medial face of the cleithrum and inserts onto the base of the first ray by a stout tendon, as antagonist to the arrector ventralis.

Biomechanical modeling of the pectoral fin.

The mechanics of fin flapping during labriform locomotion is determined by mechanical design and motor inputs to muscles. One way to integrate data on structure, kinematics, and neural patterns is by modeling of the pectoral fin complex. A 3-dimensional mechanical model of the leading edge of the pectoral fin of *Gomphosus* was derived by using lever

theory to analyze the actions of the fin ray when subjected to force generated by fin muscles. The computer model accepts morphometric data on the geometry of the pectoral girdle, the lengths of muscles, and the lever metrics of the fin rays in three views: lateral (Fig. 3A), frontal (Fig. 3B), and medial. Once the geometry of the fin is established, the model simulates various patterns and degrees of muscle contraction. The role of the computer model is to generate predictions about behavior based on the geometric arrangement of the muscles and bones and the motor pattern of muscles.

The action of the arrector ventralis muscle (Fig. 4) is critical to the start of fin abduction during which the fin is rotated forward (protraction) and rotated laterally (abduction). When the fin is in the adducted position (Figs. 4A, 4C) the leading edge fin ray is the y-axis in both left lateral (Fig. 4A) and left frontal view (Fig. 4C). In lateral view, action of the arrector ventralis pulling from point 13 to point 2, and rotating around point 1 (the origin) protracts the fin (Fig. 4B). In frontal view, the arrector ventralis pulls from point 18 to point 2, rotating the fin around point 1 to abduct the fin (Fig. 4D). The vector sum of these two rotations in the XY and YZ plane is a precise prediction of the stroke angle generated by contraction of the arrector ventralis. The model can simulate stroke angle of the fin under conditions of differential contraction strengths (weight) of muscles and differential time lags between onsets of different muscle contractions (Fig. 5).

Results from modeling three muscles of the fins in three *Gomphosus varius* specimens revealed the differential control of the motion of the leading edge of the fin. A range of muscle contractions from 1% to 15% of resting length of each muscle was simulated. For the arrector ventralis, muscle actions resulted in an anteroventral angular rotation of 40 to over 80° (Fig. 5A). Changing the contraction strength of the arrector ventralis muscle (controlling the leading edge) produced stroke angles to almost 120° (Fig. 5B). Changing the lag time between contraction of arrector ventralis and abductor muscles showed little change in stroke angle output.

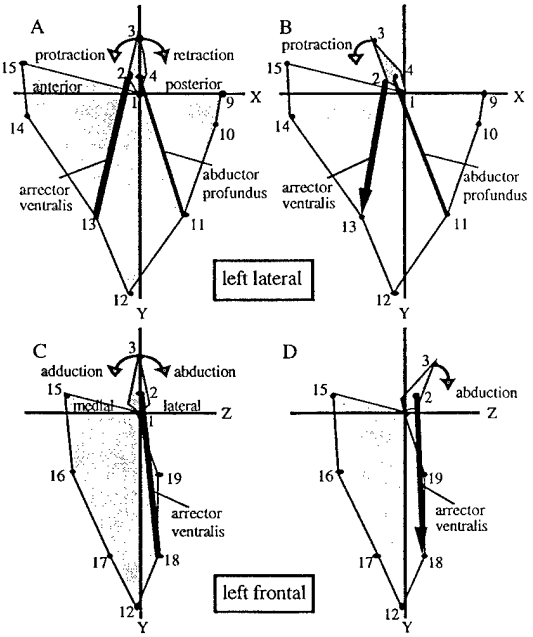

Fig. 4. Mechanical diagram illustrating the model used to compute fin kinematics from morphometric data. (A) The resting state of the mechanical model in lateral view. (B) Lateral view of simulated action of fin ray protraction by contraction of the arrector ventralis. (C) The resting state of the model in frontal view. (B) Frontal view of simulated action of fin ray abduction by contraction of the arrector ventralis.

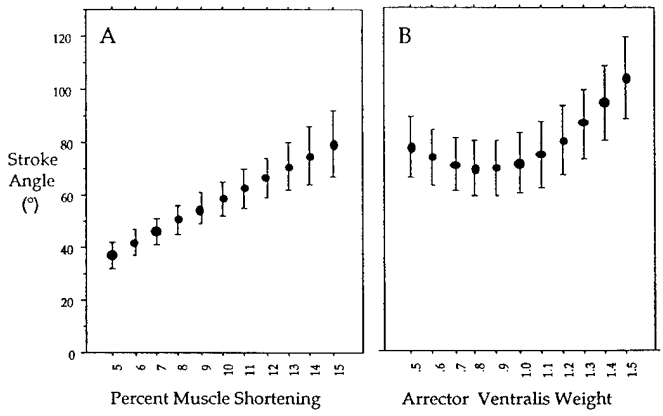

Fig. 5. Model predictions of stroke angle from variability in muscle parameters. Means for five different fishes are shown with error bars indicating one standard deviation. Stroke angle is defined as the total angle between the starting and ending positions of the leading edge. (A) Percent muscle shortening was varied with muscles weighted equally and no lag between muscle firing. (B) Relative weighting of muscles was varied with muscle shortening constant at 15% and no lag between muscle firing. An arrector ventralis weight of 1 indicates that the muscles are weighted equally. Arrector ventralis weight and abductor profundus weight always add up to 2.

Predicted stroke angles are similar to the stroke angle seen in living fishes (see below). The motion of the leading edge depends upon the velocity advantage, the output lever divided by input lever. In Fig. 4A, the velocity advantage of the leading edge is equivalent to the distance from point 2 to the fin tip divided by distance 2-1. The arrector ventralis has a velocity advantage of 16.1. The velocity ratio of the abductor profundus is 20.1, and the arrector dorsalis 12.1. Variable lever ratios enable the fin to perform forceful as well as rapid motion during locomotion.

AUV designs derived from morphology.

A variety of engineering designs are suggested by the morphology of the pectoral fin. Perhaps most useful is the biomimicry of fin shape. Labriform swimmers have a variety of fin shapes, from broad, paddle shaped fins to wing-like designs (Fig. 6). In general, the high performance swimmers using aquatic flight mechanisms have a high aspect ratio wing-like pectoral fin. In contrast, Blake (1981a) found that triangular fins with the apex of the triangle at the fin base were the optimal shape for rowing locomotion. The anatomical basis for fin motion suggests that control of the leading edge of the fin is critical for generating maximal thrust. Four of the six muscles attach to the leading edge, providing precise control of 3-dimensional rotation. The saddle joint of the leading edge base and the lever mechanisms of muscles attaching to the leading edge fin base could also be used in a flapping fin engineering design, although these features might be more easily designed using a ball-and-socket joint and linkages rather than levers that control the leading edge. We suggest that both external and internal morphology can provide new ideas for AUV design features that wait for communication between morphologists and engineers.

3-D kinematics of *Gomphosus varius*.

Walker and Westneat (1997) presented data on 3-D kinematics of the fins of *Gomphosus varius*. Our goals were to understand the complex motions of the fins across a range of speeds and to infer the hydrodynamic mechanisms of thrust from pectoral fins. To summarize the methods, fin markers were placed on the fin tip, two points on the leading edge, and two points on the trailing edge (Fig. 7). The leading and trailing edge markers established two hydrodynamic wing chords that were largely parallel to the flow across the fin during locomotion. The fish swam in a flow tank of volume 360 liters at speeds of 15 to 70 cm/s, and Re (for the fin chord) of about 4000-9000. Video images were recorded at 60Hz in two views: lateral view and a dorsal view reflected by placing a mirror at 45° in the tank (Fig. 9). X, Y, and Z coordinates were measured for each of the fin markers (Fig. 7), and the center of mass of the fish.

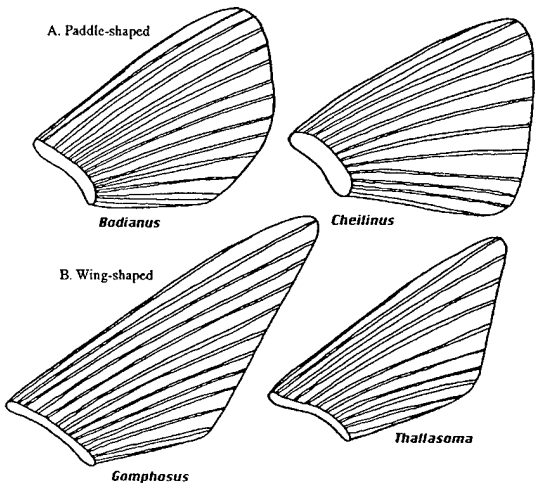

Fig. 6. Diversity of pectoral fin shapes. (A) Broad, paddle shaped fins. (B) Wing-like fins used in high performance labriform swimming.

In the bird wrasse, steady labriform locomotion occurred from about 1.2 - 6.0 TL/s. Fin beat frequency increased linearly with swimming speed across the range of 1.2 to 6 TL/s (Fig. 9A). Stroke angle, the 3-dimensional angular rotation of the leading edge, also increased with swimming speed, ranging from around 80° to nearly 140° (Fig. 9B). As velocity increased, the durations of abduction (Fig. 9C) and adduction (Fig. 9D) decreased. The percentage of the stride of each part of the fin stroke was relatively the same across swimming speeds, with abduction comprising about 60% of the stroke duration at all speeds. This pattern in *G. varius* is different from that found in *Lepomis* (Gibb et al. 1994) and *Cymatogaster* (Webb 1973) in which the percent stride time for abduction decreased and that for refractory period increased.

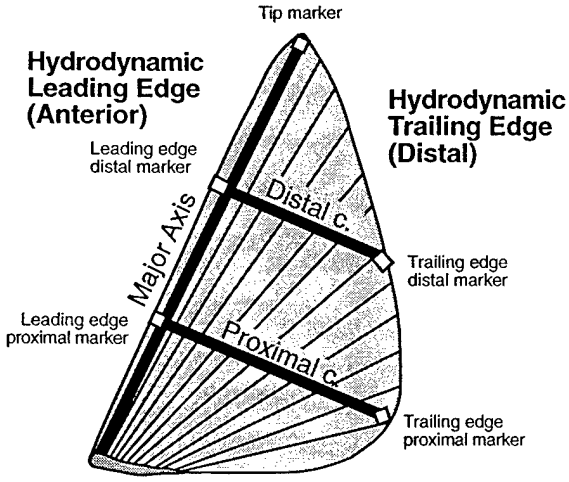

Fig. 7. Locations of the five fin markers. The distal chord is located at two-thirds the length of the fin. The proximal chord is at the widest part of the fin.

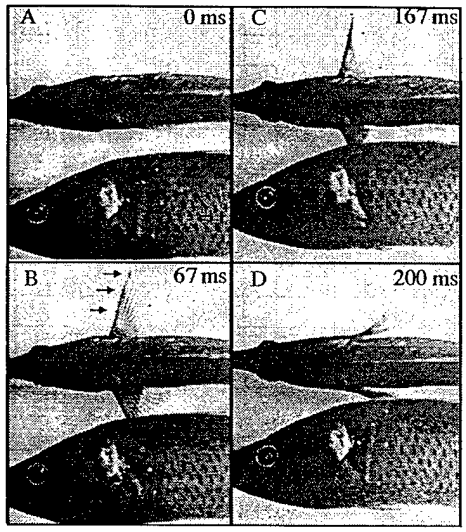

Fig. 8. Video of *G. varius* in lateral and dorsal (mirror) view (A) Abduction, in which dorsal view shows lateral motion of the fin and lateral view shows protraction of the fin. (B) Fin anterior rotation in dorsal view. (C) Start of abduction. (D) Fin is nearly fully adducted.

Motion of the Pectoral Fin Stroke

We describe the geometry of the fin in both lateral projection (onto a sagittal, or xz, plane) and in the full 3D space of the fish. The fish swims in the positive x direction. Lateral motion is on along the y-axis and up and down motion is along the z-axis (Fig. 10A). The motion of the tip marker is largely confined to oscillation along a single arc on the sphere. An arc on a sphere is a segment of the intersection between the sphere and a plane through the sphere. For the fin tip marker, this plane is the stroke plane. The stroke plane, as traditionally defined in insects (Jensen 1956), includes the base of the wing, intersects a frontal plane orthogonal to the anterior-posterior axis of the body, and intersects a sagittal plane by the inclination of the wing tip trace in lateral projection relative to the body. We used the major axis of the scatter of the fin tip points in lateral projection relative to the body to estimate the inclination of the stroke plane, or stroke plane angle, β (Fig. 10A). The mean value of β was 19.4°.

The major axis of the fin of *G. varius* (the leading edge ray) does not oscillate back and forth on the stroke plane but sweeps back and forth along the edge of a cone whose vertex is the dorsal base of the fin (Fig. 10D). A similar geometry is also observed in the hind-wing of the dragonfly (Azuma and Watanabe 1988). In *G. varius*, the fin tip marker oscillates, with some deviation, along an arc of the cone's base (Fig. 10D). We define the stroke plane as the plane containing the base of the stroke cone. In this geometry, the flapping axis, about which the fin rotates, is the central axis of the cone. The stroke plane varies in its anterolateral inclination, from being nearly orthogonal to the body axis in dorsal view to vertical or posteroventrally inclined planes with anterolateral orientations in dorsal view. Each of these geometries allows the fin tip to travel anteriorly during the downstroke.

The trace of the path of the fin tip moving relative to the fin base resembles a thin, inclined, figure-of-eight when projected onto a sagittal plane. The direction of the movement along the figure-of-eight is counter-clockwise along the dorsal loop and clockwise along the ventral loop. The traces are similar at all speeds (Fig. 11), except that the size of the dorsal loop is bigger than the ventral loop at low speeds but the reverse pattern occurs at high speeds. This pattern differs from those of the bluegill, in which the fin-tip trace changes dramatically with speed (Gibb et al. 1994). We use the figure-of-eight pattern observed in all sequences to divide the stroke cycle into four phases. phases I and II are subdivisions of abduction while phases III and IV are subdivisions of adduction.

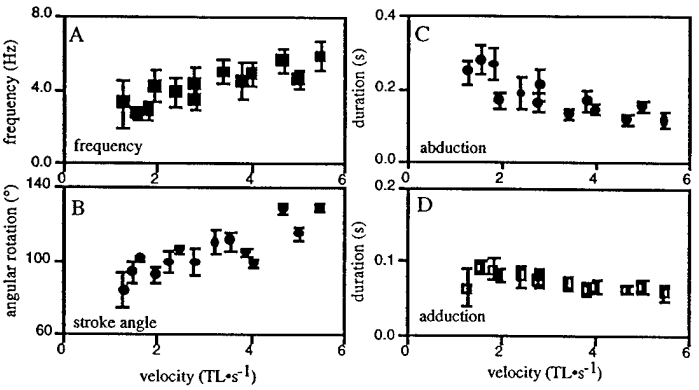

Fig. 9. Kinematic profiles of pectoral fin motion in *Gomphosus varius* across a speed range of 1-6 total lengths per second (TL•s-1). The frequency (A) and stroke angle (B) increase with increased swimming speed, whereas the durations of abduction (C), and adduction (D) decrease with increasing swimming speed.

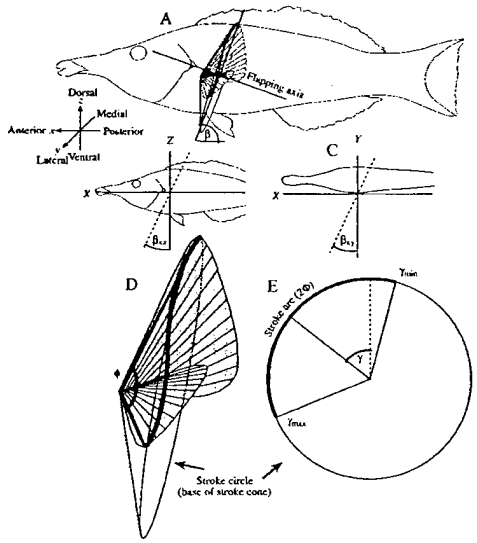

Fig. 10. Geometry of stroke parameters. A. Stroke cone and stroke plane angle, ß. B. Projection of the stroke in lateral view. C. Projection of the stroke in ventral view. D. Geometry of the stroke angle, ϕ. Curved line represents path of fin tip. E. Geometry of fin tip position, stroke arc, and stroke arc angle, 2 Φ.

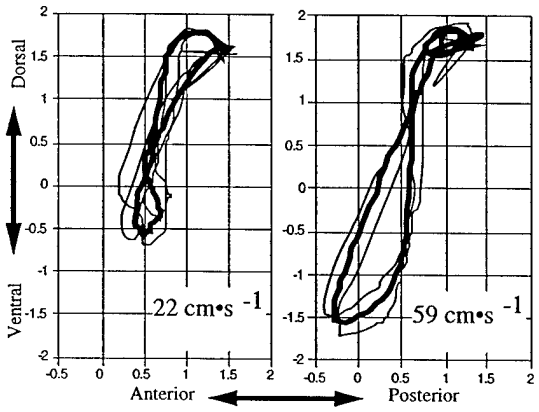

Fig. 11. Trace of fin tip path in lateral view. The figure-eights are projections of traces onto sagittal plane. Traces were estimated by a least-squares fitted Fourier function to the time-standardized data . Thin lines represent individuals, thick-lines represent mean traces.

Phase I begins with the fin tip at its maximum posterior position. In this phase the fin is protracted along the body. Phase II begins with the fin tip at its most superior position. Extension of the fin down and away from the body surface initiates phase II. This motion is led by the distal portion of the leading edge and passes distally to proximally and anteriorly to posteriorly. This has the effect of peeling the fin off the body surface by pulling the fin tip. Following this peel, the fin is depressed and may be slightly protracted or retracted. The tip of the fin is positioned caudal to the fin base throughout this downstroke giving the pair of fins a swept planform in dorsal view. During the course of the downstroke, the fin is pronated, twisting along its length in a counterclockwise direction (as seen in left lateral view). At low velocities, the fin may be maintained near maximum abduction for a short duration.

In phase III, the fin is supinated, protracting and elevating the leading edge and causing the fin to twist in a direction opposite to that in phase II. In phase IV, the fin is rapidly retracted and elevated to the initial phase I position. Supination continues in beginning of phase IV causing the distal portion of the fin to have a nearly vertical orientation.

The vertical oscillation and dynamic twisting of the fin causes the marked chords to heave (translate) and pitch (rotate) throughout the stroke cycle. Projections of the proximal and distal chords on a sagittal plane (Fig. 12)

illustrate time-dependent changes in the position (due to heave) and orientation (due to pitch) of the proximal and distal chords. Time-dependent changes in pitch for the proximal chord (Fig. 12A) are fairly simple because of the very small displacement of the proximal trailing edge marker throughout the stroke cycle. At the start of phase I, the chord has a high positive, or nose-up, pitch at all speeds. During the downstroke (phase II), the pitch gradually decreases, reaching small negative, or nose down, values at higher speeds. In phases III and IV, the pitch gradually increases with a pattern that is simply the reverse of that in phases I and II.

In contrast to that of the proximal chord, the pattern of change in pitch of the distal chord differs appreciably between the abductive and adductive phases (Fig. 12B). The leading edge fin ray begins the downstroke (phase II) while the trailing edge fin ray is still elevating andprotracting and is roughly halfway through phase II when the trailing edge begins depression. This delay in the trailing edge results in the distal chord attaining negative pitch at midway through phase II at all speeds. During the second half of the downstroke, the distal chord reaches higher negative pitch at higher speeds. In phase IV, the trailing edge reaches maximum protraction about the time the leading edge has rotated half the distance back to the starting location of phase I. At this point, the distal chord presents a distinct convex downward bend. The distal chord, therefore, reattains a high positive pitch during this phase. The highest positive pitch occurs in fish swimming at the lowest swimming speed.

Inspection of heave and pitch of the fin chords suggest that leading and trailing edges are out of phase, with the trailing edge lagging behind. This phase difference reflects an undulatory wave passing from leading to trailing edge. To illustrate the phase lag, we compared instantaneous positional angles of the leading edge distal marker trailing edge distal marker. Phase lags ranged from between 10% and 20% of the stroke cycle. The mean phase lag across all sequences, fish, and speeds is 19.2°. We found no correlation between phase lag and swimming speed.

Center of mass kinematics.

Swimming bird wrasses oscillate up and down during steady swimming, especially at higher swimming speeds. The fore-aft acceleration trace (Fig. 13) presents two acceleration peaks per cycle, one occurring about one-third of the way through abduction (0.33Ab) and the second occurring two-fifths of the way through adduction (0.4Ad). During abduction, forward, or positive, acceleration peaks relatively earlier at low speeds compared to high speeds. In adduction, the peak occurs at the same relative time at all speeds. The magnitude of the acceleration peaks vary both between abduction and adduction and with speed. The abduction peak is only slightly higher than the adduction peak at low speeds but is substantially higher at high speeds. Median maximal forward acceleration decreases with speed during abduction but increases with speed during adduction.

Acceleration minima occur at or near phase transitions between abduction and adduction. The adduction minimum, occurring when the fin is maximally adducted, is increasingly negative with increasing speed. The abduction minimum occurs not at maximal fin abduction but about 0.8Ab. Unlike the adduction minima, the abduction minima are similar at all speeds.

The dorsoventral acceleration trace varies considerably among swimming speeds (Fig. 13). At all speeds, there is a distinct upward, or positive, acceleration during abduction occurring just prior to 0.5Ab. Peak accelerations increase with speed at this point of the cycle. During adduction, dorsoventral acceleration has a second upward acceleration maximum at the lowest swimming speed (occurring at 0.4 Ad) but a downward acceleration maximum at the highest speed (occurring at 0.2 Ad).

Kinematics and AUV design.

The motions of the fins in high performance labriform swimmers that use underwater flight provide an excellent source of information for AUV engineers. Three-dimensional kinematic data of the leading and trailing fin edges, fin tip, and fin chords offer a qualitative, quasi-steady interpretation of hydrodynamic regimes that are consistent with center of mass kinematics. However, the biomechanics of this swimming mode appear to involve the use of hydrodynamic lift, drag, and a substantial set of unsteady effects from the rapidly oscillating fins.

To increase swimming speed, a fish must modify its propulsive kinematics in order to generate the extra thrust to overcome the increased drag on the body. Increased flapping frequency, stroke amplitude, or both are common mechanisms of generating increased thrust in many paired appendage propulsors. Flapping frequency increases with tank speed in all individuals tested. An increase in flapping frequency both maintains an appropriate direction of the resultant stream vector to generate a thrust component of hydrodynamic lift and increases any contribution from the acceleration reaction. These are clearly aspects of fin behavior that should be incorporated in AUV fin design.

Thrust increases with the volume of water accelerated by the flapping fins. This acceleration reflects either added mass effects or the circulation "inducing" a component of velocity normal to the resultant flow. *G. varius* apparently controls this volume by either increasing stroke amplitude or "flattening" the stroke cone. We suggest that AUV design should include the capability of modifying the stroke amplitude and the stroke plane angle in order to optimize thrust at different speeds.

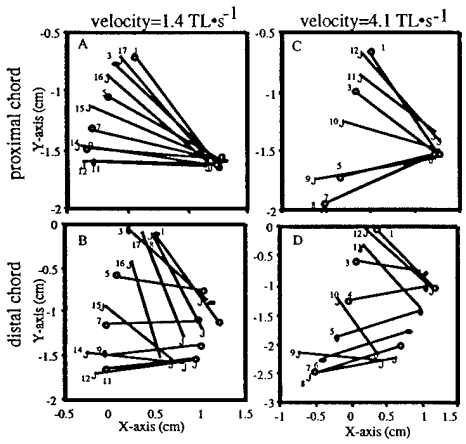

Fig. 12. Angle of attack of fin chords during swimming. Open circles are abduction, closed circles are adduction, numbers refer to video fields during one fin beat. The fin twists along its length during motion. Proximal chord (A and C) has a positive angle of attack at low speed, a negative angle of attack at higher speed. Distal chord has a negative angle of attack at both speeds.

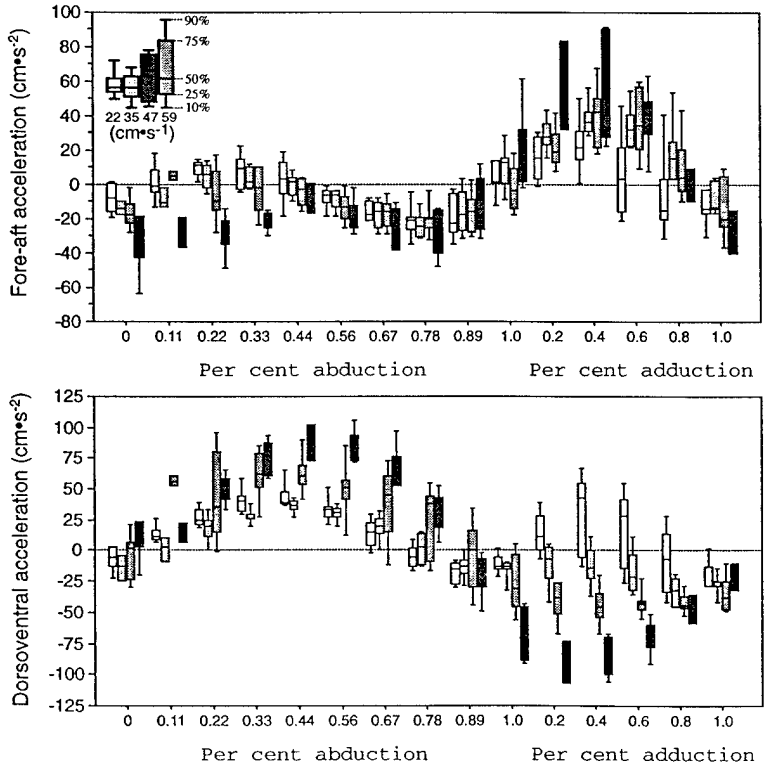

Fig. 13. Distribution of center of mass accelerations in fore-aft (A) and dorsoventral (B) directions. Each box is the pooled distribution of all sequences and individuals at a given tank speed. Both abduction and adduction in each sequence were standardized independently. Data were binned into 10 abduction-phase time classes and 6 adduction-phase time classes (Both abduction and adduction share the time class at phase transition).

It is difficult to compare our measures of fin excursion with those of previous studies because our angles reflect the actual 3D displacement of the fin tip while all previous studies report only the projection of the displacement onto a single plane (Blake 1979; Geerlink 1983; Archer and Johnston 1989; Gibb et al. 1994; Drucker and Jensen 1996). In fishes that abduct the leading edge along a largely horizontal stroke plane, a measure of amplitude from a dorsal view (as in Blake 1979 and Archer and Johnston 1989) will closely approximate a 3D measure. The leading edge of the fin rotates 120° to 140° in the frontal plane of *Coris formosa* (Figs. 2, 4 of Geerlink [1983]) but only 90° in *Cymatogaster aggregata* (Webb 1973). In *G. varius*, leading edge rotation within the frontal plane increases with swimming speed and only regularly exceeds 90° (when the tip attains negative x values) at high velocities.

The largely dorsoventral motions of the flapping fins in *G. varius* suggest that hydrodynamic lift due to a net circulation around the fins is the major steady mechanism for generating thrust at the center of mass during sustained swimming at all speeds. From kinematic patterns of the center of body mass, we have inferred three hydrodynamic features of the bird wrasse fin stroke: **(1)** A small thrust peak occurs midway through abduction (downstroke) while a larger thrust peak occurs midway through adduction (upstroke). **(2)** An upward force peak occurs during the downstroke. The magnitude of this peak increases with swimming speed. **(3)** The dorsoventral force peak occurring during the upstroke is speed dependent. At slow speeds, a small upward force occurs. At higher speeds, a downward force peak occurs. The magnitude of the downward force increases with speed.

These thrust features of the stroke could readily be imitated by fin-shaped appendages on AUVs. For control of AUV speed and stability, the frequency, amplitude, and angle of attack of the fin stroke can be modified. Walker and Westneat (1997) discuss the implications of labriform thrust mechanics in terms of the hydrodynamic regime operating on the pectoral fin. Consideration of both quasi-steady mechanics and unsteady forces yield insight into flapping fin hydrodynamics that agree with the acceleration profiles of the center of mass. However, confirmation of the role of lift and acceleration reaction forces to the thrust of labriform swimmers will depend on flow visualization studies and modeling fish wing hydrodynamics. The interaction between AUV engineers and fish biomechanics should produce useful new vehicle designs and increase our understanding of animal kinematics.

ACKNOWLEDGMENTS

Thanks to Margaret Pizer for her work on the morphology and biomechanical modeling, and to Dan Dudek for his help with swimming performance studies. This research was funded by National Science Foundation grant IBN-9407253.

REFERENCES

Archer, S. D. and I. A. Johnston. 1989. Kinematics of labriform and subcarangiform swimming in the antarctic fish *Notothenia neglecta*. J. Exp. Biol. 143: 195-210.

Arreola, V. I. and M. W. Westneat. 1996. Mechanics of propulsion by multiple fins: kinematics of aquatic locomotion in the burrfish (*Chilomycterus schoepfi*). Proc. Roy. Soc. Lond. B 263: 1689-1696.

Azuma, A. and T. Watanabe. 1988. Flight mechanics of a dragonfly. J. Exp. Biol. 137: 221-252.

Bandyopadhayay, P. R., J. M. Castano, J. Q. Rice, R. B. Philips, W. H. Nedderman, and W. K. Macy. 1997. Low-speed maneuvering hydro-dynamics of fish and small underwater vehicles. J. Fluids Eng. 119: 136-144.

Blake, R. W. 1979. The mechanics of labriform locomotion. I. Labriform locomotion in the angelfish (*Pterophyllum eimekei*): an analysis of the power stroke. J. Exp. Biol. 82: 255-271.

Blake, R. W. 1981a. Influence of pectoral fin shape on thrust and drag in labriform locomotion. J. Zool. Lond. 194: 53-66.

Blake, R. W. 1981b. Mechanics of drag-based mechanisms of propulsion in aquatic vertebrates. Symp. Zool. Soc. Lond. 48: 29-52.

Blake, R. W. 1983a. *Fish Locomotion*. Cambridge University Press, Cambridge.

Blake, R.W. 1983b. Median and paired fin propulsion. *In* P. W. Webb and D. Weihs (eds.), *Fish Biomechanics*, pp. 214-247. Praeger Press, New York.

Breder, C.M. 1926. The locomotion of fishes. Zoologica 4: 159-297.

Daniel, T. L. 1984. Unsteady aspects of aquatic locomotion. Amer. Zool. 24: 121-134.

Daniel, T. L. and E. Meyhofer. 1989. Size limits in escape locomotion of carridean shrimp. J. Exp. Biol. 143: 245-265.

Daniel, T.L. & Webb, P.W. (1987). Physical determinants of locomotion. *In* Comparative Physiology: Life in Water and on Land (ed. P.

Dejours, L. Bolis, C. R. Taylor, and E. R. Weibel), pp. 343-369. New York: Liviana Press.

Dickinson, M.H. 1994. The effects of wing rotation on unsteady aerodynamic performance at low Reynolds numbers. J. Exp. Biol. 192: 179-206.

Drucker, E. G. and J. S. Jensen. 1996. Pectoral fin locomotion in the striped surfperch. I. Kinematic effects of swimming speed and body size. J. Exp. Biol. (in press).

Geerlink, P. J. 1979. The anatomy of the pectoral fin of *Sarotherodon niloticus* Trewavas (Cichlidae). Neth. J. Zool. 29: 9-32.

Geerlink, P. J. 1983. Pectoral fin kinematics of *Coris formosa* (Teleostei, Labridae). Neth. J. Zool. 33: 515-531.

Geerlink, P. J. 1989. Pectoral fin morphology: a simple relation with movement pattern? Neth. J. Zool. 39: 166-193.

Gibb, A. C., B. C. Jayne, and G. V. Lauder. 1994. Kinematics of pectoral fin locomotion in the bluegill sunfish *Lepomis macrochirus*. J. Exp. Biol. 189: 133-161.

Jensen, M. 1956. Biology and physics of locust flight. III. The aerodynamics of locust flight. Phil. Trans. R. Soc. Lond. B 239: 511-552.

Kato, N. and M. Furushima. 1996. Pectoral fin model for maneuver of underwater vehicles. IEEE Symposium on AUV technology, Monterrey CA. pp. 49-56.

Spedding, G. R. and T. Maxworthy. 1986. The generation of circulatiuon and lift in a rigid two-dimensional fling. J. Fluid. Mech. 165: 247-272.

Vogel, S. 1994. *Life in moving fluids*. Princetom University Press, Princeton.

Van den Berg, C. and C. P. Ellington. 1997a. The vortex wake of a hovering model hawkmoth. Phil. Trans. R. Soc. Lond. B352: 317-328.

Van den Berg, C. and C. P. Ellington. 1997b. The three-dimensional leading-edge vortex of a hovering model hawkmoth. Phil. Trans. R. Soc. Lond. B352: 329-340.

Walker, J. A., and M. W. Westneat. 1997. Kinematics of underwater flight: locomotor behavior of the bird wrasse, *Gomphosus varius*. J. Exp. Biol. 1549-1569.

Webb, P. W. 1973. Kinematics of pectoral fin propulsion in *Cymatogaster aggregata*. J. Exp. Biol. 59, 697-710.

Westneat, M. W. and J. A. Walker. 1997. Motor patterns of underwater flight: an electro-myographic study of the pectoral muscles in the bird wrasse, *Gomphosus varius*. J. Exp. Biol. 200, 1881-1893.

Westneat, M. W. 1996. Functional morphology of aquatic flight in fishes: mechanical modeling, kinematics, and electromyography of labriform locomotion. Amer. Zool. 36:582-598.